Shape Measurement of Single Nanoparticles in Water Using Optical Microcavities



Yumeng Yin
Mansfield College
University of Oxford

A thesis submitted for the degree of
Doctor of Philosophy

Trinity 2024

Acknowledgements

I would like to first express my greatest thanks to Professor Jason Smith, my supervisor in my DPhil study. I really enjoy the discussions with you and performing theoretical calculations on the whiteboard with you together. You are always brilliant, patient and wise to give me advice on not only the research work but also different skills and the way of thinking. I always appreciate your support at different stages during my DPhil life in Oxford.

Next, I want to thank the PNG group and all the group members. Matt, thanks for the optical training, and advice for my experiments and career, so wonderful to have you in my DPhil. Yu, thanks for the time we spent together and all the joy we shared. Gareth, thanks for all of the discussions and your experience in different fields. Philippa, appreciate the time we worked together in the dark lab and the time we hung out in the sunshine. Jiangrui, thanks for the FIB work, and the chats you shared your experience with me. Xingrui, thanks for making my office life interesting and happy. Nick, great to work with you listen to your new ideas and see you put them into action. Shazeaa, thanks for your warmful welcome for me to the group and the amazing birthday cake and celebration for me. Amit, Aurelien and Kiana, thanks for your training and your previous work. Andrew, thanks for your humour and valuable advice.

Then, I want to thank all my good friends here in Oxford for your companionship and all the joy and happiness we share, especially Minyi and Yuhan. I really appreciate the time cooking, travelling, chatting and laughing with you, Minyi. I cherish

the moments we played the piano together, travelled together, and talked about new things to explore, Yuhan. Special thanks to Tiger for entering my life, bringing me happiness and sharing ups and downs.

Lastly, I want to express my huge thanks to my parents for your unconditional love and support for me as always. I always feel lucky to have you by my side no matter what happens and I appreciate that you always back my decisions.

Abstract

Nanoparticles have attracted significant attention with their unique properties and wide applications in diverse fields. Shape, as an important physical property of a nanoparticle, impacts the electrical, optical and chemical properties of a nanoparticle and is worth characterising. In addition, rod-shaped bacteria and viruses in water raise concerns about public health. Therefore, shape measurement can not only be applied in the quality control of nanoparticles but also acts as an early indication of harmful bacteria in water to people. In this work, a novel technique is proposed to perform the shape measurement of rod-shaped particles in water, namely measuring the aspect ratio at a single-particle scale in situ. The perturbation of a rod-shaped particle in water to the resonant mode formed by the optical microcavity is captured to obtain the shape information of the particle. Three Stokes parameters are measured to characterise the polarisation state of the transmitted light through the optical microcavity, deviating from the incident circularly-polarised light. With the theoretical model constructed, the polarisability-related parameters can be extracted from the curves of the Stokes parameters and the aspect ratio can be deduced afterwards. The experimental results of both gold nanorods and rod-shaped bacteria particles are presented along with the theoretical simulations of the diffusion behaviour and the optical field inside the microcavity. Therefore this technique can be a powerful tool in the shape measurement of rod-shaped particles in water with the potential in real-world applications and can be adapted to more complex measurements.

Contents

1 Introduction **1**

1.1 Thesis Overview 2

2 Literature Review **6**

2.1 Introduction 6

2.2 Shape Measurement Methods 7

2.2.1 Scanning Electron Microscopy (SEM) 8

2.2.2 Transmission Electron Microscopy (TEM) 10

2.2.3 Dynamic Light Scattering (DLS) 13

2.2.4 Nanoparticle Tracking Analysis (NTA) 15

2.2.5 Angle-resolved Ligh Scattering (ALS) 17

2.2.6 Interferometric Scattering Microscopy (iSCAT) 18

2.2.7 Single Particle Orientation and Rotational Tracking (SPORT) 20

2.2.8 Spectroscopy 22

2.2.9 Dark Field Microscopy 24

2.3 Optical Microcavities 25

2.3.1 Fabry-Pérot Microcavities 26

2.3.2 Whispering Gallery Mode (WGM) Microcavities 31

2.3.3 Photonic Crystal Microcavities 36

2.4 Summary 43

3 Theory **45**

3.1 Introduction 45

3.2 Gaussian Beam 45

3.3 Hermite-Gaussian Beam 47

3.4 Open-access Optical Microcavity 49

3.5 Optical Modes in the Microcavity 51

3.6 Shape Measurement Through the Microcavity With Polarised Light . 56

3.6.1 Empty Cavity . . . 56
3.6.2 Cavity with a Particle . . . 57
3.6.3 Cavity with Anisotropic Particle . . . 59
3.6.3.1 Gold Nanorod . . . 63
3.6.3.2 Rod-shaped Bacteria Particle . . . 68
3.7 Other Theoretical Calculations . . . 69
3.7.1 Rotational Diffusion . . . 69
3.7.2 Optical Torque . . . 70
3.7.3 Optical Force . . . 71
3.7.4 Cross-section Calculation . . . 71
3.7.5 Heat Calculation . . . 72
3.8 Theoretical Simulations . . . 72
3.8.1 Monte Carlo Simulation . . . 73
3.8.1.1 Langevin Equation . . . 73
3.8.1.2 Coordinate System Conversion . . . 76
3.8.2 Finite-difference Time-domain (FDTD) Simulation . . . 81
3.9 Summary . . . 84

4 Experimental Method **86**
4.1 Introduction . . . 86
4.2 Optical Microcavity Chip . . . 86
4.2.1 Ridge Fabrication . . . 86
4.2.2 Focused Ion Beam (FIB) Milling . . . 88
4.2.3 Coating and Dicing . . . 89
4.3 Experimental Apparatus . . . 90
4.3.1 Flow Cell . . . 90
4.3.2 Microfluidic System to Deliver the Solution . . . 93
4.3.3 Optical Apparatus . . . 94
4.3.4 Specifications of Cavities Used in the Experiment . . . 102
4.4 Data Processing . . . 103
4.5 Characterisations of Samples . . . 104
4.5.1 DLS . . . 104
4.5.2 UV-Vis Spectrometer . . . 106
4.5.3 SEM . . . 107
4.6 Sample Preparation . . . 108

5 Gold Nanorod Measurement **110**
5.1 Introduction . . . 110
5.2 Benchmark Characterisation Techniques . . . 111
5.2.1 DLS . . . 111
5.2.2 UV-Vis Spectrometer . . . 113
5.2.3 SEM . . . 114
5.3 User Interface for Data Processing . . . 116
5.4 A Single-Particle Event . . . 118
5.4.1 Gold Nanosphere Measurement . . . 119
5.4.2 Gold Nanorod Measurement . . . 120
5.5 Statistical Results for 30 Particles . . . 127
5.6 Other Factors to Consider . . . 129
5.6.1 Rotational Diffusion . . . 129
5.6.2 Cross-section Calculation . . . 130
5.6.3 Heat Calculation . . . 131
5.6.4 SEM Images Further Analysis . . . 131
5.6.5 Minimum Aspect Ratio Analysis . . . 132
5.6.6 Prefered Direction . . . 132
5.7 Summary . . . 134

6 Rod-shaped Bacteria Particle Measurement **136**
6.1 Introduction . . . 136
6.2 SEM Imaging . . . 137
6.3 Experimental Conditions . . . 139
6.4 Analysis . . . 139
6.4.1 Anisotropy Loss Tangent Histogram Fitting . . . 140
6.4.2 4 kHz Scanning . . . 140
6.4.3 10 Hz Scanning . . . 144
6.4.4 Aspect Ratio Deduction Analysis . . . 146
6.5 Other Factors to Consider . . . 149
6.5.1 Optical Force . . . 149
6.5.2 Rotational Diffusion Analysis . . . 149
6.5.3 Scattering Cross-section Calculation . . . 150
6.6 Limitations and Improvements . . . 150
6.7 Summary . . . 152

7 Simulation **154**
7.1 Introduction 154
7.2 Monte Carlo Simulation 155
7.2.1 Gold Nanosphere Simulation 156
7.2.2 Gold Nanorod Simulation 158
7.2.2.1 Trajectory in the Optical Microcavity 159
7.2.2.2 Angular Distribution 161
7.2.3 Rod-shaped Bacteria Particle Simulation 164
7.3 Finite-Difference Time-Domain (FDTD) Simulation 167
7.3.1 Simulation Configuration 167
7.3.2 Angle of Rod-shaped Bacteria Particle 171
7.3.2.1 Angle in xy Plane 171
7.3.2.2 Angle in xz and yz Plane 174
7.3.3 Position of Rod-shaped Bacteria Particle 176
7.4 Summary 180

8 Conclusions and Outlook **183**
8.1 Conclusions 183
8.2 Future Work 185

List of Figures

2.1 Schematic of a typical SEM, reproduced from [21]. It illustrates a source emitting a beam of electrons passing though an anode for accelaration. A series of lenses focuses the beam onto the sample. The detectors collect different electrons after interacting with the sample, including back-scattered electrons, x-ray and secondary electrons. A commerical software is utilised for monitoring and control. 9

2.2 Schematic of a typical TEM, reproduced from [21]. It illustrates a source emitting a beam of electrons passing though an anode for accelaration. A series of lenses focuses the beam onto the sample and also collects the signals better after the transmission through the sample. The detectors on the transmission side of the sample collect different electrons after interacting with the sample. A commerical software is utilised for monitoring and control. 11

2.3 Schematic of a typical DLS instrument, reproduced from [63]. The laser beam irradiates the sample cuvette and the detector collects the scattered light from the particles in the back-scattered direction for further autocorrelation analysis. 14

2.4 Schematic of NTA, reproduced from [70]. The laser beam irradiates the solution with particles and the microscope collects the scattered light from particles for further data analysis. 16

2.5 Various schematics for illumination and detection reproduced from [83]. The red arrow represents the dipole moment associated with a nano-object. Light green and shaded areas indicate the illumination (E_i) and the scattered fields (E_s), respectively. (a) Point detection in transmission via focused illumination. (b) Wide-field illumination and transmission detection on an imaging camera. (c) A reflection-based scheme for point detection with illumination similar to (a). (d) Point detection in transmission with focused illumination, similar to (a) but with an external reference beam of field (E_{ext}). (e) A scheme of illumination and wide-field imaging by means of reflection, equivalent to a folded version of (b). 18

2.6 Schematic of an automated high-speed SPORT apparatus, reproduced from [111]. Light irradiates the sample and the a series of optical componenents are used for further analysis. Bifocal plane imaging was achieved by splitting the acquired signal into two imaging channels (focused and defocused channels) by inserting a beam splitter. The automatic feedback system is added to remove noise. OBJ: objective, OS: objective scanner, WP: wedge prism, BS: beam splitter, L1 and L2: lens with different focal lengths, CCD: charge coupled device. . . 21

2.7 Schematic of a UV-Vis spectrometer, reproduced from [115]. The diffraction grating determines the optical resolution and the wavelength range of the spectrometer. The incident light is split into a reference and sample beam to pass through the reference and sample cuvette respectively. 22

2.8 Schematic of a dark field single particle spectrophotometry, reproduced from [129]. The white light from a halogen lamp (LM) is directed to an electro-optical filter (EOF) that filters the light into its constituent wavelengths. The filtered spectral wavelengths coming from the tunable optical filter are then coupled to the epi-illuminator (IL) of the microscope and focused on the sample surface through a beam-splitter (BS) and a dark-field objective (OB). A CMOS camera placed at the image plane of the experimental setup collects the scattered light for each illumination wavelength. The sample imaging is performed in transmission mode, while the sample spectrophotometry is done in reflection mode. 25

2.9 The figure is reproduced from [150]. (a) White lamp transmission of a single cavity is recorded as a function of time. (1) The glucose solution is injected. (2) The glucose solution reaches the cavity. (3) Deionised water is injected. (4) Water reaches the cavity. (b) The black line is the measured refractive index over time. The blue region is the expected refractive index from the glucose solution. The grey line is the refractive index measurement assuming no cavity length noise using a single cavity (from the spectrum of the cavity with the smallest length). The inset shows the Allan variance for the measured refractive index as a function of the sampling time. 28
2.10 The figure is reproduced from [151]. (a) Attenuation of a single cavity mode as increasing concentrations of methylene blue in ethanol are introduced into the microcavity. (b) Plot of equation 2.8 is used to determine the cavity enhancement factor. The data were fitted to a straight line passing through the origin with a regression coefficient of $R^2 = 0.9967$. 29
2.11 The figure is reproduced from [179]. Excitation of an equatorial WGM of a microsphere by evanescent coupling to a guided wave in a tapered optical fibre. Resonance positions are detected as dips in the transmitted light T at particular laser wavelengths. 32
2.12 The figure is reproduced from [180]. (a) Series of normalized transmission spectra taken at a 1550 nm wavelength band and the corresponding optical images (assisted by a visible light laser) recorded without nanoparticles (top trace) and with four successive depositions of KCl nanoparticles. The spectra are vertically shifted for clarity. (b) Normalized splitting versus particle number for KCl nanoparticles. Each discrete step (vertical lines are drawn to guide the eye) corresponds to a single nanoparticle binding event. The inset shows an enlarged plot for nanoparticles of R = 40 nm. 33
2.13 Raman enhancement of rhodamine 6G through the silica microsphere, reproduced from [187]. Background subtracted Raman spectra of rhodamine 6G for tapered fibre coupler excitation (blue), free-space excitation on a microsphere (red), and free-space excitation on the substrate (green). The spectra for free-space excitation on the microsphere and substrate are scaled by 100 times for visibility. 35

2.14 The figure is reproduced from [213]. SEM view of a photonic crystal microcavity integrated with two ridge waveguides. The regular hole and the defect hole diameter are 0.58a and 0.4a respectively with a = 440 nm of the lattice constant of the photonic crystal. 38
2.15 The figure is reproduced from [213]. (a) Normalised transmission spectra of the photonic crystal microcavity with different ambient refractive indices ranging from n = 1.446 to n = 1.454 in 0.002 increments. (b) Resonant wavelength and the corresponding refractive index over time during the evaporative process of water in a glycerol-water mixture. . 38
2.16 SEM images showing the H1-r and L3 defects in vicinity of the photonic crystal-waveguide, reproduced from [216]. 39
2.17 Dispersion properties of slotted photonic crystal with different background refractive indices, reproduced from [217]. Inset: SEM image of a slotted photonic crystal cavity with zoomed view of the (a) central and (b) external part of the slot. 40
2.18 The figure is reproduced from [218]. (a) SEM image of the device and schematic of the experimental apparatus. A polarisation controller was used to maximise the transverse electric mode. (b) Schematic of biomolecule recognition. The target molecules were captured by the probe molecules, changing the refractive index. 41
2.19 The figure is reproduced from [220]. (a) Sketch of nanoring resonator. (b) Sketch of dual nanoring resonator. 42

3.1 Variation of the spot size $w(z)$ of a Gaussian beam, reproduced from [226]. $z = 0$ has a beam waist of w_0, z_0 is the Rayleigh range where the beam width is $\sqrt{2}w_0$, $w(z)$ is the beam width at z. θ is the divergence angle of the Gaussian beam. 47
3.2 Hermite-Gaussian beam profile in xy plane with the light propagating in z direction. The labels are in the form of (m, n). 48
3.3 (a) Diagram of a microcavity at resonance with $q = 4$. I is the incident light while T is the transmission. L is the cavity length. (b) An example of the transmitted spectrum where $\triangle\lambda$ is the FSR and $\delta\lambda$ is the linewidth of a cavity mode. 49

3.4 Schematic of one planar mirror and one concave mirror forming the microcavity $z = 0$ is the planar mirror position as well as the beam waist location. $z = L$ is the concave mirror position and the RoC of the concave feature is R. 51
3.5 Schematic of two concave mirrors forming the microcavity. z_1 and z_2 are the positions of the two concave mirrors with RoC of R_1 and R_2. 52
3.6 Schematic of an optical microcavity with the incident and reflected light labelled. The microcavity used in the experiment has a depth of 600 nm and a RoC of 25 µm. 54
3.7 Intensity profile of Gaussian modes in the microcavity using equation 3.21. The planar mirror is placed at $z = 0$. The cavity RoC is 4 µm and the cavity length is 2 µm. The medium is water. 55
3.8 Schematic of the coordinate system used. xyz coordinate system is the instrumental frame. x' is the direction along the long axis of the rod-shaped particle. X is the projected direction of x' in the microcavity plane while Y is perpendicular to that. 60
3.9 Numerical relationship between the aspect ratio μ and the anisotropy loss tangent Φ with equation 3.43 at a wavelength of 640 nm. The permittivity of gold, silver and copper is taken from [236]. 66
3.10 Numerical relationship between the aspect ratio μ and the anisotropy loss tangent Φ using equation 3.10. $\theta = 0°, 45°, 90°$ are plotted. A is set as 1. 69
3.11 Schematic of the instrumental coordinate system with the flow direction and incident light direction. 74
3.12 (a) Schematic of the two coordinate systems used. xyz is the instrumental coordinate system while x'y'z' is the nanorod coordinate system. θ and ϕ are the polar and azimuthal angles of gold nanorods in the instrument frame. (b) Rotational movement in the gold nanorod coordinate system. β and χ present the rotational polar and azimuthal angle of the gold nanorod over a time step in the current nanorod frame. 76
3.13 Diagram of the Monte Carlo simulation during a time step $\triangle t$ from t_{j-1} to t_j. 81
3.14 Schematic of a Yee cell. The electric fields are along the edges of the cell while the magnetic fields are in the face centre of the cell. 83

4.1 Schematic of ridge fabrication by removing a 100 µm layer. The original substrate has a height of 500 µm. The ridge has a height of 100 µm and a width of 300 µm. 87
4.2 MicroAce machine to perform dicing work. It has a high-speed rotating blade (3000 rpm) to perform the cut. Cool deionised water keeps flowing to remove heat generated in the process. It uses microscopy for imaging. 87
4.3 SEM image of the microcavity array with the scale bar of 40 µm. The RoCs and depths of the hemisphere features are labelled. The hemisphere features on the same line have the same specifications. . . 89
4.4 Transmittance measurement of the 99.99% coating provided by Layertec GmbH. 90
4.5 Platforms to glue microcavity chips. Platform A is for the planar mirror without structures while platform B is for the mirror with concave features milled on the centre ridge. The inlet and outlet of the solution are labelled. 91
4.6 Photo of the complete flow cell assembly with plate x and actuators labelled. 91
4.7 Concave mirror side assembly. (a) The glued part of short and long piezo stacks. (b) The photo after the piezo stack part is screwed to the plate assembly. (c) Platform B is screwed to the top of (b). 92
4.8 Schematic of the microfluidic system. 93
4.9 Photo of the experimental apparatus. 94
4.10 Schematic of the experimental apparatus. 94
4.11 Polarimeter calibration. Normalised Stokes parameters S_1 and S_3 were measured with different rotating angles of the quarter-waveplate using equation4.2. Normalised differences ($\frac{measured-theoretical}{theoretical}$) compared with theoretical values were plotted. Zero reference line illustrates the ideal situation, where the measured values equal to theoretical values. . . . 99
4.12 An example of a camera image of the microcavity array with horizontal fringes. 100
4.13 Schematic of relative angles between mirrors. (a) This angle creates vertical fringes. (b) This angle creates horizontal fringes. For the mirror on the left in both cases, (a) illustrates the rotation along the z-axis while (b) displays the rotation along the y-axis. 100

4.14 Schematic of how the relative cavity length is calculated. The first point is at the node of the standing wave with the number of anitonodes $q = 4$. The second point is also at the node of the standing wave, but with $q = 5$. Therefore the relative cavity length can be determined with the wavelength of the LED λ_{LED} and the refractive index of the medium n_m. 101
4.15 Schematic of Nano Zetasizer, reproduced from [268]. 1 is the laser to provide illumination for the sample cell 2. 4 is the attenuator to avoid saturating the detector 3. 5 is the correlator to perform digital signal processing and the results are passed to the computer 6. 90° path is the design for another model. 105

5.1 Results of DLS measurements (Nano Zetasizer, Malvern Panalytical) directly from the software of the instrument. Each curve is one measurement. (a) Five measurements of gold nanorod sample A. (b) Five measurements of gold nanorod sample B. (c) Three measurements of gold nanosphere sample. 112
5.2 Absorption spectra measured by UV-Vis spectrometer with the wavelength range of 400 $\sim$ 800 nm. (a) Gold nanorod sample A shows the peak at 526 nm and 565 nm. (b) Gold nanorod sample B shows the peak at 535 nm and 574 nm. (c) Gold nanosphere sample shows the peak at 541 nm. 113
5.3 SEM secondary electron images of gold nanoparticles with different scale bars labelled (Merlin FEG-SEM, Zeiss). Gold nanorod sample A: (a) and (b). (a) is imaged with the probe current of 112 pA, EHT of 10 kV and a working distance of 3.5 mm. (b) is imaged with the probe current of 112 pA, EHT of 10 kV and a working distance of 3.3 mm. Gold nanorod sample B: (c) and (d). (c) is imaged with the probe current of 112 pA, EHT of 10 kV and a working distance of 4 mm. (d) is imaged with the probe current of 176 pA, EHT of 20 kV and a working distance of 4 mm. Gold nanosphere sample: (e) and (f), both are imaged with the probe current of 112 pA, EHT of 10 kV and a working distance of 3.3 mm. 115
5.4 User interface snapshots. 116

5.5 Summary of a single-particle event for gold nanospheres over 500 ms. (a) Transmitted peak FWHM. Two red rectangular areas labelled indicate two single-particle events. (b) Raw data of measured Stokes parameters. It is a collection of single sweeps. Green, blue and yellow data represent S_1, S_0 and S_3 signals respectively. Two red rectangular areas labelled are the corresponding single-particle events in (a). (c) Zooming into one single sweep during the single-particle event. 119
5.6 (a) Schematic of the coordinate systems used. θ is the polar angle while ψ is the azimuthal angle. (b) FWHM of the S_0 peak measured using the avalanche photodiode (APD) in a 200 ms window, showing two discrete single-particle events due to loss-induced broadening. . . 120
5.7 (a)-(d) Examples of individual S_0 and S_1 peaks as a function of frequency detuning during the second event. Blue dots are raw data and red curves are fitted curves using equations 5.1a and 5.1b. 123
5.8 (a)-(b) Histograms of ψ and Φ of a single-particle event for sample A. (c)-(d) Histograms of ψ and Φ of a single-particle event for sample B. Green and red curves are fitting curves using two models introduced in Chapter 3.6.3.1. 124
5.9 Direct fitting with equation 5.2 of Figure 5.8 (b). 126
5.10 Summary of statical results of 30 particles. (a) Aspect ratio μ distributions for 30 particles of samples A and B respectively using the optical microcavity sensing method without considering scattering. (b) Distributions of μ of 30 particles of samples A and B using SEM imaging. (c) Comparison between optical microcavity sensing method and SEM imaging. 127
5.11 Summary of μ histograms for the further analysis of SEM images assuming a random orientation of particles using equation 5.3. θ was randomly selected from $0 \sim \frac{\pi}{2}$. $\mu_{measured}$ was randomly selected from the Gaussian distribution of measured SEM results from 30 particles in Chapter 5.2.3. It was performed 100,000 times to improve the accuracy of the final result. (a) Sample A. (b) Sample B. Purple data shows the histograms of μ while the red curve shows the fitted curve of a Gaussian distribution. 132

5.12 An example of a data set over 200 ms. (a) Peak FWHM over time. (b) Raw data of three Stokes parameters measured in the experiment. Green, blue and yellow data represent S_1, S_0 and S_3 signals. Two solid red rectangular areas are labelled as two single-particle events. The dashed red rectangle is the empty cavity state. (c) Zooming into a sweep of empty cavity situation. 133
5.13 (a), (b) Histograms of azimuthal angles ψ in the microcavity plane in the two single-particle events mentioned above respectively. 134

6.1 SEM images (Merlin FEG-SEM, Zeiss) of rod-shaped bacteria particles with scale bars of 1 µm labelled. (a) is imaged with the probe current of 159 pA, EHT of 2 kV and a working distance of 4.1 mm. (b) is imaged with the probe current of 159 pA, EHT of 2 kV and a working distance of 4.1 mm. (c) is imaged with the probe current of 70 pA, EHT of 2 kV and a working distance of 4.1 mm. The column mode is high resolution and the noise reduction mode is pixel-averaged. 138
6.2 Raw data of a single rod-shaped bacteria particle in the microcavity during a 200 ms period. Green, blue and yellow curves are S_1, S_0 and S_3 signals collected from balanced photodiodes. It is a collection of resonance peaks in cavity-length sweeping. All three signals are quite stable with small fluctuations. 141
6.3 An example dataset of gold nanorod sample A for comparison. (a) Raw data of S_1, S_0 and S_3 signals over 200 ms. (b_1), (b_2) S_1, S_0 and S_3 signals of an example of consecutive sweeps, ... 142
6.4 Distribution of the azimuthal angle ψ of a bacteria particle extracted from data in Figure 6.2 within 200 ms. It shows a dominance in the range of 50° to 70°. 142
6.5 Two representative data files over 500 ms. (a), (c) Raw data file with recorded S_1, S_0 and S_3 signals. (b), (d) The corresponding azimuthal angle ψ distributions. (b) shows a dominance in the range of 60° to 80° while (d) displays bimodal distribution in the range of 80° to 100° and 150° to 170°. 143
6.6 Azimuthal angle ψ change over time of data shown in Figure 6.5(c). . 144

6.7 An example data set of a rod-shaped bacteria particle over 495 s with the scanning frequency of 10 Hz. (a) Raw data of S_1 (green), S_0 (blue) and S_3 (yellow) signals. (b) The corresponding azimuthal angle ψ distribution. 145
6.8 Examples of individual fittings of S_0 and the corresponding S_1 in the above example data set of 10 Hz scanning frequency in Figure 6.7. (a) and (b) are two different individual sweeps. 146
6.9 Histograms of anisotropy loss tangent Φ and fitting with equation 3.53. (a), (b) The fittings with different results of the aspect ratio and A with R^2 of 0.88 in both cases. (a) has the aspect ratio of 1.94 and A is 2.1943 while the aspect ratio in (b) is 4.76 and A is 2.1869. 147
6.10 Relationship between the anisotropy loss tangent Φ and the probability distribution with equation 3.53 with an example of A=2.5 and the aspect ratio of 4:1. 148

7.1 The schematic of the coordinate system in the simulation. z axis is the light propagation direction. x is the flow direction and xy plane is the microcavity plane. 155
7.2 Simulation results of gold nanospheres with a 60 nm diameter. (a) Trajectory of the center of the particle with the intra-cavity optical power of 10 mW. (b) Trajectory of the center of the particle with the intra-cavity optical power of 55 mW. (c) Light intensity profile between two mirrors with the x and z direction in the range of -3 $\sim$ 3 µm and 0 $\sim$ 1 µm respectively. 156
7.3 Simultaneous simulations of 5 particles. (a) Trajectories of the center of the particle with the intra-cavity optical power of 10 mW. (b) Trajectories of the center of the particle with the intra-cavity optical power of 55 mW. Different colours represent different particles with the same starting points. 158
7.4 (a) Schematic of the two coordinate systems used. xyz is the instrumental coordinate system while x'y'z' is the nanorod coordinate system. θ and ϕ are the polar and azimuthal angles of gold nanorods in the instrument frame. (b) Rotational movement in the gold nanorod coordinate system. β and χ present the rotational polar and azimuthal angle of the gold nanorod over a time step in the current nanorod frame. 158

7.5 Trajectory of gold nanorods with the intra-cavity optical power of 17.2 mW. (a) Trajectory of the center of a single gold nanorod. (b) Trajectories of centers of 5 particles diffusing simultaneously. Different colours represent different particles. 159
7.6 Trajectory of gold nanorods with the intra-cavity optical power of 500 mW. (a) Trajectory of the center of a single gold nanorod. (b) Trajectories of the centers of 5 particles diffusing simultaneously. Different colours represent different particles. 160
7.7 Trajectory of gold nanorods with the intra-cavity optical power of 5 W. (a) Trajectory of the center of a single gold nanorod. (b) Trajectories of the centers of 5 particles diffusing simultaneously. Different colours represent different particles. 161
7.8 Angular distributions (in degree unit) of a single gold nanorod with the intra-cavity optical power of 17.2 mW (a)-(d) and 500 mW (e)-(h). (a), (e) Polar angle β in the particle frame. (b), (f) Azimuthal angle χ in the particle frame. (c), (g) Polar angle θ in the instrument frame. (d), (h) Azimuthal angle ϕ in the instrument frame. 162
7.9 Angular distributions (in degree unit) of a single gold nanorod with the intra-cavity optical power of 5 W. (a) Polar angle β in the particle frame. (b) Azimuthal angle χ in the particle frame. (c) Polar angle θ in the instrument frame. (d) Azimuthal angle ϕ in the instrument frame. 164
7.10 Summary of the simulation of rod-shaped bacteria particles with the intra-cavity optical power of 10 mW. (a) Trajectory of a single rod-shaped bacteria particle. (b) Trajectories of 5 rod-shaped bacteria particles simultaneously. (c) Angular distribution (in degree unit) of the polar angle β in the particle frame. (d) Angular distribution (in degree unit) of the azimuthal angle χ in the particle frame. (e) Angular distribution (in degree unit) of the polar angle θ in the instrument frame. (f) Angular distribution (in degree unit) of the azimuthal angle ϕ in the instrument frame. 165

7.11 Summary of the simulation of rod-shaped bacteria particles with the intra-cavity optical power of 1 mW. (a) Trajectory of the center a single rod-shaped bacteria particle. (b) Trajectories of the centers of 5 rod-shaped bacteria particles simultaneously. (c) Angular distribution (in degree unit) of the polar angle β in the particle frame. (d) Angular distribution (in degree unit) of the azimuthal angle χ in the particle frame. (e) Angular distribution (in degree unit) of the polar angle θ in the instrument frame. (f) Angular distribution (in degree unit) of the azimuthal angle ϕ in the instrument frame. 166
7.12 Optical microcavity configuration. (a) Perspective view in Lumerical software with the coordinate system labelled. (b) Schematic of the coating composition and concave feature. 168
7.13 Refractive index profile of the optical microcavity system. 169
7.14 Simulation setting in Lumerical. The orange box is the FDTD simulation region. Yellow rectangles are the field and power monitors. The source is also labelled. (a) Perspective view. (b) XY view. 169
7.15 Simulation results of an empty cavity. (a) Transmission spectrum with the peak wavelength at 636.99 nm. (b)-(d) Electric field profiles between the two mirrors at wavelengths of 636.99nm, 628.95 nm and 645.94 nm, the latter two of which are the positions of smaller peaks, labelled in (a). 170
7.16 Summary of the simulation where the particle is placed at 10° from the x axis in the xy plane. (a) Simulation configuration in Lumerical (XY view). (b) Transmission spectrum. (c), (d) Electric field between two mirrors at 637.52 nm and 638.27 nm, wavelengths of the split peaks. 172
7.17 Summary of simulations with the particle at different angles from the x axis. (a)-(c) 30°. (d)-(f) 50°. (g)-(i) 70°. (a), (d), (g) Transmission spectrum. (b), (e), (h) Electric field between two mirrors at 637.52 nm, 637.44 nm and 637.37 nm. (c) Electric field between two mirrors at 638.27 nm. (f), (i) Electric field between two mirrors at 638.2 nm. 174
7.18 Results of the particle rotating 30° in the yz plane. (a) Transmission spectrum. (b), (c) Electric field between two mirrors of the xz plane at the wavelength of 637.44 nm and 638.2 nm. (d), (e) Electric field between two mirrors of the yz plane at the wavelength of 637.44 nm and 638.2 nm. These two wavelengths are the corresponding wavelengths of the split peak. 175

7.19 Transmitted spectrum with the particle at 30° in the xy plane and 10° in the xz plane. 176
7.20 Simulation results of a particle placed at z=1 µm away from the centre of the antinode with a rotation angle of 50° from the x axis in the xy plane. (a) Transmission spectrum with the peak wavelength at 637.14 nm. (b)-(d) Electric field profiles between the two mirrors at wavelengths of 637.14 nm, 629.02 nm and 646.02 nm. 177
7.21 Simulation results of a particle placed at y=0.1 µm and z=0.1 µm away from the centre of the antinode with a rotation angle of 50° from the x axis in the xy plane. (a) Transmission spectrum with the split peak wavelength at 637.44 nm and 638.2 nm. (b)-(c) Electric field profiles between the two mirrors at wavelengths of 637.44 nm and 638.2 nm. . 178
7.22 Simulation results of a particle placed at y=0.1 µm and z=0.1 µm away from the centre of the antinode with a rotation angle of 30° from the x axis in xy plane. (a) Transmission spectrum with the split peak wavelength at 637.52 nm and 638.27 nm. (b)-(c) Electric field profiles between the two mirrors at wavelengths of 637.52 nm and 638.27 nm. 179

List of Tables

2.1 Summary of current characterisation techniques. 8

4.1 The summary of different experimental conditions for gold nanorods and rod-shaped bacteria particles. Power is the intra-cavity power calculated from APD values of the transmitted light. Q is the quality factor of the microcavity. q is the mode number. $\mathcal{F}$ is the finesse of the cavity. The scanning rate is the sweeping frequency of the planar mirror. The sampling rate is the collection speed of PicoScope. Peak FWHM is the FWHM of the measurement peak in the time domain. . 103

5.1 The summary of aspect ratio μ results with different methods. [1] $\beta(\vec{r}) = 1$; [2] $\beta(\vec{r}) = 0.65$. 128

5.2 Summary of rotational diffusion coefficients using different models. Sample A: diameter 32 nm, length 48 nm. Sample B: diameter 28 nm, length 40 nm. The values in brackets () are the averaged angular displacement over 1 µs. 130

7.1 Summary of the findings of Monte Carlo simulations and FDTD simulations. 180

List of Abbreviations

ALS angle-resolved light scattering. 17

APD avalanche photodiode. xii, 97, 98, 102, 116, 120, 131, 139, 144, 145, 149

BS beam splitter. 97

CNN convolutional neural networks. 21

CTAB cetyltrimethylammonium bromide. 108, 113

DBR distributed Bragg reflector. 89

DDA discrete dipole approximation. 24

DDLS depolarised dynamic light scattering. 15, 43

DFM Dark-field microscopy. 24, 25

DIC differential interference contrast. 20, 21

DLS Dynamic light scattering. 13, 15, 16, 17, 104, 111, 112, 134

E.coli Escherichia coli. 1, 7, 136

EDX energy dispersive X-ray. 8

EHT extra high tension. 107, 137

FDTD Finite-difference time-domain. 4, 5, 45, 72, 81, 82, 85, 154, 167, 169, 170, 171, 181, 184, 185

FFPC fibre Fabry-Pérot cavity. 27, 30, 31

FIB focussed ion beam. 27, 28, 30, 31, 88

FSR free spectral range. 50, 51

FWHM full width at half maximum. 50, 117, 119, 120, 129, 130, 132, 186

iNTA Interferometric nanoparticle tracking analysis. 16

iSCAT interferometric scattering. 18, 19, 20, 43

LSPR localised surface plasmon resonance. 22

NTA Nanoparticle tracking analysis. 15, 16, 17, 25

OD optical density. 95

PBS polarising beam splitter. 95, 97

PCC photonic crystal cavity. 37, 40, 41, 42, 43

PID proportional-integral-derivative. 96, 102

PML perfect match layer. 169

PMMA polymethyl methacrylate. 29

PS polystyrene. 32, 34

RoC radius of curvature. 26, 47, 51, 52, 53, 55, 58, 70, 84, 88, 101, 102, 130, 150, 155, 168, 186

SEM Scanning electron microscopy. 8, 9, 10, 11, 24, 37, 42, 43, 88, 107, 114, 120, 126, 127, 128, 129, 130, 131, 134, 135, 136, 137, 138, 144, 147, 151, 152, 184, 185

SNR signal-to-noise ratio. 19, 20, 21, 31, 36, 43, 132

SPORT Single particle orientation and rotational tracking. 20, 21

SPR surface plasmon resonance. 24

SPT single particle tracking. 20

TEM transmission electron microscopy. 10, 11, 12, 14, 43, 185

WGM whispering gallery mode. 31, 32, 34, 35, 36, 44

List of Symbols

λ	Light wavelength
$\mathcal{F}$	Finesse
ϵ	Permittivity
μ	Permeability
B	Magnetic field
D	Electric displacement
E	Electric field
H	Magnetic field strength
J	Electirc current density
Q	Quality factor

Physical Constants

Planck's constant	$h = 6.62607 \times 10^{-34}\ J\ s$
Reduced Planck's constant	$\hbar = 1.05457 \times 10^{-34}\ J\ s$
Speed of light	$c = 2.99792 \times 10^{8}\ m\ s^{-1}$
Vacuum permittivity	$\epsilon_0 = 8.85418 \times 10^{-12}\ F\ m^{-1}$
Boltzmann constant	$k_B = 1.38 \times 10^{-23}\ J\ K^{-1}$
Refractive index of water	$n_w = 1.33$
Viscosity of water at 300K	$\eta = 0.82 \times 10^{-3}\ Pa\ s$

Chapter 1

Introduction

Exploring the world with a finer and finer scale always fascinates scientists and researchers. From probing micron-sized particles to nanoscale particles and even a single atom, the research has attracted scientists, transformed existing industries and inspired new inventions. The unique properties of nanoparticles make them potential candidates for a wide range of applications. Their large surface area to volume ratio enables them to be highly reactive, which is beneficial in catalysis and chemical reactions [1–3]. Additionally, nanoparticles exhibit quantum mechanical properties at the nanoscale, leading to unique electrical, optical, and magnetic behaviours [4]. The shape is an important physical property impacting various electrical, chemical and optical properties of nanoparticles and thus influences their roles in these applications [5, 6]. Therefore, shape measurement is beneficial for the quality control of nanoparticle synthesis and provides a viable method to characterise nanoparticles.

Water monitoring, in the meantime, is an important issue with increasing water pollution problems all over the world. Being able to detect harmful bacteria in drinking water systems is essential for public health. Common rod-shaped bacteria found in water, such as Legionella and Escherichia coli (E.coli) bacteria are usually harmful. Even though Coliform bacteria are harmless alone, it is an indicator of fecal contamination and, thus, pathogenic enteric bacteria [7, 8]. Within Bacillus bacteria, some

types are harmful to people while others are not [9]. Therefore, shape measurement of bacteria particles can potentially provide some initial insights into the water quality. Currently, transferring water samples into scientific labs for detection seems tedious and cannot fulfil the need for fast testing and stop the water supplies immediately if the pollution reaches the warning level. A compact and real-time monitoring device is in demand for water monitoring. Shape measurement can therefore provide an early indication of these harmful pathogens in fluids and help avoid the infection and spreading of diseases, offering benefits to public health.

Characterising the shape of particles in solution on a single-particle scale provides solutions to the aforementioned problems. Current particle characterisation techniques have limitations in various aspects. For example, the routine use of electron microscopy is limited by the high cost, the need for an operator with advanced technical skills and the challenges associated with the preparation of solution-based samples. Cryo-electron microscopy, with its strong ability to characterise biological samples, requires advanced technical skills. In addition, some optical techniques are unable to reach a single-particle scale or measure small particles accurately with inability to capture fast enough rotational diffusions.

1.1 Thesis Overview

With the demand in the qulity assessment of nanoparticles and the early warning of potential excess harmful bacteria in water, real-time aspect ratio measurement of particles in solution is needed. This project proposes a novel technique to measure the aspect ratio of a single rod-shaped particle in situ in solution without controlling the solution flow or trajectory of the particle. Gold nanorods and rod-shaped bacteria particles were tested as examples. The resolution in aspect ratio measurement

is found to be around 1% for gold nanorods. The method probes the perturbation of a rod-shaped particle in water to the resonant modes of laser light incident into an optical microcavity. The change in the polarisation state of the light as a particle diffuses through the cavity is recorded and analysed to extract the aspect ratio of the particle via the shape-dependent polarisability tensor. For gold nanorods, since each measurement of the polarisation state only takes microseconds to perform and is repeated every 100 microseconds, it allows multiple measurements to be carried out on each particle, thus lowering the standard error of the measurement. Each measurement could be considered as a 'snapshot' of the particle state and the rotational diffusion of the particle could also be extracted from the data as extra add-on. A larger fluid sampling volume allows more frequent measurements with a given particle concentration and longer events with more data points for a more accurate measurement. This thesis is structured as follows:

Chapter 2 firstly reviews current methods for shape measurement of rod-shaped particles with their advantages and limitations, including metal nanoparticles and biological samples. Electron microscopy radiates electron beams onto samples, breaking the optical diffraction limit and providing high resolution. Apart from the interaction with electron beams, interaction with light is also employed to extract shape information. The evolution from simple analysis of scattered light to more advanced ones is introduced. Then three main types of optical microcavities are discussed in detail, from the fabrication method to various applications, especially in the sensing domain.

Chapter 3 explains the theoretical backgrounds related to this project. Gaussian and Gaussian-Hermite beam profiles are deduced from the wave equation originally from Maxwell's equations. Optical microcavities are presented along with important figures of merit. Gaussian modes are displayed with the light propagation inside

optical microcavities. Additionally, the fundamental principle of the measurement, namely how the shape anisotropy can be measured with the polarisation state measurement of the transmitted light through the optical microcavities, is established for both gold nanorods and rod-shaped bacteria particles. Other theoretical calculations are included to supplement the analysis. Theoretical backgrounds of Monte Carlo simulations and Finite-difference time-domain (FDTD) simulations are discussed.

Chapter 4 describes all the experimental methods involved in this project. Firstly, the fabrication of the optical microcavity chip is introduced. Then the experimental apparatus is discussed, including the flow cell assembly, the microfluidic system construction and the functions of every optical component. Then the data preprocessing, namely converting from time domain to frequency domain, is introduced. Finally, the benchmark techniques used to characterise particles and the sample preparation are demonstrated.

Chapter 5 presents the experimental results of gold nanorod measurements. Firstly, the results of three benchmark characterisation techniques are displayed and analysed. Then the MATLAB user interface for data processing is explained along with the data processing. Measurements of gold nanospheres are presented for comparison. A single-particle event is identified and the aspect ratio of a gold nanorod is extracted from the data analysis. The same procedure was applied to reveal the statistical results of 30 particles. Other theoretical calculations are performed to evaluate the system.

Chapter 6 illustrates the experimental results of rod-shaped bacteria particles using the same experimental apparatus as gold nanorods with adjustments of experimental conditions. The aspect ratio is extracted and its accuracy is discussed from both the

experimental results and the theoretical model. Limitations and possible improvements of this experiment are discussed.

Chapter 7 elucidates the results of theoretical simulations for this work to supplement the experimental results. Monte Carlo simulations explore the dynamic diffusion of a single gold nanorod and a rod-shaped bacteria particle with different intra-cavity powers. They further confirm the diffusion state of the particle in the microcavity under experimental conditions, namely whether the particle is trapped or undergoes free diffusion. Simulation of a single gold nanosphere is also performed for comparison. Both the rotational and translational diffusions of rod-shaped particles are studied using the Langevin equation. FDTD simulations supplement the theoretical simulations of the system by studying the transmitted spectrum through the optical microcavity and the electric field in the microcavity with the rod-shaped bacteria particle in it. The particle is fixed at specific positions and angles to uncover the corresponding impacts on the optical field with some of them observed in the experiment while others could potentially be studied in the future.

Chapter 8 summarises the main contributions of this work and proposes improvements and future research directions.

Chapter 2

Literature Review

2.1 Introduction

Nanoparticles have attracted scientists for more than 20 years and become vital tools in various fields, such as drug delivery [10–12], catalysis [1–3], electronics [13, 14], etc. The fundamental physical properties of nanoparticles, such as size, shape, and refractive index, significantly impact their other properties, such as electrical and optical properties [5, 15], thereby affecting their usefulness for practical applications. Therefore, proper characterisations of nanoparticles are essential.

Among all the properties, the shape is particularly worth exploring since rod-shaped nanoparticles sometimes perform much better than their spherical counterparts and can be utilised in specific applications. For example, rod-shaped nanoparticles exhibit higher drug loading quantity thanks to their larger surface area to volume ratio [16]. In addition, it inhibits in vivo tumour growth and effectively reduces its toxicity [16] compared with its spherical counterparts, which could cause toxicity due to the insufficient biodegradability of spherical counterparts in vivo [17, 18]. As a

Apart from nanoparticles synthesised by humans, many pathogens in nature, such as Legionella and E.coli bacteria which are common in water, also have rod shapes [19, 20]. Being able to detect these harmful bacteria in water supplies is necessary for public health. In this scenario, shape measurement can provide an early indication of their presence in fluids and therefore assists in avoiding infection and wide spreading of diseases.

As a quality assessment of the synthesis of nanoparticles and to fulfill the demand of bacteria measurement, the method should be able to measure single particle from nanometer to micrometer and can be directly performed in solution to avoid complex sample preparation. This chapter focuses on reviewing developments of techniques related to this thesis. Firstly, some current common techniques for the shape measurement of nanoparticles and biological particles are reviewed while some of the techniques can measure the size at the same time. The working principles of these techniques are explained and their advantages and limitations are discussed. Secondly, different types of optical microcavities are presented with their potential applications.

2.2 Shape Measurement Methods

To obtain the shape information of particles, two main approaches involve exploring interactions with electron beams or light. Electron microscopy is well-known for breaking the optical diffraction limit and thus achieves higher resolution than normal optical microscopy. Although direct imaging with light is impossible, information can still be acquired through signals from interactions between rod-shaped particles and light. The following table shows a comparison between current techniques. As the table shows, none of the current technique can measure the aspect ratio of a single nanoparticle ($\sim$nm) in solution directly. Details of these techniques as well as

advantages and disadvantages will be introduced later in this section.

Method	Condition	Size	Aspect Ratio	Single Particle
SEM	High Vacuum	$\sim$ 10 nm	$\surd$	$\surd$
TEM	High Vacuum	<0.1 nm	$\surd$	$\surd$
DLS	Liquid	>0.3 nm	Use advanced DDLS	$\times$
NTA	Liquid	>10 nm	$\times$	$\surd$
ALS	Liquid	$\sim$ µm	$\surd$	$\surd$
iSCAT	Liquid	>2 nm	$\times$	$\surd$
SPORT	Liquid	$\sim$ 30 nm	$\surd$	$\surd$
Spectroscopy	Liquid	$\times$	$\surd$	$\times$
DFM	Liquid	$\sim$ 50 nm	$\times$	$\surd$

Table 2.1: Summary of current characterisation techniques.

2.2.1 Scanning Electron Microscopy (SEM)

Scanning electron microscopy (SEM) focuses an electron beam onto a sample and collects scattered signals. Figure 2.1 shows the schematic of various components in a typical SEM, reproduced from [21]. The anode accelerates electrons emitted from the electron source while condenser lenses and objective lenses focus the electron beam on the sample kept in a vacuum environment. A selection of detectors are installed to collect different signals, such as a secondary electron detector, a back-scattered electron detector and an X-ray detector [22]. The basic imaging mode collects the secondary electrons, generated with inelastic interactions providing surface information like surface topography. Choosing the optimum beam current and the accelerating voltage helps attain high-resolution imaging at the nanoscale for different samples. The back-scattered electron detector collects back-scattered electrons from elastic interactions, leading to unchanged wavelengths and changed directions. It penetrates deeper regions within the samples and offers topological contrast and atomic contrast [23]. The X-ray detector used in energy dispersive X-ray (EDX) analysis can determine the elements in the sample and identify any possible contaminants [24].

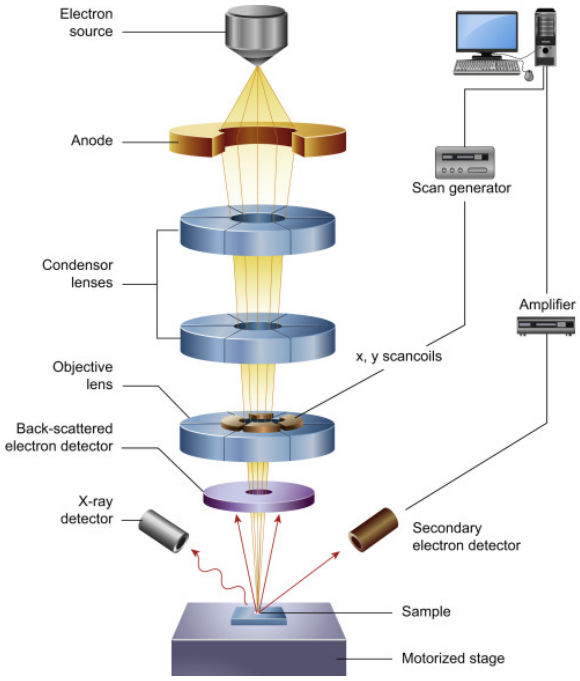


Figure 2.1: Schematic of a typical SEM, reproduced from [21]. It illustrates a source emitting a beam of electrons passing though an anode for accelaration. A series of lenses focuses the beam onto the sample. The detectors collect different electrons after interacting with the sample, including back-scattered electrons, x-ray and secondary electrons. A commerical software is utilised for monitoring and control.

Although SEM achieves higher spatial resolution than optical microscopy and it can provide the size information as well as the aspect ratio of a single nanoparticle (on the order of tens of nanometers) by direct imaging, the equipment is expensive and requires a vacuum environment. For the data interpretation, software packages like Pebbles [25] and ImageJ [26] and even machine learning methods [27] have been developed to achieve high-throughput analysis with high accuracy. In addition, it is worth considering the situation where rod-shaped particles are perpendicular to the image plane. Attention needs to be paid to avoid mistaking these particles as spherical particles [28]. For the sample preparation, Liv et al. [29] investigated the impacts of liquid membranes with a thickness of 20 nm and 50 nm on the electron beam and the imaging of nanoparticles. Their work successfully explored the possibility of dealing with particles in a hydrated environment. However, obtaining images of nanoparticles

in bulk liquids is still challenging and the relatively short penetration depth limits its application. Additionally, when the sample has poor electrical conductivity, the charge buildup can degrade the sample and distort the image data [21, 30]. Therefore, samples with non-conductive materials like polymers and ceramics along with biological samples need a thin layer of conductive coating.

2.2.2 Transmission Electron Microscopy (TEM)

Like SEM, transmission electron microscopy (TEM) also has a similar set of electrostatic lenses to focus the electron beam onto the sample. Since it analyses the transmission signals from the sample, it needs several lenses to focus the beam and collect signals with most of the detectors on the transmission side. To transmit through the sample, the accelerating voltage is much higher than SEM. Additional lenses can be added before and after the specimen to correct spherical aberration, which substantially improves the spatial resolution to <0.05 nm [31, 32]. Figure 2.2 illustrates the schematic of a typical TEM, reproduced from [21].

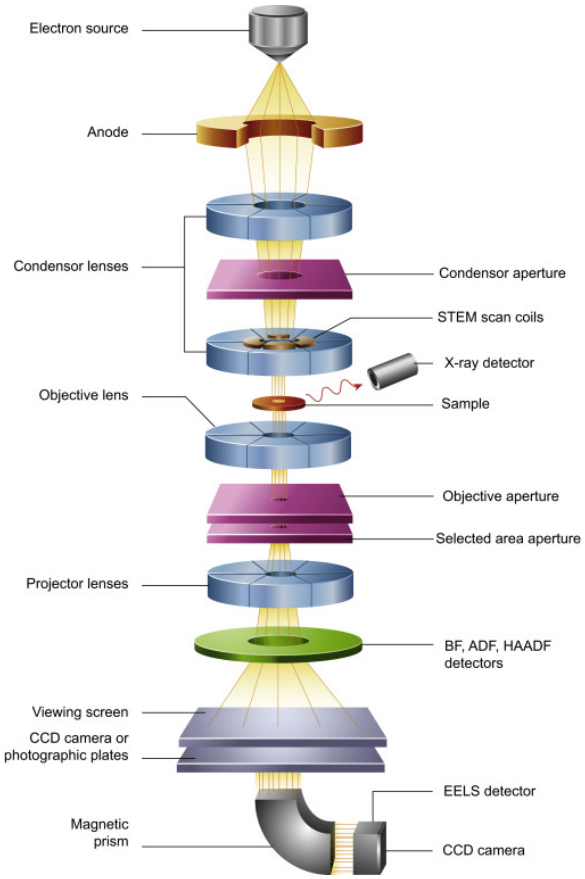


Figure 2.2: Schematic of a typical TEM, reproduced from [21]. It illustrates a source emitting a beam of electrons passing though an anode for accelaration. A series of lenses focuses the beam onto the sample and also collects the signals better after the transmission through the sample. The detectors on the transmission side of the sample collect different electrons after interacting with the sample. A commerical software is utilised for monitoring and control.

With an even higher resolution than SEM, size and shape information can be obtained with the TEM image. However, the equipment is much more complex than SEM and requires advanced technical skills. The sample preparation is often very complex to create thin samples from the original bulk samples [33]. Liquid-phase TEM has been developed to study the samples in bulk liquids while maintaining high and temporal resolution and it opens the window to study the dynamics of materials synthesis [34–37]. It can also be employed to study colloidal nanoparticles [38], including the growth mechanism, transformation and motion in fluids. However, it requires even

more advanced techniques with a complex design for the liquid cell and the frame rate limits its applications in studying faster processes.

Bacteria imaging often requires extra steps for sample preparation such as negative staining [39, 40] to overcome the lack of sufficient contrast. The low contrast is caused by several reasons. For example, when dealing with biological samples, a low electron dose is used to reduce damage to the sample. In addition, biological samples usually have a low average atomic mass, which means there are fewer interactions between the electron beam and the sample [41]. Negative staining of biological particles for TEM imaging is first put forward by Brenner and Horne [42]. The underlying principle of negative staining is that a dried amorphous or frozen-hydrated/vitreous layer of heavy metal-containing cationic or anionic salt surrounds, permeates, supports and embeds a thin layer of biological material [43]. Then the contrast between the biological sample and the surrounding stain layer is generated by the differential electron scattering caused by the mass-thickness difference. This technique has been developed since then. Negative staining in the presence of trehalose, a naturally occurring sugar made up of two glucose molecules, on continuous carbon films [44–46] benefits from the function of trehalose in the preservation of biological materials during dehydration, cold storage, freezing, UV irradiation, etc [40]. Air-dry negative staining on holey carbon support films [47, 48] provides better stability and reproducibility than the traditional way of suspending biological samples in a thin layer of negative stain alone without any underlying support. Cryoelectron microscopy combined with advances in TEM technologies allows close-to-atomic resolution data to be obtained and imaging of unstained hydrated specimens embedded in vitreous ice is possible [49], but it still suffers from low contrast and is subject to radiation damage. Cryo-negative staining produces superior sample preservation and image resolution [50–52] compared with the air-dried specimens and overcomes some of the

difficulties mentioned above. Negative staining can not only be employed to image the internal structures and shape of biological samples but can also be applied in advanced studies, such as protein-protein interactions [53], epitope-specific antibody and site-specific affinity labelling [54], etc.

Cryo-electron microscopy, winning the 2017 Nobel Prize in chemistry, provides unprecedented opportunities for the structural characterisation of biological macromolecules [55]. Cryo-electron microscopy enables the preservation of biological samples in a high vacuum and provides them with some protection against the effects of radiation damage [56]. Advances in digital electron detectors and 3D maximum-likelihood classification algorithms [57, 58] facilitate faster image capture, reduce the noise of the image and provide solutions to single-particle analysis, which was limited due to a variety of structures contained in the samples. However, the cost of cryo-electron microscopy, the complex sample preparation and the advanced technical skills required to operate limits its applications in quick tests and it is overkill in the application of only measuring the aspect ratio of a bacteria particle.

2.2.3 Dynamic Light Scattering (DLS)

Dynamic light scattering (DLS), also known as photon correlation spectroscopy, allows the calculation of diffusion coefficients related to the Brownian movement of particles in liquids [59]. It irradiates the sample with a laser beam and monitors the intensity fluctuations of the scattered light from the particles with time. The autocorrelation function $G(t)$ is defined as [60]:

$$G(t) = \langle I(t_0)I(t_0 + t)\rangle \tag{2.1}$$

where $I(t_0)$ and $I(t_0 + t)$ is the number of photons reaching the detector at time t_0 and $t_0 + t$. With different time intervals t, $G(t)$ shows a decay. Depending on the number of different types of particles in liquids, $G(t)$ can be expressed as the sum of various diffusion behaviours [61]. Below is an example of the sum of two types of diffusion:

$$G(t) = A + [B_1 e^{-t/\tau_1} + B_2 e^{-t/\tau_2}] \tag{2.2}$$

where τ_i $(i = 1, 2)$ is the decay time related to the diffusion for two types of particles and can be expressed as a function of the diffusion coefficient D_i $(i = 1, 2)$ [62]:

$$\tau_i = \frac{1}{D_i q^2} \tag{2.3}$$

where q is the scattering vector, related to the refractive index of the medium, laser wavelength and the scattering angle. After obtaining the diffusion coefficient of the particle, the diameter of the spherical particle can be acquired through the Stokes-Einstein equation $D = \frac{k_B T}{6\pi\eta R}$ where k_B is the Boltzmann constant, T is the temperature, η is the viscosity of the liquid and R is the radius of the spherical particle. The schematic of a typical instrument is shown in Figure 2.3, reproduced from [63].

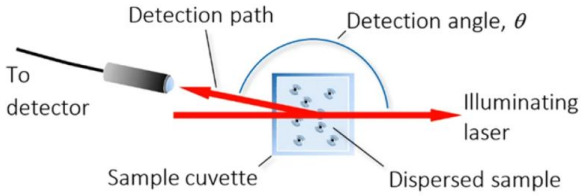


Figure 2.3: Schematic of a typical DLS instrument, reproduced from [63]. The laser beam irradiates the sample cuvette and the detector collects the scattered light from the particles in the back-scattered direction for further autocorrelation analysis.

The instrument is simple and there are commercial products on the market. It is convenient to handle liquid samples and can even detect polymer coatings, which is hard to see under TEM due to their low contrast [64]. It can measure particles that are

bigger than 0.3 nm. Since DLS relies on monitoring the scattered light from the particles, the intensity dramatically decreases when dealing with smaller nanoparticles as it is proportional to R^6 and advanced detector or data analysis is needed. Additionally, DLS can measure polydisperse samples in theory. However, if their diameters vary significantly, the scattering signals are dominated by larger particles and DLS fails to detect the polydispersity. It cannot provide shape anisotropy information of nanoparticles nor single particle analysis.

To acquire the anisotropy information, depolarised dynamic light scattering (DDLS) has been developed to fill the gap [65, 66]. It emits a linearly polarised laser beam onto the sample and collects the light intensity of the same polarised state and the orthogonal depolarised state. Time-tagged time-resolved photon counting overcomes the low photon count rates of depolarised light. Relaxation rates are extracted from the fitting of the decay curve of the autocorrelation, from which the translational and rotational diffusion coefficients are further calculated. Thus the shape information can be deduced by approximating nanorods to straight cylinders [67, 68] or prolate ellipsoids [69]. However, it can only provide information about the averaged value of the sample and cannot offer shape information for single particles.

2.2.4 Nanoparticle Tracking Analysis (NTA)

Nanoparticle tracking analysis (NTA) illuminates liquid samples with a laser beam and collects the scattered light with a microscope shown in Figure 2.4, reproduced from [70].

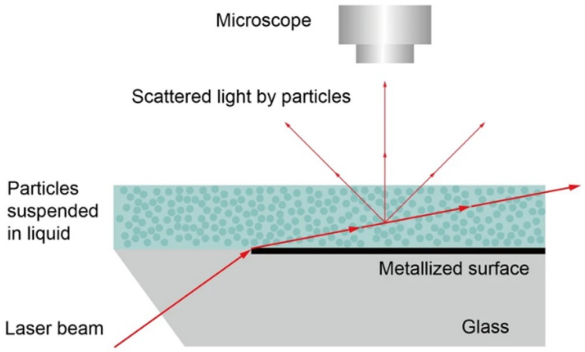


Figure 2.4: Schematic of NTA, reproduced from [70]. The laser beam irradiates the solution with particles and the microscope collects the scattered light from particles for further data analysis.

A video is captured to track each particle individually and simultaneously by monitoring the distance between adjacent frames averaged over all possible frames. The diffusion coefficient D is calculated [71] to obtain the diameter of the spherical particle with the Stokes-Einstein equation:

$$\overline{(x,y)^2} = 4Dt = \frac{2k_BTt}{3\pi\eta R} \tag{2.4}$$

where k_B is the Boltzmann constant, T is the temperature, t is the time interval between adjacent frames, η is the viscosity of the liquid and R is the radius of the spherical particle. Particles must only undergo Brownian motion with this calculation procedure so that any other interactions should be avoided, such as particle-particle interactions at high concentrations [72]. That is why the preparation for the sample normally requires dilution to $10^6 \sim 10^9$ particles/mL. NTA can measure particles ranging from 10 nm to 1000 nm in diameter [73]. Both the concentration requirement and size range measured depend on the sample type. Interferometric nanoparticle tracking analysis (iNTA) [74] explores the interference between the incident and scattered light and measures the contrast which is proportional to R^3 instead of the typical R^6 proportionality of DLS and NTA. Therefore, iNTA can detect even smaller

particles. There are commercial products for NTA on the market and they are convenient to use. However, NTA is limited in the camera speed and cannot provide any shape information.

2.2.5 Angle-resolved Ligh Scattering (ALS)

Like DLS and NTA which analyses scattered light from the particle, angle-resolved light scattering (ALS) has been employed to study the bacteria, with the order of several micrometers. This technique is easy to implement in experiments. Incident light irradiates the sample, and the detector captures signals at different angles. It has been utilised to study bacterial suspensions and colonies since last century [75–78]. Due to the difference in scattered light coming from diverse dielectric compositions of different bacteria, this technique has the potential to identify bacteria. Van De Merwe et al. [79] obtained diameters and lengths of spherical and rod-shaped bacteria in vivo based on this technique. They measured the Mueller matrix from the polarised scattered light at different scattering angles. The Mueller matrix is a 4×4 matrix describing the change in polarization of light from one state to another, with $S_{mn}(m, n = 1 - 4)$ representing the elements in the matrix. An experimental graph of $\langle S_{34}\rangle/\langle S_{11}\rangle$ versus scattering angle [80] was combined with the volume measurement of bacteria cell using a Coulter counter. The bacterial diameter was closely correlated with the location of the extrema in the scattering graph. It requires calibration using standard samples and cannot obtain information for a single bacteria cell. Individual rod-shaped bacteria information can be acquired with more advanced techniques. Jo et al. [81] measured 2D ALS patterns of individual rod-shaped bacteria in a wide range of scattering angles from -70° to 70° along the principal axes with unprecedented sensitivity. They employed the Fourier transform light scattering method based on quantitative phase imaging to generate the 2D ALS maps. To further quantify results, they defined the angular anisotropy spectrum which is the

relative difference in scattering intensities between the minor and major axes at each scattering angle. Species-specific characteristics were observed.

2.2.6 Interferometric Scattering Microscopy (iSCAT)

To achieve the detection of smaller particles using scattered light, interferometric scattering (iSCAT) microscopy was introduced by Sandoghdar et al. [82] in 2004. Before that, the extinction has been utilised to detect small particles. Figure 2.5, reproduced from [83], shows various schemes for illumination and detection.

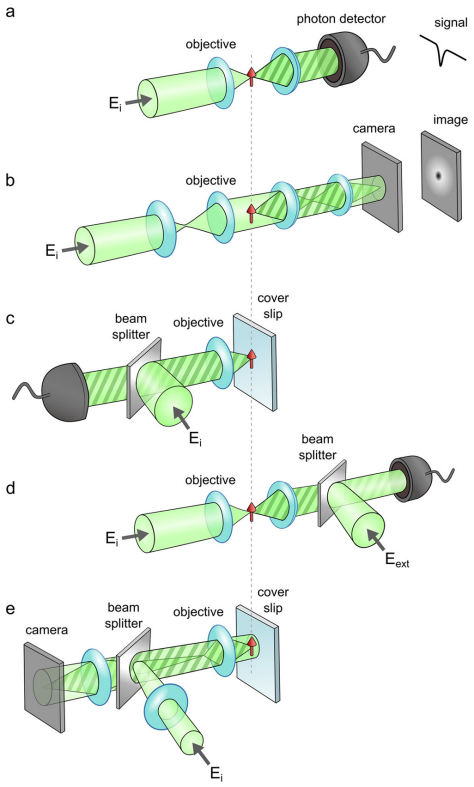


Figure 2.5: Various schematics for illumination and detection reproduced from [83]. The red arrow represents the dipole moment associated with a nano-object. Light green and shaded areas indicate the illumination (E_i) and the scattered fields (E_s), respectively. (a) Point detection in transmission via focused illumination. (b) Wide-field illumination and transmission detection on an imaging camera. (c) A reflection-based scheme for point detection with illumination similar to (a). (d) Point detection in transmission with focused illumination, similar to (a) but with an external reference beam of field (E_{ext}). (e) A scheme of illumination and wide-field imaging by means of reflection, equivalent to a folded version of (b).

(a) illustrates the simple idea of focusing the incident beam tightly to reach the most favourable ratio of the object cross-section to the beam area. Single semiconductor quantum dots and dye molecules can be detected in direct extinction [84, 85]. (b) depicts a conventional bright-field configuration. A plane-wave illumination on the sample is achieved by focusing a laser beam on the back focal plane of a microscope objective. The scattering from a nano-object is collimated into a tube lens with a second objective and is imaged onto a camera screen. The laser beam is rendered back to a plane wave, creating illumination over a large area of the camera, which generates a weak background. In this way, only a small fraction of the incident power interferes with the scattered light within the microscope point-spread function. However, it is limited in technology, as detectors normally do not have the dynamic range to process a small signal on a large background [86]. Several other techniques including dark field [87–89], phase contrast [89–91] and differential interference contrast microscopy [92] have been put forward to provide convenient ways within the limitations of the available detectors, without pushing the detection sensitivity limit of the signal-to-noise ratio (SNR). Then it was realised that a single molecule and small nanoparticles could not be detected via extinction.

The working principle of iSCAT is the superposition of a reference light field with the field emerging from the sample. The detected power is:

$$P_d \propto I_d = |E_r + E_s|^2 = I_r + I_s + 2E_r E_s cos\phi \tag{2.5}$$

where E_r and I_r are the electric field and the intensity of the reference field, E_s and I_s are the electric field and the intensity of the pure scattering field from the nano-object, and a cross-term involving the phase $\phi = \phi_r - \phi_s$, the difference between a Gouy phase and the contribution determined by the dielectric function of the object

[82]. The scheme is illustrated in Figure 2.5(c). In the small particle case, $I_r + I_s$ is dominated by I_r and the contrast can be expressed as:

$$c = \frac{I_d - I_r}{I_r} = 2\frac{E_s}{E_r}cos\phi \tag{2.6}$$

Figure 2.5(d) and (e) show developments based on iSCAT. (d) employs a separate reference beam [93] and (e) displays a wide-field version of iSCAT with a microsecond imaging capability [94]. It should be noted that although decreasing E_r results in higher contrast, the overall signal decreases, resulting in a lower SNR in the shot-noise limit [82]. However, balancing between E_r and E_s is beneficial for experiments [95, 96].

iSCAT can be applied to measure the size of particles, such as gold nanoparticles as small as 2 nm [97], viruses [98, 99], proteins [100, 101], etc. Lateral and orientational displacements can be obtained [102]. One core part in iSCAT is the analysis of noise and improving SNR ratio to push the detection limit further [103]. Self-supervised machine learning has recently been applied to push the sensitivity limit of single proteins below 10 kDa [104]. However, iSCAT cannot provide the aspect ratio of a single particle.

2.2.7 Single Particle Orientation and Rotational Tracking (SPORT)

Single particle orientation and rotational tracking (SPORT) [105] is developed on the basis of single particle tracking (SPT) technique and combines a Nomarski-type differential interference contrast (DIC) microscopy [106, 107]. SPT is used for studying live molecular and cellular processes but is limited to the study of translational motions [108]. Wang et al. [107] utilised gold nanorods as probes to resolve the rotational motions of nano-objects in engineered environments and live cells. In prin-

ciple, Nomarski-type DIC microscopes are two-beam interferometers. By measuring the relative intensity, the 2D orientation angle can be acquired. Thus the angular resolution is directly related to the SNR of DIC measurement. Combining these two techniques, Gu et al. [105] studied the real-time rotational dynamics of functionalised gold nanoparticle vectors on live cell membranes and found a strong relation to the surface charge. The particle studied has a diameter of 40 nm and a length of 118 nm and they achieved 2 ms time resolution. Machine learning methods have recently been applied to process images to obtain more information [109] or show better tolerance to noise [110]. Inspired by those developments, convolutional neural networks (CNN) have also been adapted to the SPORT system to improve the angular resolution and resistance to noise [111]. Figure 2.6 shows the schematic of the experimental apparatus, reproduced from [111].

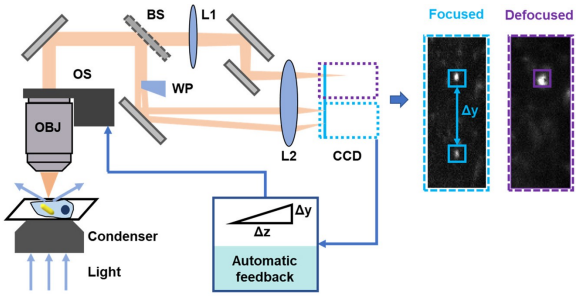


Figure 2.6: Schematic of an automated high-speed SPORT apparatus, reproduced from [111]. Light irradiates the sample and the a series of optical componenents are used for further analysis. Bifocal plane imaging was achieved by splitting the acquired signal into two imaging channels (focused and defocused channels) by inserting a beam splitter. The automatic feedback system is added to remove noise. OBJ: objective, OS: objective scanner, WP: wedge prism, BS: beam splitter, L1 and L2: lens with different focal lengths, CCD: charge coupled device.

Theoretically, with the rotational and translational diffusion of gold nanorods determined, shape information can be extracted from these diffusion coefficients. However, the temporal resolution is limited to the frame rate of the camera and the technique cannot be used to study faster motions.

2.2.8 Spectroscopy

For metallic nanorods, the aspect ratio can impact the localised surface plasmon resonance (LSPR), so analysing the absorption spectrum provides the shape information [112–114]. The oscillating electric field introduced by the incident light causes the conduction electrons to oscillate coherently. When the electron cloud is displaced relative to its original position, a Coulombic restoring force between electrons and nuclei causes the electron cloud to oscillate. The oscillation frequency is determined by the density of electrons, the effective electron mass, and the size and shape of the charge distribution [5]. It shows maximum absorption at the plasmon resonant frequency. The absorption spectrum is easily obtained with a UV-Vis spectrometer and a simple diagram of it is shown in Figure 2.7, reproduced from [115]. Using a reference cuvette removes the impacts of the solution medium, ensuring that the final spectrum only represents the information of particles.

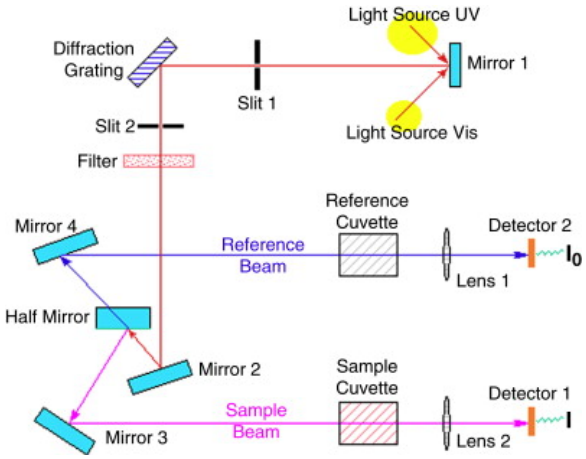


Figure 2.7: Schematic of a UV-Vis spectrometer, reproduced from [115]. The diffraction grating determines the optical resolution and the wavelength range of the spectrometer. The incident light is split into a reference and sample beam to pass through the reference and sample cuvette respectively.

With Gans theory [116, 117], adapted from Mie theory [118], the extinction coefficient

can be calculated:

$$\gamma = \frac{2\pi N V \epsilon_m^{3/2}}{3\lambda} \sum_j \frac{(\frac{1}{p_j^2})\epsilon_2}{(\epsilon_1 + \frac{1-p_j}{p_j}\epsilon_m)^2 + \epsilon_2^2} \tag{2.7}$$

where N is the number of particles per unit volume, V is the volume of each particle, ϵ_m is the dielectric constant of the surrounding medium, λ is the wavelength of the incident light, and ϵ_1 and ϵ_2 are the real and imaginary parts of the material dielectric function respectively. ϵ_1 and ϵ_2 are frequency dependent, while ϵ_m is assumed to be a constant. p_j are the depolarisation factors for the three axes A, B and C of the rod with $A > B = C$. Link et al. [112–114] discovered the linear relationship between the absorption maximum of the longitudinal mode and the aspect ratio of the particles, which could be used to determine the aspect ratio of gold nanorods. They also found that with a fixed aspect ratio, the absorption maximum of the longitudinal plasmon resonance depends on the medium dielectric constant in a linear way. However, to fit the calculations to the experimental values, they had to vary the medium dielectric constant with the aspect ratio nonlinearly. Chemically, this indicates the size-dependent micelle structures capping gold nanorods. The micelle structures are formed by the dispersant in the solution. After this initial finding, Susie Eustis and Mostafa El-Sayed fitted the absorption spectrum with a collection of homogeneously broadened spectra of nanorods with specific aspect ratios and population distributions [119]. This method still utilised the Gans theory for each aspect ratio and mapped near the longitudinal resonance wavelength as the transverse plasmon is insensitive to the aspect ratio. Recently, more complex algorithms [120] have been put forward to automate the curve-fitting process and take the impacts of impurities into account. It is still based on Gans theory and employs the Bellman principle of optimality [121] in the fitting process. However, analysing the absorption spectrum can only obtain the statistical data of the aspect ratio averaged among particles, but cannot acquire results of a single particle.

Numerical ways like discrete dipole approximation (DDA) [122–124] can also be used to calculate the absorption and scattering cross-sections of nanorods and even more complex shapes by treating the arbitrary shape as a group of finite objects. The ADDA code package improves efficiency by parallelising a single DDA calculation on a multiprocessor distributed-memory system [125]. For gold nanorods, the results from DDA are similar to Gans modification from Mie theory [126]. Slaughter et al. [127] obtained single-particle spectroscopy with the correlation of SEM and compared results with DDA. They found good agreement for the longitudinal dipole surface plasmon resonance (SPR) while other spectral features like the relative intensities of multipole SPR modes or linewidths required a more complex theoretical approach.

2.2.9 Dark Field Microscopy

Dark-field microscopy (DFM) has potential in sensitive sensing with the advantage of reducing the imaging background [128]. It can capture the scattered light from particles and can be utilised to extract the size distribution of nanoparticles. Calvo et. al [129] recently achieved the measurement of individual sizes of thousands of particles with nanometric accuracy within minutes through dark field single particle spectrophotometry. The experimental apparatus is illustrated in Figure 2.8. Nanoparticles were drop-casted on a glass slide. The imaging of the particle as well as spectral measurements of the scattering signals were performed to determine the diameter of the particle. This method used the relationship between the nanoparticle size and the wavelength of the plasmon resonance peak to deduce the diameter of the particle. Though this method has a high throughput with good accuracy, this method cannot be applied to free-diffusing particles suspended in the solution.

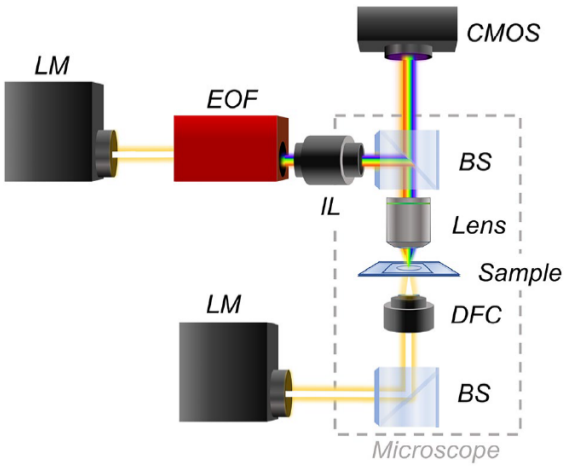


Figure 2.8: Schematic of a dark field single particle spectrophotometry, reproduced from [129]. The white light from a halogen lamp (LM) is directed to an electro-optical filter (EOF) that filters the light into its constituent wavelengths. The filtered spectral wavelengths coming from the tunable optical filter are then coupled to the epi-illuminator (IL) of the microscope and focused on the sample surface through a beam-splitter (BS) and a dark-field objective (OB). A CMOS camera placed at the image plane of the experimental setup collects the scattered light for each illumination wavelength. The sample imaging is performed in transmission mode, while the sample spectrophotometry is done in reflection mode.

To capture the size information of diffusing nanoparticles, DFM can also be combined with NTA to distinguish particles which overlap in size distribution [130]. By dark field illumination, the colour information provided by gold nanoparticles added more information to NTA measurements and made it possible to identify the particle subpopulations, in this case, differentiating between 60 nm and 80 nm overlapping distribution. However, it also had limitations in detecting non-plasmonic particles and is limited in the size of the particle due to the camera speed.

2.3 Optical Microcavities

After introducing different techniques of characterising nanoparticles and biological samples such as viruses and bacteria, the optical microcavities used in the experiment will be reviewed. Microcavities are a class of optical structures providing a versatile

approach to engineering light-matter interactions. Specifically, different types of optical microcavities will be demonstrated and potential applications will be discussed.

2.3.1 Fabry-Pérot Microcavities

The simplest Fabry-Pérot cavity consists of two planar parallel mirrors that reflect light back and forth and achieve light confinement [131, 132]. However, this simple configuration suffers from non-idealities in reality, such as non-parallelism between the mirrors and the non-plane-wave nature of the incident light [133]. These non-idealities limit its finesse. Finesse is an important figure of merit that quantifies the average number of times that a resonant photon bounces between the mirrors before being absorbed, scattered or transmitted out of the cavity. This can be mitigated by utlising curved mirrors, first studied and developed for gas lasers [134].

Using optical microcavities to explore cavity quantum electrodynamics has been widely studied [135]. A high quality factor Q and a small mode volume benefit both strong and weak coupling regimes. The quality factor Q is another figure of merit of the cavity and measures the optical energy decay rate within the cavity [136]. It is proportional to both the finesse and the antinode number q. Therefore fabricating cavities with such properties is worth exploring. Open-access microcavities were put forward for use in both atomic [137–139] and solid-state systems [140, 141]. Challenges in fabricating smooth concave surfaces with a small radius of curvature (RoC) pose difficulties for manufacturing microcavities. Accomplishing this task enables high quality coatings to be deposited on the surfaces, achieving a small mode volume and high finesse. Several techniques have been put forward for use in the application areas mentioned above. Trupke et al. reported an etching technique to produce concave surfaces in silicon [137, 138]. Steinmetz et al. and Muller et al. utilised a lift-off technique to transfer the deposited mirrors from the convex surfaces

onto fibre tips [139, 140]. Cui et al. employed a bubble-trapping method in glass to fabricate highly spherical surfaces. These techniques can produce cavities with a finesse of $10^3 \sim 10^4$ but the mode volume remains 50 µm^3. Dolan et al. [142] in our group pushed the mode volume to a markedly smaller value of 2.2 µm^3 with a Q factor exceeding 10,000. They milled the concave features into substrates using a focussed ion beam (FIB) by modulating the dwell time per pixel from 0.1 ms up to a maximum of 50 ms. It opens new possibilities for cavity quantum electrodynamics and other application domains like chemical sensing. Further detailed studies in topographic control have been performed by Trichet et al. in the same group [143]. Muller et al. [144] applied laser-ablation techniques to achieve a finesse of over 100,000. This technique should be able to produce the smoothest concave features owing to the melting and reflow of the machined glass surface [145]. However, non-spherical surfaces were discovered, leading to mode-coupling loss [146] and polarisation-dependence [147]. With the developments of 3D printing and lithography, Ortiz-Huerta et al. [148] fabricated a hybrid planar Fabry-Pérot microcavity using a two-photon polymerisation process with a direct laser writing system. In addition, fibre Fabry-Pérot cavity (FFPC)s were developed for the miniaturisation of optical devices while they could at the same time offer features of high finesse and a small mode volume. Their early versions [137, 139, 140] had moderate finesse up to a few thousand limited by the methods used to fabricate the concave surface on the fibre. However, Hunger et al. [149] proposed the usage of a single CO_2 laser pulse to shape the concave feature. Covering the concave feature with dielectric coatings increased the finesse dramatically to ≥ 130000.

With the fabrication methods developed, open-access Fabry-Pérot optical microcavities were employed for different measurements, and FFPC was developed and advanced. Trichet et al. [150] demonstrated refractive index sensing of glucose using

FIB-milled open-access cavities and reached a measured limit of 3.5×10^{-4} RIU within 54 fL detection volume. By injecting the deionised water first, and then the glucose solution, the white lamp transmission through the cavity was recorded over time during this process shown in Figure 2.9(a), reproduced from [150]. 1 denotes the time to inject the glucose solution while 2 represents the time the glucose solution reaches the cavity. 3 is the time to inject water while 4 is the time when water reaches the cavity. The refractive index change could be calculated through the resonance wavelength shift. By monitoring multiple cavities simultaneously, they decoupled the effect of a refractive index change and the impact of a mirror displacement on the wavelength change of the resonant modes and obtained the refractive index change over time as illustrated in Figure 2.9(b), reproduced from [150].

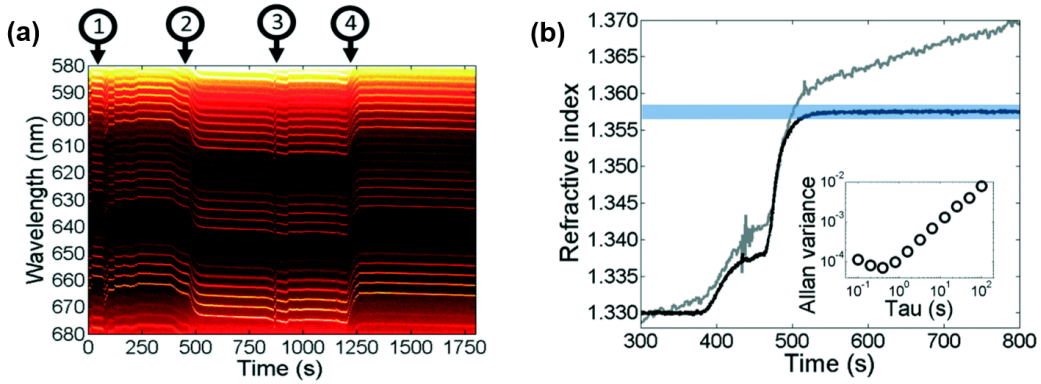


Figure 2.9: The figure is reproduced from [150]. (a) White lamp transmission of a single cavity is recorded as a function of time. (1) The glucose solution is injected. (2) The glucose solution reaches the cavity. (3) Deionised water is injected. (4) Water reaches the cavity. (b) The black line is the measured refractive index over time. The blue region is the expected refractive index from the glucose solution. The grey line is the refractive index measurement assuming no cavity length noise using a single cavity (from the spectrum of the cavity with the smallest length). The inset shows the Allan variance for the measured refractive index as a function of the sampling time.

Vallance et al. [151] employed optical microcavities to increase the effective path length by orders of magnitude, dramatically improving the detection sensitivity of

optical absorption measurements. The concentration of the sample can be calculated with the adaption from Beer-Lambert law:

$$\frac{1}{\alpha l}\left(\frac{I_0 - I}{I}\right) = CL^{-1} \tag{2.8}$$

where α is the absorption coefficient, l is the single-pass path length through the sample, I and I_0 denote the transmitted light intensity with the sample and without the sample respectively, C is the concentration of the sample and L^{-1} is the cavity enhancement factor. Figure 2.10(a), reproduced from [151], demonstrates an example data set of the wavelength shift as well as the intensity change with different concentrations of methylene blue in the microcavity. (b), reproduced from [151], uses the experimental data and equation 2.8 to obtain the cavity enhancement factor of 266. The minimum detectable concentration was deduced to be 25 µM with 0.47 fL under this experimental condition.

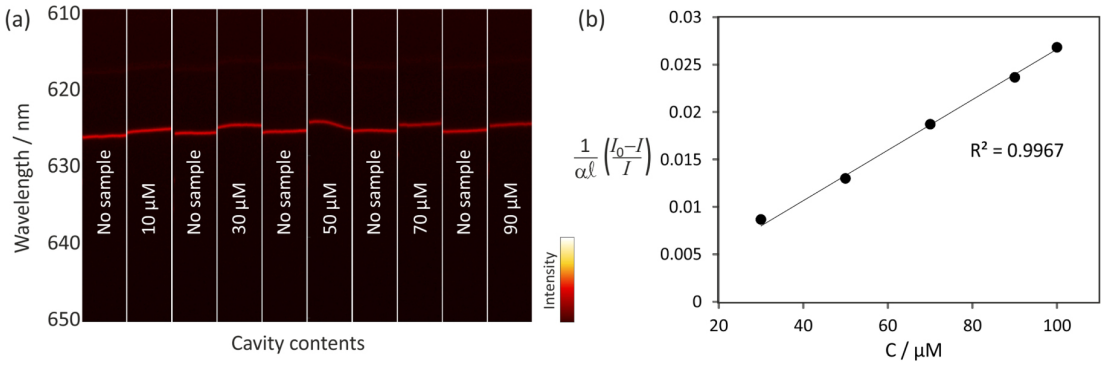


Figure 2.10: The figure is reproduced from [151]. (a) Attenuation of a single cavity mode as increasing concentrations of methylene blue in ethanol are introduced into the microcavity. (b) Plot of equation 2.8 is used to determine the cavity enhancement factor. The data were fitted to a straight line passing through the origin with a regression coefficient of $R^2 = 0.9967$.

Nanoparticle trapping and characterisation can also be achieved with optical microcavities [152]. The polarisability of a spherical polymethyl methacrylate (PMMA) and polystyrene and their coefficients of friction can be established with the cavity

mode wavelength shift as the particle diffuses through the microcavity. This work used nanotweezers to trap nanoparticles and exhibited the potential of optical microcavities for in situ sensoring of nanoparticles and biological samples, and lab-on-a-chip devices. Malmir et al. proposed a size measurement technique by analysing the competition between viscous drag and optical forces in optical microcavities [153]. The derivative of the trap rate, which represented how many particles were trapped in one minute, was analysed with different laser powers. They also performed simulations which agreed well with experimental results. Although only sensing applications are reviewed in detail for this FIB-milled Fabry-Pérot microcavity, it can also be applied in other fields, such as creating optically addressable solid-state spin qubits for the potential in scalable quantum computing applications [154] and single photon sources [155].

FFPCs can be applied to various applications. Firstly, small mode volumes enhance the electric field strengths of a single photon to realise strong coupling with single atoms in the quantum regime. FFPCs showed stronger atom field coupling strength, especially in the fast cavity regime [156–158] compared with bulk cavity experiments [159–161]. Information is carried about the quantum state of the atom-cavity system by photons leaving the cavity [162]. The emission of a photon from the FFPCs is a 'read' process while the inverse 'write' process is also possible. This makes FFPCs coupled to quantum emitters prime candidates for quantum memories in future quantum networks [163]. Additionally, FFPCs can be applied in cavity optomechanical experiments where the interaction of optical cavity modes and the motion of mechanical elements is investigated [164]. Not only can the mechanical resonator be pushed by the radiation pressure (the mechanical force exerted on a surface by light radiation that is absorbed, reflected, or emitted by matter), but also the optical mode frequency can be detuned by the mechanical resonator displacements. FFPCs bring the benefit

of tolerating large optical drive powers compared to other more miniaturised systems such as whispering gallery mode (WGM) resonators [165] and optomechanical crystals [166] where heating and thermal instabilities cause problems. Lastly, like FIB-milled optical microcavities mentioned before, FFPCs can also be utilised in sensing applications. Scanning cavity microscopes use a fibre mirror as a scanning probe above a reflective substrate. The surface mapping was achieved with this [146, 167]. In addition, it could also perform the quantitative imaging of the extinction cross-sections of gold nanoparticles and measure the birefringence and extinction contrast of gold nanorods [168]. Mader et al. [168] introduced a method to improve the spatial resolution below the diffraction limit with higher-order cavity modes. Recently, Needham et al. [169] utilised FFPC to detect unlabelled and free diffusing individual biomolecules in the solution as small as 1.2 kDa with unprecedented SNRs>100.

2.3.2 Whispering Gallery Mode (WGM) Microcavities

WGM was first introduced by Lord Rayleigh when he studied the acoustic resonance in St. Paul's Cathedral in London where whispers could be heard across the gallery [170, 171]. Optical WGM microcavities usually have a circular cross-section. Total internal reflection occurs when light propagates along the periphery with the index contrast between the cavity and its surroundings. A tail of the electric field, namely the evanescent field, extends outside the physical boundaries of the resonator while the photon energy is confined in the cavity [172]. Geometries of WGM microcavities are diverse, such as spheres [173–175], disks [176, 177], toroids [178], etc.

When the particle does not absorb light, it can be sensed by monitoring the break of the degeneracy of the WGMs. A mode shift can be detected which depends on the nanoparticle size and its position relative to the microcavity. Vollmer et al. [179] reported the detection of a single Influenza A virus by monitoring the mode shift

through the transmission spectrum with a tunable laser illustrated in Figure 2.11, reproduced from [179]. They tested their experimental setup with single standard polystyrene (PS) particles with a radius of 250 nm first. The statistical analysis of the wavelength shift step size was performed to evaluate successful binding events and unsuccessful ones. They confirmed the reactive sensing mechanism derived from first-order perturbation theory and enhanced signals by reducing the size of microspherical cavities. With the binding particles, the cavity had to be cleaned after each measurement.

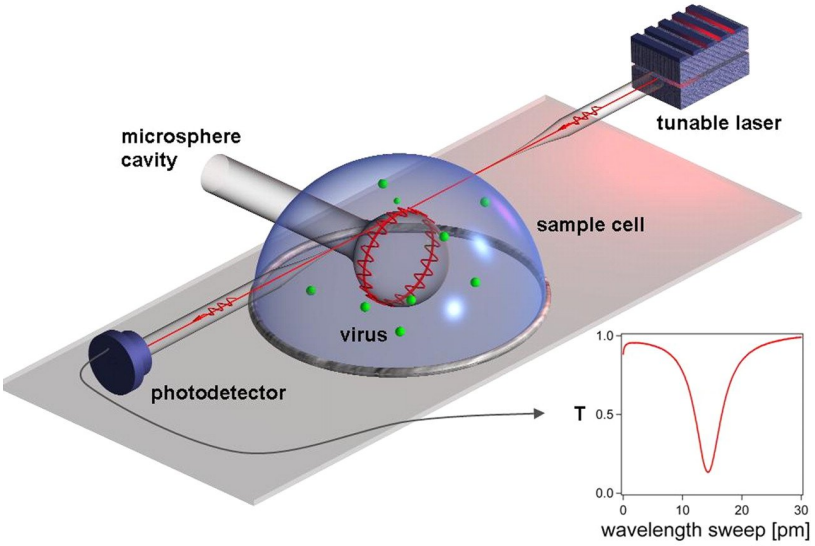


Figure 2.11: The figure is reproduced from [179]. Excitation of an equatorial WGM of a microsphere by evanescent coupling to a guided wave in a tapered optical fibre. Resonance positions are detected as dips in the transmitted light T at particular laser wavelengths.

Unlike the standing waves formed in Fabry-Pérot cavities, WGMs have travelling waves and a pair of counter-propagating modes degenerate in frequency. The degeneracy can be lifted to form a doublet due to surface roughness, material inhomogeneity and the presence of scatterers [172], such as nanoparticles. In the presence of particles, additional damping is caused by the scattered light into the environment while some part of the light scatters back into the cavity and forms a symmetric mode and an asymmetric mode. Since this sensing technique uses the incident light as the

reference and does not need additional reference light, mode splitting is robust to the laser frequency noise and thermal fluctuations. Zhu et al. [180] reported in situ detection and sizing of single nanoparticles, down to 30 nm in radius. Consecutive binding events of potassium chloride (KCl) particles to the microtoroid cavity led to different transmission spectra with different splitting magnitudes shown in Figure 2.12(a), reproduced from [180]. The KCl particle detected in this work has a radius of 40 nm while Ozdemir et. al pushed the detection limit even further to the radius of 10 nm [181]. Normalised splitting was calculated to compare the results of particles with different diameters illustrated in Figure 2.12(b), reproduced from [180].

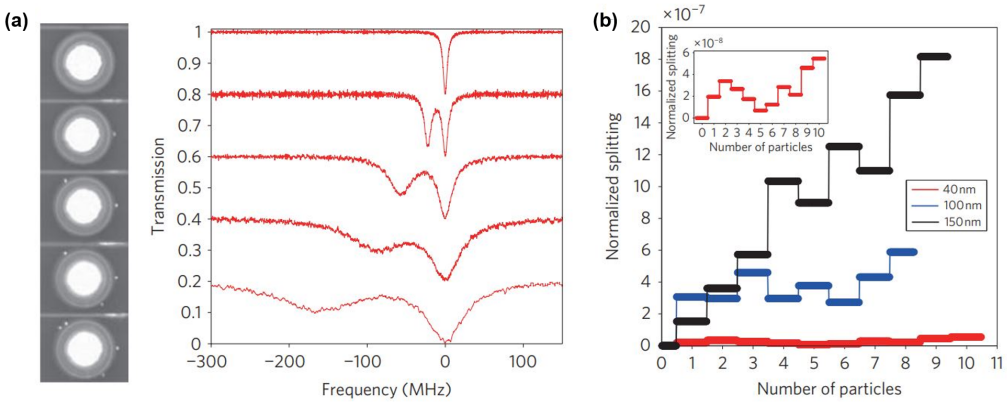


Figure 2.12: The figure is reproduced from [180]. (a) Series of normalized transmission spectra taken at a 1550 nm wavelength band and the corresponding optical images (assisted by a visible light laser) recorded without nanoparticles (top trace) and with four successive depositions of KCl nanoparticles. The spectra are vertically shifted for clarity. (b) Normalized splitting versus particle number for KCl nanoparticles. Each discrete step (vertical lines are drawn to guide the eye) corresponds to a single nanoparticle binding event. The inset shows an enlarged plot for nanoparticles of R = 40 nm.

When the splitting is smaller than the mode linewidth, the doublet is not obvious and appears as a mode with a broadened linewidth [172]. The coupling strength and the particle-induced scattering loss determine the broadening [182, 183]. With small enough nanoparticles, the broadening is dominated by the coupling strength. This detection scheme is also insensitive to laser frequency noise and thermal fluctuations,

like the previous mode splitting method. In addition, it does not require an ultra-high quality factor Q to resolve the doublet in the spectrum. Shao et al. detected single PS nanoparticles and lentiviruses using mode broadening. They fabricated a slightly deformed microcavity to efficiently excite the cavity mode and collect in free space [184, 185]. The linewidth of a WGM was obtained with the fitting to Lorentz lineshapes, improved by an iteration of weighted least squared regression.

Apart from the linear optical interaction, nonlinear optical processes can also be employed for sensing in WGMs. The Raman and Brillouin scatterings are one of the most commonly observed nonlinear processes in microcavities with a high quality factor and high finesse [186]. They are inelastic scattering processes of atoms or molecules. During the scattering, a photon loses or gains some energy from the vibrations of the atoms and bonds, creating the Stokes and anti-Stokes sidebands separated in frequency by the differences in the phonon energies. With sufficient excitation power, the stimulated emission happens among the Stokes photons, generating Raman/Brillouin gain and lasing. These photon-phonon interactions of WGMs enable the detection of analyte molecules with spectral fingerprinting. Huang et al. [187] reported enhanced Raman signals of a single rhodamine 6G on the silica microsphere with tapered fibre pumping, compared with free-space pumping and on the substrate near the microsphere, illustrated in Figure 2.13, reproduced from [187]. It offers an alternative to metallic surface-enhanced Raman scattering substrate with the advantage of stability improvement under high-temperature and harsh electrochemical conditions [188, 189], and reduced perturbation to the analyte both chemically and thermally [190, 191].

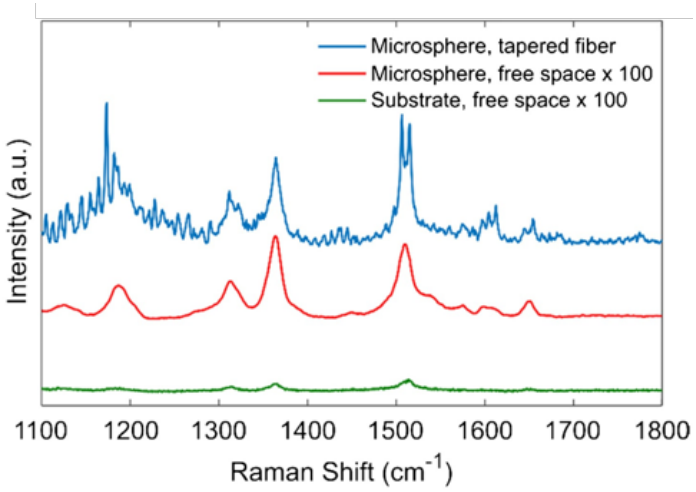


Figure 2.13: Raman enhancement of rhodamine 6G through the silica microsphere, reproduced from [187]. Background subtracted Raman spectra of rhodamine 6G for tapered fibre coupler excitation (blue), free-space excitation on a microsphere (red), and free-space excitation on the substrate (green). The spectra for free-space excitation on the microsphere and substrate are scaled by 100 times for visibility.

The Harmonic generation process is where multiple identical photons convert into one photon with multiplied frequency. Second and third harmonic generations are commonly observed [186]. They can be enhanced with WGM microcavities with ultrahigh quality factor. Second harmonic generation can only be significant at the microcavity surface due to the inversion symmetry breaking [192]. This property can be employed to monitor molecules absorbed onto the microcavity surface. Dominguez-Juarez et al. [193] reported a detection limit of 50 to 100 molecules deposited on the outer surface of the microresonator. It required phase matching in the WGMs achieved by a periodically patterned molecular surface monolayer. Third harmonic generation was also studied in WGM microcavities. Chen et al. reported enhanced conversion efficiency of third harmonic generation by coating a thin layer of organic molecules on the surface of the silica microsphere [194]. It showed potential for tunable photonic devices and sensitive surface molecule sensing. Lastly, WGM combined with other techniques, such as the frequency comb spectroscopy, further expands its applications. The frequency comb spectroscopy had its original revolution in time

and frequency metrology in the late 1990s [195]. Suh et al. [196] proposed the first microcavity-based dual-comb spectroscopy with silica WGM microcavities working at telecom wavelength. They achieved high-coherence pulsed mode locking, and broad and reproducible spectral envelopes. With the experimental apparatus, they studied the absorption spectrum of the $H^{13C}N$ in the $2v_3$ band with submillisecond acquisition time and over 30 dB SNR.

2.3.3 Photonic Crystal Microcavities

Photonic crystals are periodic dielectric structures that control and manipulate light. They affect the properties of photons in much the same way a semiconductor affects the properties of an electron [197]. The photonic band gap of the periodic structures forbids light propagation. An intentionally created defect in the periodic structures can create a resonant mode highly confined within the vicinity of the defect, which forms a microcavity with low loss and a small mode volume [172, 197]. Apart from the conventional way of introducing defects, the air-slot [198, 199] or the air mode [200] photonic crystal nanobeam cavities have been developed to offer a higher quality factor and a smaller mode volume by creating one row of regular air holes with a slot (air-slot mode) or without a slot between two adjacent cells. Thanks to the engineerable propagation of light by adjusting the structural parameters or infiltrating suitable materials in the air holes, many photonic crystal based devices are widely used in light flow control. Examples include filters [201, 202], electro-optical modulators [203, 204], delay devices [205], etc. Detailed discussions on applications in sensing will be introduced.

Photonic crystals take 1D, 2D and 3D forms with remarkable interest in 2D owing to the relatively easy manufacturing process while maintaining almost all the significant characteristics. The fabrication process normally includes film deposition, pattern

defining, and pattern transfer [206]. Film deposition includes chemical deposition where a chemical reaction takes place between the hot substrate and inert gases in the chamber [207] and physical deposition where the raw materials are released and moved physically onto the upper surface of the substrate. Examples of chemical deposition are chemical vapour deposition, atomic layer deposition, etc. while physical deposition includes thermal evaporation, molecular beam epitaxy, etc. Developments of pattern defining for the fabrication of photonic crystal began from e-beam lithography used by Cheng et al. [208] and new techniques were employed afterwards, such as deep x-ray lithography [209], holographic lithography [210], deep UV lithography [211] and nanoimprint lithography [212]. Pattern transfer is usually achieved by wet or dry etching techniques, such as reactive ion etching, inductively coupled plasma etching, etc.

With the engineered defect structures, a photonic crystal cavity (PCC) creates an optical mode with a resonant wavelength, which is highly sensitive to the refractive index change. Thus PCC can be applied in refractive index sensors. Chow et al. [213] achieved the ambient refractive index change of 0.002 with two ridge waveguides to couple light in and out of the photonic crystal microcavity. The fabricated photonic crystal microcavity is illustrated in Figure 2.14, reproduced from [213], with the SEM view.

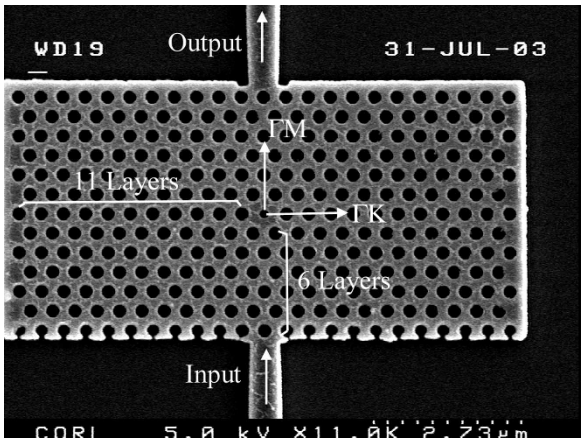


Figure 2.14: The figure is reproduced from [213]. SEM view of a photonic crystal microcavity integrated with two ridge waveguides. The regular hole and the defect hole diameter are 0.58a and 0.4a respectively with a = 440 nm of the lattice constant of the photonic crystal.

The normalised transmission spectrum was recorded with different ambient refractive indices ranging from 1.446 to 1.454 with 0.002 increments, displayed in Figure 2.15(a), reproduced from [213]. (b), reproduced from [213], demonstrates the capability of in-situ time-resolved sensing. A droplet of 5% glycerol in deionised water was applied to the sensor and the evaporative process of water was observed with the refractive index change indicated by the resonant wavelength change.

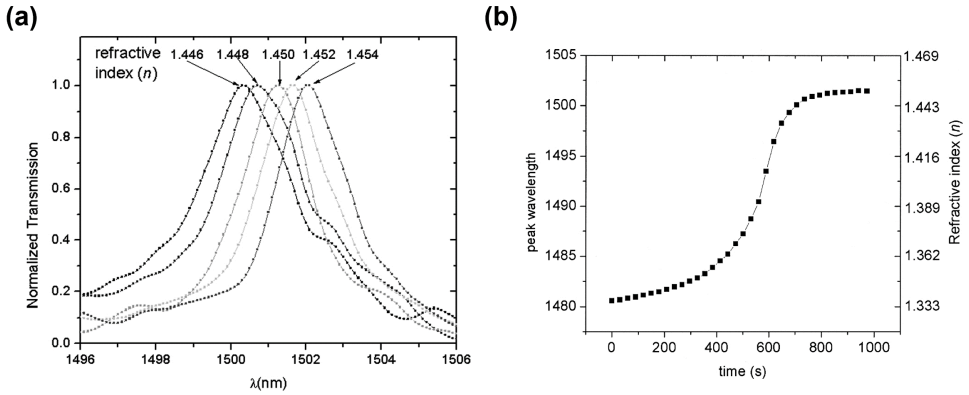


Figure 2.15: The figure is reproduced from [213]. (a) Normalised transmission spectra of the photonic crystal microcavity with different ambient refractive indices ranging from n = 1.446 to n = 1.454 in 0.002 increments. (b) Resonant wavelength and the corresponding refractive index over time during the evaporative process of water in a glycerol-water mixture.

Several experimental and simulation-based studies have been put forward to improve the detection limit by engineering the structures and reducing noise. L3 cavities with three missing holes [214] and H1-r defects [215] on the substrate were studied by Dorfner et al. in the sensitivity of refractive index sensing [216]. The H1-r defects are shown in Figure 2.16 with a single hole which can be tuned in radius surrounded by other holes with the same radius. The two structures are displayed in Figure 2.16, reproduced from [216]. Air, water and isopropanol were measured and the detection limits were extrapolated as 0.018 and 0.006 for the H1-r design and L3 cavity. Although the sensitivity did not increase in this case, the structure consisting of a resonant cavity between two spatially separated photonic crystal-waveguide combinations allows many detectors to be selectively addressed in parallel. Also, it can readily be operated in a liquid flow cell.

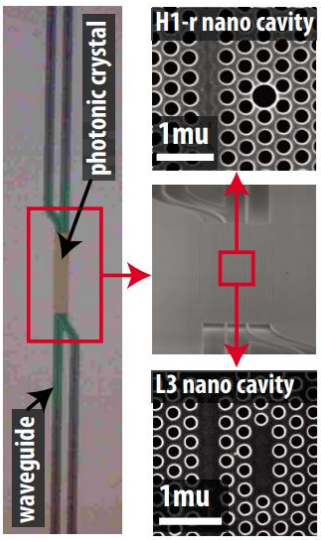


Figure 2.16: SEM images showing the H1-r and L3 defects in vicinity of the photonic crystal-waveguide, reproduced from [216].

Di et al. studied and optimised the slotted photonic crystal cavity to enhance the sensitivity further [217] with the structures illustrated in Figure 2.17, reproduced from [217]. They reached 7.8×10^{-6} with the optimal design.

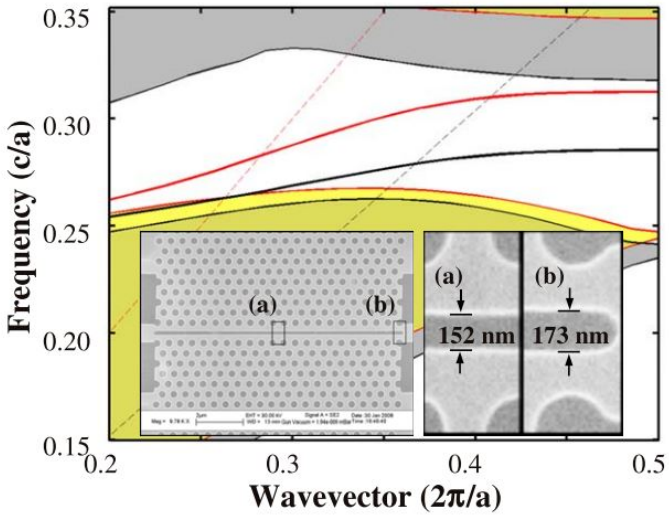


Figure 2.17: Dispersion properties of slotted photonic crystal with different background refractive indices, reproduced from [217]. Inset: SEM image of a slotted photonic crystal cavity with zoomed view of the (a) central and (b) external part of the slot.

Apart from use as refractive index sensors, PCCs can also be applied in biochemical sensors. Lee et al. [218] proposed sensing the target molecules with a 2D photonic crystal microcavity covered with a monolayer of probe molecules. The schematic of the experimental apparatus is shown in Figure 2.18(a), reproduced from [218] and the schematic of bio-molecule recognition is illustrated in Figure 2.18(b), reproduced from [218]. They used glutaraldehyde as the probe molecule and bovine serum albumin as the target molecule as an example system to test. They monitored the binding by the spectral resonance redshift and quantitatively measured the dehydrated protein size.

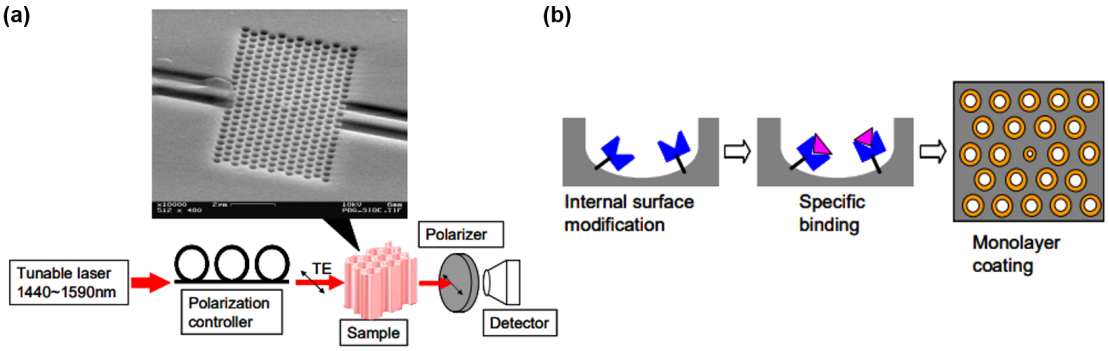


Figure 2.18: The figure is reproduced from [218]. (a) SEM image of the device and schematic of the experimental apparatus. A polarisation controller was used to maximise the transverse electric mode. (b) Schematic of bio-molecule recognition. The target molecules were captured by the probe molecules, changing the refractive index.

Hsiao et al. employed a ring PCC to monitor the reaction kinetics and protein concentration with the minimum detectable biomolecule weight of only 0.2 fg [219], illustrated in Figure 2.19(a), reproduced from [220]. This structure allows the function integration to be achieved. Measurements of multiple biomolecules can be performed with the same input port [221]. The structure of two ring PCCs is shown in Figure 2.19(b), reproduced from [220]. The forward and backward drops were defined when the propagated dropped light was parallel and antiparallel to the input light. The dropped light was coupled into the drop waveguide above the dual nanoring resonator while the input waveguide was below. They have different resonant modes that can be manipulated respectively.

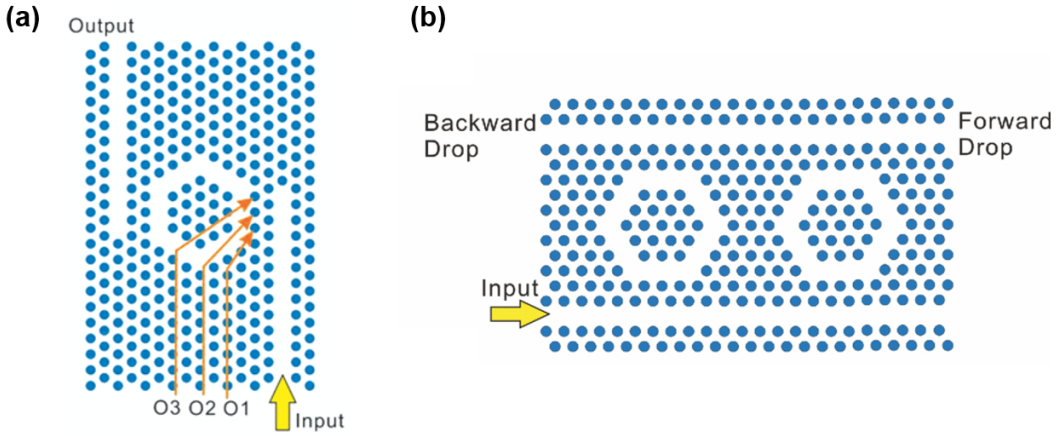


Figure 2.19: The figure is reproduced from [220]. (a) Sketch of nanoring resonator. (b) Sketch of dual nanoring resonator.

Nanoparticles can be detected and size information can be extracted with PCC [198, 200]. Liang et. al reported detecting and sizing single gold nanoparticles down to 1.8 nm in diameter (equivalently single polystyrene nanoparticle of 3 nm in diameter) using air-mode photonic crystal nanobeam cavity at telecom wavelength. The air-mode cavity has strong field localisation and improves the sensitivity to detect nanoparticles. The strong field gradient attracts the nanoparticles to its field maximum. SEM images of the device were also taken to confirm the presence of the single trapped nanoparticle. Resonance shifts were measured to distinguish between 1.8 nm gold nanoparticles and 5 nm nanoparticles. Apart from experimental results, Wang et. al [222] performed simulations for on-chip trapping and sorting of nanoparticles using a single slotted photonic crystal nanobeam cavity. They simulated the optical trapping force for 120 nm and 30 nm particles, and by optimising the width of the slot and choosing the appropriate input power range, only the 120 nm particle could be trapped while the 30 nm particle could not. And the resonant wavelength shifts could be monitored to further confirm the trapping events.

The sensing application is not limited to the liquid phase, but can also be applied in

the gas domain. The gas concentrations in a gas mixture of two gases with different refractive indices or relative gas pressures could be measured with heterostructure PCC [223] and heterostructure slot PCC [224].

2.4 Summary

In this chapter, current common methods for shape measurement are reviewed, both for nanoparticles and for biological samples. Electron microscopy including SEM and TEM provides high-resolution images for both types of samples with appropriate sample preparations. They require advanced technical skills and careful data interpretation. All the other techniques that have been reviewed employ interactions between particles and light to obtain shape information. Analysis of scattered light from the particles provides the size information and due to the R^6 dependence, bigger SNR is pursued when dealing with smaller particles, such as monitoring the interference between scattered light and incident light to reduce the dependence to R^3 in iSCAT. Capturing shape anisotropy often requires the state change of the incident light, adding complexity to a single wavelength and linearly polarised laser light. With a more complex state of the incident light, the output light will contain more information in response to the anisotropy for researchers to extract, such as the polarisation state in DDLS, and broad spectrum in spectroscopy. Camera speed is a limited factor when monitoring the rotational and translational diffusion of small particles. Quantitative analysis at a single-particle scale is also difficult to achieve.

Apart from the review of shape measurement techniques, three types of common optical microcavities are also introduced, including their constructions, fabrication methods and their applications, especially in the sensing domain. Optical microcavities enhance the interactions between particles and light by confining light over a

small area. Fabry-Pérot microcavities allow particles to freely diffuse through or be trapped and can be utilised to perform single-particle characterisations, such as refractive index change, polarisability and size. WGM sometimes needs the binding of the particle to the microsphere, which exerts an extra cleaning step between experiments. However, it is worth mentioning that measuring the size of nanoparticles suspended in the vicinity of a WGM biosensor, not bonded, has also been explored [225]. Nonlinear optical processes to obtain spectral fingerprinting of different analytes are also reviewed. Sensitivities of measurements using photonic crystal microcavities depend on engineering defect structures to optimise the performance. Applications in refractive index sensing, biochemical sensing and gas sensors are investigated.

Chapter 3

Theory

3.1 Introduction

This chapter introduces the theoretical background required for this work. Firstly, the Gaussian beam and Hermite-Gaussian beam as a more general form are introduced. Then the open-access optical microcavity is briefly explained and several important metrics are presented. Combined with the electric field of the Gaussian beam introduced in the first section, the optical field in the optical microcavity can be derived. Additionally, how the polarised light through an optical microcavity can be utilised to perform shape measurement is explained. Equations of Stokes parameters of the transmitted light through the optical microcavity in the presence of a rod-shaped particle are presented. Some supplementary theoretical calculations are displayed. Lastly, the theory behind Monte Carlo simulations and FDTD simulations are discussed.

3.2 Gaussian Beam

A Gaussian beam is an idealised beam of electromagnetic radiation whose amplitude envelope in the transverse plane is given by a Gaussian function. The detailed deriva-

tions of equation 3.1 to equation 3.5 can be found in textbooks [226]. The expressions of the electric field can be derived from Maxwell's equations. For a dielectric medium with no free electric charges or currents, Maxwell's equations are:

$$\nabla \cdot \boldsymbol{D} = 0 \tag{3.1a}$$

$$\nabla \cdot \boldsymbol{B} = 0 \tag{3.1b}$$

$$\nabla \times \boldsymbol{E} = -\frac{\partial \boldsymbol{B}}{\partial t} \tag{3.1c}$$

$$\nabla \times \boldsymbol{H} = \frac{\partial \boldsymbol{D}}{\partial t} \tag{3.1d}$$

The electric displacement $\boldsymbol{D}$ and the magnetic intensity vector $\boldsymbol{H}$ are defined as: $\boldsymbol{D} = \epsilon_0 \boldsymbol{E} + \boldsymbol{P}$, where $\boldsymbol{P}$ is the polarisation density and ϵ_0 is the permittivity of free space, and $\boldsymbol{B} = \mu_0 \boldsymbol{H}$, where μ_0 is the permeability of free space assuming a nonmagnetic medium. Applying the curl operation to both sides of equation 3.1c and using $\nabla \times (\nabla \times \boldsymbol{E}) = \nabla(\nabla \cdot \boldsymbol{E}) - \nabla^2 \boldsymbol{E}$, the wave equation can be derived:

$$\nabla^2 \boldsymbol{E} - \frac{1}{c^2} \frac{\partial^2 \boldsymbol{E}}{\partial t^2} = 0 \tag{3.2}$$

As we are interested in the monochromatic laser beam and we assume that light propagates in the z direction, the electric field can be expressed as $E(\vec{r}, t) = E(\boldsymbol{r}) e^{-iwt} e^{ikz}$ where $E(\boldsymbol{r})$ is the magnitude of the electric field as a function of the position. With approximations, equation 3.2 could be further simplified into the paraxial wave equation:

$$\left(\frac{\partial^2}{\partial x^2} + \frac{\partial^2}{\partial y^2} + 2ik \frac{\partial}{\partial z} \right) E(\boldsymbol{r}) = 0 \tag{3.3}$$

The Gaussian beam profile is one of the solutions to the above equation:

$$E(\boldsymbol{r}) = \frac{E_0 e^{ikz} e^{-i\phi(z)}}{\sqrt{1 + z^2/z_0^2}} e^{ik(x^2+y^2)/2R(z)} e^{-(x^2+y^2)/w^2(z)} \tag{3.4}$$

where E_0 is a constant. $\phi(z)$, $R(z)$ and $w(z)$ are expressed below with some of the parameters illustrated in Figure 3.1:

$$\phi(z) = \tan^{-1}\left(\frac{z}{z_0}\right),\ R(z) = z + \frac{z_0^2}{z},\ w(z) = w_0\sqrt{1 + z^2/z_0^2} \tag{3.5}$$

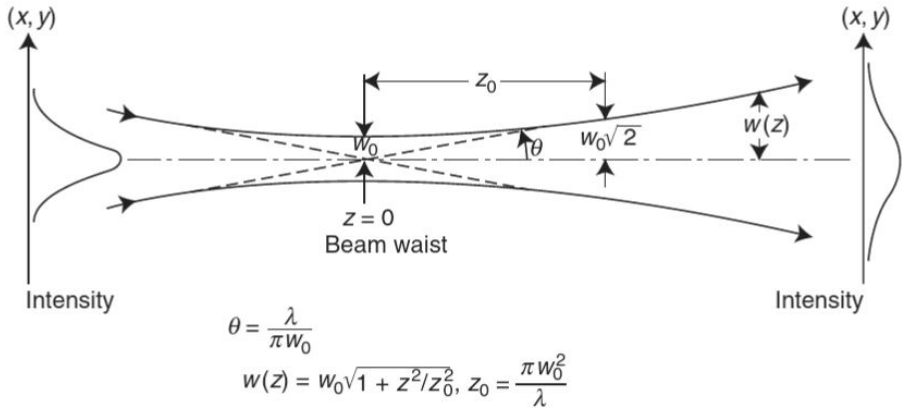


Figure 3.1: Variation of the spot size $w(z)$ of a Gaussian beam, reproduced from [226]. $z = 0$ has a beam waist of w_0, z_0 is the Rayleigh range where the beam width is $\sqrt{2}w_0$, $w(z)$ is the beam width at z. θ is the divergence angle of the Gaussian beam.

where $z_0 = \frac{\pi w_0^2}{\lambda}$, known as the Rayleigh range where w_0 is the beam waist, $w(z)$ is the beam width at z, $R(z)$ is the wavefront RoC at z and $\phi(z)$ is the Gouy phase shift at z.

3.3 Hermite-Gaussian Beam

It is worth mentioning that the Gaussian beam is not the only solution to the paraxial wave equation 3.3 [226]. It is a special case of a more general solution with the electric field below:

$$E_{mn}(x, y, z) = \frac{E_0 w_0}{w(z)} H_m\left[\sqrt{2}\frac{x}{w(z)}\right] H_n\left[\sqrt{2}\frac{y}{w(z)}\right] e^{i[kz-(m+n+1)\phi(z)]} \times e^{ik(x^2+y^2)/2R(z)} e^{-(x^2+y^2)/w^2(z)}\ (\ m = 0,\ 1,\ 2, ...;\ n = 0,\ 1,\ 2, ...) \tag{3.6}$$

where $w(z)$, $\phi(z)$ and $R(z)$ are the same as in equation 3.5. H_m and H_n are Hermite polynomials, the first few of which are:

$$H_0(u) = 1 \tag{3.7a}$$

$$H_1(u) = 2u \tag{3.7b}$$

$$H_2(u) = 4u^2 - 2 \tag{3.7c}$$

$$H_3(u) = 8u^3 - 12u \tag{3.7d}$$

$$H_4(u) = 16u^4 - 48u^2 + 12 \tag{3.7e}$$

When $m = n = 0$, this is the previously mentioned Gaussian beam, also called the 'zero-order' case. Figure 3.2 shows the intensity profile of Hermite-Gaussian beams with $m = 0,\ 1,\ 2$ and $n = 0,\ 1,\ 2$.

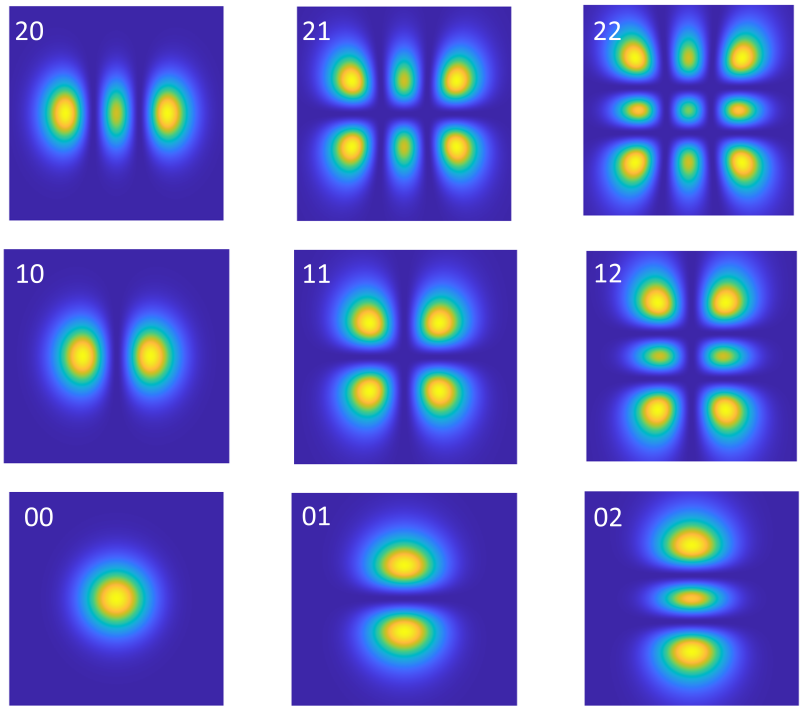


Figure 3.2: Hermite-Gaussian beam profile in xy plane with the light propagating in z direction. The labels are in the form of (m, n).

3.4 Open-access Optical Microcavity

The optical microcavity in this work consists of a concave and planar mirror with highly reflective coatings. When the light irradiates the cavity, the reflected light interferes with the incident light. If the cavity length satisfies:

$$L = \frac{q\lambda}{2n_m} \tag{3.8}$$

where q is the number of antinodes, λ is the wavelength of the incident light and n_m is the refractive index of the medium, it can form resonant modes. The transmitted light intensity reaches a maximum as the reflected light interferes constructively. Figure 3.3(a) shows the diagram of the situation when $q = 4$ and the surface is at the node. Whether the surface is at the node or antinode could be adjusted with a certain design of coating, which will be introduced in Chapter 4.2.3.

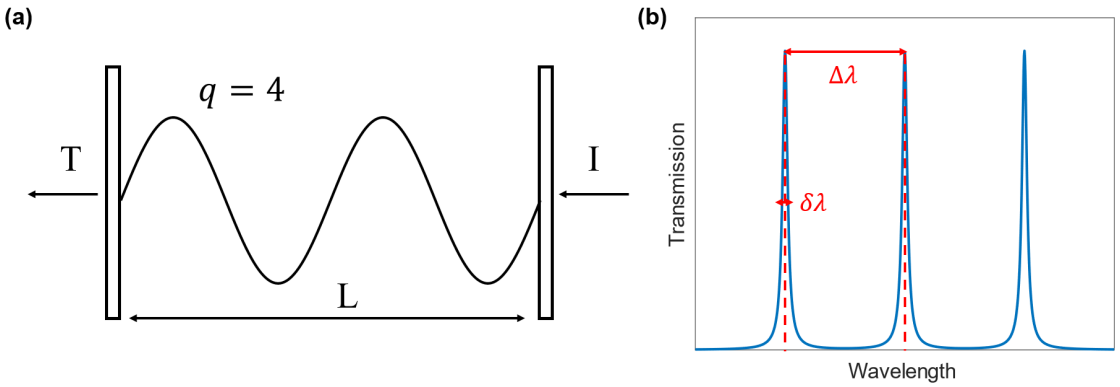


Figure 3.3: (a) Diagram of a microcavity at resonance with $q = 4$. I is the incident light while T is the transmission. L is the cavity length. (b) An example of the transmitted spectrum where $\triangle\lambda$ is the FSR and $\delta\lambda$ is the linewidth of a cavity mode.

There are three important metrics describing optical microcavities. The first one is the finesse of the cavity $\mathcal{F}$, which determines how many round trips light can make before exiting the cavity. It can be expressed as a function of the reflectivities of two

mirrors R_1 and R_2 [227, 228]:

$$\mathcal{F} = \frac{\pi\sqrt{g_m}}{1-g_m},\ g_m = \sqrt{R_1 R_2 e^{-\beta p}} \tag{3.9}$$

where β is the loss coefficient for internal absorption or scattering, p is the optical path length for one round-trip and $e^{-\beta p}$ represents the round-trip intensity loss of the cavity. In practice, it can be measured with the transmitted spectrum:

$$\mathcal{F} = \frac{\triangle\lambda}{\delta\lambda} \tag{3.10}$$

where $\triangle\lambda$ is the free spectral range (FSR), the wavelength separation between adjacent longitudinal cavity modes and $\delta\lambda$ is the linewidth of a cavity mode, namely full width at half maximum (FWHM). Figure 3.3(b) presents an example of the transmitted spectrum with these parameters labelled.

The second metric is the quality factor Q, which is a measure of the rate at which optical energy decays from within the cavity [136]. For example, the decay could come from the absorption and scattering in the cavity or leakage through the imperfect mirrors. It is expressed as:

$$Q = \frac{\lambda}{\delta\lambda} = q\mathcal{F} \tag{3.11}$$

where λ is the centre wavelength at resonance, q is the mode number.

The third metric is the FSR mentioned above. From equation $q = \frac{2n_m L}{\lambda}$ rearranged by equation 3.8, we can get when $\triangle\lambda$ is small:

$$\triangle q = -\frac{2n_m L}{\lambda^2}\triangle\lambda \tag{3.12}$$

For adjacent longitudinal modes, $\triangle q = 1$ and $\triangle\lambda$ is the FSR. Therefore $L = \frac{\lambda^2}{2n_m \triangle\lambda}$,

which can be employed to determine the cavity length in practice.

Theoretically, the finesse $\mathcal{F}$ should be an intrinsic property of the cavity, not dependent on the cavity length. However, in practice, the cavity length is required to be smaller than approximately $\frac{1}{3}$ of the RoC of the concave mirror [229] to achieve a nearly constant finesse $\mathcal{F}$. The quality factor Q and FSR depends on the cavity length with the expressions shown above. It is worth mentioning that when the cavity length is very small, the FSR becomes too big to be measured through the transmission spectrum in practice.

3.5 Optical Modes in the Microcavity

Equation 3.4 describes the Gaussian beam profile propagating in free space without any constraints. Certain conditions need to be fulfilled with the cavity in place. The microcavity used in this work consists of a planar and a hemispherically featured mirror with specific geometrical parameters to support a unique set of Gaussian modes. The planar mirror position is the beam waist location, namely the $z = 0$ position in Figure 3.1. The hemispherically featured mirror is placed at $z = L$, and the wavefront RoC should match the physical RoC of the hemisphere feature R.

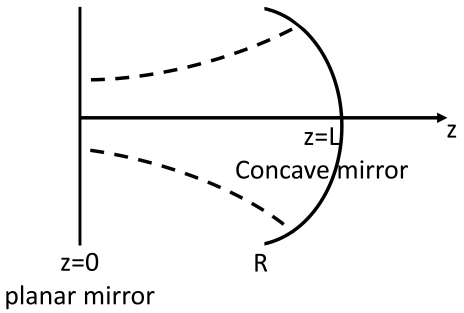


Figure 3.4: Schematic of one planar mirror and one concave mirror forming the microcavity $z = 0$ is the planar mirror position as well as the beam waist location. $z = L$ is the concave mirror position and the RoC of the concave feature is R.

Therefore with equation 3.5, R should satisfy:

$$R = L + \frac{\pi^2 w_0^4}{\lambda^2 L} \tag{3.13}$$

Thus the beam waist can be expressed as a function of the RoC of the concave mirror R and the cavity length L:

$$w_0^2 = \frac{\lambda L}{\pi}\sqrt{\frac{R}{L} - 1} \tag{3.14}$$

This can also be deduced from a general case where the cavity consists of two concave mirrors having RoCs of R_1 and R_2 shown in Figure 3.5.

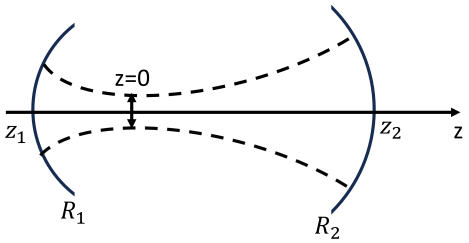


Figure 3.5: Schematic of two concave mirrors forming the microcavity. z_1 and z_2 are the positions of the two concave mirrors with RoC of R_1 and R_2.

Then they satisfy:

$$-R_1 = z_1 + \frac{z_0^2}{z_1} \tag{3.15a}$$

$$R_2 = z_2 + \frac{z_0^2}{z_2} \tag{3.15b}$$

where $z_2 - z_1 = L$. Then if the mirror g parameter is defined as $g_i = 1 - \frac{L}{R_i}$ $(i = 1,\ 2)$,

the beam waist w_0, beam width w_1 and w_2 at z_1 and z_2 are expressed as:

$$w_0^2 = \frac{\lambda L}{\pi}\sqrt{\frac{g_1 g_2(1-g_1 g_2)}{(g_1+g_2-2g_1 g_2)^2}} \tag{3.16a}$$

$$w_1^2 = \frac{\lambda L}{\pi}\sqrt{\frac{g_2}{(g_1(1-g_1 g_2)}} \tag{3.16b}$$

$$w_2^2 = \frac{\lambda L}{\pi}\sqrt{\frac{g_1}{(g_2(1-g_1 g_2)}} \tag{3.16c}$$

In the scenario of a planar and a concave mirror, the planar mirror has a RoC of ∞, then w_0 becomes equation 3.14. Equation 3.16 also indicates the criteria of resonator stability, $R \geq L$, for the planar and concave mirror situation. In a general circumstance of two concave mirrors, it becomes $0 \leq g_1 g_2 \leq 1$.

Apart from the zero-order Gaussian beam, higher-order Gaussian beams mentioned in Chapter 3.3 can also form modes of stable resonators with different resonance frequencies from the zero-order mode:

$$\upsilon_{qmn} = \frac{c}{2L}\left[q + \frac{1}{\pi}(m+n+1)\cos^{-1}\sqrt{g_1 g_2}\right] \tag{3.17}$$

where c is the speed of light, L is the cavity length. Gaussian modes characterised by different values of m and n are different transverse modes, while different values of q correspond to different longitudinal modes. Although Figure 3.2 shows all the situations with m and n ranging from 0 to 2 respectively, their appearance order is determined by $m+n$ in the spectrum. Therefore it should be noted that TEM_{30} and TEM_{03} (TEM: Transverse Electromagnetic Mode), though not shown in Figure 3.2, appear before TEM_{22} mode.

With the beam waist determined, the electric field of a Gaussian beam shown in

equation 3.4 is:

$$E(x,y,z) = E_0 \frac{w_0}{w(z)} \exp\left(-\frac{x^2+y^2}{w^2(z)}\right) \exp\left(ikz + ik\frac{x^2+y^2}{2R(z)} - i\tan^{-1}\left(\frac{z}{z_R}\right)\right) \quad (3.18)$$

A simple schematic of the microcavity is shown in Figure 3.6 with the directions of the incident and reflected light labelled.

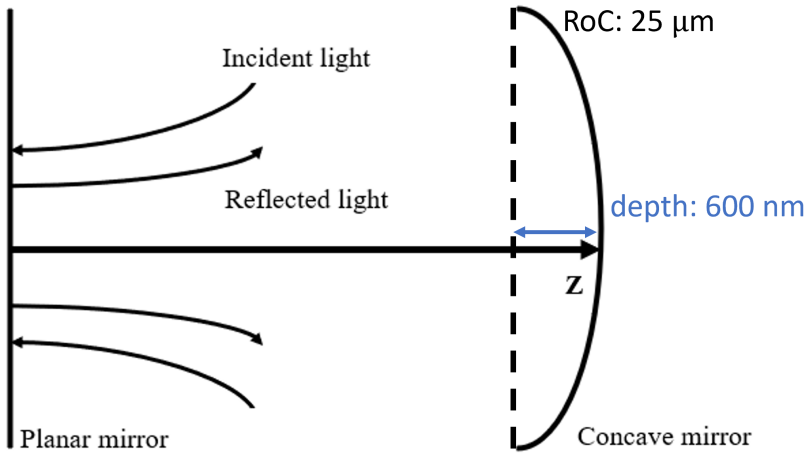


Figure 3.6: Schematic of an optical microcavity with the incident and reflected light labelled. The microcavity used in the experiment has a depth of 600 nm and a RoC of 25 µm.

The electric fields of the incident and reflected beams are expressed respectively as:

$$E_i(x,y,z) = E_0 \frac{w_0}{w(z)} \exp\left(-\frac{x^2+y^2}{w^2(z)}\right) \exp\left(-ikz - ik\frac{x^2+y^2}{2R(z)} + i\tan^{-1}\left(\frac{z}{z_R}\right)\right) \quad (3.19a)$$

$$E_r(x,y,z) = E_0 \frac{w_0}{w(z)} \exp\left(-\frac{x^2+y^2}{w^2(z)}\right) \exp\left(ikz + ik\frac{x^2+y^2}{2R(z)} - i\tan^{-1}\left(\frac{z}{z_R}\right)\right) \quad (3.19b)$$

The intensity of the field averaged over an optical period between the two mirrors is

calculated as [226]:

$$
\begin{aligned}
I(x,y,z) &= \frac{n_m \epsilon_0 c}{2} |E_i(x,y,z) + E_r(x,y,z)|^2 \\
&= n_m \varepsilon_0 c E_0^2 \frac{w_0^2}{w^2(z)} \exp\left(-\frac{2(x^2+y^2)}{w^2(z)}\right) \left[1 + \cos\left(2kz + k\frac{x^2+y^2}{R(z)} - 2\tan^{-1}\left(\frac{z}{z_R}\right)\right)\right]
\end{aligned} \tag{3.20}
$$

where n_m is the refractive index of the medium, ϵ_0 is the permittivity of vacuum. c is the light speed in a vacuum. To match the experimental conditions where the surface of the planar mirror is at a node, the phase is shifted by π and the intensity is:

$$
\begin{aligned}
I(x,y,z) = n_m \varepsilon_0 c E_0^2 \frac{w_0^2}{w^2(z)} \exp\left(-\frac{2(x^2+y^2)}{w^2(z)}\right) \\
\times \left[1 + \cos\left(\pi + 2kz + k\frac{x^2+y^2}{R(z)} - 2\tan^{-1}\left(\frac{z}{z_R}\right)\right)\right]
\end{aligned} \tag{3.21}
$$

Figure 3.7 illustrates the intensity profile using the above equation between the two mirrors with a cavity RoC of 4 µm and a cavity length of 2 µm in water. It displays six antinodes between two mirrors.

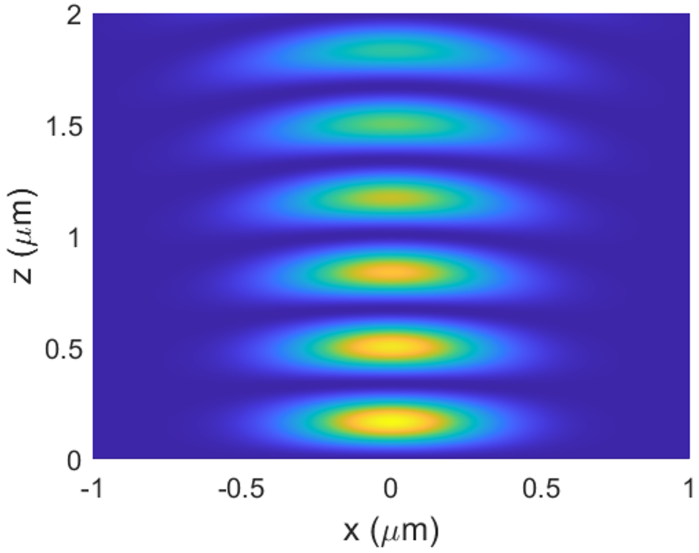


Figure 3.7: Intensity profile of Gaussian modes in the microcavity using equation 3.21. The planar mirror is placed at $z = 0$. The cavity RoC is 4 µm and the cavity length is 2 µm. The medium is water.

The electric field between the two mirrors becomes:

$$\begin{aligned} E(x,y,z) &= E_i(x,y,z) + E_r(x,y,z) \\ &= 2E_0\frac{w_0}{w(z)}\exp\left(-\frac{x^2+y^2}{w^2(z)}\right)\cos\left(\frac{\pi}{2}+kz+k\frac{x^2+y^2}{2R(z)}-\tan^{-1}\left(\frac{z}{z_R}\right)\right) \end{aligned} \tag{3.22}$$

3.6 Shape Measurement Through the Microcavity With Polarised Light

In this section, the cavity field is derived through using the Schrödinger equation. Beginning from the simple empty cavity, complexities are added sequentially and the equations are finally derived to deduce the shape anisotropy.

3.6.1 Empty Cavity

The Hamiltonian of a single photon in an empty cavity mode of frequency ω_c and loss rate Γ is $\hbar\omega_c - i\hbar\Gamma$. With the incident laser field of $E_0e^{-i\omega t}$, the cavity field amplitude ψ conforms to:

$$i\hbar\frac{d\psi}{dt} = (\hbar\omega_c - i\hbar\Gamma)\psi + \hbar\omega_i e^{-i\omega t} \tag{3.23}$$

where ω_i is the angular frequency of the incident light. Assuming that the cavity field takes the form $\psi = \psi_0 e^{-i\omega t}$, the complex response amplitude then shows the following dependence on the frequency:

$$\psi_0 = \frac{\omega_i}{\triangle_1 + i\Gamma} \tag{3.24}$$

where $\triangle_1 = \omega - \omega_c$ is the detuning of the laser from the cavity. The field intensity is thus calculated through:

$$I = |\psi|^2 = \frac{w_i^2}{\triangle_1^2 + \Gamma^2} \tag{3.25}$$

It has a Lorentzian shape with a linewidth of 2Γ.

3.6.2 Cavity with a Particle

When a tiny particle enters the cavity, the optical response from the microcavity has been introduced quantitatively in the cavity perturbation theory which was initially proposed by Bethe and Schwinger in optics [230] and then by Waldron in the radio-frequency domain [231]. The perturbation leads to a modification $\tilde{\triangle\omega}$ in the resonant frequency. It involves the real and imaginary part change, representing the frequency shift and linewidth change. Assuming a small and isotropic polarisability α, $\triangle\tilde{\omega}$ can be expressed as:

$$\frac{\triangle\tilde{\omega}}{\tilde{\omega}} \approx \frac{-\iiint \triangle\epsilon \mid \tilde{\boldsymbol{E}}(\boldsymbol{r}) \mid^2 dr^3}{\iiint[\epsilon_0 \mid \tilde{\boldsymbol{E}} \mid^2 + \mu_0 \mid \tilde{\boldsymbol{H}} \mid^2] d^3\boldsymbol{r}} \tag{3.26}$$

where $\triangle\epsilon$ is the change of the permittivity introduced by the particle, ϵ_0 and μ_0 are vacuum permittivity and permeability, $\tilde{\boldsymbol{E}}$ and $\tilde{\boldsymbol{H}}$ are the electric field and magnetic fields of the unperturbed cavity.

For consistency between sections, I derived the change following the way in Chapter 3.6.1 and presented the impact of the particle from the above equation assuming a small polarisability $\tilde{\alpha}$. When a polarisable particle enters the cavity, it changes the Hamiltonian to:

$$H = H_{cav} + H_{par} \tag{3.27}$$

In general, the interaction Hamiltonian H_{par} introduces a change in energy and additional loss so that it can be written as $H_{par} = \hbar(\delta - i\gamma)$. In the classical picture, the Lorentz oscillator model is used [232]. The displacement of electrons x in a polarisable object in response to an electric field E at angular frequency ω is described by the differential equation:

$$\frac{d^2x}{dt^2} + \gamma\frac{dx}{dt} + \omega_0^2 x = \frac{qE}{m} \tag{3.28}$$

where m is the electron mass, q is the charge of a single electron, γ is the damping rate and ω_0 is the resonant frequency. E can be expressed as $E = E_0 e^{-i\omega t}$. This equation balances the forces acting on the electrons with the Newtonian acceleration. The solution to this equation can be assumed as $x = x_0 e^{-i\omega t}$ and the amplitude of oscillation x_0 is derived as:

$$x_0 = \frac{qE_0}{m} \frac{1}{\omega_0^2 - \omega^2 - i\omega\gamma} \tag{3.29}$$

The fact that it is complex indicates a phase shift between the driving electric field and the response of the motion of the electron. The polarisability is given by the ratio of the induced dipole moment to the applied field:

$$\tilde{\alpha} = \frac{nqx}{E} = \frac{nq^2/m}{\omega^2 - \omega_0^2 - i\omega\gamma} = \alpha + i\beta \tag{3.30}$$

where n is the number of electrons, q is the charge of a single electron, α and β are the real and imaginary parts of the polarisability. Therefore the Hamiltonian of a particle placed in the centre of the cavity is:

$$H_{par} = -\frac{\tilde{\alpha}|E|^2}{2} = -(\alpha + i\beta)\frac{\hbar\omega_c}{2\epsilon V_m} \tag{3.31}$$

where ϵ is the permittivity of the medium in the cavity and V_m is the mode volume of the cavity. Mode volume is a measure of how concentrated the electromagnetic energy of a single cavity mode is in space and it is defined as the volume integral of the electric field intensity in and around the cavity, normalized to the maximum field intensity. In this work, it is approximated as a cylindrical with a radius of the Gaussian beam waist w_0 shown in 3.14 and a length of the cavity length L: $V_m = \frac{\lambda L^2}{4n_m}\sqrt{\frac{R}{L} - 1}$, where R is the RoC of the cavity and n_m is the refractive index of the medium. The new equation of motion for the cavity field amplitude in response to a coherent incident

field is:

$$i\hbar\frac{d\psi}{dt} = (\hbar\omega_c - i\hbar\Gamma)\psi - (\alpha + i\beta)\frac{\hbar\omega_c}{2\epsilon V_m}\psi + \hbar\omega_i e^{-i\omega t} \tag{3.32}$$

If the cavity field is assumed as $\psi = \psi_0 e^{-i\omega t}$, the complex response amplitude is:

$$\psi_0 = \frac{\omega_i}{(\triangle_1 + \delta) + i(\Gamma + \gamma)},\ \delta = \frac{\alpha\omega_c}{2\epsilon V_m},\ \gamma = \frac{\beta\omega_c}{2\epsilon V_m} \tag{3.33}$$

The corresponding field intensity becomes:

$$I(\omega) = |\psi_0|^2 = \frac{\omega_i^2}{(\triangle_1 + \delta)^2 + (\Gamma + \gamma)^2} \tag{3.34}$$

This modified equation elucidates a Lorentzian line shape with a peak position $\omega = \omega_c(1 - \frac{\alpha}{2\epsilon V_m})$ and a linewidth of $2(\gamma + \frac{\beta\omega_c}{2\epsilon V_m})$, representing a shift to a lower frequency by $\delta\omega = -\frac{\alpha\omega_c}{2\epsilon V_m}$ and a broadening of the linewidth by $\frac{\beta\omega_c}{\epsilon V_m}$ compared with equation 3.25. This equation shows a general case which can be adapted for more complex situations.

3.6.3 Cavity with Anisotropic Particle

If the particle has a rod shape, the incident light needs to be circularly polarised to excite modes both parallel and transverse to the long axis of the particle. The presence of the particle changes the electric field response in the cavity. The incident light is prepared with a left-hand circular polarisation. The theory in this section was originally derived by my supervisor Professor Jason Smith and then developed further with me.

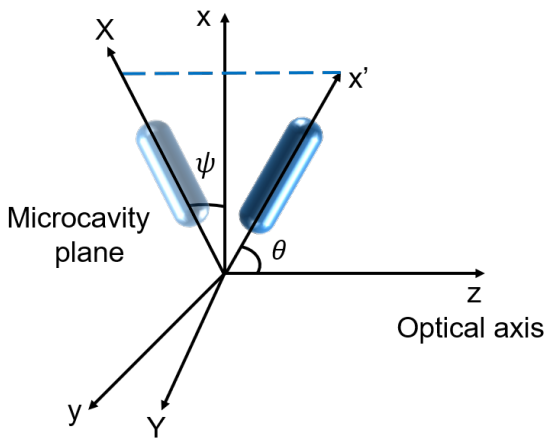


Figure 3.8: Schematic of the coordinate system used. xyz coordinate system is the instrumental frame. x' is the direction along the long axis of the rod-shaped particle. X is the projected direction of x' in the microcavity plane while Y is perpendicular to that.

The electric field of the transmitted beam through the cavity, along the directions parallel (X) and perpendicular (Y) to the major axis of the projected rod illustrated in Figure 3.8, can be written respectively as:

$$e_X = \frac{\omega_i e^{-iwt}}{(\triangle + \varepsilon) + i(\gamma + \eta)} \tag{3.35a}$$

$$e_Y = \frac{i\omega_i e^{-iwt}}{(\triangle - \varepsilon) + i(\gamma - \eta)} \tag{3.35b}$$

where ω_i is the angular frequency of the incident light, $\triangle$ represents the detuning between the resonant frequency of the cavity with just the laser and in the presence of a spherical particle of equal volume, and γ is the total photon loss rate in the cavity were the particle spherical. 2ε and 2η represent the particle anisotropy and are the differences in the resonant frequency and in the loss between the two orthogonal eigenstates. Equation 3.35 is adapted from equation 3.33 and is written in a symmetrical way to simplify the following calculations. Four Stokes parameters [233,

234] are shown below:

$$S_{00} = |e_X|^2 + |e_Y|^2 \tag{3.36a}$$

$$S_{10} = |e_X|^2 - |e_Y|^2 \tag{3.36b}$$

$$S_{20} = \frac{1}{2}|e_X + e_Y|^2 - \frac{1}{2}|e_X - e_Y|^2 \tag{3.36c}$$

$$S_{30} = \frac{1}{2}|e_X + ie_Y|^2 - \frac{1}{2}|e_X - ie_Y|^2 \tag{3.36d}$$

where S_{00} represents the intensity of the light, S_{10} describes the degree of linear polarisation, S_{20} gives the degree of linear polarisation in the diagonal basis, and S_{30} provides the degree of circular polarisation. For a rod-shaped particle oriented at an azimuthal angle ψ between the projected rod-shaped particle frame of reference (X, Y) and the instrument frame of reference (x, y) (Figure 3.8), the Stokes parameters in the instrument frame are calculated by:

$$\begin{pmatrix} S_0 \\ S_1 \\ S_2 \\ S_3 \end{pmatrix} = \begin{pmatrix} 1 & 0 & 0 & 0 \\ 0 & -\cos 2\psi & \sin 2\psi & 0 \\ 0 & -\sin 2\psi & \cos 2\psi & 0 \\ 0 & 0 & 0 & 1 \end{pmatrix} \begin{pmatrix} S_{00} \\ S_{10} \\ S_{20} \\ S_{30} \end{pmatrix} \tag{3.37}$$

Therefore the Stokes parameters in the instrument frame are:

$$S_0(\triangle) = \frac{\omega_i^2}{(\triangle + \varepsilon)^2 + (\gamma + \eta)^2} + \frac{\omega_i^2}{(\triangle - \varepsilon)^2 + (\gamma - \eta)^2} \tag{3.38a}$$

$$S_1(\triangle) = 4\omega_i^2 \frac{\gamma(\varepsilon \sin 2\psi - \eta \cos 2\psi) - \triangle(\eta \sin 2\psi + \varepsilon \cos 2\psi)}{(\triangle^2 - \varepsilon^2 + \gamma^2 - \eta^2)^2 + 4(\triangle\eta - \varepsilon\gamma)^2} \tag{3.38b}$$

$$S_2(\triangle) = 4\omega_i^2 \frac{\gamma(\varepsilon \cos 2\psi + \eta \sin 2\psi) - \triangle(\eta \cos 2\psi - \varepsilon \sin 2\psi)}{(\triangle^2 - \varepsilon^2 + \gamma^2 - \eta^2)^2 + 4(\triangle\eta - \varepsilon\gamma)^2} \tag{3.38c}$$

$$S_3(\triangle) = -2\omega_i^2 \frac{\triangle^2 - \varepsilon^2 + \gamma^2 - \eta^2}{(\triangle^2 - \varepsilon^2 + \gamma^2 - \eta^2)^2 + 4(\triangle\eta - \varepsilon\gamma)^2} \tag{3.38d}$$

When these equations are treated as functions of $\triangle$, S_0 is a double Lorentzian while S_1 and S_2 depend on ψ. The equations above build the relationship between the Stokes parameters and particle-related parameters. In particular, ε and η are polarisability-related parameters containing the shape anisotropy information of the particle. It is worth mentioning that ε and η are proportional to the real and imaginary part of the polarisability difference of the particle along X and Y directions respectively. X and Y directions are the projected directions in the microcavity plane regarding the long and short axes of a rod-shaped particle. Thus, with the particle rotating in the microcavity, ε and η will change accordingly.

The anisotropy loss tangent $\Phi = \frac{\eta}{\varepsilon}$ is defined to calculate the aspect ratio. It is expressed as below:

$$\Phi = \frac{\eta}{\varepsilon} = \frac{\frac{w_c(\triangle\alpha_i + \triangle\text{scattering part})}{4V_m} I(\vec{r})}{\frac{w_c \triangle\alpha_r}{4V_m} I(\vec{r})} = \frac{\triangle\alpha_i + \triangle\text{scattering part}}{\triangle\alpha_r} \tag{3.39}$$

where w_c is the light frequency at the probe laser wavelength, V_m is the mode volume, $I(\vec{r})$ is the relative intensity at the particle position normalised to the strongest intensity in the cavity, $\triangle\alpha_i$ and $\triangle\alpha_r$ are differences in the imaginary and real part of the polarisability along the X and Y direction in Figure 3.8. $\triangle$scattering part displays the difference in the scattering part along the X and Y direction in Figure 3.8.

Analysing the polarisation state of the transmitted light with Stokes parameters gives a full picture of the impacts of the particle introduced to the system. The aspect ratio of the particle can be determined with multiple measurements during a single-particle event no matter what the rotational angle of the particle is in the cavity. Therefore, the diffusion of the particle does not need to be controlled and the free diffusing particles in the solution can be directly measured. Measuring the light intensities of

two fixed orthogonal directions alone cannot give the aspect ratio of the particle due to the impact of ψ. The frequent measurements could also reduce the measurement uncertainty. In addition, the azimuthal angle ψ could also be obtained, which offers insights into the rotational diffusion of the particle. ψ only appears in $S_1(\triangle)$ and $S_2(\triangle)$ so it can be determined individually. From the equation itself, $S_1(\triangle)$ and $S_2(\triangle)$ have a linear relationship of ε and η and should be most sensitive to those parameters. However, they both have ψ embedded and thus may not be a direct way to determine ε and η. Since $S_0(\triangle)$ and $S_3(\triangle)$ do not have ψ, they could potentially be a straightforward measurement to determine ε and η. Although this work only focuses on the analysis related to the aspect ratio of the particle, other information could also be potentially extracted from the system that will be discussed in Chapter 8.2. It allows a more thorough analysis of particles in solution and adds more value to the system. Examples of gold nanorods and rod-shaped bacteria particles are discussed in detail below.

3.6.3.1 Gold Nanorod

The polarisabilities along the projected long and short axes of the gold nanorod in the microcavity plane are deduced from α_L and α_W, the polarisabilities along the long and short axes of the gold nanorod. The polarisability of a gold nanorod is described as a complex second-rank tensor. In the nanorod's frame of reference, the tensor takes a diagonal form:

$$\alpha = \begin{pmatrix} \alpha_L & 0 & 0 \\ 0 & \alpha_W & 0 \\ 0 & 0 & \alpha_W \end{pmatrix} \tag{3.40}$$

Gans modification to Mie theory [116, 117, 235] relates the polarisabilities to the particle aspect ratio μ as follows:

$$\alpha_{W,L} = \frac{\epsilon - \epsilon_m}{\epsilon_m + p_{W,L}(\epsilon - \epsilon_m)} \tag{3.41a}$$

$$p_L = \frac{1}{\mu^2 - 1}\left(\frac{\mu}{2\sqrt{\mu^2 - 1}} ln\left(\frac{\mu + \sqrt{\mu^2 - 1}}{\mu - \sqrt{\mu^2 - 1}}\right) - 1\right),\ p_W = \frac{1 - p_L}{2} \tag{3.41b}$$

where ϵ is the permittivity of gold [236] at the probe laser wavelength, ϵ_m is the permittivity of the surrounding medium, and $p_{W,L}$ are the depolarisation factors. The complex nature of ϵ results in $\alpha_{W,L}$ being complex also. Projecting the polarisability tensor onto the plane transverse to the optical axis of the apparatus (the z direction in Figure 3.8) gives:

$$\alpha' = \begin{pmatrix} \alpha'_L & 0 \\ 0 & \alpha'_W \end{pmatrix} = \begin{pmatrix} \cos^2\theta\alpha_W + \sin^2\theta\alpha_L & 0 \\ 0 & \alpha_W \end{pmatrix} \tag{3.42}$$

where θ is the angle of the nanorod to the optical axis (Figure 3.8). α'_L and α'_W are the polarisability along X and Y axis respectively (Figure 3.8). The real and imaginary parts of α' result in shifts in the mode position and increases in mode width respectively.

For small particles, in which losses are dominated by absorption, and scattering can be neglected, the anisotropy loss tangent Φ is:

$$\Phi = \frac{Im(\alpha'_L - \alpha'_W)}{Re(\alpha'_L - \alpha'_W)} = \frac{Im(\alpha_L sin^2\theta + \alpha_W cos^2\theta - \alpha_W)}{Re(\alpha_L sin^2\theta + \alpha_W cos^2\theta - \alpha_W)} = \frac{Im(\alpha_L - \alpha_W)}{Re(\alpha_L - \alpha_W)} \tag{3.43}$$

The anisotropy loss tangent is a property of the particle and is independent of both the position and orientation of the particle in the cavity mode. With the relationship

between the aspect ratio and the polarisability mentioned in equation 3.41, the aspect ratio μ can be determined.

To further confirm that the anisotropy loss tangent Φ has an injective mapping relationship with μ, both analytical and numerical methods are used. From equation 3.41:

$$\alpha_L - \alpha_W = \frac{\epsilon - \epsilon_m}{\epsilon_m + p_L(\epsilon - \epsilon_m)} - \frac{\epsilon - \epsilon_m}{\epsilon_m + \frac{1-p_L}{2}(\epsilon - \epsilon_m)} \tag{3.44}$$

Let $\frac{\epsilon}{\epsilon_m} - 1 = \epsilon' - 1 = C + iD$ where C and D is the real and imaginary part of $\frac{\epsilon}{\epsilon_m} - 1$ respectively, it becomes:

$$\alpha_L - \alpha_W = \frac{(C+iD)^2(1-3p_L)}{2 + (1+p_L)C + (1-p_L)p_L(C^2 - D^2) + iD(1+p_L) + 2iCDp_L(1-p_L)} \tag{3.45}$$

Therefore, the anisotropy loss tangent Φ becomes:

$$\Phi = \frac{Im(\alpha_L - \alpha_W)}{Re(\alpha_L - \alpha_W)} = \frac{D[4C + (C^2 + D^2)(1+p_L)]}{2(C^2 - D^2) + [C + CP_L + (C^2 + D^2)p_L - (C^2 + D^2)p_L^2](C^2 + D^2)} \tag{3.46}$$

The numerator is not a factor of the denominator. Therefore, the loss tangent is a function of the aspect ratio. In addition, Figure 3.9 below illustrates the relationship numerically with the permittivity of gold, silver and copper at the wavelength of 640 nm [236]. All three materials show the trend that with the aspect ratio increasing, the anisotropy loss tangent also increases. They both show the injective mapping between the aspect ratio and the anisotropy loss tangent. In addition, it illustrates different responses between different materials, with silver having the weakest mapping, while copper has the strongest one.

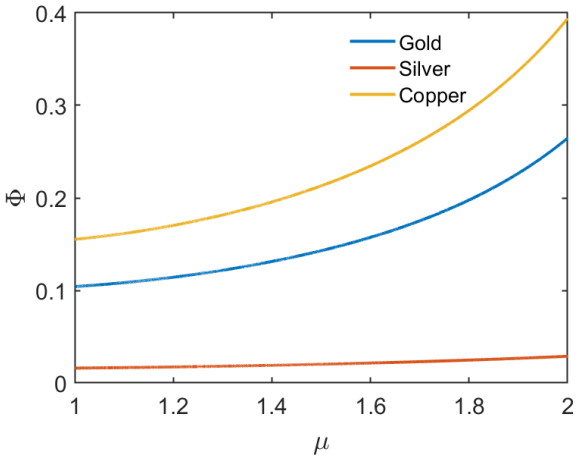


Figure 3.9: Numerical relationship between the aspect ratio μ and the anisotropy loss tangent Φ with equation 3.43 at a wavelength of 640 nm. The permittivity of gold, silver and copper is taken from [236].

For larger particles, scattering is not negligible. The photon loss rate introduced by scattering from the particle is:

$$\Gamma = \frac{\sigma_{sca} I(\vec{r})}{A_{mode}} \frac{2}{\tau_{round\ trip}} = \frac{\sigma_{sca}}{A_{mode}} \frac{2I(\vec{r})}{\frac{2L}{\frac{c}{n_m}}} = \frac{\sigma_{sca} c}{n_m V_m} I(\vec{r}) = \frac{w_c}{2V_m} \frac{8\pi^2 n_m^3 V_p}{3\lambda^3} \alpha^2 I(\vec{r}) \quad (3.47)$$

where σ_{sca} is the scattering cross-section of the particle, A_{mode} is the mode cross-section, $I(\vec{r})$, V_m and w_c are the same as in equation 3.39, $\tau_{round\ trip}$ is the time of a round trip that light travels between two mirrors, L is the cavity length, n_m is the refractive index of the medium and c is the speed of light. The polarisability α is proportional to the particle volume V_p but the volume particle V_p is extracted in the above equation so that α^2 in the above equation is proportional to the particle volume V_p. Therefore, the loss difference is $2\eta = \frac{w_c \triangle \alpha_i}{2V_m} I(\vec{r}) + \frac{w_c}{2V_m} \frac{8\pi^2 n_m^3 V_p}{3\lambda^3} \triangle(\alpha^2) I(\vec{r})$, where both $\triangle \alpha_i$ and $\triangle(\alpha^2)$ are proportional to V_p. A volume-related factor $A = \frac{8\pi^2 n_m^3 V_p}{3\lambda^3}$ is

defined. The anisotropy loss tangent becomes:

$$\Phi = \frac{Im(\alpha_L - \alpha_W)}{Re(\alpha_L - \alpha_W)} + \frac{A\beta(\vec{r})\{\sin^2\theta\alpha_L^2 - (\cos^2\theta + 1)\alpha_W^2 + 2\cos^2\theta[Re(\alpha_L)Re(\alpha_W) + Im(\alpha_L)Im(\alpha_W)]\}}{Re(\alpha_L - \alpha_W)} \tag{3.48}$$

where θ is the same as in equation 3.42. Now the anisotropy loss tangent is dependent both on the particle's position and orientation within the cavity mode. The positional dependence comes about because the optical density of states in the cavity mode is a function of position [152], leading to a variation in scattering rates shown as $\beta(\vec{r})$ in equation 3.48. It is different from the scattering in free space. The orientational dependence is because the scattering is quadratically dependent on the polarisability and it cannot be cancelled out with the denominator as in the scenario of small particles. It is necessary to generate a histogram of Φ for the single-particle event and fit an assumed analytic probability distribution to extract the aspect ratio with the equation 3.48. When the nanorod is in the free diffusion with no preferred orientation, the distribution for θ is $\sin\theta$ with θ in the range of $0 \sim \frac{\pi}{2}$. Therefore it satisfies:

$$p(\Phi)d\Phi = p(\theta)d\theta = \sin\theta d\theta \tag{3.49}$$

With equation 3.48, $d\Phi$ and $\cos\theta$ could be calculated:

$$\sqrt{B(\Phi)} = \cos\theta = \sqrt{\frac{\Phi Re(\alpha_L - \alpha_W) - Im(\alpha_L - \alpha_W) - A\beta(\vec{r})(\alpha_L^2 - \alpha_W^2)}{A\beta(\vec{r})[2Re(\alpha_L)Re(\alpha_W) + 2Im(\alpha_L)Im(\alpha_W) - \alpha_L^2 - \alpha_W^2]}} \tag{3.50}$$

Then the probability distribution of the anisotropy loss tangent Φ is:

$$p(\Phi) = \frac{Re(\alpha_L - \alpha_W)}{2A\beta(\vec{r})[\alpha_L^2 + \alpha_W^2 - 2Re(\alpha_L)Re(\alpha_W) - 2Im(\alpha_L)Im(\alpha_W)]\sqrt{B(\Phi)}} \tag{3.51}$$

In both circumstances, the aspect ratio can be derived from the anisotropy loss tan-

gent and the detailed data processing will be introduced in Chapter 5.4.2.

3.6.3.2 Rod-shaped Bacteria Particle

Unlike the gold nanorod which involves both the scattering and absorption as the loss mechanism, the rod-shaped bacteria particle only introduces the scattering to the system as it is not an electrical conductor. Also, the permittivity of the dielectric particle is real without an imaginary part. Adapted from equation 3.39 and 3.48, the anisotropy loss tangent of a rod-shaped bacteria particle is:

$$\Phi = \frac{\eta}{\varepsilon} = \frac{A\triangle(\alpha^2)}{\triangle\alpha_r} = \frac{A[(\alpha_L \sin^2\theta + \alpha_W \cos^2\theta)^2 - \alpha_W^2]}{\alpha_L \sin^2\theta + \alpha_W \cos^2\theta - \alpha_W} = A\sin^2\theta(\alpha_L - \alpha_W) + 2A\alpha_W \tag{3.52}$$

where this A embeds $\beta(\vec{r})$ and $A = \beta(\vec{r})\frac{8\pi^2 n_m^3 V_p}{3\lambda^3}$. Using $p(\Phi)d(\Phi) = p(\theta)d\theta$ again, the probability distribution of Φ can be derived as:

$$p(\Phi) = \frac{1}{2A(\alpha_L - \alpha_W)\sqrt{1 - \frac{\Phi - 2A\alpha_W}{A(\alpha_L - \alpha_W)}}} \tag{3.53}$$

Like gold nanorods, the aspect ratio of a rod-shaped bacteria particle can be derived with the anisotropy loss tangent Φ. Like Figure 3.9, I also plotted the relationship for a rod-shaped bacteria particle using equation 3.53 in Figure 3.10. A is set as 1 in this graph, and I plotted the situations with different angles θ of 0°, 45° and 90°.

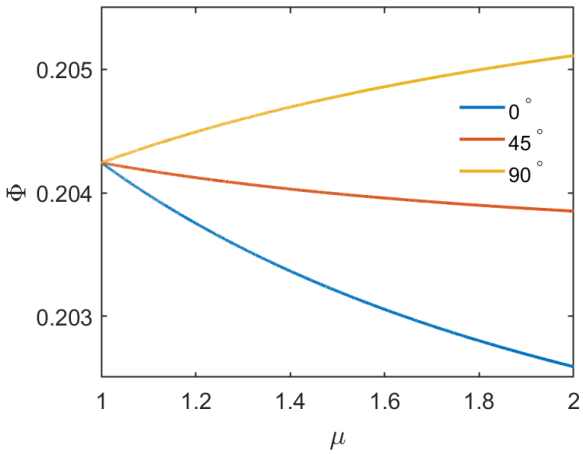


Figure 3.10: Numerical relationship between the aspect ratio μ and the anisotropy loss tangent Φ using equation 3.10. $\theta = 0°, 45°, 90°$ are plotted. A is set as 1.

3.7 Other Theoretical Calculations

There are additional theoretical calculations performed to supplement the experimental findings. The theoretical background is introduced in this section while the results will be discussed in Chapter 5.6 and 6.5.

3.7.1 Rotational Diffusion

There are three common models of calculating the rotational diffusion coefficient of a rod-shaped particle, with different applicable ranges of the aspect ratio μ, including Perrin theory [237–240] for $\mu < 2$, Tirado and Garcia de la Torre (TG) theory [241, 242] for $2 < \mu < 30$ and Broersma's relations (BR) [242, 243] for $\mu > 5$. Equations of Perrin theory and TG theory are shown below. With Perrin theory, equation 3.54a

[239] and 3.54b [240] display a slightly different value:

$$D_{r-pe-k} = \frac{3k_BT}{2\pi\eta L^3}\frac{\mu^4}{\mu^4-1}\left[\frac{(2\mu^2-1)ln(\mu+\sqrt{\mu^2-1})}{\mu\sqrt{\mu^2-1}}-1\right] \tag{3.54a}$$

$$D_{r-pe-h} = \frac{k_BT}{4\pi\eta V}\frac{\mu^4}{\mu^4-1}\left[\frac{(2\mu^2-1)ln(\mu+\sqrt{\mu^2-1})}{\mu\sqrt{\mu^2-1}}-1\right] \tag{3.54b}$$

$$D_{r-TG} = \frac{3k_BT}{\pi\eta L^3}\left(\ln\mu - 0.662 + \frac{0.917}{\mu} - \frac{0.05}{\mu^2}\right) \tag{3.54c}$$

where η is the viscosity of the fluid, L is the length of the particle, V is the particle size, T is the temperature and k_B is the Boltzmann constant.

3.7.2 Optical Torque

Apart from the collisions from the surrounding fluid molecules, the maximum rotational angle originating from the optical torque $\boldsymbol{M}$ [244, 245] can be calculated where the electric field is maximum:

$$\boldsymbol{M} = \frac{(\boldsymbol{\alpha E})^* \times \boldsymbol{E}}{2} \tag{3.55a}$$

$$\boldsymbol{E} = \begin{pmatrix} \sqrt{2}E_0 \\ i\sqrt{2}E_0 \\ 0 \end{pmatrix},\ \boldsymbol{\alpha} = \begin{pmatrix} \alpha_L & 0 & 0 \\ 0 & \alpha_W & 0 \\ 0 & 0 & \alpha_W \end{pmatrix} \tag{3.55b}$$

$$E_0 = \sqrt{\frac{I_0}{c\epsilon_0 n_m}},\ I_0 = \frac{P}{\pi w_0^2},\ w_0^2 = \frac{\lambda L_{cav}}{\pi}\sqrt{\frac{R}{L_{cav}}-1} \tag{3.55c}$$

where $\boldsymbol{\alpha}$ is the polarisability tensor in the nanorod frame, $\boldsymbol{E}$ is the electric field, E_0 is the electric field amplitude, I_0 is the light intensity,c is the light speed, ϵ_0 is the permittivity of vacuum, n_m is the refractive index of the medium, P is the intra-cavity power, w_0 is the beam waist, R is the RoC of the feature and L_{cav} is the cavity length.

3.7.3 Optical Force

The optical forces are calculated for the comparison between gold nanorods and rod-shaped bacteria particles. The translational diffusion for every time step $\triangle t$ caused by the optical force $F_{optical} = \frac{\alpha}{2}\nabla \boldsymbol{E}^2$ can be calculated with Langevin equation [246–248]:

$$\triangle x = \frac{\alpha \triangle t}{2 n_m \epsilon_0 c \gamma} \frac{\partial I}{\partial x} \tag{3.56}$$

where α is the polarisability of the particle, I is the light intensity, n_m is the refractive index of the medium, ϵ_0 is the permittivity of vacuum, c is the light speed, γ is the friction coefficient. The detailed derivation will be introduced in Chapter 3.8.1.1 and the more complex version will be shown in 3.79 as a more accurate one considering the angular conversion between the instrumental coordinate system and rod-shaped particle coordinate system. However, the equation above is enough to calculate the difference for a rough comparison between rod-shaped bacteria particles and gold nanorods. The detailed discussion will be elucidated in Chapter 6.5.1.

3.7.4 Cross-section Calculation

The scattering and absorption cross-sections are worth exploring as they provide insights into the loss mechanism of the system. For gold nanorods, the absorption and scattering cross-sections can be calculated with the following equations with Gans modification from Mie theory [116–118, 235]:

$$C_{abs} = \frac{2\pi V \epsilon_m^{3/2}}{3\lambda} \left[\frac{\epsilon_2}{(\epsilon_1 p_L + (1-p_L)\epsilon_m)^2 + \epsilon_2^2 p_L^2} + 2 \frac{\epsilon_2}{(\epsilon_1 p_W + (1-p_W)\epsilon_m)^2 + \epsilon_2^2 p_W^2} \right] \tag{3.57a}$$

$$C_{sca} = \frac{8\pi^3 V^2 \epsilon_m^2}{9\lambda^4} \left[\frac{(\epsilon_1 - \epsilon_m)^2 + \epsilon_2^2}{(\epsilon_1 p_L + (1-p_L)\epsilon_m)^2 + \epsilon_2^2 p_L^2} + 2 \frac{(\epsilon_1 - \epsilon_m)^2 + \epsilon_2^2}{(\epsilon_1 p_W + (1-p_W)\epsilon_m)^2 + \epsilon_2^2 p_W^2} \right] \tag{3.57b}$$

where V is the particle volume, ϵ_1 and ϵ_2 are the real part and imaginary part of gold permittivity at the incident light wavelength and ϵ_m is the permittivity of the medium. p_L and p_W are the depolarisation factors displayed in equation 3.41b.

For the rod-shaped bacteria particles, the only loss in the system is the scattering as the bacteria particle is not an electrical conductor and the permittivity is real without any imaginary part. Adapted from the equation 3.57b, the scattering cross-section is expressed as:

$$C_{sca} = \frac{8\pi^3 V^2 \epsilon_m^2}{9\lambda^4} \left[\frac{(\epsilon_1 - \epsilon_m)^2}{(\epsilon_1 p_L + (1 - p_L)\epsilon_m)^2} + 2\frac{(\epsilon_1 - \epsilon_m)^2}{(\epsilon_1 p_W + (1 - p_W)\epsilon_m)^2} \right] \tag{3.58}$$

3.7.5 Heat Calculation

Heating of the nanorod by the optical field could in principle result in shape change [249], so the temperature increase on the surface of the gold nanorod during the resonance is calculated [250]:

$$\triangle T = \frac{C_{abs} I}{4\pi R_{eff} \kappa \beta} \tag{3.59}$$

where C_{abs} is the absorption cross-section calculated in equation 3.57a, I is the intensity of incident light, R_{eff} is the effective radii were the particle spherical, κ is the thermal conductivity of water, and $\beta = 1 + 0.96587 ln^2(\frac{L}{2r})$ is the thermal capacitance coefficient of a rod-shaped particle with a length of L and a radius of r [250].

3.8 Theoretical Simulations

Theoretical simulations are performed to explore the system and can be compared with experimental results. Monte Carlo simulation focuses on the time-evolved diffusion behaviour while FDTD simulations concentrate on the change of optical field with the particle in the microcavity. This section introduces the theoretical backgrounds

of these simulations.

3.8.1 Monte Carlo Simulation

Firstly, the Langevin equation is presented to describe the diffusion behaviour. With the anisotropy of a rod-shaped particle, coordinate system conversion is introduced to accomplish the simulation.

3.8.1.1 Langevin Equation

The Langevin equation is a stochastic differential equation describing the evolution of a system subjected to a combination of deterministic and fluctuating forces [251]. The particle in water in the optical microcavity experiences both the deterministic perturbations from the optical force and the random collisions from the surrounding fluid molecules [248]. The random process is dependent on both the temperature and fluid viscosity [252]. In one dimension, the Langevin equation is expressed below [248]:

$$m\ddot{x} = -\gamma\dot{x} + kx + \sqrt{2k_BT\gamma}W \tag{3.60}$$

where x is the particle position, m is the mass of the particle, γ is the friction coefficient, k is the trap stiffness, $\sqrt{2k_BT\gamma}W$ is the fluctuating force due to random impulses from neighbouring fluid molecules, k_B is Boltzmann constant and T is the absolute temperature. W can be expressed as $W = \frac{w}{\sqrt{\triangle t}}$, where w is a Gaussian random number between 0 and 1.

For nanoparticles, the strong damping limit can be assumed whereby $m\ddot{x} = 0$, and equation 3.60 can be extended into three dimensions with all the forces in the system included. As shown in Figure 3.11, the water flow comes from the x direction and the light propagation direction is the z direction.

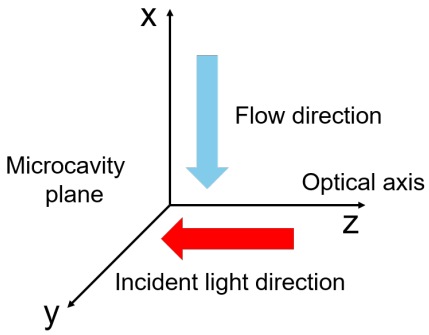


Figure 3.11: Schematic of the instrumental coordinate system with the flow direction and incident light direction.

Therefore, the forces in the system include 4 types. Optical forces are in the x, y and z directions. Flow force only appears in the flow direction, namely the x direction. Damping forces and fluctuating forces in the x, y and z directions come from the viscosity of the fluid and molecular collisions respectively. The finite time difference was utilised to convert $\dot{x} = \frac{dx}{dt}$ into $\frac{dx}{dt} = \frac{x_j - x_{j-1}}{\triangle t}$. The equations for x, y and z directions are shown below [253]:

$$\gamma_x \frac{x_j - x_{j-1}}{\triangle t} = F_{optical,x} + \sqrt{2k_B T \gamma_x} \frac{w_{j,x}}{\sqrt{\triangle t}} + F_{flow} \tag{3.61a}$$

$$\gamma_y \frac{y_j - y_{j-1}}{\triangle t} = F_{optical,y} + \sqrt{2k_B T \gamma_y} \frac{w_{j,y}}{\sqrt{\triangle t}} \tag{3.61b}$$

$$\gamma_z \frac{z_j - z_{j-1}}{\triangle t} = F_{optical,z} + \sqrt{2k_B T \gamma_z} \frac{w_{j,z}}{\sqrt{\triangle t}} \tag{3.61c}$$

Since $F_{optical} = \frac{\alpha}{2} \nabla \boldsymbol{E}^2$, where α is the polarisability of the particle and $\boldsymbol{E}$ is the

electric field of the incident light, the optical forces in x, y and z directions are:

$$F_{optical,x} = \frac{\alpha_x}{2n_m\epsilon_0 c}\frac{\partial I}{\partial x} \tag{3.62a}$$

$$F_{optical,y} = \frac{\alpha_y}{2n_m\epsilon_0 c}\frac{\partial I}{\partial y} \tag{3.62b}$$

$$F_{optical,z} = \frac{\alpha_z}{2n_m\epsilon_0 c}\frac{\partial I}{\partial z} \tag{3.62c}$$

where n_m is the refractive index of the medium, ϵ_0 is the vaccumm permittivity, c is the speed of light, and I is the intensity of the incident light. For spherical particles, both γ and α are isotropic, namely it is the same along the x, y and z axes. However, for anisotropic particles, γ and α are anisotropic, with different values along the long and short axes.

For gold nanospheres, the polarisability of the particle and the friction coefficient can be expressed as:

$$\alpha = 3V\epsilon_0\frac{\epsilon - \epsilon_m}{\epsilon + 2\epsilon_m} \tag{3.63}$$

$$\gamma = 6\pi\eta r \tag{3.64}$$

where ϵ is the gold permittivity at the incident light wavelength, ϵ_m is the water permittivity and η is the viscosity of the water. V is the particle volume and r is the radius of the nanosphere. The optical cavity is designed to support Gaussian modes and the light intensity in the cavity with the Gaussian beam profile is shown in equation 3.21. With equations 3.61 and 3.62, the position of the gold nanosphere can be calculated with time evolving. While there is no boundary condition for x and y directions, the z direction is bounded by mirrors. The reflected position in regards to the mirror position (0 and L_{cav}) is chosen if the z position is out of the range of $r \sim L_{cav} - r$.

3.8.1.2 Coordinate System Conversion

It is worth mentioning that the anisotropy of γ and α aligns with the long and short axes of a gold nanorod. They are different from the aforementioned instrumental axes of x, y and z, and change with the rotation of the gold nanorod. Therefore two coordinate systems are constructed, one is the original instrumental coordinate system of xyz and the other is the gold nanorod coordinate system of x'y'z', illustrated in Figure 3.12(a). x' is along the long axis of the gold nanorod. θ and ϕ are polar and azimuthal angles of gold nanorods in the instrumental coordinate system. β and χ represent the rotational polar and azimuthal angle of the gold nanorod over a time step in the current nanorod frame.

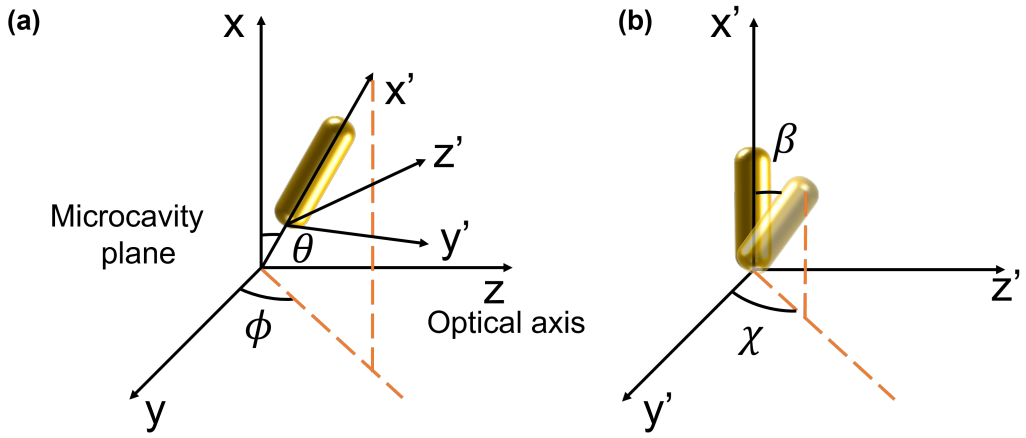


Figure 3.12: (a) Schematic of the two coordinate systems used. xyz is the instrumental coordinate system while x'y'z' is the nanorod coordinate system. θ and ϕ are the polar and azimuthal angles of gold nanorods in the instrument frame. (b) Rotational movement in the gold nanorod coordinate system. β and χ present the rotational polar and azimuthal angle of the gold nanorod over a time step in the current nanorod frame.

A circularly polarised light is prepared as introduced in Chapter 3.6.3. With the intensity of light unchanged from the optical resonant mode in the cavity with Gaussian beam profile in equation 3.21, the electric field of the incident light, adapted from

equation 3.22, can be expressed as:

$$E_x(x,y,z) = \sqrt{2}E_0\frac{w_0}{w(z)}\exp\left(-\frac{x^2+y^2}{w^2(z)}\right)\cos\left(\frac{\pi}{2}+kz+k\frac{x^2+y^2}{2R(z)}-\tan^{-1}\left(\frac{z}{z_R}\right)\right) \tag{3.65a}$$

$$E_y(x,y,z) = i\sqrt{2}E_0\frac{w_0}{w(z)}\exp\left(-\frac{x^2+y^2}{w^2(z)}\right)\cos\left(\frac{\pi}{2}+kz+k\frac{x^2+y^2}{2R(z)}-\tan^{-1}\left(\frac{z}{z_R}\right)\right) \tag{3.65b}$$

The intensity of the light field is the same as equation 3.21. The diffusion of a single gold nanorod from time t_{j-1} to t_j after a time step $\triangle t$ is considered. The position of the particle at time t_{j-1} is $(x_{j-1},\ y_{j-1},\ z_{j-1})$. The electrical field is $\boldsymbol{E} = (E_x,\ E_y,\ 0)$ with the substitution of x_{j-1}, y_{j-1} and z_{j-1} to x, y and z in equation 3.65.

Firstly, the rotational movement in the gold nanorod coordinate system is examined, shown in Figure 3.12(b). The solid gold nanorod is at time t_{j-1} while the opaque one is at time t_j. The azimuthal angle χ is a random number between 0 to 2π if it is only a free Brownian motion. And the optical torque in the x' direction is added:

$$\chi_j = random(0, 2\pi) + \frac{\triangle t}{\gamma_r}M_{x'} \tag{3.66}$$

where γ_r is the rotational friction coefficient and $\gamma_r = \frac{k_BT}{D_r}$ with the rotational diffusion coefficient D_r [240]:

$$D_r = \frac{k_BT}{4\pi\eta V}\frac{\mu^2}{\mu^4-1}\left[\frac{(2\mu^2-1)ln(\mu+\sqrt{\mu^2-1})}{\mu\sqrt{\mu^2-1}}-1\right],\ \mu = \frac{L}{2r} \tag{3.67}$$

where μ is the aspect ratio of the particle. The polar angle also results from the combination of a free Brownian motion using rotational Langevin equation and optical

torque from the optical field [254–256]:

$$\beta_j = \sqrt{2D_r \triangle t} w_{j,r,1} + \frac{(M_{z'} cos\chi_j - M_{y'} sin\chi_j)\triangle t}{\gamma_r} \tag{3.68}$$

$M_{x'}$, $M_{y'}$ and $M_{z'}$ can be calculated from M_x, M_y and M_z by performing the frame conversion from the instrument frame (xyz coordinate system) to the particle frame (x'y'z' coordinate system). The anticlockwise direction is set to be the positive angle. The conversion matrix $\boldsymbol{R_{j-1}}$ and the torque conversion are:

$$\boldsymbol{R_{j-1}} = \begin{pmatrix} \cos\theta_{j-1} & \sin\theta_{j-1} & 0 \\ -\sin\theta_{j-1} & \cos\theta_{j-1} & 0 \\ 0 & 0 & 1 \end{pmatrix} \begin{pmatrix} 1 & 0 & 0 \\ 0 & \cos\phi_{j-1} & -\sin\phi_{j-1} \\ 0 & \sin\phi_{j-1} & \cos\phi_{j-1} \end{pmatrix} \tag{3.69}$$

$$\begin{pmatrix} M_{x'} \\ M_{y'} \\ M_{z'} \end{pmatrix} = \boldsymbol{R_{j-1}} \begin{pmatrix} M_x \\ M_y \\ M_z \end{pmatrix} \tag{3.70}$$

The optical torque is calculated in the instrument frame since the electric field of the incident light is defined in the xyz coordinate system.

$$\begin{pmatrix} M_x \\ M_y \\ M_z \end{pmatrix} = \frac{(\boldsymbol{\alpha_{xyz,j-1}} \boldsymbol{E})^* \times \boldsymbol{E}}{2} \tag{3.71}$$

$$\boldsymbol{\alpha_{x'y'z'}} = \begin{pmatrix} \alpha_{x'} & 0 & 0 \\ 0 & \alpha_{y'} & 0 \\ 0 & 0 & \alpha_{z'} \end{pmatrix}, \ \boldsymbol{\alpha_{xyz,j-1}} = \boldsymbol{R_{j-1}^{-1}} \boldsymbol{\alpha_{x'y'z'}} \boldsymbol{R_{j-1}} \tag{3.72}$$

$\alpha_{x'}$, $\alpha_{y'}$, and $\alpha_{z'}$ are the intrinsic polarisabilities along the long and short axes of the gold nanorod. Since the optical torque is calculated in the instrument frame, the

polarisability tensor is converted from the particle frame to the lab frame. The scalar polarisabilities along the long and short axes of the gold nanorod are [116, 117, 235]:

$$\alpha_{x'} = V\epsilon_0 \frac{\epsilon - \epsilon_m}{\epsilon_m + p_x(\epsilon - \epsilon_m)} \tag{3.73}$$

$$\alpha_{y'} = \alpha_{z'} = V\epsilon_0 \frac{\epsilon - \epsilon_m}{\epsilon_m + p_y(\epsilon - \epsilon_m)} \tag{3.74}$$

where p_x and p_y are depolarisation factors as a function of the aspect ratio $\mu = \frac{L}{2r}$ of the gold nanorod where L and $2r$ is the length and width of the gold nanorod respectively. The volume is calculated by assuming a gold nanorod as a hemisphere-capped cylinder.

$$p_x = \frac{1}{\mu^2 - 1}\left(\frac{\mu}{2\sqrt{\mu^2 - 1}} ln\left(\frac{\mu + \sqrt{\mu^2 - 1}}{\mu - \sqrt{\mu^2 - 1}}\right) - 1\right),\ p_y = p_z = \frac{1 - p_x}{2} \tag{3.75}$$

$$V = \frac{4}{3}\pi r^3 + \pi r^2(L - 2r) \tag{3.76}$$

The vector of the gold nanorod is (1, 0, 0) in the particle frame at time t_{j-1} before the rotation. The relationship between θ_j, ϕ_j and θ_{j-1}, ϕ_{j-1} can be determined through the coordinate system conversion.

$$\boldsymbol{R'_{j-1}} = \begin{pmatrix} 1 & 0 & 0 \\ 0 & \cos\phi_{j-1} & \sin\phi_{j-1} \\ 0 & -\sin\phi_{j-1} & \cos\phi_{j-1} \end{pmatrix} \begin{pmatrix} \cos\theta_{j-1} & -\sin\theta_{j-1} & 0 \\ \sin\theta_{j-1} & \cos\theta_{j-1} & 0 \\ 0 & 0 & 1 \end{pmatrix} \tag{3.77}$$

$$\boldsymbol{R'_{j-1}} \begin{pmatrix} \cos\beta_j \\ \sin\beta_j\cos\chi_j \\ \sin\beta_j\sin\chi_j \end{pmatrix} = \begin{pmatrix} \cos\theta_j \\ \sin\theta_j\cos\phi_j \\ \sin\theta_j\sin\phi_j \end{pmatrix} \tag{3.78}$$

Apart from the rotational diffusion of the gold nanorod, the translational diffusion is also simulated since the position of the particle impacts the optical field it experiences,

changing the exerted optical force and torque. Adapted from equations 3.61a to 3.61c, the position of the gold nanorod centre, namely x_j, y_j and z_j, at time t_j is calculated by:

$$\begin{pmatrix} x_j - x_{j-1} \\ y_j - y_{j-1} \\ z_j - z_{j-1} \end{pmatrix} = \boldsymbol{\gamma}_{\boldsymbol{xyz,j}}^{\boldsymbol{-1}} \left[\frac{\triangle t}{2n_m \epsilon_0 c} \boldsymbol{\alpha}_{\boldsymbol{xyz,j}} \begin{pmatrix} \partial I/\partial x \\ \partial I/\partial y \\ \partial I/\partial z \end{pmatrix} + \sqrt{2k_B T \triangle t} \sqrt{\boldsymbol{\gamma}_{\boldsymbol{xyz,j}}} \begin{pmatrix} w_{j,x} \\ w_{j,y} \\ w_{j,z} \end{pmatrix} + \boldsymbol{\gamma}_{\boldsymbol{xyz,j}} \triangle t \begin{pmatrix} v \\ 0 \\ 0 \end{pmatrix} \right] \tag{3.79}$$

where $\boldsymbol{\gamma_{xyz}}$ is the friction coefficient tensor and can be calculated with the coordinate system conversion, same as the polarisability tensor:

$$\boldsymbol{\gamma_{x'y'z'}} = \begin{pmatrix} \gamma_{x'} & 0 & 0 \\ 0 & \gamma_{y'} & 0 \\ 0 & 0 & \gamma_{z'} \end{pmatrix}, \ \boldsymbol{\gamma_{xyz}} = \boldsymbol{R_j^{-1}} \boldsymbol{\gamma_{x'y'z'}} \boldsymbol{R_j} \tag{3.80}$$

where $\gamma_{x'}$, $\gamma_{y'}$ and $\gamma_{z'}$ can be calculated below [257, 258]:

$$\gamma_{x'} = \frac{2\pi\eta L}{ln\frac{L}{2r} + \beta_x}, \ \beta_x = 0.19 \tag{3.81}$$

$$\gamma_{y'} = \gamma_{z'} = \frac{4\pi\eta L}{ln\frac{L}{2r} + \beta_y}, \ \beta_y = 1.19 \tag{3.82}$$

The starting point of the position of the nanorod centre was set as (-1 µm, 0, r). The starting points of polar angles θ and β were random numbers between 0 and $\frac{\pi}{2}$. For azimuthal angles, ϕ and χ, the starting points were random numbers between 0 and 2π. With the starting points set, the electric field and the light intensity at

that position were calculated with equation 3.65 and 3.21. The calculation of optical torques in the instrument and particle frame was performed afterwards with equation 3.71 and 3.70. Then the rotational diffusion in the particle frame was modelled and the azimuthal and polar angles of χ and β were acquired with equation 3.66 and 3.68. Equation 3.77 and 3.78 were employed to explore the azimuthal and polar angle in the instrument frame. With the updated angles, the new position was investigated with equation 3.79. The diagram of this process is shown in Figure 3.13.

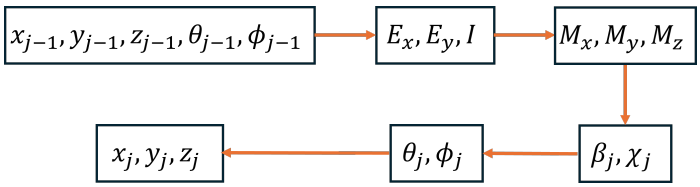


Figure 3.13: Diagram of the Monte Carlo simulation during a time step $\triangle t$ from t_{j-1} to t_j.

Boundary conditions were also taken into account in this scenario. The gold nanorod centre positions still followed the same boundary conditions as the gold nanosphere mentioned in Chapter 7.2.1. β, θ and ϕ were set to be bigger than 0, smaller than $\pi/2$ and smaller than π respectively.

3.8.2 Finite-difference Time-domain (FDTD) Simulation

FDTD is an algorithmic approach to obtaining electromagnetic field propagation by solving Maxwell's curl equations in time and space. Kane Yee first put it forward [259] and then the incorrect numerical stability conditions were corrected by other

scientists [260, 261]. Maxwell's equations in an isotropic medium [262] are:

$$\frac{\partial \boldsymbol{B}}{\partial t} = -\nabla \times \boldsymbol{E} \tag{3.83a}$$

$$\frac{\partial \boldsymbol{D}}{\partial t} = \nabla \times \boldsymbol{H} + \boldsymbol{J} \tag{3.83b}$$

$$\boldsymbol{B} = \mu \boldsymbol{H} \tag{3.83c}$$

$$\boldsymbol{D} = \epsilon \boldsymbol{E} \tag{3.83d}$$

where $\boldsymbol{B}$ is the magnetic field, $\boldsymbol{E}$ is the electric field, $\boldsymbol{D}$ is the electric displacement, $\boldsymbol{H}$ is the magnetic field strength and $\boldsymbol{J}$ is the electric current density. ϵ and μ are frequency-dependent permittivity and permeability of the medium. ϵ is usually complex to represent material absorption and μ is equated to unity for the non-magnetic medium.

In a Cartesian coordinate system, equation 3.83a and 3.83b becomes a set of six scalar partial differential equations after combining with equation 3.83c and 3.83d:

$$\frac{\partial H_x}{\partial t} = \frac{1}{\mu}\left(\frac{\partial E_y}{\partial z} - \frac{\partial E_z}{\partial y}\right) \tag{3.84a}$$

$$\frac{\partial H_y}{\partial t} = \frac{1}{\mu}\left(\frac{\partial E_z}{\partial x} - \frac{\partial E_x}{\partial z}\right) \tag{3.84b}$$

$$\frac{\partial H_z}{\partial t} = \frac{1}{\mu}\left(\frac{\partial E_x}{\partial y} - \frac{\partial E_y}{\partial x}\right) \tag{3.84c}$$

$$\frac{\partial E_x}{\partial t} = \frac{1}{\epsilon}\left(\frac{\partial H_z}{\partial y} - \frac{\partial H_y}{\partial z}\right) \tag{3.84d}$$

$$\frac{\partial E_y}{\partial t} = \frac{1}{\epsilon}\left(\frac{\partial H_x}{\partial z} - \frac{\partial H_z}{\partial x}\right) \tag{3.84e}$$

$$\frac{\partial E_z}{\partial t} = \frac{1}{\epsilon}\left(\frac{\partial H_y}{\partial x} - \frac{\partial H_x}{\partial y}\right) \tag{3.84f}$$

It also assumes that there is no free current in this region, so the $\boldsymbol{J}$ term disappears. FDTD discretises both the space and time to solve the equations above numerically. The finite-sized mesh and time step is the only approximation. It starts with time

0 and advances until the stopping point of the simulation. The simulation region is divided into cuboidal Yee cells [259] and every grid point of the space can be denoted as $(i\triangle x,\ j\triangle y,\ k\triangle z)$, where $\triangle x$, $\triangle y$ and $\triangle z$ are the cell dimensions. A Yee cell is illustrated in Figure 3.14.

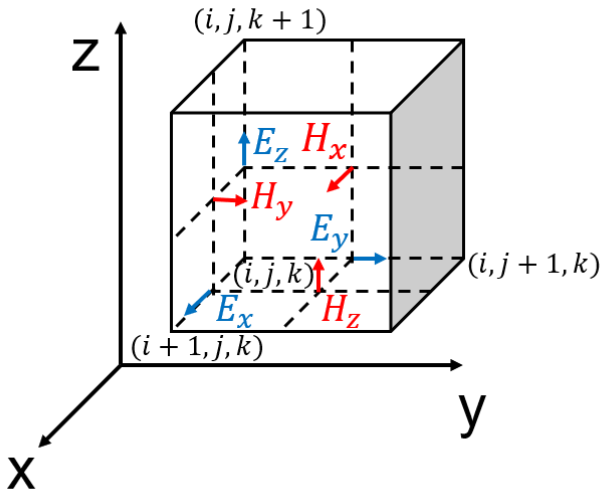


Figure 3.14: Schematic of a Yee cell. The electric fields are along the edges of the cell while the magnetic fields are in the face centre of the cell.

The electric fields are calculated along the edges while the magnetic fields are calculated perpendicular to the surfaces. And all the derivative equations in 3.84 can be expressed in the following way (only show the x direction case, but y and z follow the same principle):

$$\frac{H_x^{n+\frac{1}{2}}(i,j,k) - H_x^{n-\frac{1}{2}}(i,j,k)}{\triangle t} = \frac{E_y^n(i,j,k+\frac{1}{2}) - E_y^n(i,j,k-\frac{1}{2})}{\mu\triangle z} - \frac{E_z^n(i,j+\frac{1}{2},k) - E_z^n(i,j-\frac{1}{2},k)}{\mu\triangle y} \tag{3.85}$$

$$\frac{E_x^{n+\frac{1}{2}}(i,j,k) - E_x^{n-\frac{1}{2}}(i,j,k)}{\triangle t} = \frac{H_z^n(i,j+\frac{1}{2},k) - H_z^n(i,j-\frac{1}{2},k)}{\epsilon\triangle y} - \frac{H_y^n(i,j,k+\frac{1}{2}) - H_y^n(i,j,k-\frac{1}{2})}{\epsilon\triangle z} \tag{3.86}$$

With these two updated equations and the start point of $\boldsymbol{E}^{-\frac{1}{2}} = 0$ and $\boldsymbol{H}^0 = 0$, all the electric and magnetic fields can be calculated accordingly. E and H cannot be calculated at the same position or time.

3.9 Summary

This chapter introduces related theories of this project. Firstly, the wave equation is derived from Maxwell's equations. Solutions to the paraxial wave equation which simplifies from the wave equation are discussed, including the Gaussian beam and the Hermite-Gaussian beam as a general case.

Secondly, the optical microcavity is introduced with three significant metrics to characterise the cavity. Then the optical modes in the microcavity are discussed. The electric field between the two mirrors is derived from the Gaussian beam profile. The waist beam is expressed as a function of the concave mirror RoC and the cavity length with the constraints to form resonant modes.

Thirdly, the interaction between the particle in the microcavity and the incident light is discussed. The cavity field is deduced from Schrödinger equation using the Hamiltonian of the system. The empty cavity is first analysed, followed by the scenario of a polarisable particle in the cavity. Circularly polarised light is utilised to study the situation with a rod-shaped particle in the cavity. The polarisation state of the transmitted light is described with Stokes parameters. It establishes the theoretical foundation for the experimental section about how measuring Stokes parameters of the transmitted light from the microcavity obtains the shape anisotropy of the particle. The anisotropy loss tangent is defined to extract the shape anisotropy. In addition, other related theoretical calculations to supplement the experiment are in-

troduced.

Lastly, the theories of simulations are elucidated, including the Langevin equation and coordinate system conversion in Monte Carlo simulations for diffusional behaviour and FDTD simulations for optical fields with the presence of a particle in the microcavity.

Chapter 4

Experimental Method

4.1 Introduction

This chapter introduces all the experimental methods used in this thesis. Firstly, the fabrication of the optical microcavity chip is briefly introduced. The experimental apparatus to perform all the measurements for gold nanorods and rod-shaped bacteria is then discussed, including the assembly of the flow cell, the microfluidic system and the optical components. Furthermore, three benchmark techniques to characterise the samples and their settings are explained. Finally, the sample preparation is presented.

4.2 Optical Microcavity Chip

The optical microcavity array is fabricated on a UV-fused silica chip with a thickness of 0.5 mm (UQG Optics Ltd.) with the following steps.

4.2.1 Ridge Fabrication

A ridge is fabricated onto a chip with a width of 300 µm and height of 100 µm to make it easier to locate the microcavity array milled on the ridge in the experiment.

Using a motorised blade to remove a layer of 100 µm creates the ridge. The schematic of the ridge on the substrate is shown in Figure 4.1.

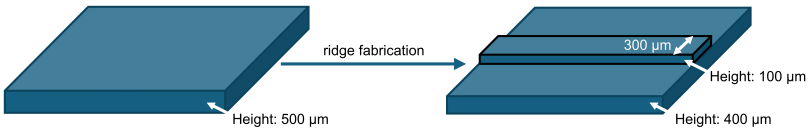


Figure 4.1: Schematic of ridge fabrication by removing a 100 µm layer. The original substrate has a height of 500 µm. The ridge has a height of 100 µm and a width of 300 µm.

MicroAce machine (LoadPoint Ltd.) shown in Figure 4.2 was employed for the fabrication.



Figure 4.2: MicroAce machine to perform dicing work. It has a high-speed rotating blade (3000 rpm) to perform the cut. Cool deionised water keeps flowing to remove heat generated in the process. It uses microscopy for imaging.

The instrument uses a high-speed rotating blade (3000 rpm) to remove the layer stripe by stripe, which is determined by the thickness of the blade. The vacuum ensures sample stability when performing the cut. Cool deionised water keeps flowing to remove heat generated in the process. Two different blades were used, a thin and thick blade with a thickness of 200 µm and 1 mm respectively. The thin blade was used to

create the ridge with more accuracy and the thick blade was utilised to remove the rest of the layer to speed up the process.

Apart from dicing to remove the extra parts mechanically, etching is another way to complete the task such as inductively coupled plasma etching (ICP RIE) to deliver high etch rates, high selectivity and low damage. Shadow masks need to be designed and optimal etching conditions require exploring to fit our specific needs.

4.2.2 Focused Ion Beam (FIB) Milling

After the ridge was created on the substrate, a FIB was used to mill the hemispherical shapes on the surface of fused silica ridges. This was done by my colleague Jiangrui Qian. Various hemispherical patterns have been designed using a MATLAB stream file generator developed by Dr Aurelien Trichet and they are highly reproducible [143]. Through randomisation of the dwell sequence of the FIB beam, geometrical shapes and surface smoothness have been optimised. The Zeiss Crossbeam 540 was used to mill all the features in this project. Samples were sputtered with a layer of 10 nm gold with Leica EM ACE600 to reduce the degree of charging effects during the SEM imaging and FIB milling process. Before the milling started, samples were brought to the eccentric height and electron beams and ion beams were aligned in coincidence. The milling duration depends on the feature size, depth, and the ion beam current, ranging from several seconds to a few minutes. An SEM image of a microcavity array is shown in Figure 4.3. The RoCs and depths of the hemisphere features are labelled. The hemisphere features on the same line have the same specifications.

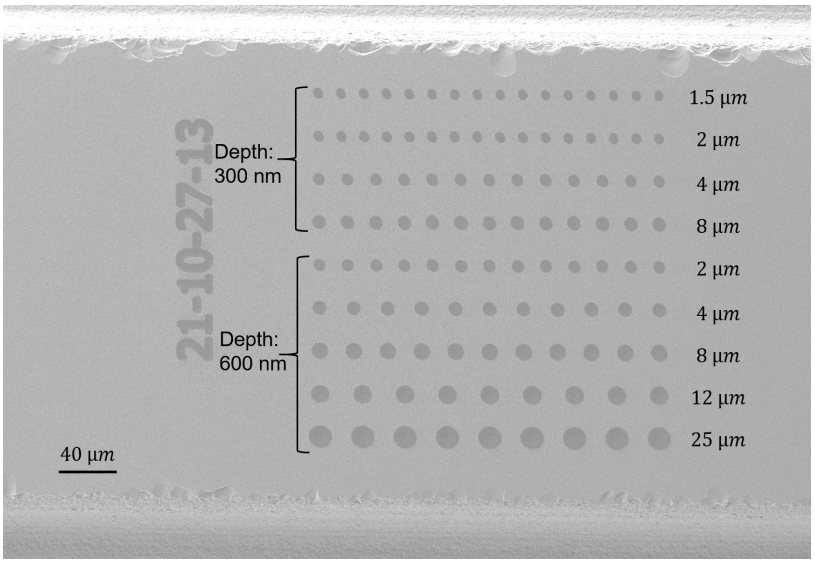


Figure 4.3: SEM image of the microcavity array with the scale bar of 40 µm. The RoCs and depths of the hemisphere features are labelled. The hemisphere features on the same line have the same specifications.

4.2.3 Coating and Dicing

After FIB milling and taking SEM images for the microcavity array, potassium iodide (KI) solution was applied to remove the 10 nm gold layer on the chip. The substrate was sonicated with acetone for 15 mins 3 times and air-dried. A high reflectivity distributed Bragg reflector (DBR) coating was applied using ion beam sputtering by Layertec GmbH. The coating was on the entire surface of the substrate, not only where features are positioned. The reflectivity of the DBR coating can be calculated theoretically with [263]:

$$R = \left[\frac{n_0(n_2)^{2N} - n_s(n_1)^{2N}}{n_0(n_2)^{2N} + n_s(n_1)^{2N}}\right]^2 \tag{4.1}$$

where n_0, n_1, n_2 and n_s are the refractive indices of the originating medium, the two alternating materials, and the terminating medium respectively. N is the number of repeated pairs of low/high refractive index material. Each layer has a thickness of $\frac{\lambda}{4n}$. A more accurate way of calculating the reflectivity is using Sellmeier's equation

[264] with the empirical relationship between refractive index and wavelength. The matrixes of high index and low index material single layer are used to calculate the reflectance and transmittance over the wavelength. In this work, the coating is terminated with high refractive index material to achieve a node on the surface. In other applications, such as putting an emitter on the surface, the coating is terminated with low refractive index material to achieve antinode on the surface. The mirror with concave features has a reflectivity of 99.99% with approximately 16 layers of TiO_2/SiO_2 while the planar mirror has a reflectivity of 99.92% and 99.6% for the measurements of gold nanorods and rod-shaped bacteria particles. The transmittance curve of the coating of the concave mirror is illustrated in Figure 4.4.

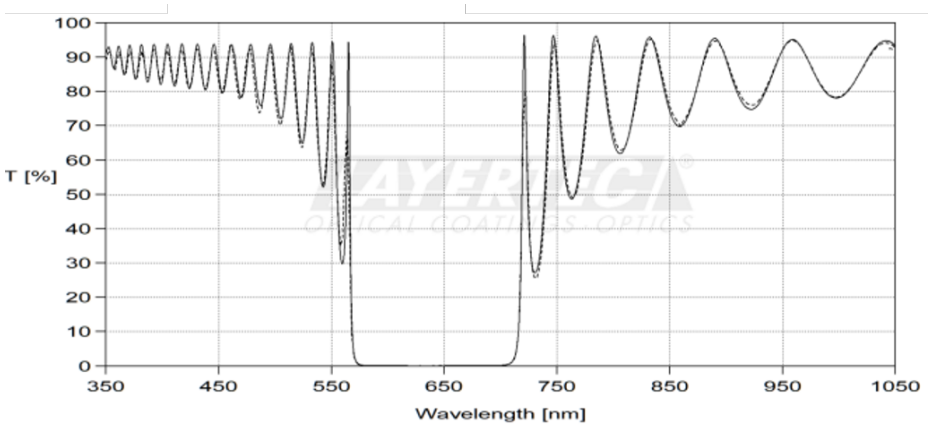


Figure 4.4: Transmittance measurement of the 99.99% coating provided by Layertec GmbH.

After the coating process, the dicing machine mentioned in Chapter 4.2.1 was used with the thin blade to dice the substrate into smaller pieces of 3 mm × 3 mm.

4.3 Experimental Apparatus

4.3.1 Flow Cell

The flow cell is an important component of this work, providing the introduction of the solution and detuning of the microcavity. There are two stainless steel platforms

where the 3 mm × 3 mm chips with concave features and without those respectively fabricated in Chapter 4.2 can be placed. They are shown in Figure 4.5 as platforms A and B.

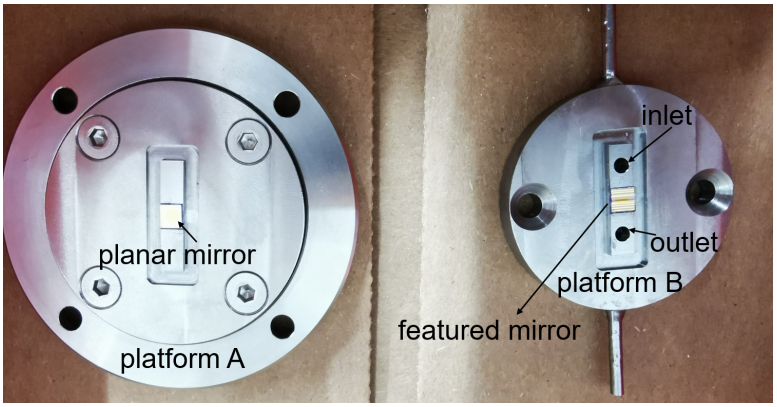


Figure 4.5: Platforms to glue microcavity chips. Platform A is for the planar mirror without structures while platform B is for the mirror with concave features milled on the centre ridge. The inlet and outlet of the solution are labelled.

Platform A is screwed to plate x which is connected to 3 piezo inertia actuators (PIAK10, Thorlabs Inc.) as shown in the photo of the complete flow cell assembly in Figure 4.6. The actuators can be adjusted both manually and through the four-channel K-cube piezo inertia motor controller (KIM101, Thorlabs Inc.) to provide finer adjustment with a typical step size of 20 nm. In this way, the cavity length can be adjusted to an appropriate value before the experiment starts.

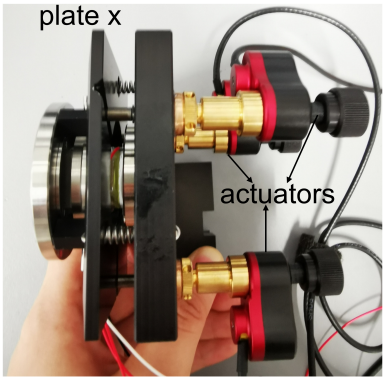


Figure 4.6: Photo of the complete flow cell assembly with plate x and actuators labelled.

Platform B is screwed to another plate glued with a long piezo stack and a short piezo stack (Piezomechanik GmbH) which can accomplish the modulation of the cavity length shown in Figure 4.7(c). Figure 4.7(a) and (b) show the previous assembly steps. (a) shows the glued part of short and long piezo stacks and (b) is the photo after the piezo stack part is screwed to the plate assembly.

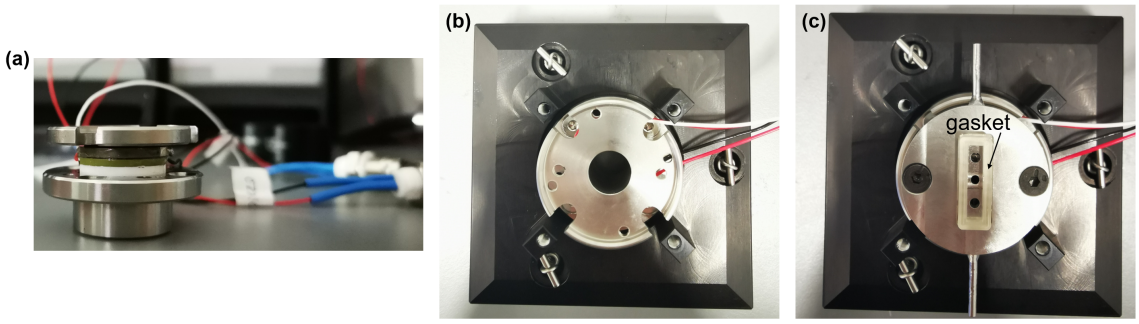


Figure 4.7: Concave mirror side assembly. (a) The glued part of short and long piezo stacks. (b) The photo after the piezo stack part is screwed to the plate assembly. (c) Platform B is screwed to the top of (b).

As shown in Figure 4.5, platform B has two holes through which the solution is delivered into and out of the flow cell. To avoid any leakage with the solution injection, a gasket, printed with the 3D printer (Form 2, Formlabs) in elastic 50A resin (Formlabs), was placed in the trench around the concave mirror side to seal around the inlet and outlet shown in Figure 4.7(c).

All the parts were designed by former group members Dr Aurelien Trichet et. al and I assembled them sequentially. The wires were soldered to a BNC connector for long and short piezo stacks respectively. The gasket was designed using AutoCAD and loaded into the PreForm software with a dimension of 6.7 mm $\times$ 18.5 mm $\times$ 3.5 mm (width $\times$ length $\times$ height). The supports were generated with the automatic algorithm in the software. After the printing process, IPA was used to wash the gasket (Form Wash, Formlabs) for 20 minutes and it was then cured at 60°C for 20 minutes (Form Cure, Formlabs). The piezo spacer between the piezo stacks and the stainless

part was also printed using the 3D printer but with the tough resin (Formlabs), so the curing process was at 60°C for 60 minutes.

4.3.2 Microfluidic System to Deliver the Solution

The microfluidic system delivers the sample solution and washing liquid into the flow cell with the diagram illustrated in Figure 4.8 without further flow control. There is no flow during the measurement after the particles are delivered to the flow cell.

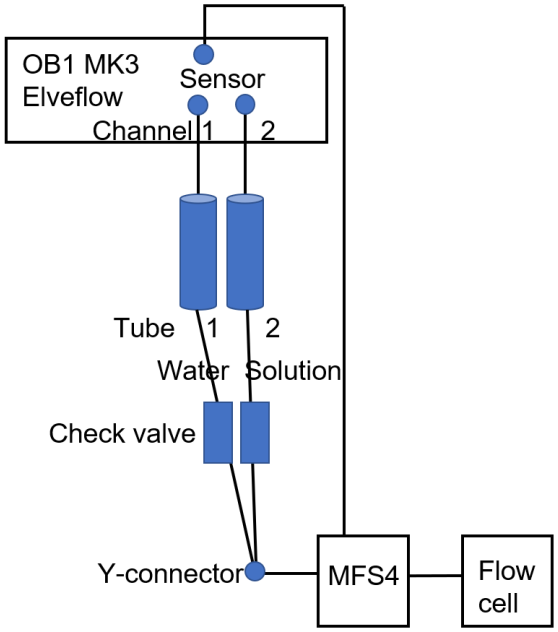


Figure 4.8: Schematic of the microfluidic system.

A pressure controller (OB1 MK3, Elveflow) applies pressure into the tube to empty the solution. Two channels are connected to two tubes, controlling the sample solution and washing liquid flow separately. The tubing is connected to a check valve and a y-connector before a microfluidic flow sensor (MFS4, Elveflow). The check valve only allows the flow in one direction and avoids backflow. Therefore, when one channel is used, the liquid will flow through the flow sensor, not going into the other channel at the y connector position. With the mismatch of the tubing dimensions and different connector types, several adapters are required to connect all the parts.

4.3.3 Optical Apparatus

Figure 4.9 and Figure 4.10 display the optical apparatus I built in the lab and its schematic.

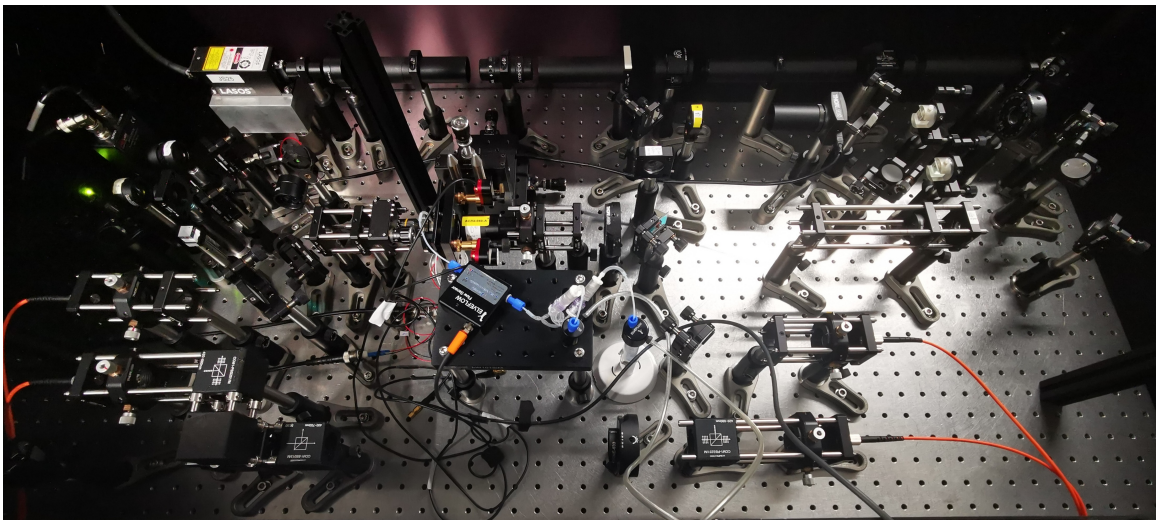


Figure 4.9: Photo of the experimental apparatus.

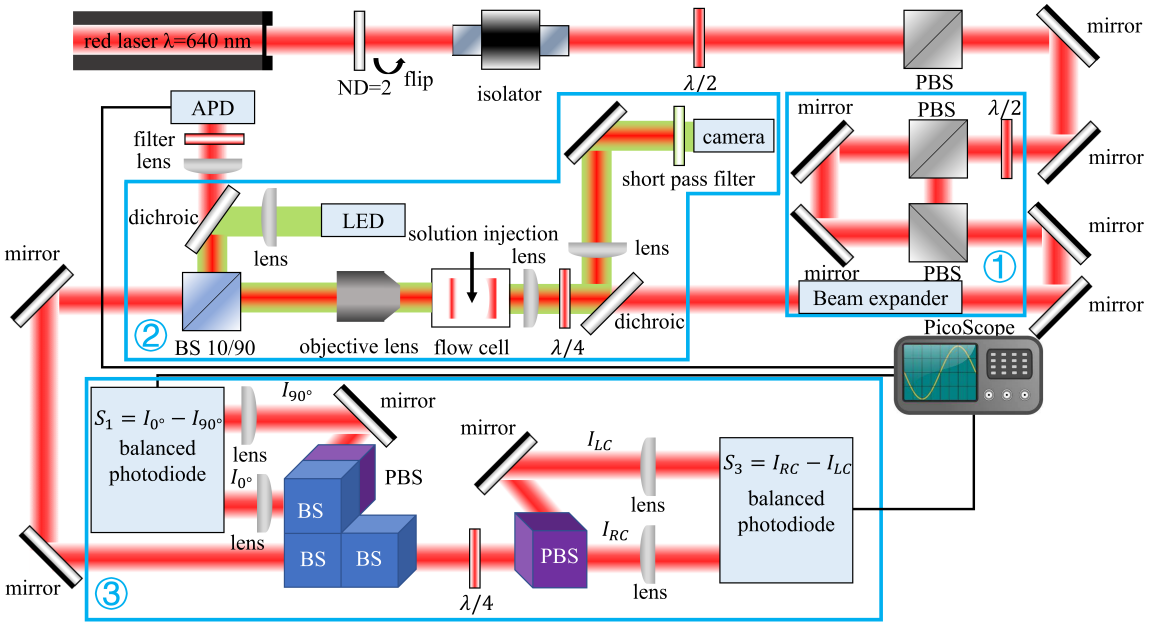


Figure 4.10: Schematic of the experimental apparatus.

The experiment uses a diode-pumped solid-state laser with a centred wavelength of

640 nm and a maximum output power of 150 mW (RLK 40150 TS, LASOS Lasertechnik GmbH). A neutral density filter with optical density (OD) = 2 (NE20A, Thorlabs Inc.) is on a flip mount to attenuate light intensity for alignment while irradiating light without attenuation for the experiment. The optical isolator (IO-3-633-LP, Thorlabs Inc.) is a magneto-optic device and ensures transmitting light along a single direction preferentially. It shields upstream optics from back reflections. The combination of a half-wave plate (WPMH10M-633, Thorlabs Inc.) and a polarising beam splitter (PBS) (CCM5-PBS201/M, Thorlabs Inc.) controls the light intensity for the experiment. With the rotation of the half-wave plate, the originally p-polarised light will be converted to a linear polarised light with a different polarisation direction. Since the PBS transmits p-polarised light while reflecting s-polarised light, the intensity of the transmitted light after the PBS changes with different rotation angles of the half-wave plate. The reflected beam is blocked with black tape.

The schematic in Figure 4.10 has three labelled blue squares, representing three core parts of the system. Part 1 splits the light into two beams, one reference beam and one sensing beam. As mentioned above, the combination of a half-wave plate and a PBS can adjust the intensities of transmitted and reflected light. In this scenario, it can change the relative intensity of the reference and sensing beam. The reference beam transmits through the PBS and is p-polarised. Then it is reflected by two mirrors while the sensing beam is s-polarised and reflected by the second PBS. The two mirrors can adjust the reference beam slightly away from the sensing beam to irradiate a different microcavity in the array. The reference beam was intended to remove background noise, but in the data analysis process, we did not use the wavelength shift which could be extracted from the data and would benefit from this reference beam setting. Therefore, although the experiment was conducted with the reference beam, the data was not used. The beam expander is built with a plano-concave lens

with a focal length of -25 mm (LC4210-A, Thorlabs Inc.) and a plano-convex lens with a focal length of 75 mm (LA1608-A-ML, Thorlabs Inc.). There are two types of beam expander construction. One is the Keplerian design with two convex lenses with positive focal lengths. The distance between two lenses is the sum of two focal lengths. This is not preferred for high-energy beams. Focusing pulses with nanosecond duration and optical powers around $\sim$1 MW or higher, for example, can ionize the air and create a spark, which undesirably reduces the power of the pulse and can negatively affect the beam quality [265]. The other one is the Galilean design, with a convex and a concave lens having a positive and negative focal length respectively. It can minimise the spherical aberration of the beam expander, with the concave lens cancelling out the impact of the convex lens. I chose Galilean design to achieve a more compact configuration. The beam expander was used to further decrease the focus spot diameter in the microcavity.

Part 2 of the apparatus includes the optical microcavity chip embedded in the flow cell introduced in Chapter 4.3.1 and an imaging system used both for alignment and to perform cavity locking through a proportional-integral-derivative (PID) control system. With this PID system, it can make sure the planar mirror is back to its original position during the process of scanning the cavity length. It can help eliminate drifts due to background noise, such as temperature fluctuations. LED light with a wavelength of 570 nm shines through the planar side of the cavity. LED light is collected by the lens (LA1131-A-ML, Thorlabs Inc.) to provide enough light for illumination. As the reflection spectrum of the coating in Figure 4.4 shows, the LED light is off-resonance and can illuminate the microcavity array for imaging with the complementary metal oxide semiconductor (CMOS) camera (DCC1545M, Thorlabs Inc.) on the other side of the flow cell. The long-pass dichroic mirrors (DMLP605R, Thorlabs Inc.) on both sides of the flow cell transmit the red laser light while reflecting

the green LED light. The short pass filter (FES0600, Thorlabs Inc.) blocks the laser light into the camera and avoids saturation in the experiment. The quarter wave-plate (WPQ10ME-633, Thorlabs Inc.) is rotated to 45° relative to the polarisation direction of the sensing beam to convert the linear polarised light into a left-circularly polarised light. As a result, the reference beam is converted into a right-circularly polarised light. The incident light is focused on the microcavity array through an achromatic lens of 40 mm focal length (AC254-040-A-ML, Thorlabs Inc.). The lens before the camera is an achromatic lens of 300 mm focal length (AC254-040-A-ML, Thorlabs Inc.) to provide the magnification of the microcavity array in the camera image. The objective lens (plan achromat RMS10X, Olympus) collects transmitted light through the microcavity. The non-polarising beam splitter (BS) (BS040, Thorlabs Inc.) after the objective lens transmits 90% light for further polarisation state measurement while reflecting 10% light for the intensity data collection. This ratio is chosen to maximise light entering into the polarimeter for better signals. The reflected light is focused by a lens (LA1951-A, Thorlabs Inc.) to the APD (APD120A-M, Thorlabs Inc.) filtered by a BrightLine single-band bandpass filter centred at 640 nm with a linewidth of 14 nm (FF01-640/14-25, Semrock Inc.). This ensures that only the laser light is collected while the LED light is blocked.

Part 3 is the polarimeter used to analyse the polarisation state of the transmitted laser light. Within the polarimeter, two 50:50 BSs (CCM1-BS013M, Thorlabs Inc.) remove the linear retardance and diattenuation to preserve the original polarisation state of the light [266]. Two PBSs (CCM1-PBS251/M, Thorlabs Inc.) split the light into orthogonal components. Then they are focused and coupled by multi-mode fibre (M72L02, Thorlabs Inc.) into balanced photodiodes (PDB425A, Thorlabs Inc.) to measure intensity differences between them. A quarter-wave plate (WPQ10ME-633, Thorlabs Inc.) is used to convert circularly polarised components to linearly polarised

components to obtain the intensity of left-circularly polarised and right-circularly polarised components. A picoscope (Picoscope 5442D, Pico Technology) is triggered by signs of single-particle events and collects the voltage data from the APD and two balanced photodiodes as a function of time simultaneously for further data analysis. Before inserting the flow cell with the cavity, the polarimeter was used to measure Stokes parameters of a prepared laser beam to check its performance. The quarter-waveplate in part 2 of the apparatus shown in Figure 4.10 was used to prepare the incident light with different polarisation states by rotating at different angles. The Stokes parameters were normalised:

$$\tilde{S}_1 = \frac{I_{0^\circ} - I_{90^\circ}}{I_{0^\circ} + I_{90^\circ}} \tag{4.2a}$$

$$\tilde{S}_3 = \frac{I_{RC} - I_{LC}}{I_{RC} + I_{LC}} \tag{4.2b}$$

These measured values were compared with the standard theoretical values [267] and the difference was plotted as a function of the rotating angle. Measurements were performed both directly using a power meter and after fibre coupling. The results in Figure 4.11 show that the measured polarisation states agree with theoretical predictions to within 5% across all measurements. The zero reference line represents the ideal situation where the measured values match theoretical values.

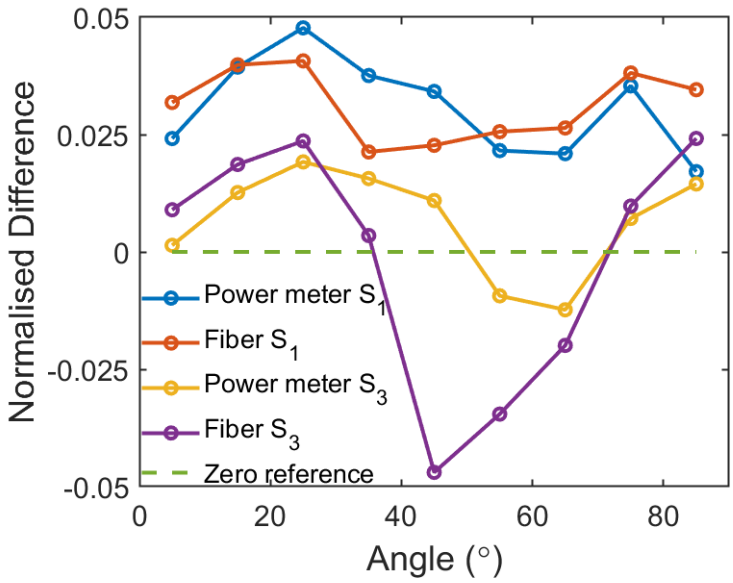


Figure 4.11: Polarimeter calibration. Normalised Stokes parameters S_1 and S_3 were measured with different rotating angles of the quarter-waveplate using equation4.2. Normalised differences ($\frac{measured-theoretical}{theoretical}$) compared with theoretical values were plotted. Zero reference line illustrates the ideal situation, where the measured values equal to theoretical values.

After the introduction of different optical components in the optical apparatus, the setting of the experimental conditions will be discussed sequentially. Three piezo actuators are manually adjusted sequentially to close the cavity gradually and the camera image of the ridge is monitored. When the two mirrors become closer, the interferometric fringes appear in the camera image of the ridge. An example is shown in Figure 4.12.

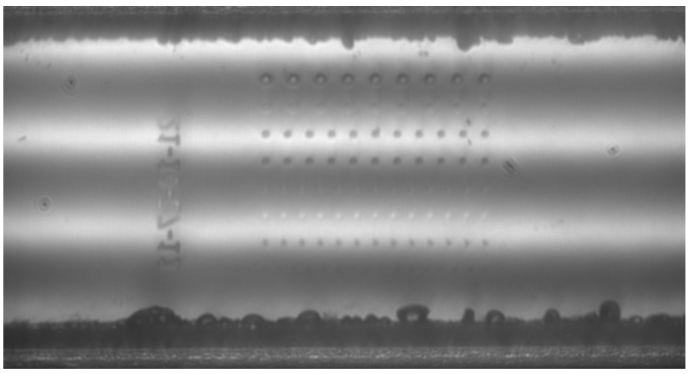


Figure 4.12: An example of a camera image of the microcavity array with horizontal fringes.

The direction and number of fringes indicate the relative orientation of the two mirrors as shown in Figure 4.13. The relative angle illustrated in Figure 4.13(a) generates vertical fringes while the relative angle in (b) brings horizontal fringes, illustrated in Figure 4.12. Take horizontal fringes as an example, it means that every point in the horizontal direction has the same cavity length. The combination of these two angles creates diagonal fringes.

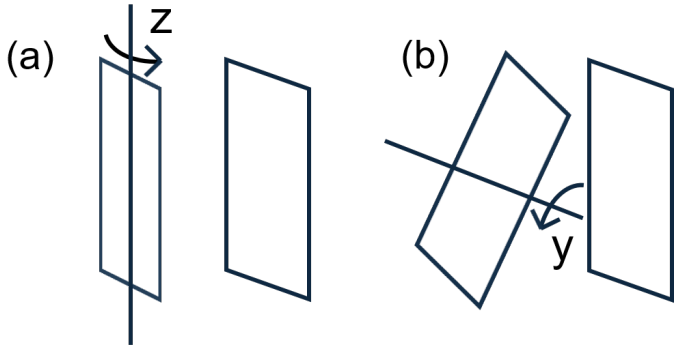


Figure 4.13: Schematic of relative angles between mirrors. (a) This angle creates vertical fringes. (b) This angle creates horizontal fringes. For the mirror on the left in both cases, (a) illustrates the rotation along the z-axis while (b) displays the rotation along the y-axis.

The phase or the contrast between constructive and destructive interference (whether the surface is at the antinode or node of the standing wave) can be used to determine the relative cavity length as shown in Figure 4.14. It illustrates an example of how the

relative cavity length can be determined. Since these two points are at consecutive nodes of the standing wave, the relative cavity length between these two points are $\frac{\lambda_{LED}}{2n_m}$ where λ_{LED} is the wavelength of the LED and n_m is the refractive index of the medium.

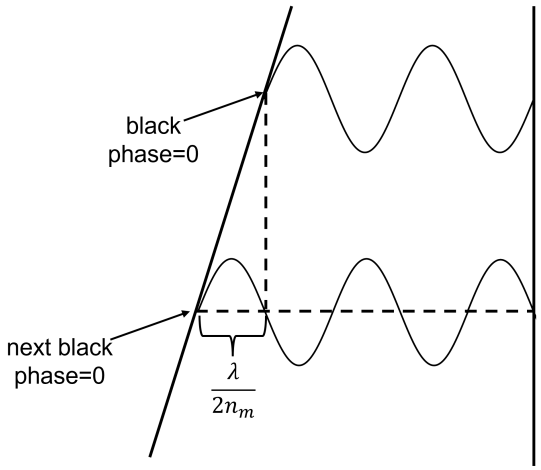


Figure 4.14: Schematic of how the relative cavity length is calculated. The first point is at the node of the standing wave with the number of anitonodes $q = 4$. The second point is also at the node of the standing wave, but with $q = 5$. Therefore the relative cavity length can be determined with the wavelength of the LED λ_{LED} and the refractive index of the medium n_m.

Since all the hemisphere features on the same line share the same specifications, horizontal fringes are required to ensure that the microcavities on the same line have the same cavity length. The light leakage is the smallest and the best state of the cavity can be achieved when the two mirrors are parallel to each other. However, the fringes are necessary for the cavity-locking, which will be introduced later in detail. Since the first line of the microcavity with a RoC of 25 µm and a depth of 600 nm was utilised in the experiment shown in Figure 4.12, there was only misorientation about the y-axis shown in Figure 4.13(b) and the relative positions of the two mirrors were shown in Figure 4.14 so that the top edge touched first. When the cavity is closed more, the fringes bend or do not move any more, indicating the two mirrors touch. Then the piezo actuators are adjusted one by one slowly to open the cavity and the

number of fringes (m) moving up are counted to roughly estimate the cavity length. Each fringe corresponds to a relative cavity length difference of $\frac{\lambda_{LED}}{2n_m}$, and since the process starts from two mirrors touching, namely 0 cavity length, $L_{cav} = \frac{m\lambda_{LED}}{2n_m}$.

The long piezo stack is first connected to the function generator to perform the alignment. A sinusoidal wave of 500 Hz and 9 V is utilised to scan the cavity length within a big range. The xyz translator to mount the flow cell is adjusted to align the laser spot of the sensing beam to the microcavity and obtain the main mode. The reference beam is aligned to the adjacent microcavity of the sensing cavity with the two mirrors in Part 1 (Figure 4.10). Then the short piezo stack is connected to the function generator to perform the smaller-range scanning with a sinusoidal wave while a data acquisition (DAQ) card controls the long piezo stack to generate cavity length offset with a constant voltage. A MATLAB user interface was designed by Dr William Okell to perform the cavity locking [253]. With a setpoint stored, the image of the fringes is monitored in real-time and compared with the phase of the setpoint during the experiment. The phase difference can be converted to an additional response voltage applied to the long piezo stack in addition to the constant voltage mentioned above to lock the cavity through a PID control system. The exact values for P, I and D settings may vary slightly between different experiments due to the fine environment changes.

4.3.4 Specifications of Cavities Used in the Experiment

For both experiments of gold nanorods and rod-shaped bacteria particles, a red laser with a wavelength of 640 nm was used. The biggest microcavity of the array shown in Figure 4.3 was used. It has a RoC of 25 µm and a depth of 600 nm. The differences between the two experiments are summarised in the following table. Power is the intra-cavity power calculated from APD recordings of the transmitted light. Q is

the quality factor of the microcavity. q is the mode number. $\mathcal{F}$ is the finesse of the cavity. The scanning rate is the sweeping frequency of the planar mirror. The sampling rate is the collection speed of PicoScope. Peak FWHM is the FWHM of the measurement peak in the time domain. The choice of the scanning frequency for rod-shaped bacteria particles will be discussed in Chapter 6.4.

	Power	Q	q	$\mathcal{F}$	scanning	sampling	peak FWHM
Gold	17.2 mW	16000	6	2667	5 kHz	41.7 MHz	1 µs
Bacteria	10 mW	19000	20	950	10 Hz	50 kHz	400 µs

Table 4.1: The summary of different experimental conditions for gold nanorods and rod-shaped bacteria particles. Power is the intra-cavity power calculated from APD values of the transmitted light. Q is the quality factor of the microcavity. q is the mode number. $\mathcal{F}$ is the finesse of the cavity. The scanning rate is the sweeping frequency of the planar mirror. The sampling rate is the collection speed of PicoScope. Peak FWHM is the FWHM of the measurement peak in the time domain.

4.4 Data Processing

With the scanning of the short piezo stack, data is recorded in the time domain. It is then converted to the frequency domain:

$$\omega = \frac{2\pi c}{\lambda} \tag{4.3}$$

whereby differentiating it and combining the relationship between L and λ ($L = \frac{q\lambda}{2n_m}$) gives:

$$\frac{\triangle}{\omega_c} = -\frac{\triangle\lambda}{\lambda} = -\frac{2n_m}{q}\frac{\triangle L}{\lambda} \tag{4.4}$$

where $\triangle$ is the frequency detuning, ω_c is the frequency for the probe laser light, n_m is the refractive index of the medium, q is the mode number, and $\lambda = 640$ nm is the wavelength of the probe laser. $\triangle L$ is achieved by the sinusoidal wave scanning with

the short piezo stack. Therefore, the frequency detuning is:

$$\triangle = -\frac{n_m w_c}{q\lambda} \times A_s \times [\sin(\omega_s(t - t_0)) - \sin(\omega_s(t_{mid} - t_0))] \tag{4.5}$$

where A_s and ω_s are the amplitude and angular frequency of the cavity length modulation, and t_{mid} and t_0 correspond to the times at which the mid-point of the two modes and the mid-point of the modulation are respectively reached. A_s is estimated according to the expected response of the piezoelectric stack to the applied voltage. Taking one of the gold nanorod experimental conditions as an example, n_m is 1.33 for water. ω_c is around 470 THz. A_s is 4.17 nm. ω_c is 0.01π and time is in the microsecond range. It will give us the frequency detuning of several tens of GHz.

4.5 Characterisations of Samples

4.5.1 DLS

DLS has already been reviewed in Chapter 2.2.3. DLS measurements were performed with Nano Zetasizer (Malvern Panalytical) for two types of gold nanorod and gold nanosphere samples and the results are reported in Chapter 5.2.1. The schematic is shown in Figure 4.15, reproduced from [268].

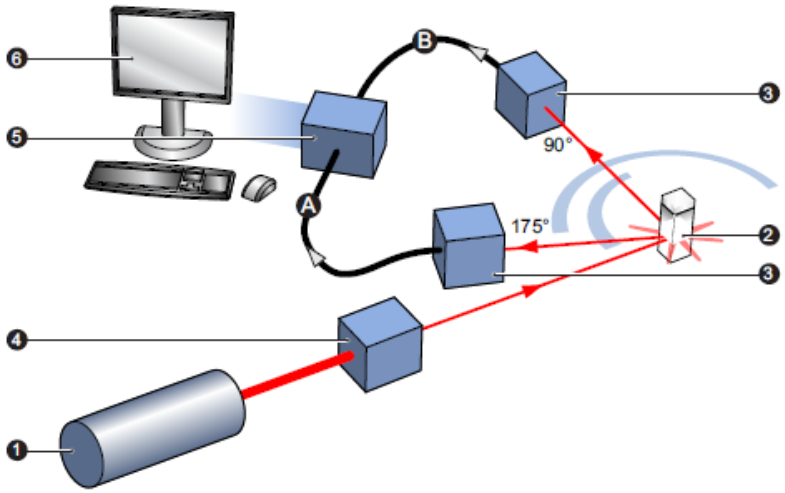


Figure 4.15: Schematic of Nano Zetasizer, reproduced from [268]. 1 is the laser to provide illumination for the sample cell 2. 4 is the attenuator to avoid saturating the detector 3. 5 is the correlator to perform digital signal processing and the results are passed to the computer 6. 90° path is the design for another model.

It measures backscattered light at 175° and the autocorrelator labelled as 5 in Figure 4.15 compares the history of signals nanoseconds/milliseconds later to derive the diffusion coefficient as explained in Chapter 2.2.3. The attenuator labelled as 4 in Figure 4.15 is equipped to avoid saturating the detector labelled as 3 in Figure 4.15 with too much scattered light. It is non-invasive since the optics do not contact the sample. There are multiple advantages in monitoring backscattered signals [268]. The incident beam passes through a shorter path length of the sample without the need to transmit through the entire sample, enabling measurements of samples with higher concentrations. It also reduces the multiple scattering effects, where the scattered light from one particle is scattered by other particles. The effect of contaminants such as dust particles can be greatly reduced since they are typically large compared to the sample size and mainly scatter in the forward direction. For the size measurement, it has two values to display [268]. One is the z-average size with the fit of a polynomial

to the log of the correlation function $G(t)$:

$$\ln G(t) = a + bt + ct^2 + dt^3 + et^4... \tag{4.6}$$

The value of b is known as the second order cumulant, or the z-average diffusion coefficient. This is converted to the z-average size using the dispersant viscosity and some instrumental constants. The polydispersity index ($\frac{2c}{b^2}$) represents the distribution width of the samples. And a is the intercept value. Another one is the distribution analysis which shows the distribution of the size with the percentage of the scatttered light intensity. The z-average size is obtained by force-fitting only the initial part of the correlation function, up to 10% of the intercept, to a single exponential decay while the distribution analysis fits the correlation function to longer times, typically up to 1% of the intercept. When the distribution is very narrow, z-average size is a better number to use while when the distributions becomes wider, the peak value is more representative.

The instrument can also measure the zeta potential of the samples, which is an important parameter to determine whether the particles in a solution aggregates or not. Malvern developed its patented M3-PALS technique [268] to measure zeta potential, combining an improved laser Doppler velocimetry method with phase analysis light scattering. Samples with a zeta potential in the range of >30 mV or <-30 mV are considered stable.

4.5.2 UV-Vis Spectrometer

As explained in Chapter 2.2.8, metallic particles have a maximum absorption at the plasmon resonance frequency which provides shape information. The absorption spectra of two types of gold nanorods and gold nanospheres were measured using

Cary 5000 UV-Vis spectrometer (Varian) and the results are illustrated in Chapter 5.2.2. The smallest spectral bandwidth is 0.01 nm. Firstly, the baseline correction was performed so that the sample transmission spectrum could be corrected to $\frac{S-0\%T\ Baseline}{100\%T\ Baseline-0\%T\ Baseline}$. 100% and 0% transmission were measured with no samples in the sample cell and by blocking the beam respectively. In addition, the reference cell is filled with the solvent, namely deionised water in this scenario, so that the measured absorption spectrum only contains the information of the particles.

4.5.3 SEM

SEM has been briefly introduced in Chapter 2.2.1. SEM measurements were performed (Merlin FEG-SEM, Zeiss) for all the samples utilised in this work, including two types of gold nanorods, gold nanosphere and rod-shaped bacteria particles. The results are reported in Chapter 5.2.3 and 6.2.

After mounting the sample to the stage, the plasma cleaner introduces a radio frequency plasma for a set period of time and the hydrocarbon contaminants can be removed through the pump connected to the SEM. The chamber is pumped down and the extra high tension (EHT) can be turned on. For different samples, different appropriate working distances, accelerating voltages and currents were chosen for best image quality.

The alignment process consists of gun alignment, aperture alignment and astigmatism correction. The astigmatism correction uses a magnetic field to reduce the aberrations of the electron beam. The latter two may need to be adjusted one by one repeatedly until an optimal working condition is achieved. To achieve higher resolution, the working distance can be shortened. At this short working distance, the secondary electron detector does not collect much signal, and the in-lens detector, located above

the pole-piece is used instead. Additionally, the imaging mode can be switched to high resolution and different noise reduction modes are explored to find the best one.

4.6 Sample Preparation

Gold nanorods are dispersed in deionised water with 5 mM cetyltrimethylammonium bromide (CTAB) as the stabiliser. The zeta potential has been measured for the original solution and after dilution to make sure there is no aggregation. The solution was mixed with the deionised water using a vortex mixer for better dilution. The two types of gold nanorods have a nominal 25 nm diameter, 34 nm length (A12-25-550-CTAB-DIH-1-25, Nanopartz Inc.) and 40 nm diameter, 60 nm length (A12-40-550-CTAB-DIH-1-25, Nanopartz Inc.) respectively. They have a concentration of 2.5×10^{11} nanoparticles/mL and 4.9×10^{10} nanoparticles/mL. Samples A and B were diluted to 1/100 and 1/50 the original concentration, providing concentrations of 2.5×10^{9} nanoparticles/mL and 9.8×10^{8} nanoparticles/mL. Gold nanospheres are also in solution form, stably suspended in citrate buffer with a nominal diameter of 60 nm and a concentration of 1.9×10^{10} nanoparticles/mL (742015-25mL, Sigma-Aldrich). The sample used in the experiment was diluted to 1/100 the original concentration, providing a concentration of 1.9×10^{8} nanoparticles/mL. These concentrations were chosen due to the fact that the intervals between particle events were long enough. Under these circumstances, I could deduce that a particle entered the cavity and left with transmitted light intensity dropping and resuming. Lower concentrations have been investigated, however, longer time was required for the next particle to enter the cavity. Take gold nanorods as an example. The throughput of our experiment was about 18 minutes to collect data for 30 particles. Using slightly higher concentrations, the throughput could potentially improve but since it was not the focus of the work, I did not optimise this setting.

The rod-shaped bacteria are in powder form (Lactobacillus Casei Freeze Dried Powder, ECP4111202, Creative Enzymes) with a concentration of 2.07×10^{11} CFU/g. The sample solution used in the experiment was prepared by resolving 0.009 g powder into 450 µL deionised water and then diluting it to 1/40, providing the concentration of 1.04×10^{8} particles/mL.

Chapter 5

Gold Nanorod Measurement

5.1 Introduction

As mentioned in Chapter 2.1, it is significant to perform shape measurement of nanoparticles due to the impacts of shape on other properties of nanoparticles, which contributes to diverse applications in different fields. Current common methods have been reviewed in Chapter 2.2 with the analysis of their advantages and disadvantages. In this work, the optical microcavity sensing method is put forward to measure the aspect ratio of gold nanorods in situ at a single-particle scale. Since the experimental apparatus introduced in Chapter 4.3 only includes optical parts, the instrumentation can be miniaturised for real-world applications.

Firstly, the results of three benchmark characterisation techniques introduced in Chapter 4.5 are reported. Then, the results obtained with the optical microcavity sensing method are demonstrated, from gold nanosphere measurements to gold nanorod ones. In detail, a single-particle event of a gold nanorod is introduced, followed by statistical results of 30 particles. Theoretical calculations are also included to provide insights into other factors in the experiment like the heating effect. Ex-

perimental data with the preferred orientation of gold nanorods is also analysed and the reason behind this phenomenon is discussed.

5.2 Benchmark Characterisation Techniques

The original solutions without any dilution are measured in this section.

5.2.1 DLS

The principle of DLS has been introduced in Chapter 2.2.3 and the measurement has been presented in Chapter 4.5.1. As introduced in Chapter 2.2.3, DLS analyses the autocorrelation of scattered light intensity from the particles reaching the detector with the time interval of t. The diameter of the spherical sample is extracted from the analysis. If the sample has multiple types of particles with different diameters, DLS is also able to display it. Five measurements were performed for gold nanorod samples A and B while the gold nanosphere sample took three measurements. The size-intensity graphs are illustrated in Figure 5.1, which is directly generated with the software of the instrument.

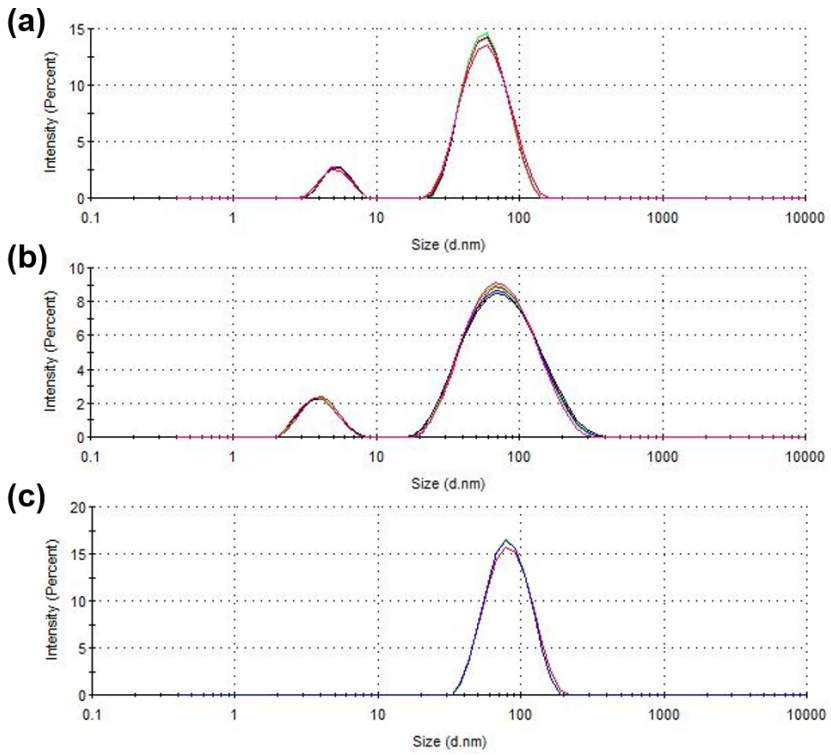


Figure 5.1: Results of DLS measurements (Nano Zetasizer, Malvern Panalytical) directly from the software of the instrument. Each curve is one measurement. (a) Five measurements of gold nanorod sample A. (b) Five measurements of gold nanorod sample B. (c) Three measurements of gold nanosphere sample.

Several measurements maintain consistency for each sample. Gold nanorod samples show 2 peaks while gold nanosphere sample only shows one peak at a diameter of 85 nm. Peaks of gold nanorod sample A appear at a size of 60 nm and 5 nm with the light intensity of 90% and 10% while the two peaks for sample B are located at 85 nm and 4 nm with the light intensity of 89% and 11%. The z-average sizes are 39.16 nm, 41.36 nm and 75.99 nm respectively. The difference between the z-average size and the peak value is due to the methodology difference as introduced in Chapter 4.5.1.

From the results, DLS cannot provide information about the length and width of rod-shaped particles. The peak with a bigger diameter may reveal the length infor-

mation while the peak with a smaller diameter value may indicate CTAB micelles in the solution. CTAB acts as stablisers in gold nanorod solution. It forms bialyers on the surface of a gold nanorod and prevent aggregation [269]. Extra CTAB molecules often aggregate and form micelles in the solution. For the gold nanosphere sample, the z-average value also differs from the distribution peak value, which may be due to a small polydispersity or CTAB micelles in the solution. The zeta potential was also measured and it was around 40 mV, which was above 30 mV and could be considered stable without aggregation.

5.2.2 UV-Vis Spectrometer

The absorption spectra of gold nanoparticles measured with a UV-Vis spectrometer are illustrated in Figure 5.2. They were measured in 200 $\sim$ 800 nm and shown in 400 $\sim$ 800 nm with the peak area.

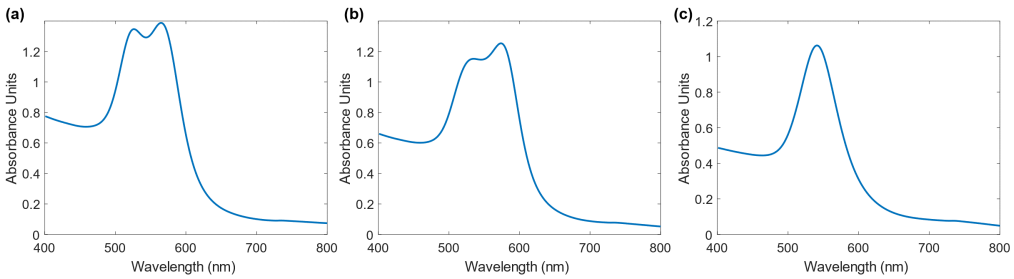


Figure 5.2: Absorption spectra measured by UV-Vis spectrometer with the wavelength range of 400 $\sim$ 800 nm. (a) Gold nanorod sample A shows the peak at 526 nm and 565 nm. (b) Gold nanorod sample B shows the peak at 535 nm and 574 nm. (c) Gold nanosphere sample shows the peak at 541 nm.

Gold nanorod samples A and B display two peaks, the transverse and longitudinal plasmon resonance. For sample A, they are at 526 nm and 565 nm while they are at 535 nm and 574 nm for sample B. The peak is at 541 nm for the gold nanosphere sample. As mentioned in Chapter 2.2.8, the aspect ratio could be obtained by either employing the simple relationship of the longitudinal plasmon resonance with the

aspect ratio or fitting the whole spectrum. However, a single-particle analysis cannot be performed.

5.2.3 SEM

Since the solution sample cannot be directly used for SEM imaging, the sample preparation procedure needs to be explored. Firstly, spin-coating was attempted on a copper foil with a 2000 rpm speed for 60 s and on a silicon substrate with a 2000 rpm speed for 120 s. The copper foil has good conductivity to prevent the charging effect and any distortions to the image. For the silicon substrate, a 4 nm platinum coating was applied to increase the surface conductivity. However, particles could not be observed, with only some traces in both circumstances. Particles may not be able to stick to the surface during the spin-coating process. Therefore, the droplets were directly left on the substrate, the 400 mesh copper TEM grid (AGG2400C, Agar Scientific Ltd.). Heating of the substrate to 40°C was also endeavoured to speed up the evaporation of the water. It is found that high-quality SEM images could be obtained regardless of heating.

SEM images are illustrated in Figure 5.3 which collects secondary electrons. All the images apart from (d) were taken with the accelerating voltage of 10 kV and probe current of 112 pA while (d) was taken with 20 kV and 176 pA. The working distance for (c) and (d) was 4 mm while (a) was 3.5 mm and (b), (e) and (f) was 3.3 mm. The imaging mode was set to high resolution and signals were captured from the in-lens detector. (a) and (b) are gold nanorod sample A while (c) and (d) are gold nanorod sample B. (e) and (f) are gold nanosphere samples.

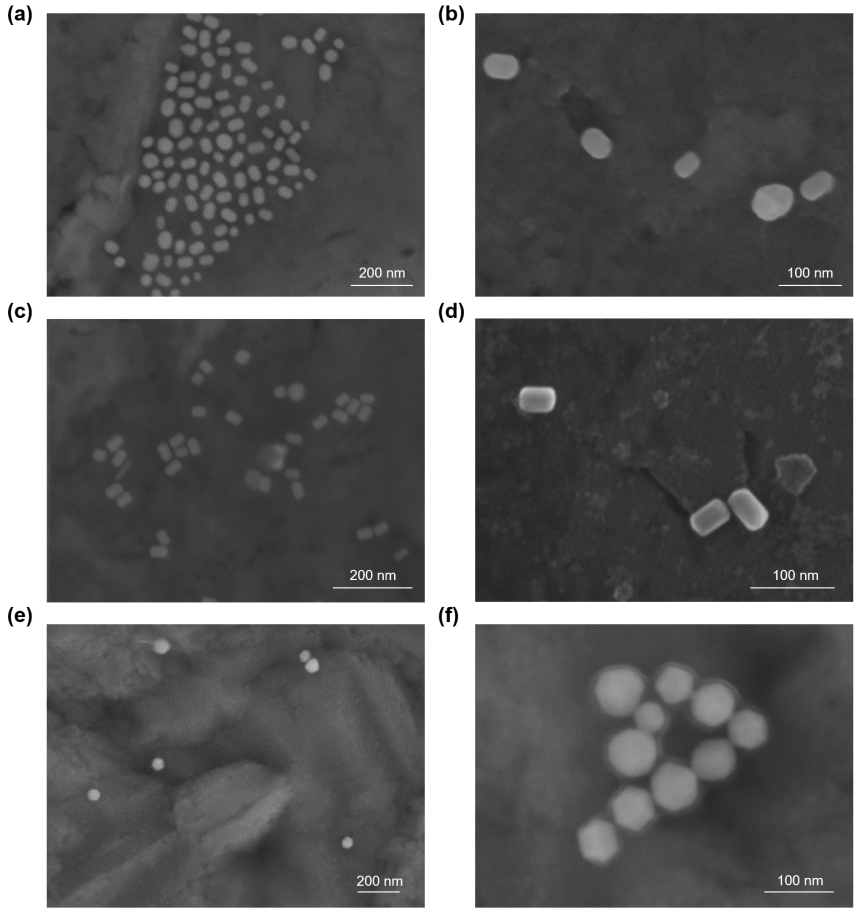


Figure 5.3: SEM secondary electron images of gold nanoparticles with different scale bars labelled (Merlin FEG-SEM, Zeiss). Gold nanorod sample A: (a) and (b). (a) is imaged with the probe current of 112 pA, EHT of 10 kV and a working distance of 3.5 mm. (b) is imaged with the probe current of 112 pA, EHT of 10 kV and a working distance of 3.3 mm. Gold nanorod sample B: (c) and (d). (c) is imaged with the probe current of 112 pA, EHT of 10 kV and a working distance of 4 mm. (d) is imaged with the probe current of 176 pA, EHT of 20 kV and a working distance of 4 mm. Gold nanosphere sample: (e) and (f), both are imaged with the probe current of 112 pA, EHT of 10 kV and a working distance of 3.3 mm.

Heterogeneous distributions of all the samples from these images were observed. In the images of nanorods, some particles seem more spherical. However, it is worth mentioning that if the nanorod is perpendicular to the image plane, it will seem more spherical than it is. In the image with a higher magnification presented in Figure 5.3(f), some of the nanospheres have rough edges, which may be due to the imperfect

growth in the fabrication process. Despite that, they show a nearly isotropic state. The water traces were still left with the sample preparation, leaving the background some contrast under the electron beam. ImageJ was utilised to measure the lengths and widths of these gold nanorods. For 30 particles, sample A has an averaged length with a standard deviation of 48.45 ± 6.23 nm and a width of 33.21 ± 4.1 nm, while sample B has a length of 41.59 ± 3.93 nm and a width of 28.1 ± 1.84 nm. Sample A has an averaged aspect ratio with a standard deviation of 1.46 ± 0.1 while it is 1.48 ± 0.1 for sample B.

5.3 User Interface for Data Processing

Due to the complexity of the fitting and big data files with over 8 million data points in each file, I designed a user interface in MATLAB shown in Figure 5.4 to perform the processing sequentially and facilitate automation of this process.

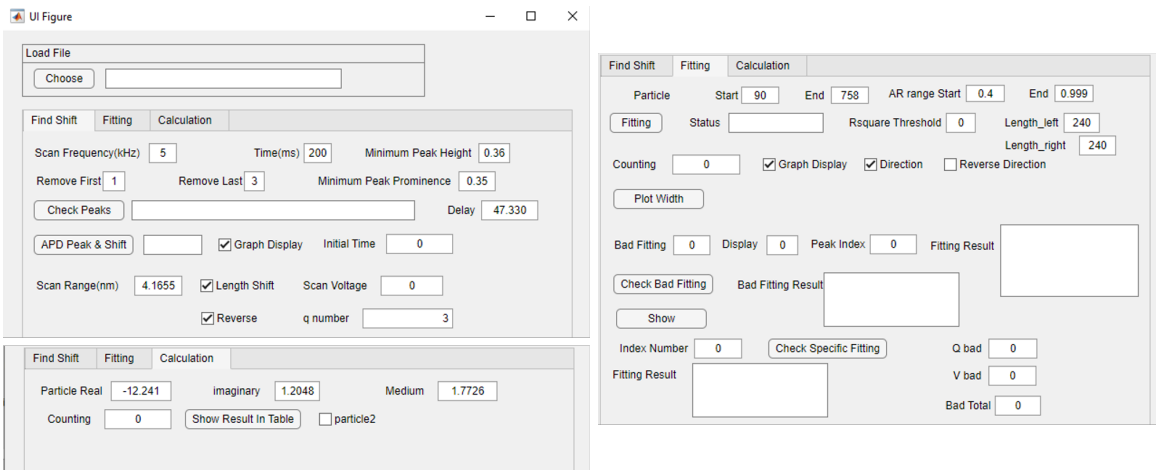


Figure 5.4: User interface snapshots.

For each complete sinusoidal cavity-length scan, there should be 4 peaks, within which reference peak and sensing peaks appear twice respectively. Therefore, the incomplete scan peaks need to be removed before further processing the data. In the experiment, the data record was triggered by APD voltage attenuation, so every data file had

a different starting point. The 'Delay' represents the response time delay between the function generator output and the actual short piezo stack scanning, which is usually similar between data files. The 'Initial time' is automatically detected by the software, which is the time difference between the data file start point and the first complete sinusoidal scan start point. With these parameters and the scan range determined, every data point on the time scale can be mapped into the relative cavity length domain, and then to the wavelength and frequency domain.

Firstly, by choosing the appropriate minimum peak height and prominence, both the reference and sensing beam peaks were detected in the 200 ms window. With the reference beam, the wavelength shift can be calculated [152] and plotted. At the same time, for each detected sensing beam peak, FWHM can be measured and plotted. These two measurements can both be used as evidence of a particle entering the cavity. For simplicity, I only showed the result of FWHM change in Chapter 5.4. Then by setting the start and end peak index numbers in a data file, fittings were only performed during a single-particle event. For each scan, only one peak was processed. After all the fittings, the results were exported to an Excel file for further analysis. The user interface also integrates functions of checking bad fittings and specific fittings for initial parameters adjustment and abnormality check. With many parameters to fit simultaneously, choosing appropriate starting points for different parameters is essential for good fittings.

As mentioned in Chapter 3.6.3, the zero-detuning point considers the impact of a spherical gold nanosphere having the same volume as the gold nanorod, so it is different on a particle-by-particle case. Starting from fitting a single peak manually to gain an understanding and checking bad fittings, the data processing is developed to handle all the situations automatically. For S_0 fitting, a double Lorentzian fitting on

the time scale was first performed to obtain a rough zero-detuning point, with fine tuning to a more accurate one. After the determination of an accurate zero-detuning point, the time period during a peak can be converted to the frequency detuning. Then S_1 and S_3 can be fitted with the corresponding equations. For S_1 fitting, the starting point for ψ is adjusted from $\frac{\pi}{2}$ to $\frac{2\pi}{3}$ when reaching limits of 0 or 2π.

5.4 A Single-Particle Event

With the experimental apparatus introduced in Chapter 4.3, measurements of two different types of gold nanorods samples A and B with nominal slightly different aspect ratios were performed. When a particle enters the microcavity, it generates three changes to the system. Firstly, the polarisability of the particle relative to the water medium causes a spectral shift in the resonance. The modulation of the cavity length ensured that the cavity mode was repeatedly swept through resonance. The cavity length was modulated at a frequency of 5 kHz with the short piezo stack, connected to the function generator which generated a sinusoidal wave of 0.2 V. Secondly, the particle introduced extra loss to the system, including absorption and scattering. Thirdly, the polarisability of the gold nanorod is highly anisotropic, it splits the cavity resonance mode into two eigenstates parallel to the principal axes of the rod projected onto the cavity plane (X and Y in Figure 5.6(a)). These two orthogonal linearly polarised eigenstates induce different phase shifts at the laser wavelength caused by differences in polarisabilities along these two directions. Thus, the transmitted light obtains a degree of linear polarisation which is a function of detuning and non-zero S_1 signals appear.

The concentration of the solution was chosen to be situable to ensure single particle detection as explained in the sample preparation Chapter 4.6. There were long

enough intervals (longer than the duration of a particle event) between events so that it was clear that a particle entered the cavity and left. Under this circumstance, the probability that two particles pass through the microcavity simultaneously was very low. The data files were not processed when there were no clear intervals. With the original concentration of the particles in the solution, for example, it could be possible that one particle had not left the cavity while the next one entered. When this single-particle event condition was not met, the data obtained was not valid to be processed further.

5.4.1 Gold Nanosphere Measurement

According to the theory, spherical particles have no anisotropy in polarisability and shape, so they should not change the polarisation state of the circularly polarised light. To demonstrate that non-zero S_1 signals are introduced by the particle's anisotropy, gold nanospheres with a 60 nm diameter were measured for a comparison, illustrated in Figure 5.5.

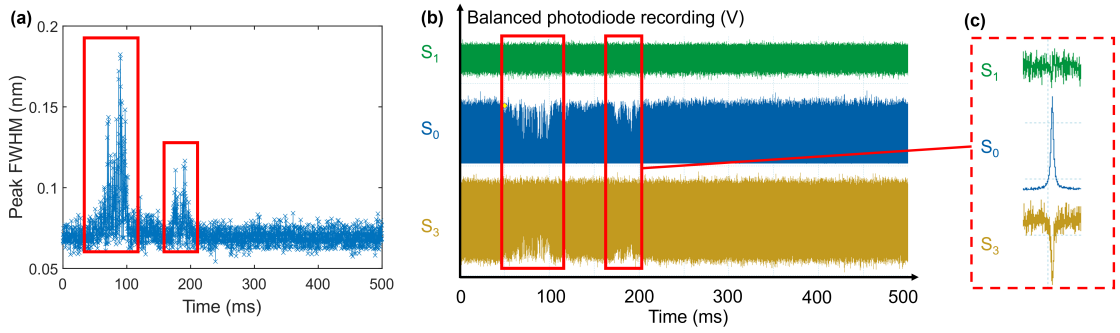


Figure 5.5: Summary of a single-particle event for gold nanospheres over 500 ms. (a) Transmitted peak FWHM. Two red rectangular areas labelled indicate two single-particle events. (b) Raw data of measured Stokes parameters. It is a collection of single sweeps. Green, blue and yellow data represent S_1, S_0 and S_3 signals respectively. Two red rectangular areas labelled are the corresponding single-particle events in (a). (c) Zooming into one single sweep during the single-particle event.

From the FWHM of S_0 signals in the 500 ms window, increases in photon loss are

clearly visible, indicating the presence of a particle. Two red rectangular areas in Figure 5.5(a) represent two single-particle events. The corresponding S_0, S_1 and S_3 traces in the same 500 ms time window are shown in Figure 5.5(b), revealing that the S_0 and S_3 peaks both attenuate as a result of this increased loss while no signal is seen in the S_1 trace. Zooming into individual sweeps (Figure 5.5(c)) confirms this result. Upon evaluating the rough edges shown in SEM images in Figure 5.3, the optical microcavity sensing method may not be so sensitive to the surface details.

5.4.2 Gold Nanorod Measurement

After the comparison with spherical particles, gold nanorod data was analysed in detail.

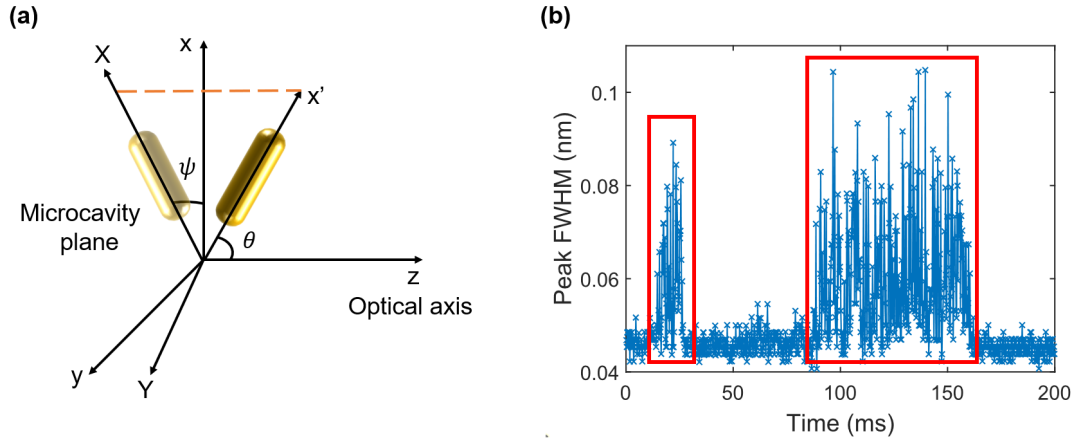


Figure 5.6: (a) Schematic of the coordinate systems used. θ is the polar angle while ψ is the azimuthal angle. (b) FWHM of the S_0 peak measured using the APD in a 200 ms window, showing two discrete single-particle events due to loss-induced broadening.

The increase in intra-cavity losses broadens the resonant mode peak such that the peak width provides a convenient signature of the presence of a particle. Figure 5.6(b) shows the time evolution of FWHM in an example data set of 200 ms. The two red rectangle areas present two discrete single-particle events. With the single-particle event sign, the transmitted light was recorded as a function of time and then

converted to a function of frequency detuning $\triangle$ between the resonance with just the probe laser light and in the presence of a particle (Chapter 3.6.3). Each event provides multiple measurements of $S_0(\triangle)$ and $S_1(\triangle)$, with both spectra changing as the particle diffuses in the cavity mode. As introduced in Chapter 3.6.3, $S_0(\triangle)$ and $S_1(\triangle)$ can be expressed as:

$$S_0(\triangle) = \frac{\omega_i^2}{(\triangle+\varepsilon)^2+(\gamma+\eta)^2} + \frac{\omega_i^2}{(\triangle-\varepsilon)^2+(\gamma-\eta)^2} \tag{5.1a}$$

$$S_1(\triangle) = 4\omega_i^2 \frac{\gamma(\varepsilon sin2\psi - \eta cos2\psi) - \triangle(\eta sin2\psi + \varepsilon cos2\psi)}{(\triangle^2-\varepsilon^2+\gamma^2-\eta^2)^2+4(\triangle\eta-\varepsilon\gamma)^2} \tag{5.1b}$$

where ω_i is the frequency of the incident field and γ is the total photon loss rate from the cavity in the presence of a spherical particle. 2ε and 2η represent the particle anisotropy and are the differences in the resonant frequency and in the loss between the two orthogonal eigenstates. ψ is the azimuthal angle of the nanorod about the optical axis of the cavity as referred to the instrument axes (Figure 5.6(a)). Here S_1 provides the most sensitive measurement of ε and η since its amplitude is proportional to these parameters, but the dependence on ψ complicates data analysis. Alternatively, with sufficient anisotropy that the mode splitting is comparable in magnitude to the mode width, ε and η can be established from S_0 alone. With these two equations, a double Lorentzian fitting for S_0 was performed first to obtain ε and η, followed by the fittings of S_1 signals to acquire the azimuthal angle ψ.

Figure 5.7 illustrate examples of individual fittings of $S_0(\triangle)$ and $S_1(\triangle)$ signals during the second single-particle event in Figure 5.6(b). Equation 5.1 (a) and (b) were utilised for fittings. ε, γ, η and ψ are the fitting parameters in these two equations. The splittings of S_0 peaks were different in different sweeps. The shapes of S_1 peaks included positive and negative Lorentzians and different s-shapes. All differences can be explained by the various positions and orientations of the gold nanorod in the

microcavity. As the nanorod undergoes rotational diffusion, changes in polar angle θ translate to changes in the magnitude of the splitting of the S_0 peak and the amplitude of the S_1 response, while changes in ψ translate to changes only in the shape of the S_1 response.

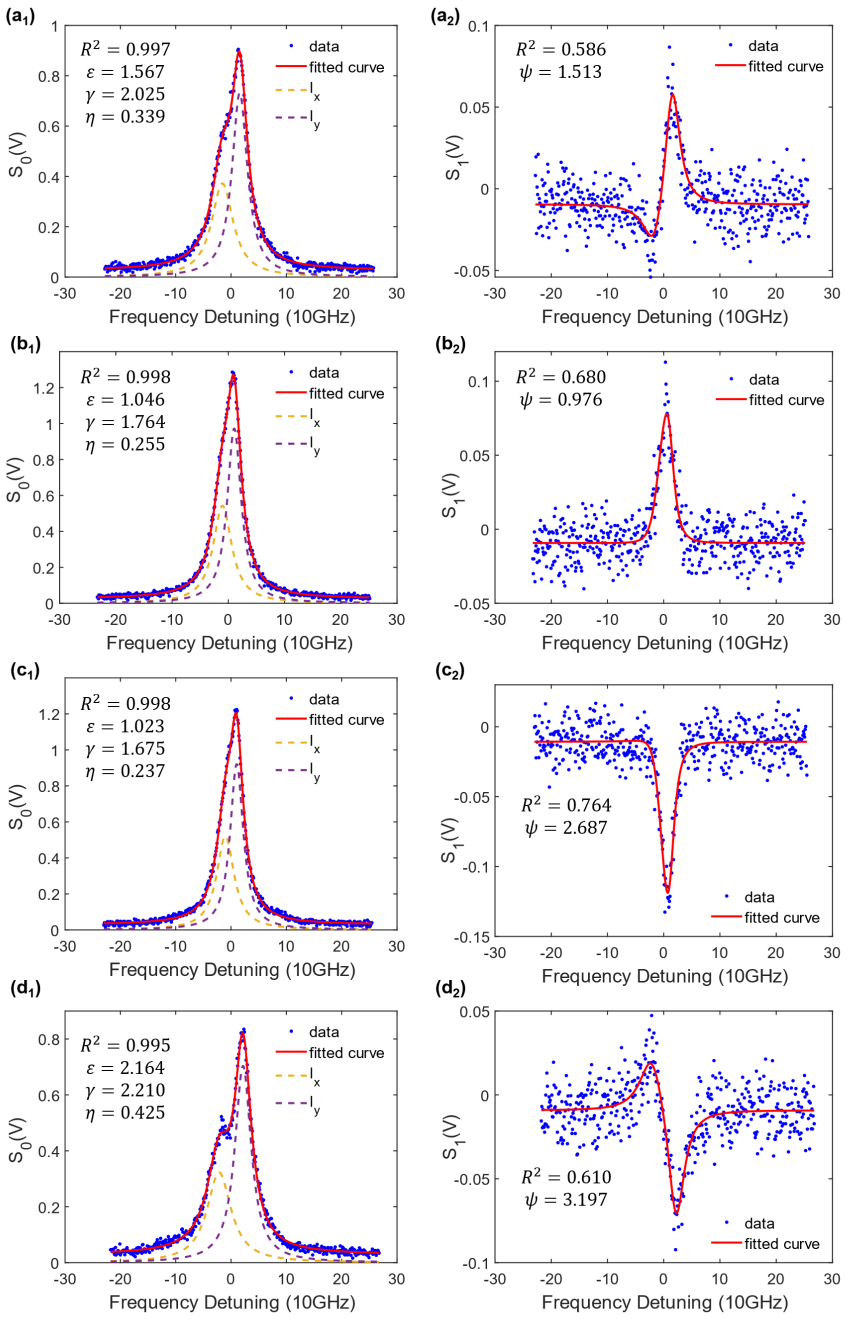


Figure 5.7: (a)-(d) Examples of individual S_0 and S_1 peaks as a function of frequency detuning during the second event. Blue dots are raw data and red curves are fitted curves using equations 5.1a and 5.1b.

After fitting individual peaks, the summary of a single-particle event could be obtained, including the summary of fitting parameters ε, η and ψ for every scan in the

single-particle event. ε and η are polarisability-related parameters, containing the shape anisotropy information that could be extracted from the anisotropy loss tangent $\Phi = \frac{\eta}{\varepsilon}$ defined in Chapter 3.6.3. The histograms of ψ and Φ in a single-particle event from each of samples A and B are shown in Figure 5.8.

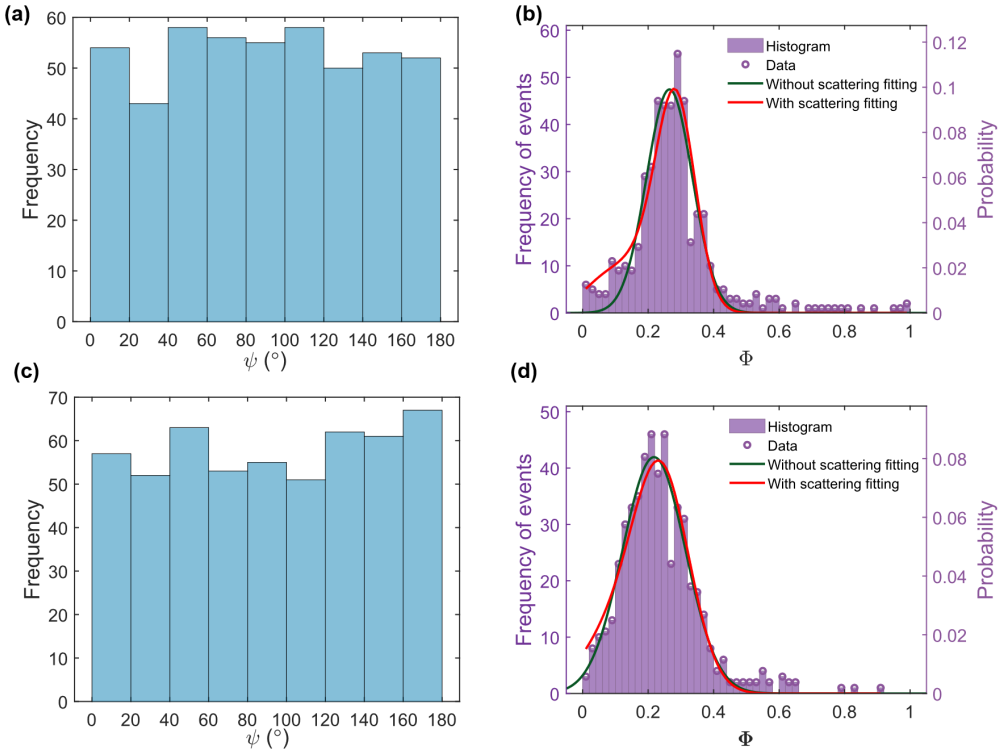


Figure 5.8: (a)-(b) Histograms of ψ and Φ of a single-particle event for sample A. (c)-(d) Histograms of ψ and Φ of a single-particle event for sample B. Green and red curves are fitting curves using two models introduced in Chapter 3.6.3.1.

For each single-particle event, there were data points out of the range of $0 \sim 1$ shown in Figure 5.8. However, the points were scarce (about 6%) in the distribution and will not impact the final fitting result. These outliers can be explained by the failure to resolve double Lorentzians. When the projected particle did not show much anisotropy in the instrumental xy plane (for example, when the particle is perpendicular to the xy plane), S_0 signals would resemble more of a single Lorentzian and the extracted parameters are not accurate enough. The histograms of ψ in Figure 5.8

include all the data points after the removal of these data points. In each case, the ψ distribution is flat indicating no preferred orientation of the particle in the lab frame. The Φ distributions in each case show a clear single peak in the range $0.2 < \Phi < 0.3$.

As introduced in Chapter 3.6.3.1, assuming the particle is small and scattering can be neglected, the anisotropy loss tangent is only dependent on the particle intrinsic property, and the aspect ratio can be extracted directly from the anisotropy loss tangent. As equation 3.43 ($\Phi = \frac{Im(\alpha_L - \alpha_W)}{Re(\alpha_L - \alpha_W)}$) shows, the anisotropy loss tangent is only dependent on the aspect ratio of the particle, so under ideal circumstances, it is a single value. However, the measurement would introduce extra noises into the final result, so instead of a single value, a distribution of the anisotropy loss tangent was obtained from the experimental results. Thus a Gaussian instrumental response was applied to fit the histograms of the anisotropy loss tangent Φ and obtain the standard error for this fitting. Then the the standard error of μ could be deduced from Φ with the error propagation equation $SE(\Phi) = \frac{\partial \Phi}{\partial \mu} SE(\mu)$. Figure 5.8 provides the fitting results of $\Phi = 0.27 \pm 0.01$ and $\Phi = 0.22 \pm 0.01$ for the sample A and B particle respectively. With the equation 3.43 and the relationship illustrated in 3.9, $\mu = 2.00 \pm 0.02$ and $\mu = 1.87 \pm 0.02$ are obtained. The magnitudes of the standard errors in μ suggest a basic measurement resolution of around 1%.

If the scattering is not negligible, the probability distribution of Φ with the equation 3.51 and 3.50 derived in Chapter 3.6.3.1 is employed to extract the aspect ratio:

$$p(\Phi) = \frac{Re(\alpha_L - \alpha_W)}{2A\beta(\vec{r})[\alpha_L^2 + \alpha_W^2 - 2Re(\alpha_L)Re(\alpha_W) - 2Im(\alpha_L)Im(\alpha_W)]\sqrt{B(\Phi)}} \tag{5.2a}$$

$$\sqrt{B(\Phi)} = \sqrt{\frac{\Phi Re(\alpha_L - \alpha_W) - Im(\alpha_L - \alpha_W) - A\beta(\vec{r})(\alpha_L^2 - \alpha_W^2)}{A\beta(\vec{r})[2Re(\alpha_L)Re(\alpha_W) + 2Im(\alpha_L)Im(\alpha_W) - \alpha_L^2 - \alpha_W^2]}} \tag{5.2b}$$

As $B(\Phi)$ must be bigger than 0, the probability distribution of the anisotropy loss tangent Φ, under ideal circumstances, would have a cutoff point. The fitting result of Figure 5.8 (b) is shown below in Figure 5.9.

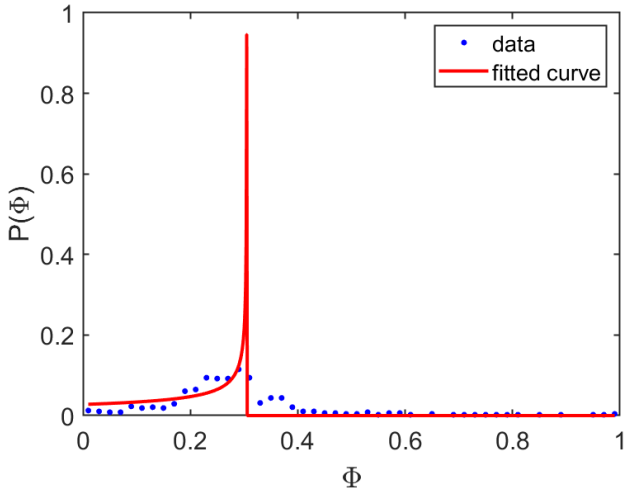


Figure 5.9: Direct fitting with equation 5.2 of Figure 5.8 (b).

Therefore a Gaussian instrumental response was considered to explain the broadening of the distribution and the smoothing near the cutoff point. The probability distribution of the anisotropy loss tangent Φ was convoluted with the Gaussian instrumental response to perform the fitting. The standard deviation of the Gaussian instrumental response was treated as a fitting parameter. Among different measurements, this instrumental response remains stable. The standard error of μ was obtained with the percentile range of 0.68 in the bootstrap method. It yields the results of $\mu = 1.66 \pm 0.05$ and $\mu = 1.69 \pm 0.04$ for samples A and B respectively. The degree of scattering depends on the particle volume which, in this work, is estimated from SEM data. It also depends on the optical density of states in the microcavity, which is lower than that of free space and is a function of position within the cavity mode [152]. A detailed analysis of scattering is beyond the scope of this work. The red curves in Figure 5.8(b) and Figure 5.8(d) assume the same density of states as in free space.

5.5 Statistical Results for 30 Particles

With the data analysis of a single-particle event introduced above, statistical analysis can be performed with more particles. For all the data files collected, the data where gold nanorods stayed in the cavity for shorter than 30 ms was not processed. If the particle leaves the cavity too quickly, it is possible that the collected data does not include all the possible rotational states and the data is biased. All the single-particle events below display clear S_1 signals without further data selection.

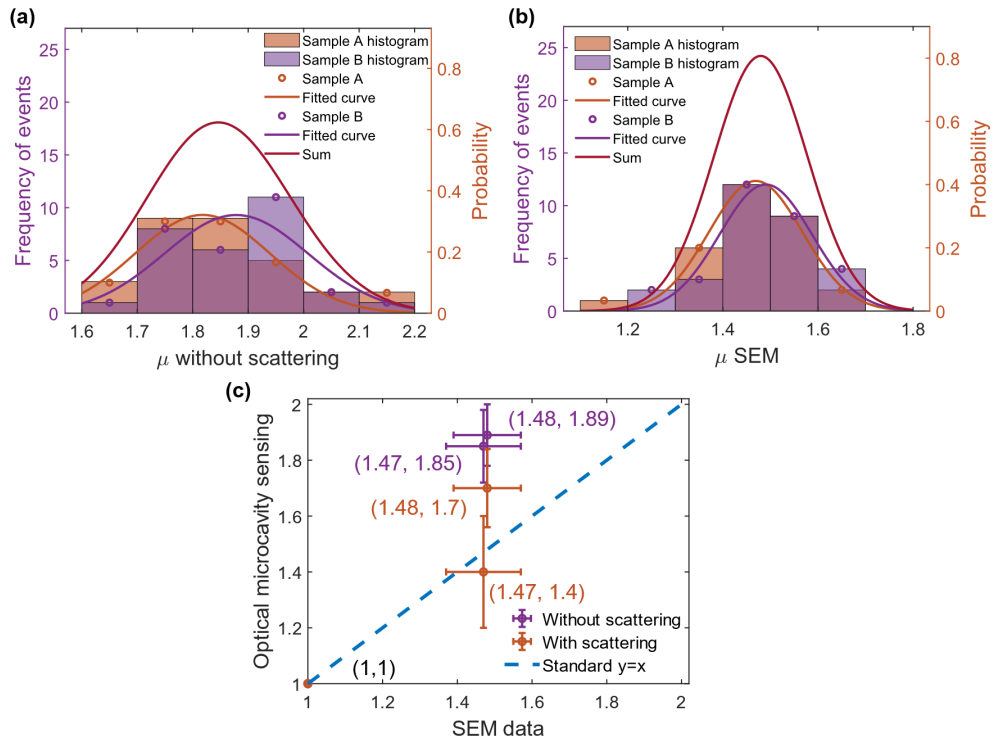


Figure 5.10: Summary of statical results of 30 particles. (a) Aspect ratio μ distributions for 30 particles of samples A and B respectively using the optical microcavity sensing method without considering scattering. (b) Distributions of μ of 30 particles of samples A and B using SEM imaging. (c) Comparison between optical microcavity sensing method and SEM imaging.

Figure 5.10(a) shows the measured aspect ratios of 30 particles in samples A and B neglecting scattering effects. The mean values and standard deviations are $\mu = 1.85 \pm 0.13$ and $\mu = 1.89 \pm 0.11$ for samples A and B respectively. SEM images of

nanoparticles from the two samples were used to provide an independent measure of μ, with the histograms illustrated in Figure 5.10(b). Although the mean values produced by the two methods differ, the distributions are similar with samples A and B overlapping with both methods. If scattering is included in the analysis using the averaged volume calculated from the SEM images, the aspect ratios of the 30 particles for samples A and B become $\mu = 1.4 \pm 0.2$ and $\mu = 1.7 \pm 0.14$. The nanorods in sample A are larger than those in sample B, which induces a more pronounced effect of scattering in reducing the calculated values of μ. When the scattering is included, the anisotropy loss tangent is related to the position of a particle due to the difference in the optical density of states in the cavity compared with the free space [152]. If the scattering is reduced to 0.65 times that of the free space [152], the calculated aspect ratios become $\mu = 1.59 \pm 0.16$ and $\mu = 1.82 \pm 0.12$ respectively.

Method	μ of sample A	μ of sample B
SEM assuming rods lay flat	1.47 ± 0.1	1.48 ± 0.09
SEM assuming random orientation	1.56 ± 0.17	1.57 ± 0.16
Optical microcavity sensing (without scattering)	1.85 ± 0.13	1.89 ± 0.11
Optical microcavity sensing (with scattering[1])	1.4 ± 0.2	1.7 ± 0.14
Optical microcavity sensing (with scattering[2])	1.59 ± 0.16	1.82 ± 0.12

Table 5.1: The summary of aspect ratio μ results with different methods.
[1] $\beta(\vec{r}) = 1$; [2] $\beta(\vec{r}) = 0.65$.

Table 5.1 displays the summary of the aspect ratios of samples A and B, each having 30 particles. SEM assuming rods lay flat is the values directly measured from SEM images using ImageJ introduced in Chapter 5.2.3. However, as mentioned before, some particles seem more spherical, which may be caused by the orientation of particles in the image plane. Therefore, a random orientation was also assumed to acquire a corrected result for samples A and B, which will be detailed in Chapter 5.6.4. Optical microcavity sensing results without considering scattering are demonstrated as well as considering scattering in free space and with a reduced optical density of states. One point to note is that the SEM and optical microcavity sensing data measured

different sets of nanoparticles from the two samples. While there is no obvious reason for selective bias in these measurements, it cannot be discounted entirely. Potential sources of systematic error include the calibration of the frequency axis, which could be minimised by in-situ calibration or direct monitoring of the cavity modulation, and approximations made within the theoretical model, in particular where the effects of scattering are considered. It may require more future efforts to study those in detail and provide insights into the improvements.

5.6 Other Factors to Consider

It is necessary to consider other factors that may impact the accuracy of the results. The rotational diffusion over a sweep period is considered. The heat generated on the surface of the particles is also calculated to determine whether that would change the aspect ratio of the particle. When extracting the aspect ratio in the final data processing step, two models considering scattering and without are utilised, and it is worth checking how valid it is. In addition, assuming random orientations of particles on the image plane for SEM is discussed. At last, data with anisotropy introduced from the optical microcavity is described and analysed.

5.6.1 Rotational Diffusion

In the analysis, it is assumed that every sweep takes a 'snapshot' of the particle. It is worth calculating the theoretical angular change during a sweep. With gold nanorods in the range of $\mu < 2$, it is calculated with Perrin theory (equation 3.54a and 3.54b) and compared with TG theory (equation 3.54c) introduced in Chapter 3.7.1. With the rotational diffusion coefficient, the averaged angular displacement over 1 µs is calculated using $< \theta^2 >= 2D_r t$. 1 µs was chosen as it was the averaged FWHM of the resonant peak of a single sweep measurement, which was only a small portion of

the period of 0.2 ms with the sweeping frequency of 5 kHz. The characteristic angular diffusion time $\tau = \frac{\pi^2}{8D_r}$ is also calculated and the peak FWHM is much smaller than the characteristic time. The summary is shown in Table 5.2.

	Perrin (3.54a)	Perrin (3.54b)	TG theory
sample A	2.74×10^4 (13.41°)	2.35×10^4 (12.42°)	1.45×10^4 (9.76°)
characteristic time	45 µs	53 µs	85 µs
sample B	4.43×10^4 (17.03°)	3.85×10^4 (15.9°)	2.35×10^4 (12.42°)
characteristic time	28 µs	32 µs	52 µs

Table 5.2: Summary of rotational diffusion coefficients using different models. Sample A: diameter 32 nm, length 48 nm. Sample B: diameter 28 nm, length 40 nm. The values in brackets () are the averaged angular displacement over 1 µs.

In this calculation, the size information from the SEM images was utilised. Apart from the Brownian rotational diffusion, the particle also experiences the optical torque. The angular displacement over 1 µs was calculated using $\theta = \frac{MtD_r}{k_B T}$ with the maximum optical torque introduced in Chapter 3.7.2 and the diffusion coefficient calculated from equation 3.54b. The intra-cavity power P is 17.2 mW. The RoC of the cavity R is 25 µm and the cavity length L_{cav} is 1.5 µm. Angular displacements of 0.12° and 0.19° were found for samples A and B respectively, small enough to be neglected. With this calculation, the dominance of free Brownian motion is also observed.

5.6.2 Cross-section Calculation

The loss mechanism of gold nanorods in the microcavity involves scattering and absorption, the cross-sections of which have been presented in Chapter 3.7.4. Inserting the size information of samples A and B from SEM images, absorption was calculated to be 75% of the overall extinction for sample A and 83% for sample B.

5.6.3 Heat Calculation

From the APD voltage of the transmitted light from the empty cavity, the intra-cavity light intensity was calculated. The calculated temperature increases for samples A and B were 11 K and 7 K respectively with equations displayed in Chapter 3.7.5. These temperature changes are too small to induce any shape change in the nanoparticles.

5.6.4 SEM Images Further Analysis

Assuming a random distribution of the orientation of gold nanorods, the true aspect ratio can be calculated with the distribution of measured SEM results:

$$\mu = \frac{\mu_{measured} - 1}{\sin\theta} + 1 \tag{5.3}$$

where θ is the same as in equation 3.42. For each calculation, $\mu_{measured}$ was randomly selected from the Gaussian distribution of measured SEM results from 30 particles in Chapter 5.2.3 and θ was randomly selected from $0 \sim \frac{\pi}{2}$. The calculation was performed 100,000 times to improve the accuracy of the final result, shown in Figure 5.11. After generating the corrected μ, a Gaussian fitting was utilised to obtain the new centred value with the standard deviation of 1.56 ± 0.17 and 1.57 ± 0.16 for samples A and B, shown before in Table 5.1.

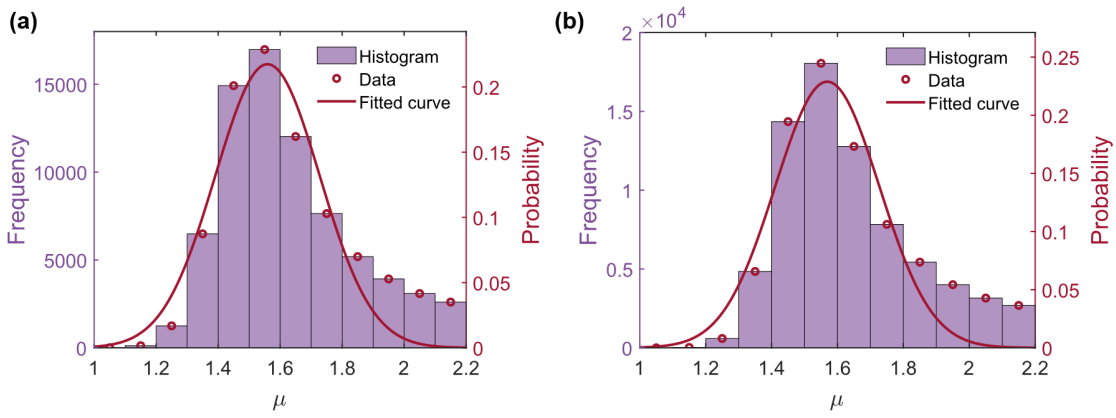


Figure 5.11: Summary of μ histograms for the further analysis of SEM images assuming a random orientation of particles using equation 5.3. θ was randomly selected from $0 \sim \frac{\pi}{2}$. $\mu_{measured}$ was randomly selected from the Gaussian distribution of measured SEM results from 30 particles in Chapter 5.2.3. It was performed 100,000 times to improve the accuracy of the final result. (a) Sample A. (b) Sample B. Purple data shows the histograms of μ while the red curve shows the fitted curve of a Gaussian distribution.

5.6.5 Minimum Aspect Ratio Analysis

The particles measured here, with aspect ratios of around 1.5, give SNRs of approximately 7:1 in the S_1 traces shown in Figure 5.7. In the limit where $\varepsilon, \eta \ll \gamma$, and selecting $\triangle = 0$, equation 5.1a reduces to:

$$S_1(\triangle) = \frac{4\omega_i^2(\varepsilon \sin 2\psi - \eta \cos 2\psi)}{\gamma^3} \tag{5.4}$$

which is linearly dependent on $\triangle\alpha$ and, in turn, on $\mu - 1$. The aspect ratio that would give SNR = 1 is therefore approximately $\mu = 1.07$.

5.6.6 Prefered Direction

In the experiment, a strange behaviour of gold nanorods was observed in some data sets, illustrated in Figure 5.12. (a) shows the FWHM over 200 ms and (b) illustrates the raw data set. Two single-particle events were observed in this data set, labelled

with red solid rectangles.

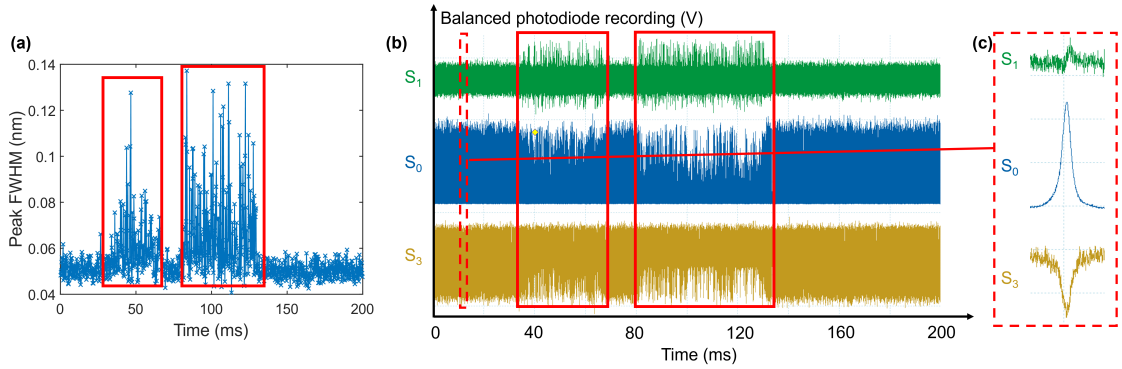


Figure 5.12: An example of a data set over 200 ms. (a) Peak FWHM over time. (b) Raw data of three Stokes parameters measured in the experiment. Green, blue and yellow data represent S_1, S_0 and S_3 signals. Two solid red rectangular areas are labelled as two single-particle events. The dashed red rectangle is the empty cavity state. (c) Zooming into a sweep of empty cavity situation.

However, with the same data processing procedures mentioned before, both particles displayed preferred orientations in Figure 5.13(a) and (b). If zooming into empty cavity sweeps with one example shown in Figure 5.12(c), it displays a non-zero S_1 signal, which means that the cavity has already introduced anisotropy to the system before the particle entered. Therefore, it indicates that an anisotropic cavity impacts the measurement of the anisotropy of the particle and shows a preferred orientation in the rotational diffusion of a particle with the same data processing procedures.

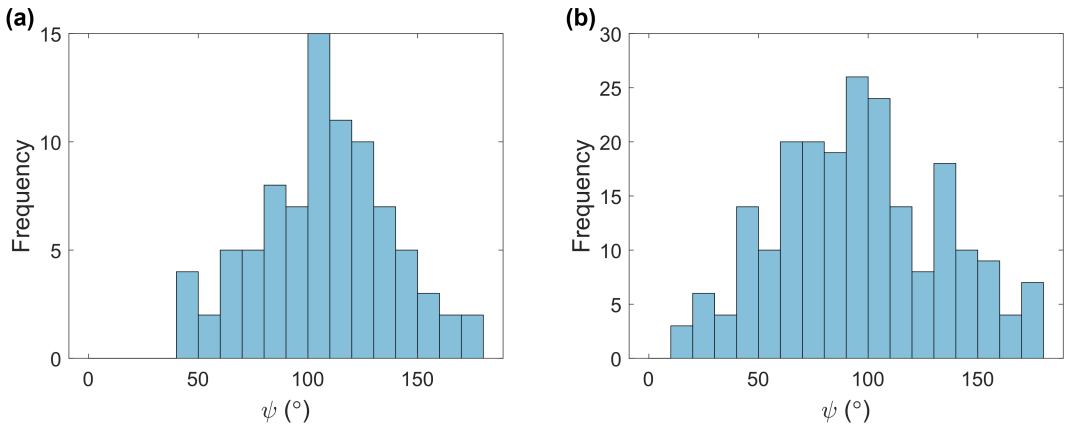


Figure 5.13: (a), (b) Histograms of azimuthal angles ψ in the microcavity plane in the two single-particle events mentioned above respectively.

5.7 Summary

This chapter discusses the results of experiments and related theoretical calculations of gold nanorods and the comparison sample of gold nanospheres. Firstly, the samples were measured using three common benchmark characterisation methods. DLS and UV-Vis spectrometers deal with solution samples directly and do not require advanced skills. However, they could not directly provide shape information on a single-particle scale. SEM provides single-particle analysis through direct imaging. Sample preparation procedures were explored to accomplish the imaging. However, the instrument is quite expensive and it requires advanced training. It cannot deal with liquids directly, limiting its applications in real-time monitoring. In addition, the accuracy of results is also impacted by the angles of particles on the image plane.

Secondly, the user interface for data processing is introduced. A detailed analysis of a single-particle event of a gold nanorod is presented with the theoretical model introduced in Chapter 3.6 after the comparison with gold nanosphere samples. The aspect ratio of a single particle is extracted for samples A and B and the statistical

results of 30 particles for each sample are studied.

Lastly, results of related theoretical calculations introduced in Chapter 3.7 are elucidated, including the rotational diffusion, the comparison between absorption and scattering cross-sections and heat generated on the surface of the gold nanorod. SEM images are analysed again with the assumption of random orientations on the image plane. Measurements of a single particle displaying preferred orientation are also shown and analysed and it turns out to be the impact of the state of the empty cavity.

Chapter 6

Rod-shaped Bacteria Particle Measurement

6.1 Introduction

Water quality is an important issue that has gathered public attention and has critical implications for our society. Nowadays, water quality detection usually takes a water sample and sends it to the microorganism or biology lab for further tests. Although it provides high accuracy, it requires professional staff and cannot provide on-site and real-time monitoring. Many common bacteria in water are rod-shaped, such as Legionella and E.coli bacteria. Detecting these bacteria in water helps avoid possible disease infection and spread. The transparency of particles and weak interaction with light pose difficulties in the characterisation. The shape measurement provides an early warning of the potential problem and further analysis can be conducted.

In this work, the same experimental apparatus was utilised to measure rod-shaped bacteria particles. Firstly, SEM images are shown and discussed. Experimental conditions are introduced, especially changes compared with the gold nanorod measure-

ments. Then the data collected using two scanning speeds are analysed. Additionally, the results of theoretical calculations are discussed to evaluate the impacts of other factors. Lastly, limitations of the current experimental configurations are assessed and possible improvements are put forward accordingly.

6.2 SEM Imaging

0.018 g Lactobacillus Casei bacteria powder was weighed and dissolved into 360 µL deionised water, followed by mixing with a vortex mixer at 2000 rpm speed for 1 minute. It was then diluted again with 10 µL of the solution and 490 µL deionised water. Thus the double-diluted solution has a concentration of 2.07×10^8 CFU/mL. Heating with a heat plate at 48°C helps the evaporation of the water on the 400 mesh copper TEM grid (AGG2400C, Agar Scientific Ltd.). Then it was coated with a 4 nm platinum coating. SEM images of rod-shaped bacteria particles are presented in Figure 6.1. They were all taken with EHT of 2 kV and a working distance of 4.1 mm with the in-lens detector. Figure 6.1(a) and (b) were imaged with the probe current of 159 pA while it was 70 pA for (c). The column mode was high resolution and the noise reduction mode was pixel-averaged.

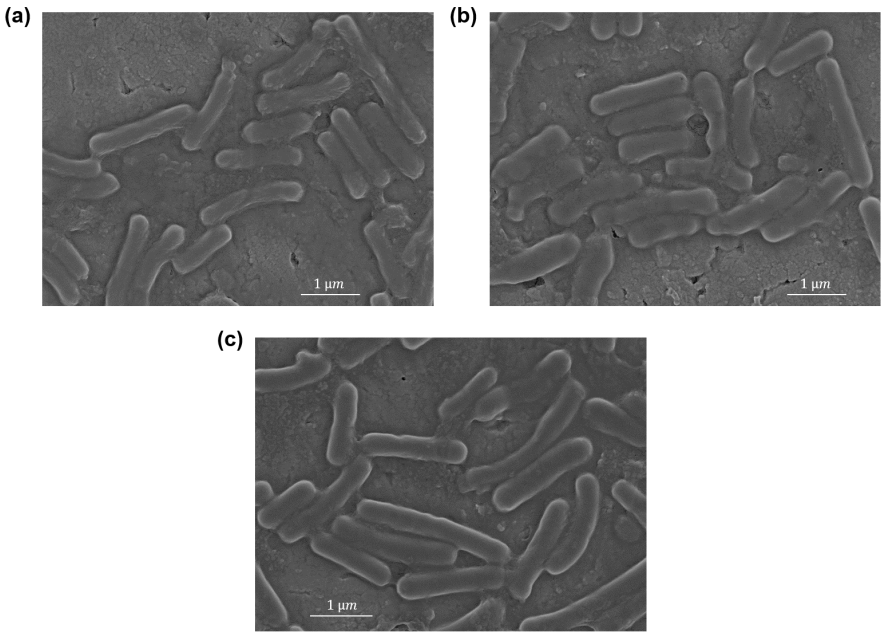


Figure 6.1: SEM images (Merlin FEG-SEM, Zeiss) of rod-shaped bacteria particles with scale bars of 1 µm labelled. (a) is imaged with the probe current of 159 pA, EHT of 2 kV and a working distance of 4.1 mm. (b) is imaged with the probe current of 159 pA, EHT of 2 kV and a working distance of 4.1 mm. (c) is imaged with the probe current of 70 pA, EHT of 2 kV and a working distance of 4.1 mm. The column mode is high resolution and the noise reduction mode is pixel-averaged.

As the images show, the samples have a wider distribution in both the size and the aspect ratio than gold nanorods. They are not straight rods. The hairy features around the edges of the particles could be observed in Figure 6.1(a) due to the electron damage to the sample. ImageJ was used to measure 27 particles in these SEM images, which provided an averaged length with the standard deviation of 1.55± 0.34 µm and a width of 0.36± 0.04 µm while the aspect ratio was 4.29 ± 1. The average size and aspect ratio of the bacteria particle is approximately 3.6×10^4 times and 2.94 times respectively as a gold nanorod.

6.3 Experimental Conditions

Firstly, the same mirrors as in the gold nanorod measurements were employed: the concave mirror of 99.99% reflectivity and the planar one of 99.92% reflectivity. When the particle diffused through the cavity, the transmitted light intensity decreased dramatically with the markedly stronger scattering of rod-shaped bacteria particles than gold nanorods. Although they do not absorb light in the same way as gold nanorods, the scattered light scales with V^2 (particle volume). Therefore, cavities with a lower finesse are required and the planar mirror was changed to 99.6% reflectivity. The cavity length was around 5 µm.

Choosing an appropriate incident light intensity is also not trivial for this experiment. When the incident light intensity is too high, the particle gets trapped more quickly and the transmitted light intensity attenuates more quickly. At the same time, however, a high enough incident light intensity is required to capture S_1 signals due to the weaker mapping of shape anisotropy to polarisability anisotropy for dielectric materials than metal materials. After some trials, 30% power, 45 mW, was decided for the incident light intensity. A neutral density filter of OD=0.3 was added before the APD to avoid saturation.

6.4 Analysis

The data processing of the rod-shaped bacteria particles is introduced, followed by the data analysis of two different scanning speeds of the cavity-length sweeping. The data in these two cases show different behaviours of rod-shaped bacteria particles within the collected time frame.

6.4.1 Anisotropy Loss Tangent Histogram Fitting

The data processing of rod-shaped bacteria particles is similar to the gold nanorod data. Some experimental settings, such as the sampling rate and time need to be changed in the user interface setting, but fitting S_0 and S_1 signals is performed using the same method. The major difference is the final step of fitting the anisotropy loss tangent histogram to deduce the aspect ratio of the particle, which has been introduced in Chapter 3.6.3.2. Convoluting the probability distribution in equation 3.53 with a Gaussian instrumental response gives the final fitting model of the anisotropy loss tangent to derive the aspect ratio of a rod-shaped bacteria particle. In the fitting, the width of the Gaussian instrumental response, the aspect ratio and A are parameters to extract. A is related to the particle volume as well as the position of the particle in the optical mode.

6.4.2 4 kHz Scanning

Firstly, considering the bigger size of a single rod-shaped bacteria particle than a gold nanorod, the translational and rotational diffusion of the particle is slower. It is necessary to collect data over a longer period. On the one hand, if the sampling rate is maintained and only the collected period is increased, the data collection instrument PicoScope has an upper limit on the data points that can be collected. On the other hand, if the maximum collected data points are maintained and the collected time is increased, the sampling rate decreases. However, enough data points during a scan are required to perform the curve fitting. Therefore it is necessary to scan slower to increase the collected period. Additionally, it is essential to ensure that the scanning is not too slow to break the assumption that the particle is stationary during a sweep. A 4 kHz scanning frequency with a scanning voltage of 1.5 V was attempted first. Both the reference beam and the sensing beam were recorded. Lower frequencies were also tested. However, there were sweeps where the sensing peak overlapped with the

reference peak, creating artificial S_1 signals. The overlap is caused by a bigger shift which is proportional to the larger polarisability, as shown in equation 3.33, with a much bigger volume compared with gold nanorods. Figure 6.2 illustrates a raw data file when a particle was in the microcavity during a 200 ms period.

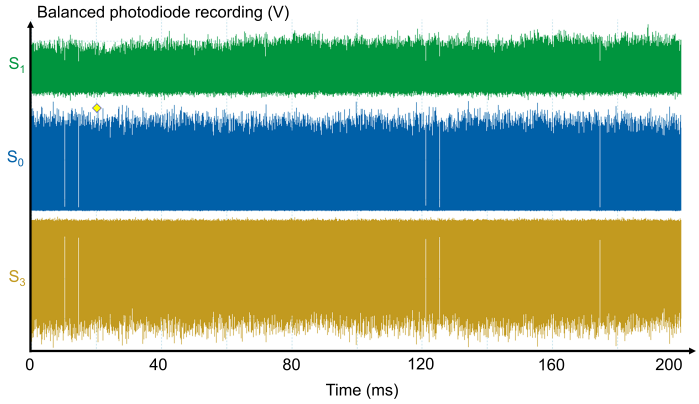


Figure 6.2: Raw data of a single rod-shaped bacteria particle in the microcavity during a 200 ms period. Green, blue and yellow curves are S_1, S_0 and S_3 signals collected from balanced photodiodes. It is a collection of resonance peaks in cavity-length sweeping. All three signals are quite stable with small fluctuations.

200 ms was too short to record a complete single-particle event where a rod-shaped bacteria particle entered the microcavity and left. Several data files were recorded sequentially before the particle left the cavity. The data file shown in Figure 6.2 was in this process, where a particle was in the microcavity and the data displayed strong S_1 signals. The data file was an aggregation of multiple cavity-length sweeps, and each sweep can be detailed when zooming in. From the trend in the raw data file in Figure 6.2, S_1 signals were stable with a small fluctuation, different from the gold nanorod measurement, an example of which is illustrated in Figure 6.3. Figure 6.3(a) is the raw data of 200 ms of gold nanorod sample A while (b_1) and (b_2) illustrate an example of consecutive sweeps where S_1 signals change from negative to positive. For gold nanorods, S_1 signals can be quite different even between consecutive sweeps. However, the more stable S_1 signals for bacteria particles shown in Figure 6.2 indicate a slower rotation of the rod-shaped bacteria particle than the gold nanorod.

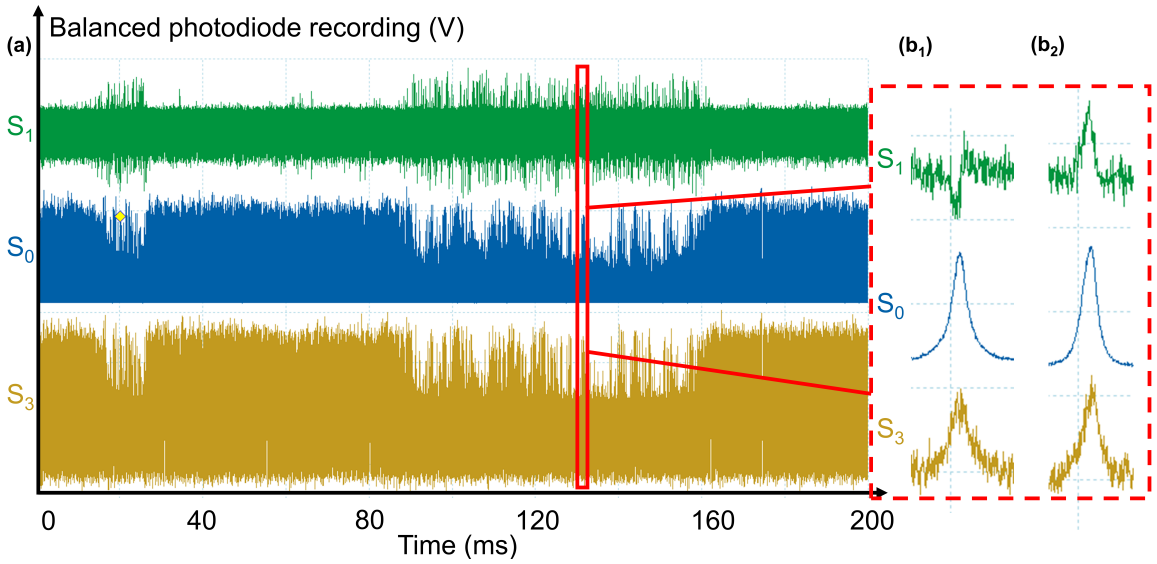


Figure 6.3: An example dataset of gold nanorod sample A for comparison. (a) Raw data of S_1, S_0 and S_3 signals over 200 ms. (b_1), (b_2) S_1, S_0 and S_3 signals of an example of consecutive sweeps, .

The same data processing procedure of fitting S_0 and S_1 signals was applied to obtain the histograms of the azimuthal angle ψ and the anisotropy loss tangent Φ. Figure 6.4 shows the distribution of ψ in this data set.

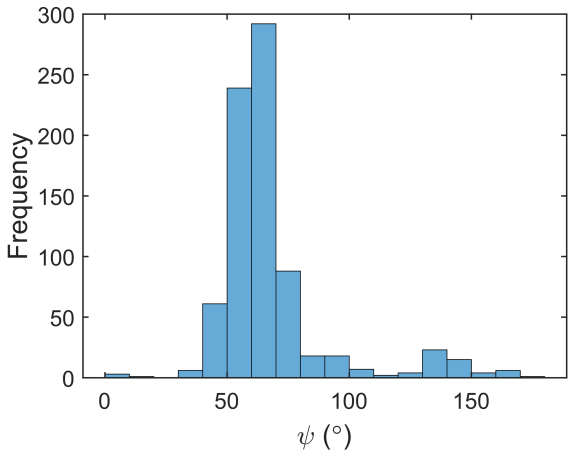


Figure 6.4: Distribution of the azimuthal angle ψ of a bacteria particle extracted from data in Figure 6.2 within 200 ms. It shows a dominance in the range of 50° to 70°.

This distribution manifested a preference in the angle, a dominance in the range of 50° to 70°. It could be explained by the high sweeping frequency so that between

adjacent sweeps, the particle did not have enough time to rotate much. In addition, since this is only part of the data during a single-particle event, it is biased due to not covering all the scenarios. Figure 6.5 illustrates two other examples with the same sweeping frequency but a longer collected period of 500 ms. (a) and (c) displays the raw data with S_0, S_1 and S_3 signals collected. Compared with Figure 6.2, S_1 signals were less stable and elucidated changes during the 500 ms period. (b) and (d) are the corresponding distributions of ψ. With equation 3.38, magnitudes of S_1 signals give indications of distributions of ψ. As expected, (a) and (c) displayed more values of ψ. With all S_1 signals positive in (a), ψ had a dominance in the range of 60° to 80° in (b). However, with a bigger fluctuation in the data set than Figure 6.2, other values of ψ also appeared. With S_1 signals first positive and then negative in (c), the distribution of ψ displayed bimodal distribution in the range of 80° to 100° and 150° to 170°.

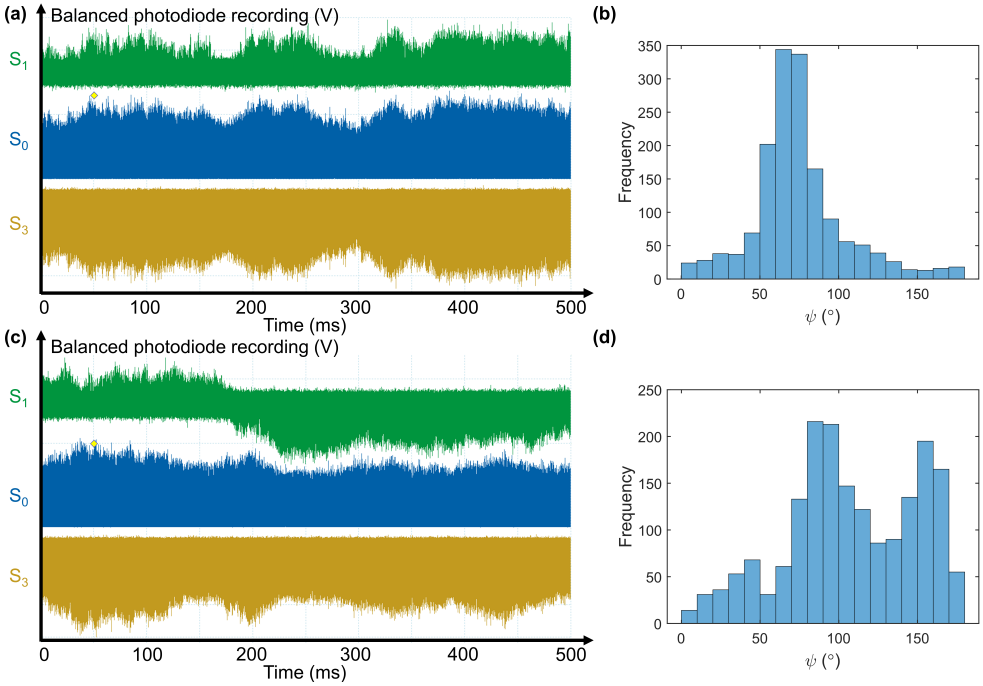


Figure 6.5: Two representative data files over 500 ms. (a), (c) Raw data file with recorded S_1, S_0 and S_3 signals. (b), (d) The corresponding azimuthal angle ψ distributions. (b) shows a dominance in the range of 60° to 80° while (d) displays bimodal distribution in the range of 80° to 100° and 150° to 170°.

The azimuthal angle ψ was plotted with time evolution for (c) in Figure 6.6. The angle range changed around 200 ms which was the point where S_1 signals changed from positive to negative values in Figure 6.5(c).

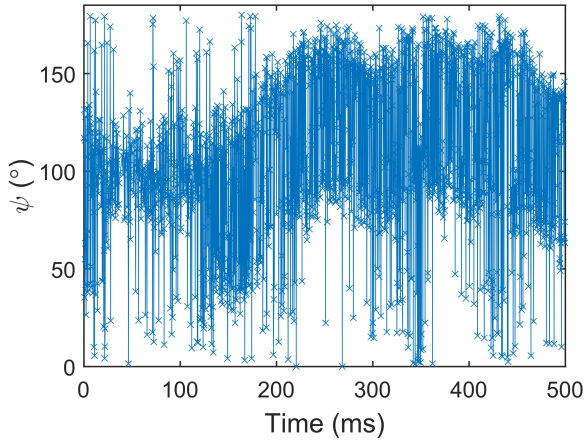


Figure 6.6: Azimuthal angle ψ change over time of data shown in Figure 6.5(c).

The three examples mentioned above correspond to different rod-shaped bacteria particles, whose diffusion speed may vary slightly with the big deviation between particles confirmed with SEM images in Figure 6.1.

6.4.3 10 Hz Scanning

To capture a data set with longer collected time to have a full picture of the single-particle event, the reference beam was blocked to avoid overlapping with the sensing beam when the particle was in the microcavity. The presence of the particle can be confirmed with attenuating APD signals and broadened resonance peak widths. The scanning frequency decreased to 10 Hz with a scanning voltage of 2.5 V and the collected time was 495 s. Figure 6.7 showed one example of the collected data set.

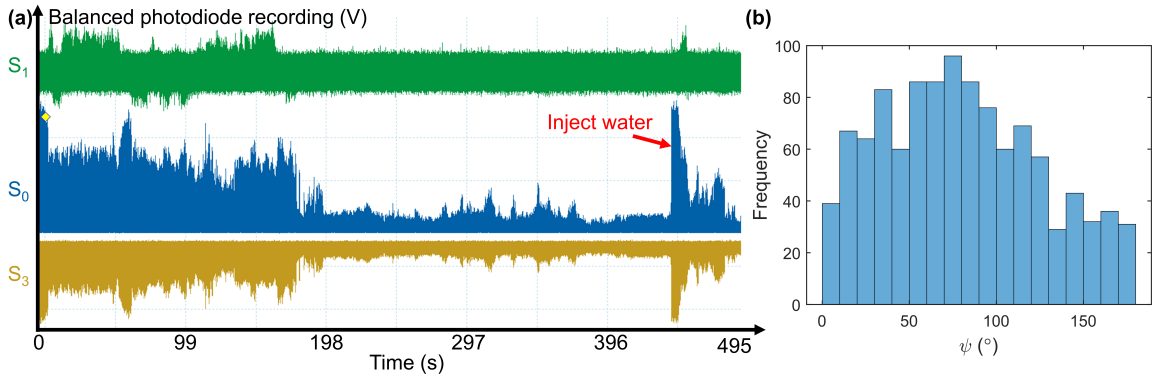


Figure 6.7: An example data set of a rod-shaped bacteria particle over 495 s with the scanning frequency of 10 Hz. (a) Raw data of S_1 (green), S_0 (blue) and S_3 (yellow) signals. (b) The corresponding azimuthal angle ψ distribution.

After the particle entered the cavity, APD signals dropped, which triggered the data collection. After a while, APD signals attenuated to a low level and S_1 signals were too weak to be detected during this period. The particle could not leave the microcavity so an external water flow was introduced labelled in Figure 6.7(a). From the signal evolution, it seemed that the particle gradually diffused from the edge of the microcavity to the centre and got trapped there. When the particle was closer to the centre, the scattering was stronger and the transmitted light was weaker, leading to S_1 signals quenching. Figure 6.7(b) illustrates the distribution of the azimuthal angle ψ when S_1 signals were detectable. It displays a flatter distribution compared with the measurements of 4 kHz scanning as expected. Ideally, the collected time should be long enough to show a complete single-particle event, and the particle should not be trapped or moved closer to the centre of the optical mode to allow detectable signals for S_1. However, the experimental condition was constrained and this ideal condition could not be achieved. Therefore, further data processing was conducted and possible improvements to this experiment will be discussed in Chapter 6.6.

6.4.4 Aspect Ratio Deduction Analysis

Since the data sets with a slower sweeping frequency contained more sweeps and provided a more complete picture of the rotational diffusion process, the aspect ratio analysis was conducted using these data sets. Examples of fittings of individual sweeps using the above example data of 10 Hz scanning frequency in Figure 6.7 are displayed in Figure 6.8.

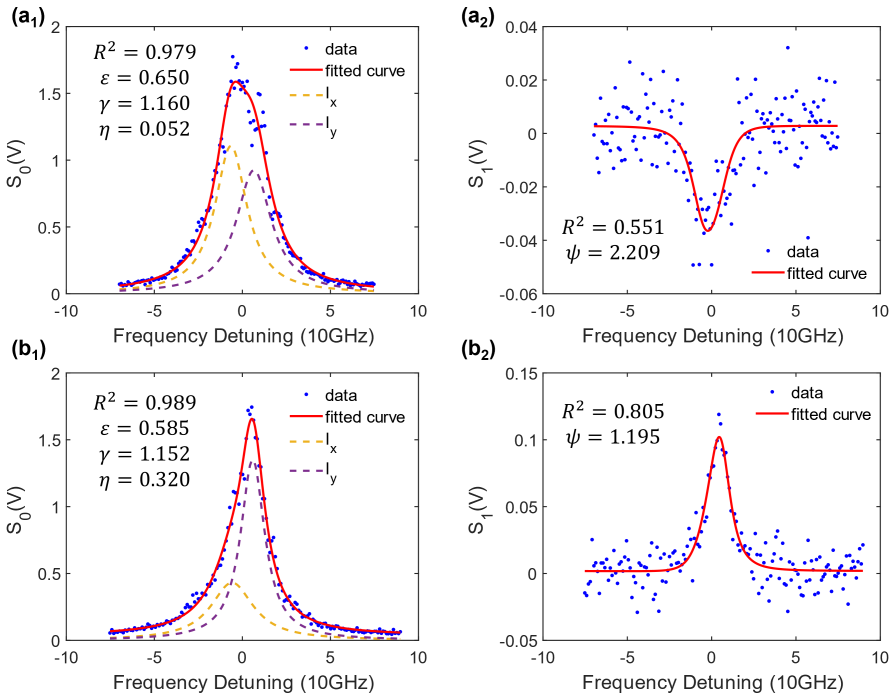


Figure 6.8: Examples of individual fittings of S_0 and the corresponding S_1 in the above example data set of 10 Hz scanning frequency in Figure 6.7. (a) and (b) are two different individual sweeps.

Like the gold nanorod measurement, within a single-particle event, individual resonant peaks in different sweeps had different broadening widths depending on the status of the particle inside the optical mode. Although S_0 signals did not display splittings as the gold nanorod measurement, the broadening and the shape deviation from a single Lorentzian fitting were different in various individual sweeps. S_1 signals were similar to the gold nanorod measurement, showing a positive and negative

Lorentzian shape in these individual sweeps. After fitting individual sweeps and obtaining fitting parameters of each sweep, the histogram of anisotropy loss tangent Φ and the fitting curve using the model introduced in Chapter 3.6.3.2 are demonstrated in Figure 6.9.

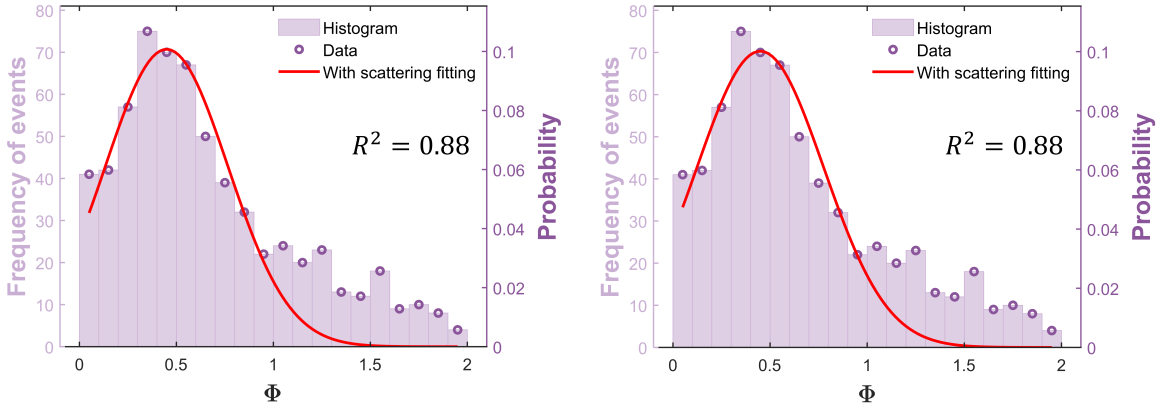


Figure 6.9: Histograms of anisotropy loss tangent Φ and fitting with equation 3.53. (a), (b) The fittings with different results of the aspect ratio and A with R^2 of 0.88 in both cases. (a) has the aspect ratio of 1.94 and A is 2.1943 while the aspect ratio in (b) is 4.76 and A is 2.1869.

Unlike the gold nanorod analysis where the volume-related parameter was fixed as the averaged particle volume obtained from SEM images, A in equation 3.53 was treated as a fitting parameter for the rod-shaped bacteria particle. It was treated this way because $\beta(\vec{r})$ was embeded in A and A was not only determined by the volume of the bacteria particle, but also by the relative position of the particle within an optical mode. Figure 6.9 (a) and (b) showed fitting results with different values of aspect ratio and A. While the fitting result for A only differed by 0.0074, the fitted aspect ratio result was 1.94 in (a) and 4.76 in (b). The r-squared values for both cases were around 0.88. It uncovers the insensitivity of the anisotropy loss tangent Φ to the aspect ratio. This anisotropy loss tangent Φ is impacted by both the volume of the particle and the aspect ratio. With this feature, it is hard to obtain the standard deviation because the aspect ratio can vary markedly with a slightly different volume-related factor A while maintaining a similar fitting accuracy. Examining equation

3.53 ($p(\Phi) = \frac{1}{2A(\alpha_L-\alpha_W)\sqrt{1-\frac{\Phi-2A\alpha_W}{A(\alpha_L-\alpha_W)}}}$) also confirms this finding. α_L and α_W have an injective relationship with the aspect ratio, while A appears everywhere α_L or α_W appears. Increasing the aspect ratio can counteract the impact of decreasing A, thus achieving a similar fitting result. It is worth mentioning that there are data points out of the range of 0 to 2, but their occurrences are relatively infrequent. The peak value of the histogram determines the aspect ratio, so those points having a low occurrence rate were not included. Although they did not impact the aspect ratio result, the occurrences of these data points provide more insights into the model. Based on equation 3.53, it should have a cut-off point as the example shown in Figure 6.10 with the constraint of $1 - \frac{\Phi-2A\alpha_W}{A(\alpha_L-\alpha_W)} \geq 0$.

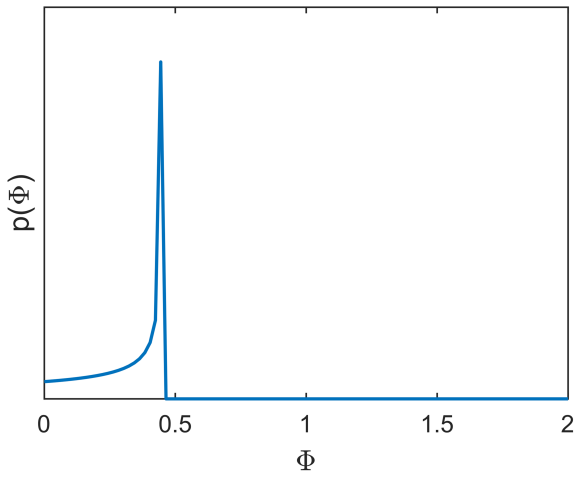


Figure 6.10: Relationship between the anisotropy loss tangent Φ and the probability distribution with equation 3.53 with an example of A=2.5 and the aspect ratio of 4:1.

The cut-off point is determined by the combination of the aspect ratio and the volume-related factor. Theoretically, with the convolution, it would not change the cut-off point, so the data points out of the range were examined in detail. Some of the data points had big variations in the magnitudes of the two Lorentzians in the double Lorentzian fittings of S_0 signals. It indicates that the S_0 resonance peaks of these data points resemble a single Lorentzian, and it was the situation where the state of the particle in the microcavity did not induce enough anisotropy. Therefore, the

double Lorentzian fitting did not provide accurate enough results.

6.5 Other Factors to Consider

Firstly, as the experimental results show, once the APD signals have attenuated, they do not easily resume. This indicates that the particle is probably trapped. Thus a theoretical calculation of optical force and optical torque is necessary. In addition, the theoretical analysis of the rotational diffusion is performed. Lastly, the scattering cross-section is calculated to compare with the gold nanorod scenario.

6.5.1 Optical Force

The theoretical background has been introduced in Chapter 3.7.3. The intra-cavity light power is similar in the two experiments of gold nanorods and rod-shaped bacteria particles. If it is assumed that a gold nanorod and a rod-shaped bacteria particle are located in the same relative position of the optical mode profile, $\frac{\partial I}{\partial x}$ is identical for both scenarios. Thus $\triangle x$ is proportional to $\frac{\alpha_x}{\gamma_x}$. Inserting the size information of the gold nanorod and rod-shaped bacteria particle into 3.73 and 3.81 gives around 10 times the result for a rod-shaped bacteria particle as the gold nanorod. The optical force is about 100 times while the friction coefficient is about 10 times. The result indicates that the rod-shaped bacteria particle is more likely to be pulled into the optical mode. Simulations in Chapter 7.2.3 also confirm the trapping behaviour under this experimental condition.

6.5.2 Rotational Diffusion Analysis

The rotational diffusion coefficient has been introduced in Chapter 3.7.1. D_r was calculated using equation 3.54c to be 1.31. The time duration of a single sweep is around 400 µs. Therefore the angular displacement brought by the random collisions

of the fluid molecules around the particle was 1.85° using $< \theta^2 >= 2D_r t$. The angular displacement caused by the optical field was calculated using $\theta = \frac{MtD_r}{k_B T}$. The optical torque has the magnitude of 10^{-35}, making this angular displacement negligible.

6.5.3 Scattering Cross-section Calculation

The rod-shaped bacteria particle should have a refractive index between water and lipid layers, which is between 1.33 and 1.41. 1.37 was used as its refractive index in the calculation and 1.88 was utilised as the permittivity at the incident light wavelength of 640 nm. The scattering cross-section is about 2×10^4 times the gold nanorod scattering cross-section and 3×10^3 times the gold nanorod extinction cross-section combining both the scattering and absorption. The loss is a significant increase compared to the gold nanorod scenario due to the bigger size of the rod-shaped bacteria particle and the experiment requires a cavity with a lower finesse.

6.6 Limitations and Improvements

As the experimental results show, once the particle diffuses to a more centralised position of one optical antinode, it is trapped and cannot easily escape. The scattering of the particle causes the transmitted light intensity to attenuate significantly, and it is hard to obtain strong enough S_1 signals in this scenario. The particle diffuses without any external control, such as optical tweezer or fluid flow, in this work. The trapping problem can be solved by either decreasing the optical power to reduce the optical force and the possibility of particles being trapped or using external force, like the flow force. However, as mentioned previously, with the current optical microcavity setting, reducing the incident light intensity cannot provide strong enough S_1 signals, but it is possible if the optical microcavity configuration is changed. For example, the reflectivities of both mirrors can be reduced or using cavities with a bigger RoC.

The external flow adds complexity to the system and requires further exploration. Utilising the external flow to push the particle out of the cavity was attempted. It did not succeed every time, but a continued slow flow is still worth investigating.

In this experiment, rod-shaped bacteria particles are more likely to stick to the mirror surface and this sticking behaviour degrades the performance of the sensor. The transmitted light intensity cannot resume after injecting the cleaning solvent, deionised water, into the cavity. The flow cell has to be removed from the experimental apparatus and opened to clean the surface of two mirrors with acetone. This could cause issues for real-world applications as a long-standing and robust monitor is required. The reason could be the bigger size of the particle or the difference in surface structures. Other types of cleaning solvents are worth exploring and studies into the surface structures can be beneficial.

Additionally, the continuance of S_1 signals is worth noticing. Unlike the gold nanorods measurement, where S_1 signals always appear with the particle presence, S_1 signals do not always appear for rod-shaped bacteria particles. It was observed that sometimes during a single-particle event, some data had stronger S_1 signals than others with similar transmitted light intensities. One possibility behind this phenomenon is due to the status of the particle within the optical mode, namely what the polar angle of z axis is in the instrumental cooordianate system and whether the particle bends. As SEM images show in Chapter 5.2.3 and 6.2, rod-shaped bacteria particles sometimes bend with the same drop-and-dry sample preparation method as gold nanorods and display their flexibility [270]. The rod-shaped bacteria particle may bend and deviate from the rod shape subject to optical fields. Further studies into this offers more insights and potential ways to improve.

6.7 Summary

This chapter introduced the application of the optical microcavity sensing method in rod-shaped bacteria particles. The same optical apparatus and measurement method were used with some changes in experimental conditions, such as the scanning frequency and the incident light intensity. Firstly, the samples were analysed with the benchmark technique SEM. Bacteria samples were more flexible than gold nanorods [270] and were likely to bend illustrated in SEM images.

Secondly, the experimental conditions were explored and results with two different scanning frequencies, 4 kHz and 10 Hz, were demonstrated. With the bigger size and thus slower rotational diffusion, 10 Hz scanning data were further analysed to deduce the aspect ratio of a single rod-shaped bacteria particle. With a similar theoretical model to the gold nanorod analysis, and considering scattering in the system, the anisotropy loss tangent probability distribution was convoluted with a Gaussian instrumental response to perform the fitting. However, both the theoretical equation and the fitting result displayed the dependence of anisotropy loss tangent on the aspect ratio and the A, which is related to the volume of the particle as well as the position of the particle within the optical mode. The accuracy of determining A impacts the accuracy of extracting the aspect ratio.

In addition, other theoretical calculations were performed to compare with gold nanorods and better understand the system with the rod-shaped bacteria particle. The optical force was around 100 times the gold nanorod and the friction coefficient was 10 times. This calculation, along with the experimental results and Monte Carlo simulations, confirmed the trapping phenomenon. The collisions from the surrounding fluid molecules brought around 1.85° angular displacement within a resonance sweep, while the one caused by the optical torque was negligible. The scattering

cross-section was also calculated and was 2×10^4 times the gold nanorod scattering cross-section and 3×10^3 times the gold nanorod extinction cross-section with scattering and absorption combined due to a markedly bigger size.

Lastly, the limitations of experimental conditions were discussed and possible improvements were put forward to overcome the limitations of this measurement.

Chapter 7

Simulation

7.1 Introduction

To better understand the system and confirm phenomenon observed in experiments, theoretical simulations have been performed to study the diffusion of rod-shaped particles in water in the optical microcavity and their interactions with light. The theories of simulations have been introduced in Chapter 3.8 and the results of these simulations will be discussed in this chapter. Firstly, the results of Monte Carlo simulations are demonstrated to investigate the Brownian motions of rod-shaped particles in water in an optical microcavity. Based on the investigations of spherical particles, which is a fundamental and simplified scenario, both translational and rotational diffusions of rod-shaped particles are studied. Both gold nanorods and rod-shaped bacteria particles are simulated for comparison. Secondly, the FDTD method is applied in Lumerical software to monitor the transmitted light from the optical microcavity with the presence of rod-shaped bacteria particles. The spectrum and the electric field between two mirrors are investigated with different orientations and positions of the particle in the microcavity.

By using some of the experimental settings in the simulations, the phenomenon shown in the experiments can be confirmed by the simulations, such as the diffusion of the particles. It shows whether particles diffuse freely or are trapped in antinodes as well as the rotational diffusion behaviour. In addition, the simulations provide supplementary information to the experiments that could potentially be future directions to explore.

7.2 Monte Carlo Simulation

Monte Carlo simulations offer insights into the dynamic diffusion process of particles in the microcavity. Simulations of gold nanospheres are studied before looking into the more complex circumstances of gold nanorods. Rod-shaped bacteria particles are also simulated. The time step was set appropriately as a good trade-off between the simulation accuracy and the simulation time in the following simulations. The flow rate was set to 0, which is the same as the experimental condition, to monitor the diffusion of a particle in water. The cavity has a RoC of 25 µm and a depth of 600 nm, the same as the experimental configurations. Figure 7.1 illustrates the schematic of the coordinate system used in the simulation. The x-axis is the flow direction and the z-axis is the light propagation direction. The xy plane is the optical microcavity plane.

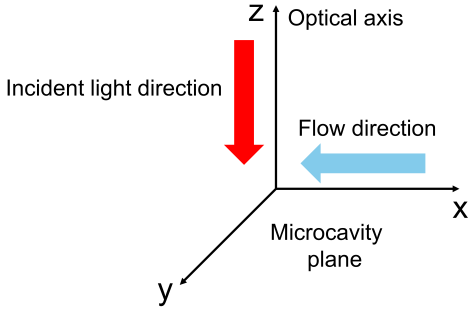


Figure 7.1: The schematic of the coordinate system in the simulation. z axis is the light propagation direction. x is the flow direction and xy plane is the microcavity plane.

7.2.1 Gold Nanosphere Simulation

The theory has been introduced in Chapter 3.8.1.1. The cavity length was set to 10 µm. Figure 7.2 (a) and (b) show the trajectories of the center of a gold nanosphere (60 nm diameter) over 1 s with the time step of 1 µs under different intra-cavity optical powers of 10 mW and 55 mW respectively.

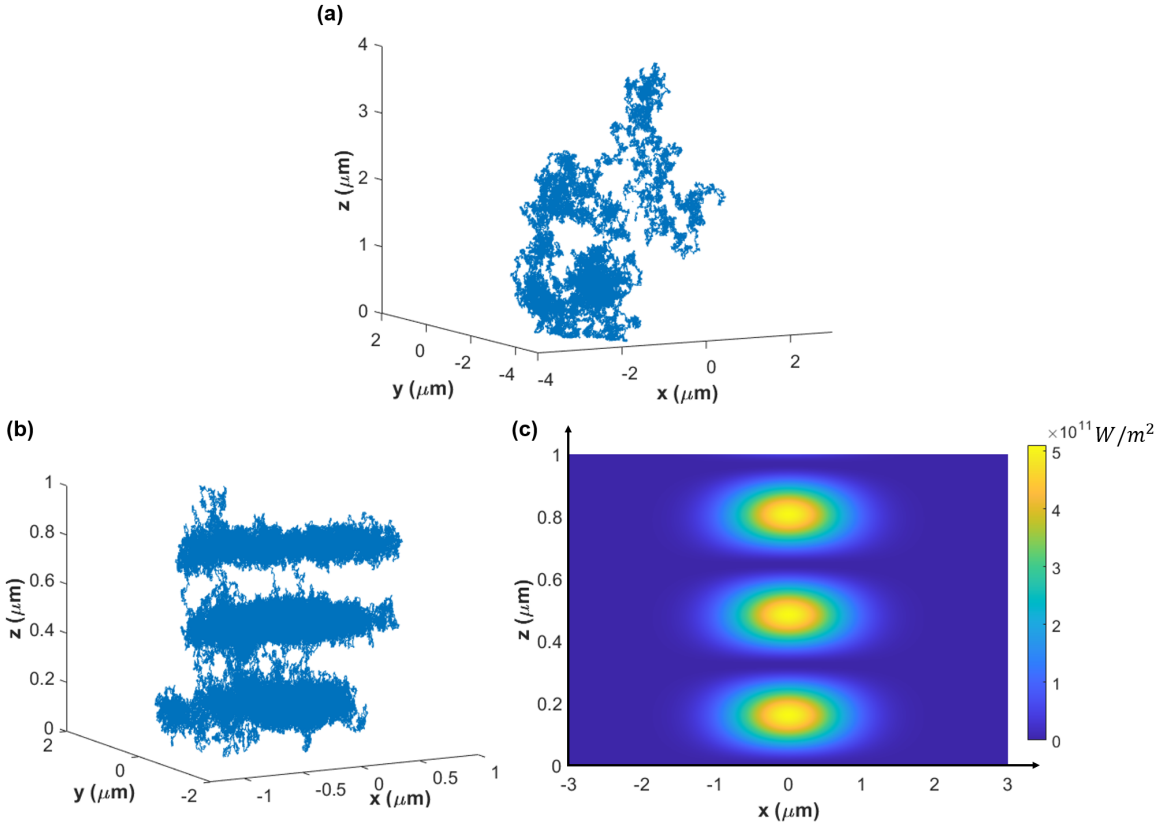


Figure 7.2: Simulation results of gold nanospheres with a 60 nm diameter. (a) Trajectory of the center of the particle with the intra-cavity optical power of 10 mW. (b) Trajectory of the center of the particle with the intra-cavity optical power of 55 mW. (c) Light intensity profile between two mirrors with the x and z direction in the range of -3 $\sim$ 3 µm and 0 $\sim$ 1 µm respectively.

A higher optical power generates a stronger optical force, leading to the trapping phenomenon shown in Figure 7.2(b) compared with the free diffusion illustrated in Figure 7.2(a). The free diffusion refers to the state where the particle undergoes only the Brownian diffusion and the optical force is not strong enough to exert an

obvious impact on the trajectory of the particle. The particle is trapped in the 3 antinodes, which have the strongest light intensities between the two mirrors, shown in the light intensity profile in Figure 7.2(c). Apart from the z direction, the particle also displays more constrained diffusion behaviour in both the x and y directions than the free diffusion scenario. Additionally, the trajectories of several particles could be visualised simultaneously to confirm the universality of the phenomenon. Different colours represent different particles in Figure 7.3. The intra-cavity optical powers are 10 mW and 55 mW in Figure 7.3(a) and (b). With 5 particles simulated simultaneously (Figure 7.3(a)) compared with only one particle (Figure 7.2(a)), the overall diffusion range becomes bigger. The 5 particles display random behaviour even if they have the same starting point. Different starting points of the particles can add more differences to the trajectories among different particles, which is expected under experimental conditions. It is worth mentioning that in the trapping scenario (Figure 7.3(b)), the specific number of antinodes where particles are trapped seems to be random in this case. For example, particle 2 was only trapped in one antinode while particle 4 moved between three antinodes. Moreover, the trapping correlation between specific antinodes and trapped particles also seems to be random. For example, particle 2 was trapped in the antinode closest to $z = 0$ while particle 4 was trapped in three antinodes near $z = 1.5$ µm. It makes sense because this case can be seen as a combination of the Brownian motion and the optical force dragging the particle to the antinode. If the particle diffuses to a position where the optical force is stronger, it may be dragged to the center of the antinode and stay there, otherwise, it may pass the edge of the antinode, and be trapped to the next antinode.

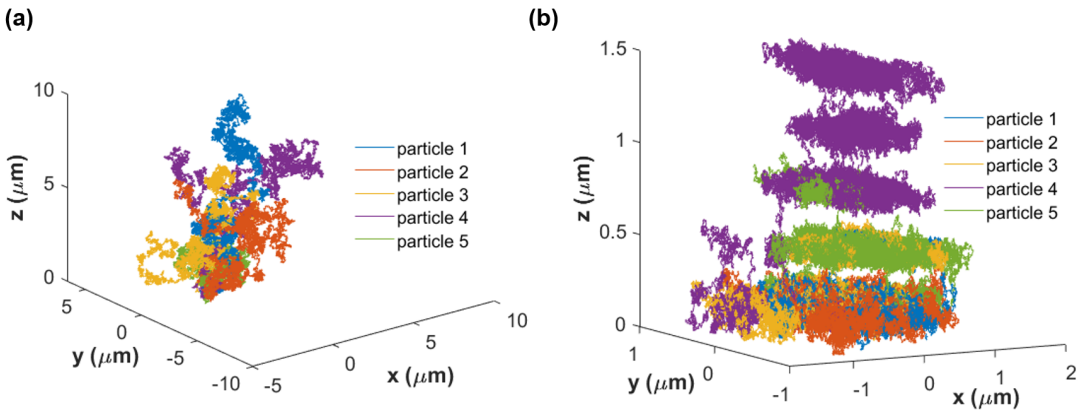


Figure 7.3: Simultaneous simulations of 5 particles. (a) Trajectories of the center of the particle with the intra-cavity optical power of 10 mW. (b) Trajectories of the center of the particle with the intra-cavity optical power of 55 mW. Different colours represent different particles with the same starting points.

7.2.2 Gold Nanorod Simulation

The complexity of gold nanorods compared with their spherical counterparts not only lies in the anisotropy for γ and α but also in the rotational diffusion. The theory has been elucidated in Chapter 3.8.1.2. Figure 7.4 is the same as Figure 3.12 and illustrates all the angles that will appear later in the results.

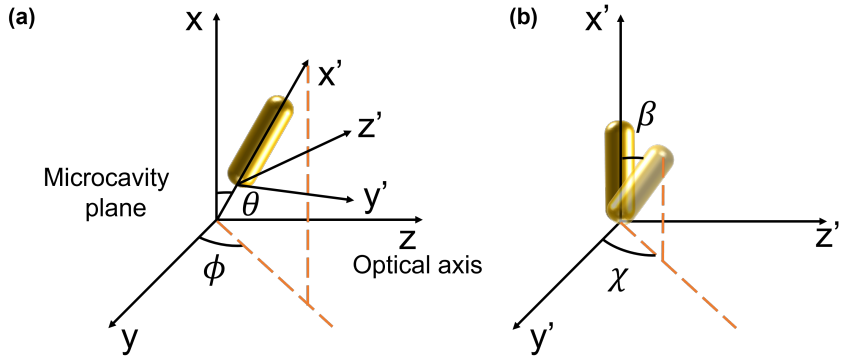


Figure 7.4: (a) Schematic of the two coordinate systems used. xyz is the instrumental coordinate system while x'y'z' is the nanorod coordinate system. θ and ϕ are the polar and azimuthal angles of gold nanorods in the instrument frame. (b) Rotational movement in the gold nanorod coordinate system. β and χ present the rotational polar and azimuthal angle of the gold nanorod over a time step in the current nanorod frame.

With this simulation, the positions of two ends of the long axis of the nanorod can also be calculated. The diffusion of the gold nanorod in water in the optical microcavity is visualised dynamically with various conditions that can be tuned in the experiment, such as cavity length, intra-cavity optical power, etc. In the following simulations, the gold nanorod has a length of 48 nm and a diameter of 32 nm, which the size of sample A in the experiment. The cavity length was set to 1.5 µm, the same cavity length used in gold nanorod measurements in Chapter 5.4.2. The simulation time and the time step were set as 0.5 s and 1 µs.

7.2.2.1 Trajectory in the Optical Microcavity

Firstly, the intra-cavity power was set to 17.2 mW, the same power used in gold nanorod measurements in Chapter 5.4.2. The trajectories of the center of a single gold nanorod and the centers of 5 gold nanorods were illustrated in Figure 7.5(a) and (b). In both cases, the traces of the particle shows randomness and particles do not get trapped in the antinodes, indicating free diffusion under this condition. Upon closer examination of the trajectories of these 5 particles (Figure 7.5(b)), their positions distributed widely in both x and y directions due to the randomness of the particle diffusion and big deviations between particles.

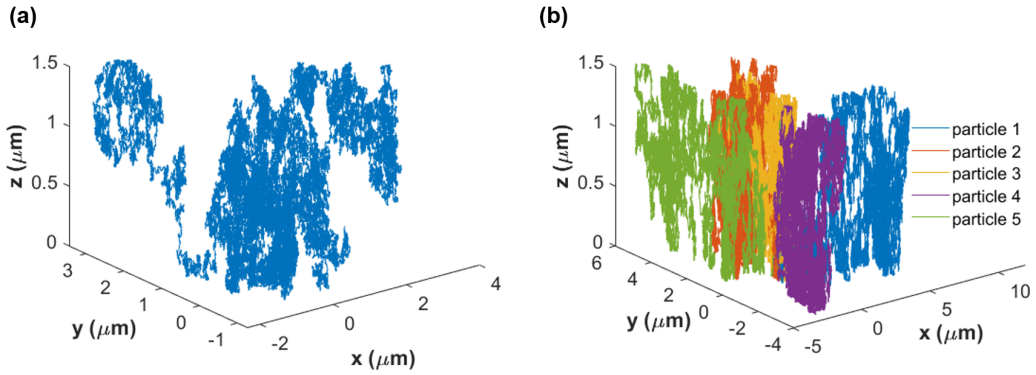


Figure 7.5: Trajectory of gold nanorods with the intra-cavity optical power of 17.2 mW. (a) Trajectory of the center of a single gold nanorod. (b) Trajectories of centers of 5 particles diffusing simultaneously. Different colours represent different particles.

Increasing the intra-cavity power to 500 mW resulted in the particles becoming trapped at antinodes, as shown in Figure 7.6(a). The simulations of five particles diffusing simultaneously in Figure 7.6(b) reveals the trapping phenomenon again. Gold nanorods showed similar behaviour to gold nanospheres mentioned before, with different particles trapping in different antinodes and moving between different numbers of antinodes.

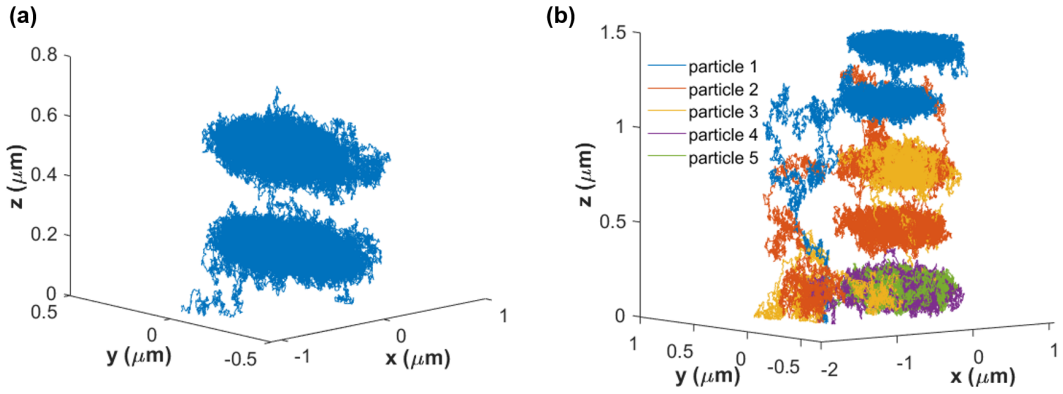


Figure 7.6: Trajectory of gold nanorods with the intra-cavity optical power of 500 mW. (a) Trajectory of the center of a single gold nanorod. (b) Trajectories of the centers of 5 particles diffusing simultaneously. Different colours represent different particles.

If the intra-cavity power is increased further to 5 W, the particle is tightly trapped in one antinode, shown in Figure 7.7. Unlike the previous case with the intra-cavity power of 500 mW, the 5 particles are trapped to the same antinode under this high power shown in 7.7 (b).

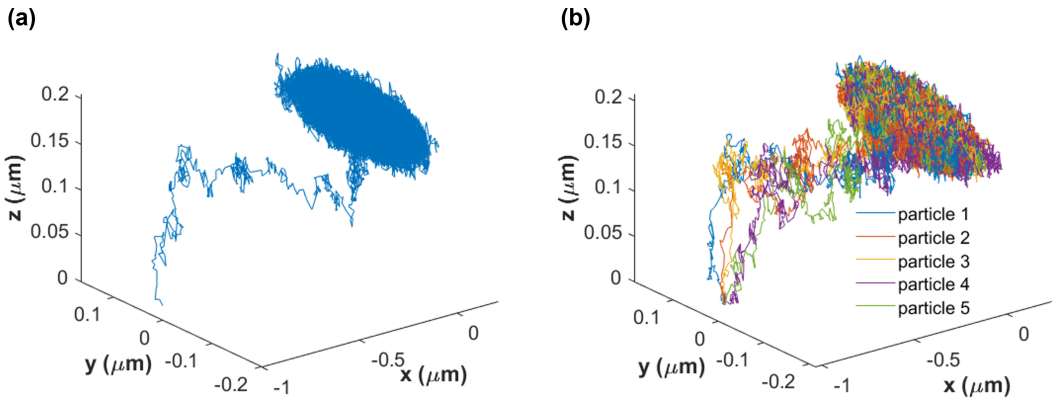


Figure 7.7: Trajectory of gold nanorods with the intra-cavity optical power of 5 W. (a) Trajectory of the center of a single gold nanorod. (b) Trajectories of the centers of 5 particles diffusing simultaneously. Different colours represent different particles.

When the optical power is weak and particle is not trapped in the antinode, the trajectory of the particle is not determined by the start position and it shows randomness among particles, exemplified in Figure 7.5. When the optical field is stronger, but not strong enough to drag the particle directly into the nearest antinode, it is possible that the particle escapes and passes the edge of the nearest antinode and is trapped into another antinode afterwards, or moves between antinodes. One example is demonstrated in in Figure 7.6. At last, when the optical field is stronger, as shown in Figure 7.7, the particle is directly dragged into the nearest antinode from its start position.

7.2.2.2 Angular Distribution

Distributions of the four angles defined in Chapter 3.8.1.2 are plotted with different intra-cavity optical powers. 17.2 mW and 500 mW were employed and the angular distributions of β, χ, θ and ϕ are demonstrated in Figure 7.8 (a)-(d) and (e)-(h) respectively for comparison.

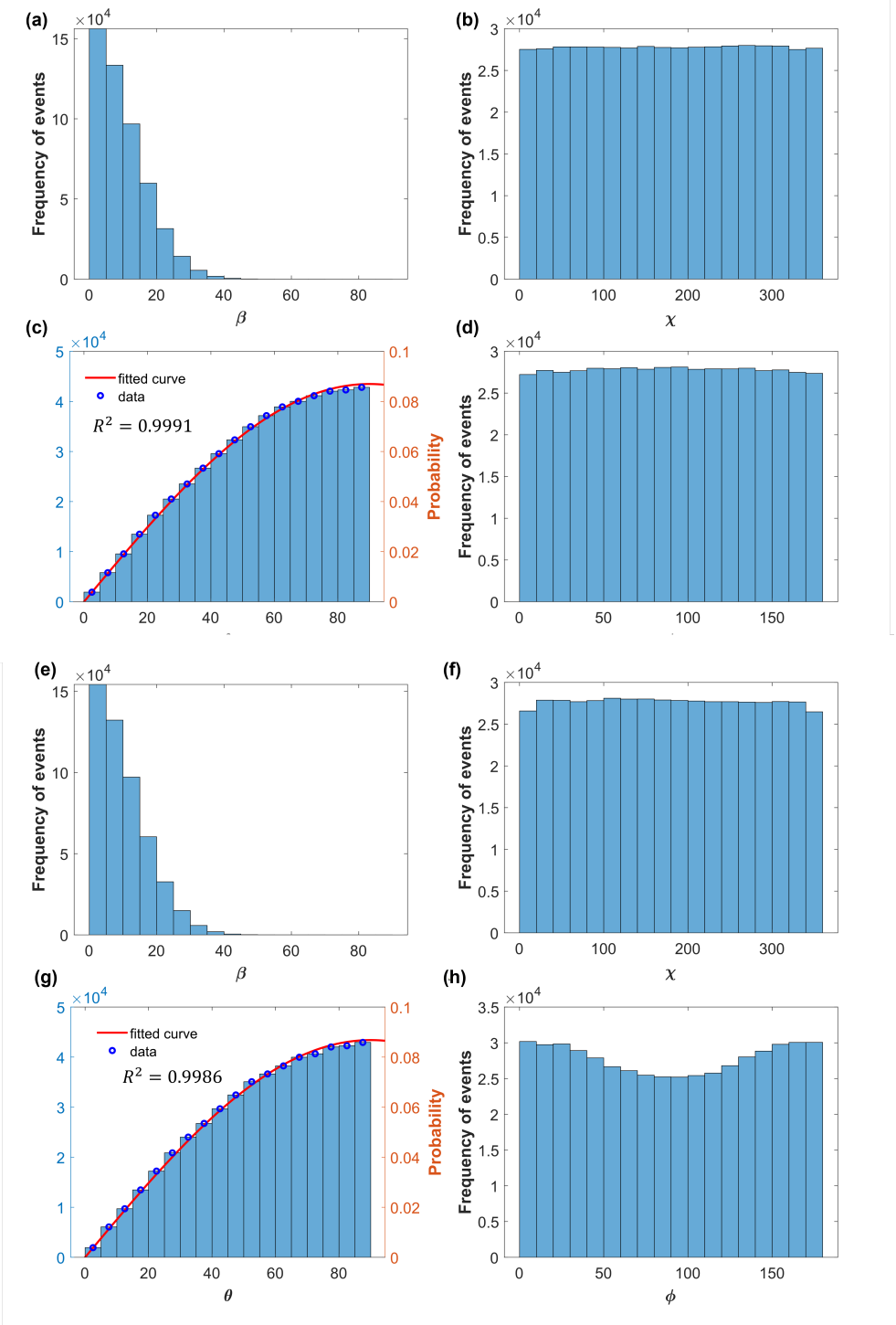


Figure 7.8: Angular distributions (in degree unit) of a single gold nanorod with the intra-cavity optical power of 17.2 mW (a)-(d) and 500 mW (e)-(h). (a), (e) Polar angle β in the particle frame. (b), (f) Azimuthal angle χ in the particle frame. (c), (g) Polar angle θ in the instrument frame. (d), (h) Azimuthal angle ϕ in the instrument frame.

The probability distribution of a random polar angle can be derived by:

$$p(\theta)d\theta = \frac{2\pi r \sin\theta r d\theta}{2\pi r^2},\ \theta : 0 \sim \frac{\pi}{2} \tag{7.1}$$

In the case with the intra-cavity power of 17.2 mW, the distribution of θ conformed to the $\sin\theta$ probability distribution with the fitting R^2 of 0.9991 and the distribution for ϕ was flat, indicating the particle was undergoing a free diffusion. β and χ show changes of the polar and azimuthal angle between two consecutive rotations. β shows preference of smaller angles while χ has a flat distributions over different values. For comparison, the case where the intra-cavity power is 500 mW, is plotted in Figure 7.8 (e)-(h). They reveal a small difference compared with the previous scenario. β displays more occurrences in larger angles, though subtle. χ displays fewer occurrences around 0° and 360° while ϕ exhibits fewer occurrences near 90°. θ reveals a lower R^2 but still shows a good agreement with $\sin\theta$ distribution.

When the intra-cavity power is increased more, the impact of the optical field can be manifested more clearly, as shown in Figure 7.9 with the intra-cavity power of 5 W.

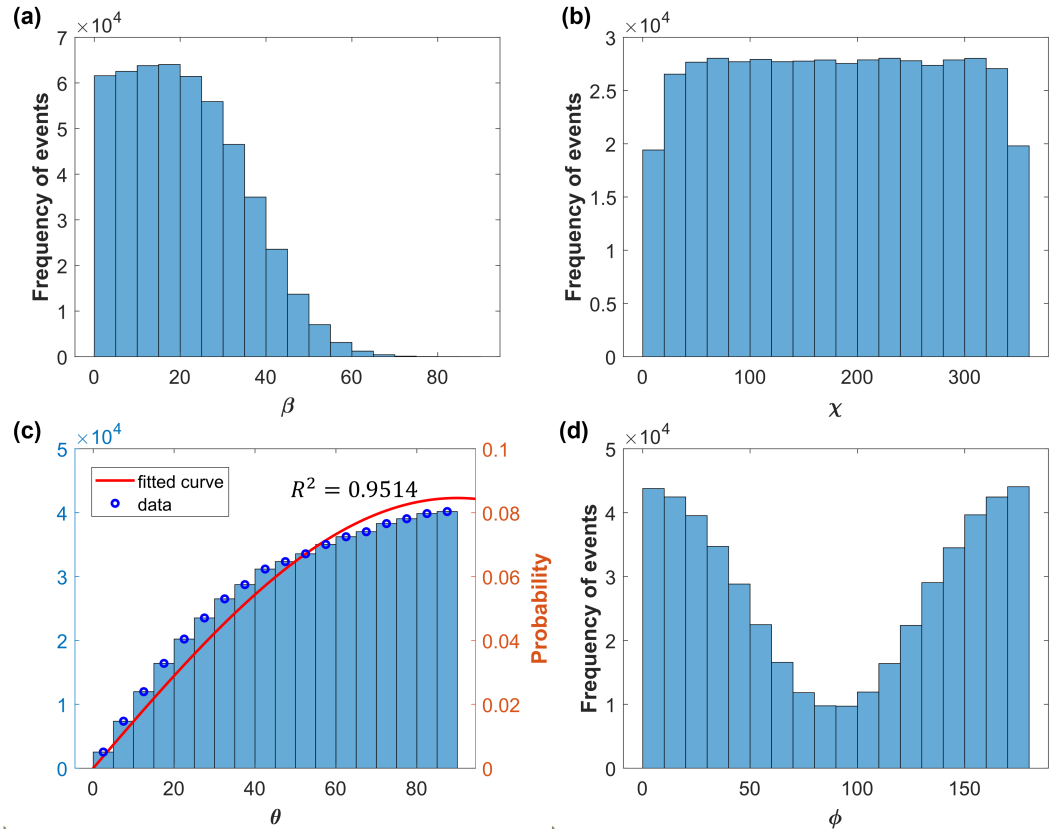


Figure 7.9: Angular distributions (in degree unit) of a single gold nanorod with the intra-cavity optical power of 5 W. (a) Polar angle β in the particle frame. (b) Azimuthal angle χ in the particle frame. (c) Polar angle θ in the instrument frame. (d) Azimuthal angle ϕ in the instrument frame.

All the trends mentioned in Figure 7.8 of angular distributions became more prominent in this higher optical power situation illustrated in Figure 7.9, highlighting stronger dominance of optical forces in driving the rotational diffusion of gold nanorods.

7.2.3 Rod-shaped Bacteria Particle Simulation

A single rod-shaped bacteria particle can also be simulated with the same model introduced in Chapter 3.8.1.2. The length and diameter of the particle are 1.54 µm and 0.36 µm, the same as in the experiment. Since the particle is noticeably larger compared with the gold nanoparticle, the time step was set to 100 µs and the simulation time was 500 s, so the time steps were ten times larger than the gold

nanorod simulation. The cavity configuration was the same as the gold nanoparticle simulation while the cavity length was 6.5 µm. The start point of the particle was set to (-1 µm, 0, $\frac{L_{cav}}{2}$). The intra-cavity power of 10 mW was chosen first as it was close to the experimental condition.

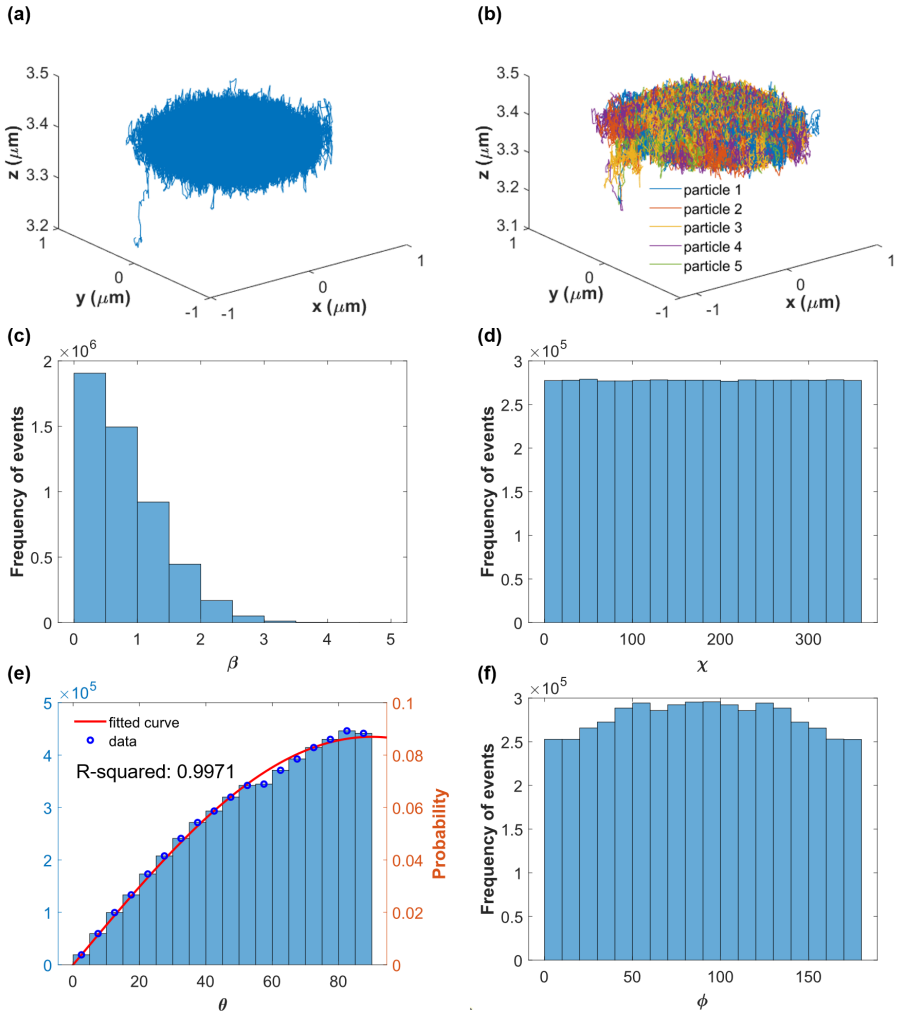


Figure 7.10: Summary of the simulation of rod-shaped bacteria particles with the intra-cavity optical power of 10 mW. (a) Trajectory of a single rod-shaped bacteria particle. (b) Trajectories of 5 rod-shaped bacteria particles simultaneously. (c) Angular distribution (in degree unit) of the polar angle β in the particle frame. (d) Angular distribution (in degree unit) of the azimuthal angle χ in the particle frame. (e) Angular distribution (in degree unit) of the polar angle θ in the instrument frame. (f) Angular distribution (in degree unit) of the azimuthal angle ϕ in the instrument frame.

As Figure 7.10(a) and (b) demonstrate, the light field trapped the particle tightly in the nearest antinode around the start position of the particle. With even higher intra-cavity optical power, the particle did not display a more prominent trend than this, different from the gold nanorod scenario. To compare with the free diffusion of a bacteria particle, the intra-cavity optical power decreased to 1 mW and the results are illustrated below in Figure 7.11.

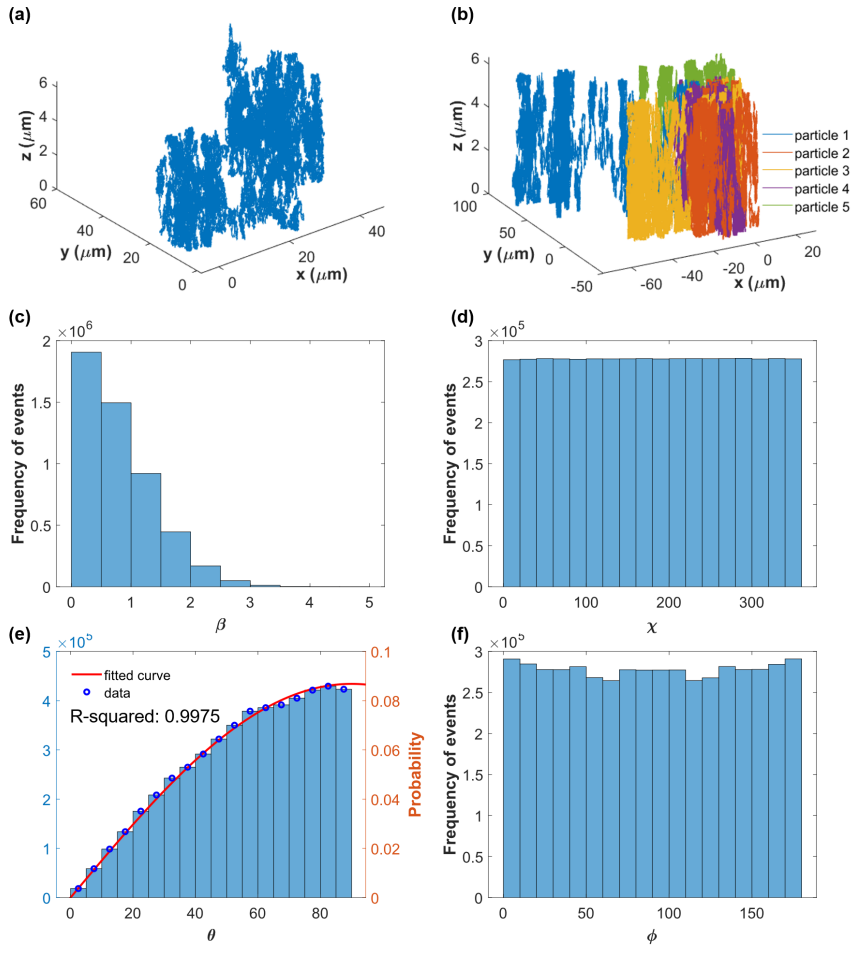


Figure 7.11: Summary of the simulation of rod-shaped bacteria particles with the intra-cavity optical power of 1 mW. (a) Trajectory of the center a single rod-shaped bacteria particle. (b) Trajectories of the centers of 5 rod-shaped bacteria particles simultaneously. (c) Angular distribution (in degree unit) of the polar angle β in the particle frame. (d) Angular distribution (in degree unit) of the azimuthal angle χ in the particle frame. (e) Angular distribution (in degree unit) of the polar angle θ in the instrument frame. (f) Angular distribution (in degree unit) of the azimuthal angle ϕ in the instrument frame.

The particle experienced free diffusion in this scenario, and its positions were distributed more widely in the x and y directions compared with the gold nanoparticle case due to the longer simulation time. Comparing this with the situation of trapped particles above, only a small difference in ϕ was observed. In both cases, β showed a markedly smaller angle ($0° - 4°$) than the gold nanorod ($0° - 40°$), resulting from the significant decrease in D_r. The small difference between the free diffusion and trapping case highlights that the optical torque does not maintain a strong dominance in the rotational diffusion of bacteria particles.

7.3 Finite-Difference Time-Domain (FDTD) Simulation

Although the Monte Carlo simulation is powerful in examining the particle diffusion in water in the optical microcavity, it cannot provide information about the transmitted light, which FDTD simulations can achieve. The FDTD software package used in this work is a commercially available one (Lumeircal). With the theoretical background introduced in Chapter 3.8.2, the simulation configuration is shown and the results of a rod-shaped bacteria particle placed at different angles and positions in the microcavity are demonstrated.

7.3.1 Simulation Configuration

Since the incident light is circularly polarised, and the impacts of various angles and positions of a single rod-shaped bacteria particle in the optical microcavity are explored, it is necessary to simulate in a 3D setting. However, the 3D simulation memory requirement scales with $(\frac{\lambda}{\triangle x})^3$ and the simulation time scales with $(\frac{\lambda}{\triangle x})^4$. Thus 2D simulations were performed first to set up the optical microcavity and different settings were attempted before advancing to a 3D simulation.

Figure 7.12(a) shows the perspective view of the optical microcavity construction in Lumerical. Figure 7.12 (b) illustrates the schematic of the optical microcavity system. Both planar and concave mirrors consist of stacks of high/low refractive index thin films with $\frac{\lambda}{4n}$ thickness. At incident light wavelength λ =640 nm, the refractive index of TiO_2 and SiO_2 is 2.58 and 1.46, so each TiO_2 and SiO_2 layer was set to 62 nm and 109.8 nm. According to the more accurate way of calculating the reflectivity using Sellmeier's equations mentioned in Chapter 4.2.3, 6 and 8 pairs were chosen for planar and concave mirrors. They corresponded to 99.45% and 99.92% reflectivity at the centre wavelength, slightly lower than the experimental conditions of 99.6% and 99.99%. They were chosen to reduce the simulation time. The RoC of the hemisphere feature R and the milling depth d was set to 25 µm and 600 nm for the cavity. The cavity length was set to 5.18 µm.

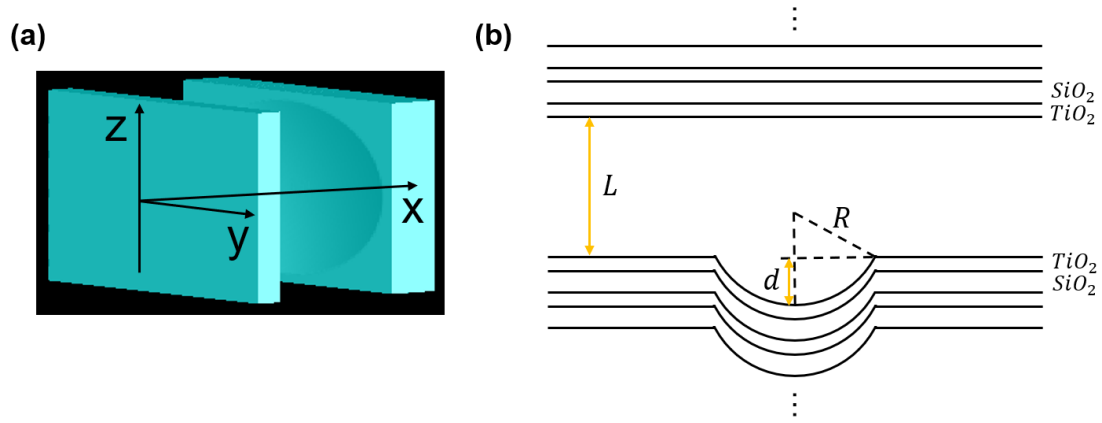


Figure 7.12: Optical microcavity configuration. (a) Perspective view in Lumerical software with the coordinate system labelled. (b) Schematic of the coating composition and concave feature.

The refractive index profile is shown in Figure 7.13 with the background of water:

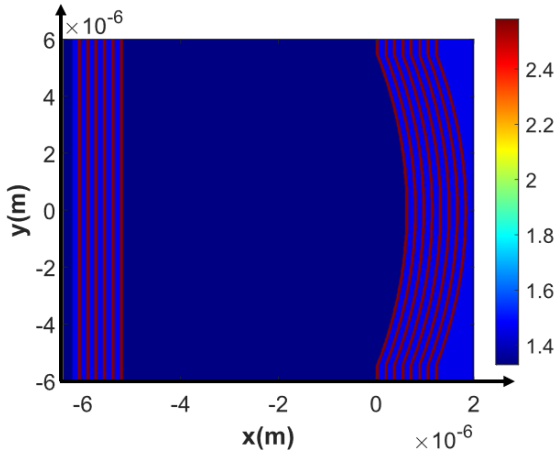


Figure 7.13: Refractive index profile of the optical microcavity system.

A 3D simulation region with span (8.4 µm × 12 µm × 3 µm) in the x, y and z direction was set with each boundary having a perfect match layer (PML). Considering the simulation time and memory requirements, the FDTD simulation region did not cover the whole optical microcavity, but only part of it as shown in Figure 7.14(a) and (b) with the perspective view and XY view. It was configured in this manner considering the symmetry in the yz plane. Propagating waves are absorbed completely when they reach the PMLs at the boundary of FDTD simulation region.

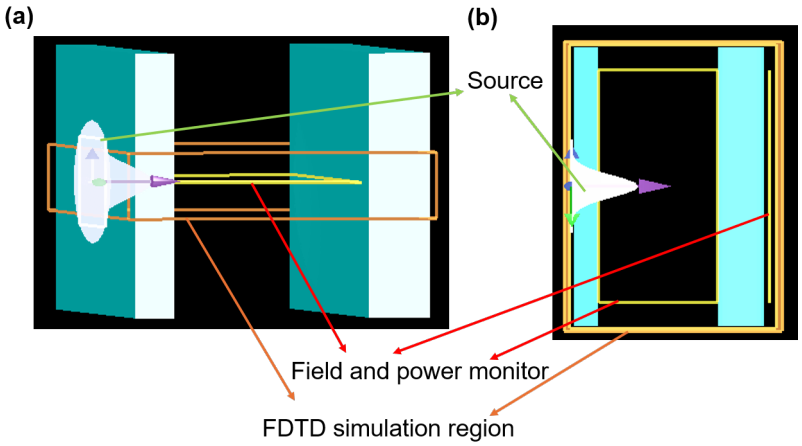


Figure 7.14: Simulation setting in Lumerical. The orange box is the FDTD simulation region. Yellow rectangles are the field and power monitors. The source is also labelled. (a) Perspective view. (b) XY view.

Within the FDTD simulation region, a Cartsian mesh made up of Yee cells is defined, where Maxwell's equations are solved numerically in the time domain for each Yee cell as introduced in Chapter 3.8.2. The mesh type was set to auto-non-uniform with a maximum override mesh step of 8 nm in the x, y and z directions. The mesh accuracy was set to 2 for the following simulations considering the trade-off between the simulation time and the accuracy. The simulation time was 5000 fs and the simulation temperature was 300 K. A 2D z-normal frequency-domain field and power monitor was placed between the two mirrors to monitor the electric field and how the rod-shaped bacteria particle impacted it. Another 2D x-normal frequency-domain field and power monitor was placed after the concave mirror to monitor the transmission spectrum. Two Gaussian beams with a $\frac{\pi}{2}$ phase shift constructs left circularly polarised light to irradiate the optical microcavity. Figure 7.15 shows the simulation results of an empty cavity.

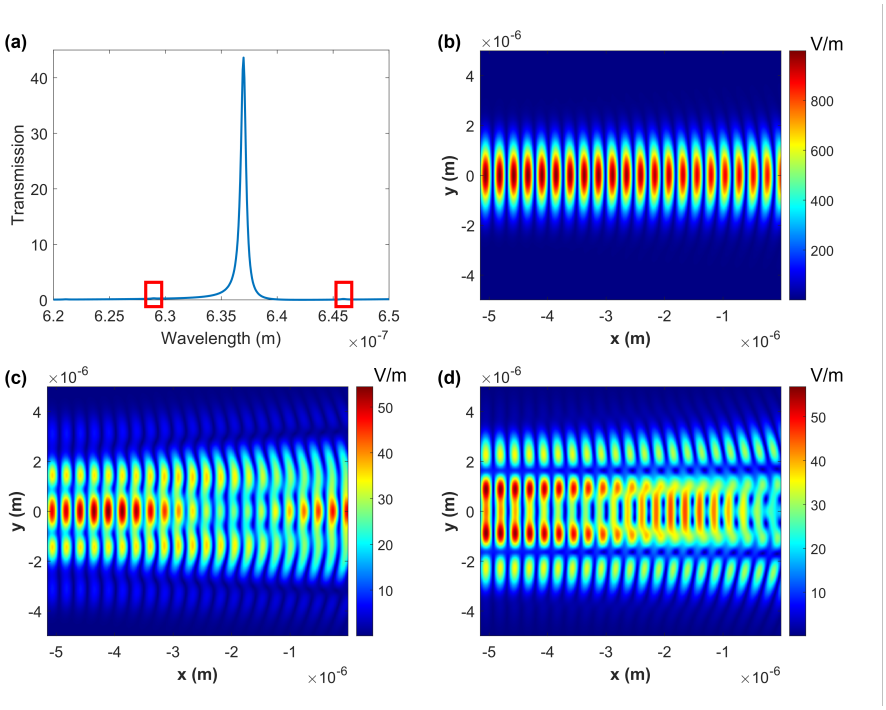


Figure 7.15: Simulation results of an empty cavity. (a) Transmission spectrum with the peak wavelength at 636.99 nm. (b)-(d) Electric field profiles between the two mirrors at wavelengths of 636.99nm, 628.95 nm and 645.94 nm, the latter two of which are the positions of smaller peaks, labelled in (a).

(a) is the transmission spectrum with the peak wavelength at 636.99 nm while (b) illustrates the electric field between the two mirrors at this wavelength. It is TEM_{00} (TEM: Transverse Electromagnetic Mode) with the index number $q = 22$. From the transmission spectrum, there are also two pretty small peaks on either side of the main peak, labelled with red rectangles in Figure 7.15(a), with a wavelength of 628.95 nm and 645.94 nm, which are higher-order modes of $q = 22$ and $q = 21$.

After monitoring the empty cavity scenario, a single rod-shaped bacteria particle with a length of 1.54 µm and a diameter of 0.36 µm was placed between the two mirrors, at different positions and orientations in the cavity. The impacts of the particle on the system are discussed below.

7.3.2 Angle of Rod-shaped Bacteria Particle

Experimentally, the rod-shaped bacteria particle both diffuses and rotates in the optical microcavity and the resonant peak of the transmitted light changes accordingly. FDTD simulations in Lumerical cannot take into account this dynamic process, but the static situation can be explored where the position and angle of the particle are fixed.

7.3.2.1 Angle in xy Plane

Firstly, the particle was placed at one antinode in the middle of the two mirrors. The transmitted spectrum is illustrated in Figure 7.16(b) when the particle rotates 10° from the x axis in the xy plane (XY view in Figure 7.16(a)).

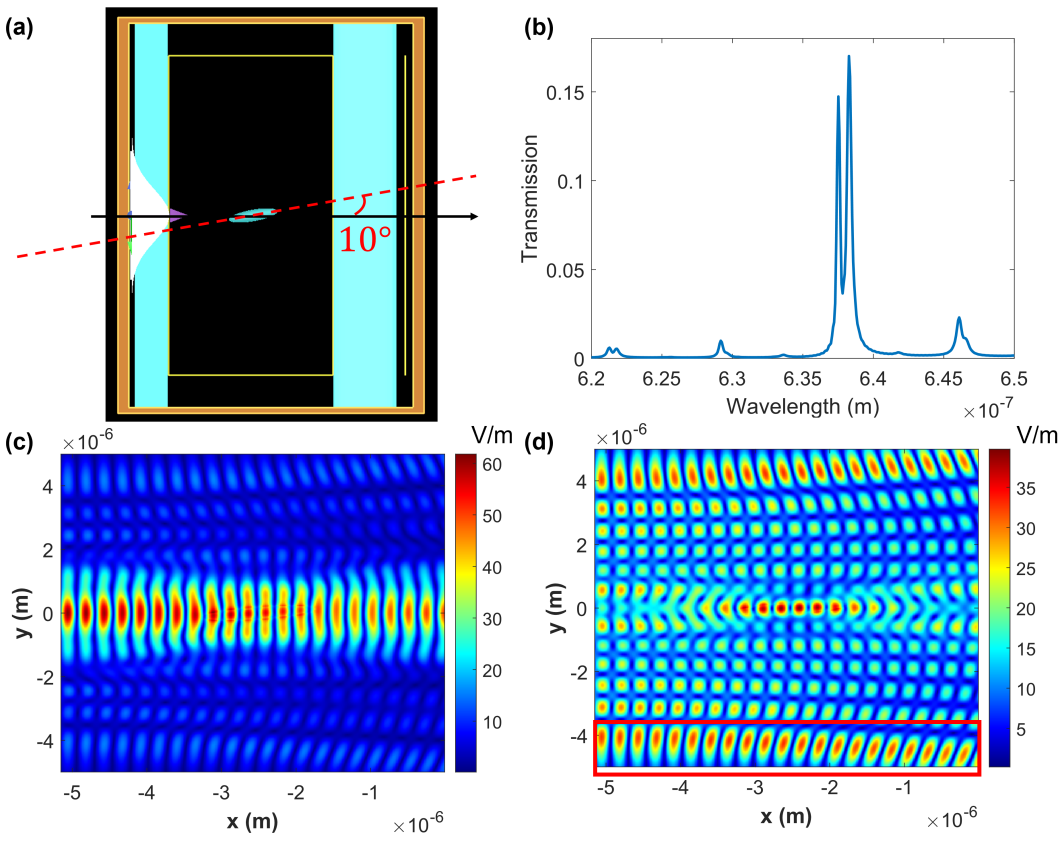


Figure 7.16: Summary of the simulation where the particle is placed at 10° from the x axis in the xy plane. (a) Simulation configuration in Lumerical (XY view). (b) Transmission spectrum. (c), (d) Electric field between two mirrors at 637.52 nm and 638.27 nm, wavelengths of the split peaks.

A split of the main peak was observed, and the two wavelengths of the split peaks were 637.52 nm and 638.27 nm. The electric fields at these two wavelengths between the two mirrors were explored with the frequency-domain field and power monitor, as demonstrated in Figure 7.16(c) and (d). The edge of the particle and the perturbation it exerted on the electric field could be observed by zooming into the antinodes where the particle stayed. The wavelength shifts from 636.99 nm to 637.52 nm. And the other wavelength of the main split peak shows the higher-order mode profile, introduced in Chapter 3.3. Therefore, it did not generate new modes and the split peak was owing to the combination of higher-order modes. By counting the antinode

number, the index number q of different higher-order modes could be determined. For example, in Figure (d), the red rectangle area shows 21 antinodes, meaning it has a $q = 21$. (c) shows the dominance of TEM_{00} of $q = 22$, with the combination of higher-order modes from $q = 21$ and $q = 20$. (d) shows the combination of higher-order modes from $q = 20,\ 21,\ 22$.

The angle of the particle was increased to monitor further impacts. Figure 7.17 highlights the results of the simulations with the particle at 30°, 50° and 70° from the x axis. The transmission spectrum and the electric fields between the two mirrors at the two wavelengths of the splits in the main peak are illustrated in Figure 7.17. With different angles, these two wavelengths changed slightly, from 637.52 nm to 637.37 nm, and from 638.27 nm to 638.2 nm. The absolute and relative transmission at these two wavelengths changed, too. The wavelength at the dip point changed slightly from 637.74 nm to 637.9 nm. Apart from the main peak, the splittings of other smaller peaks disappeared or became less prominent gradually. The electric field profile near 637 nm shown in Figure 7.17(b)(e)(h) displayed less hybridisation with other high-order modes with increasing angles. Additionally, the electric field profile around 638 nm displayed in Figure 7.17(c)(f)(i) illustrated stronger dominance of the higher-order mode of $q = 22$ in the centre with increasing angles.

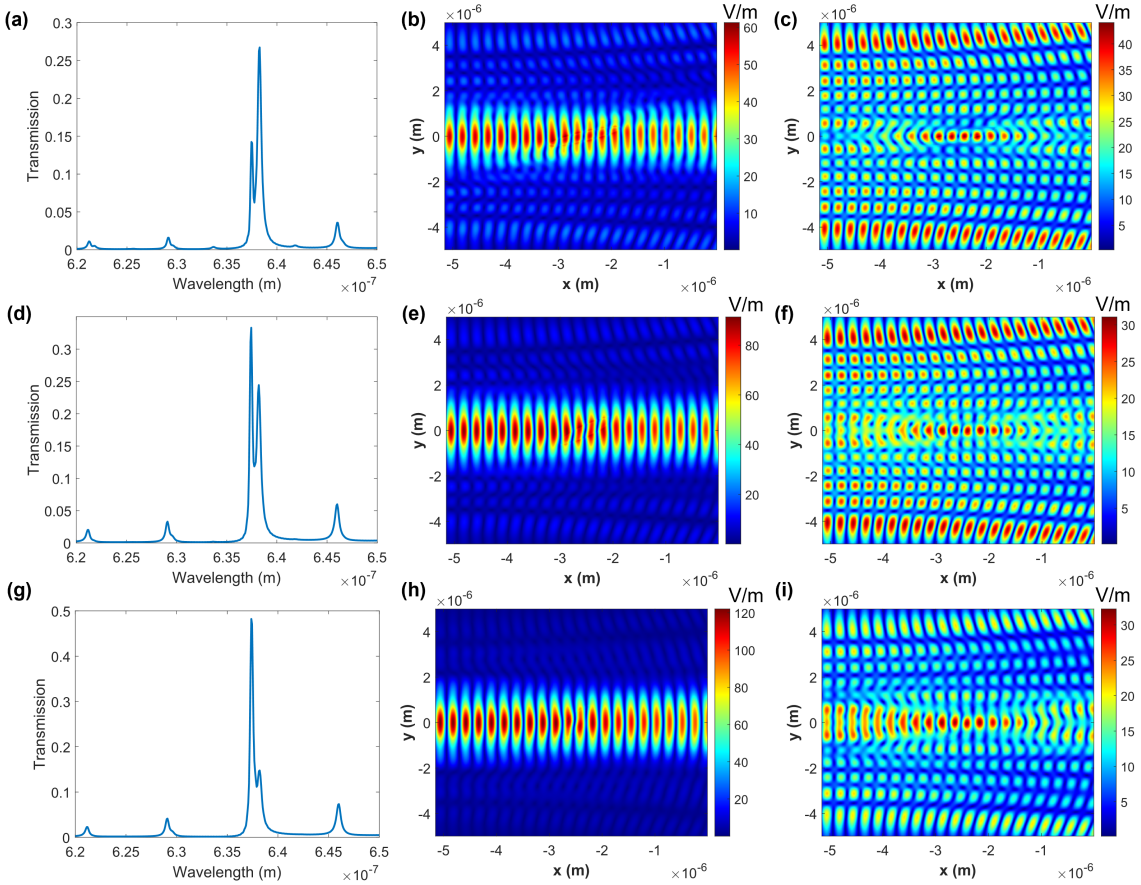


Figure 7.17: Summary of simulations with the particle at different angles from the x axis. (a)-(c) 30°. (d)-(f) 50°. (g)-(i) 70°. (a), (d), (g) Transmission spectrum. (b), (e), (h) Electric field between two mirrors at 637.52 nm, 637.44 nm and 637.37 nm. (c) Electric field between two mirrors at 638.27 nm. (f), (i) Electric field between two mirrors at 638.2 nm.

7.3.2.2 Angle in xz and yz Plane

Due to the symmetry, rotating the particle in the xy plane is the same as the xz plane, so circumstances of a particle with rotating angles in the xz plane were not simulated. When the particle rotated in the yz plane, the monitor after the concave mirror was unchanged, while monitors between the two mirrors were changed to a 2D x-normal and a 2D y-normal frequency-domain field and power monitor. Figure 7.18 illustrates the results when the particle rotates 30° in the yz plane.

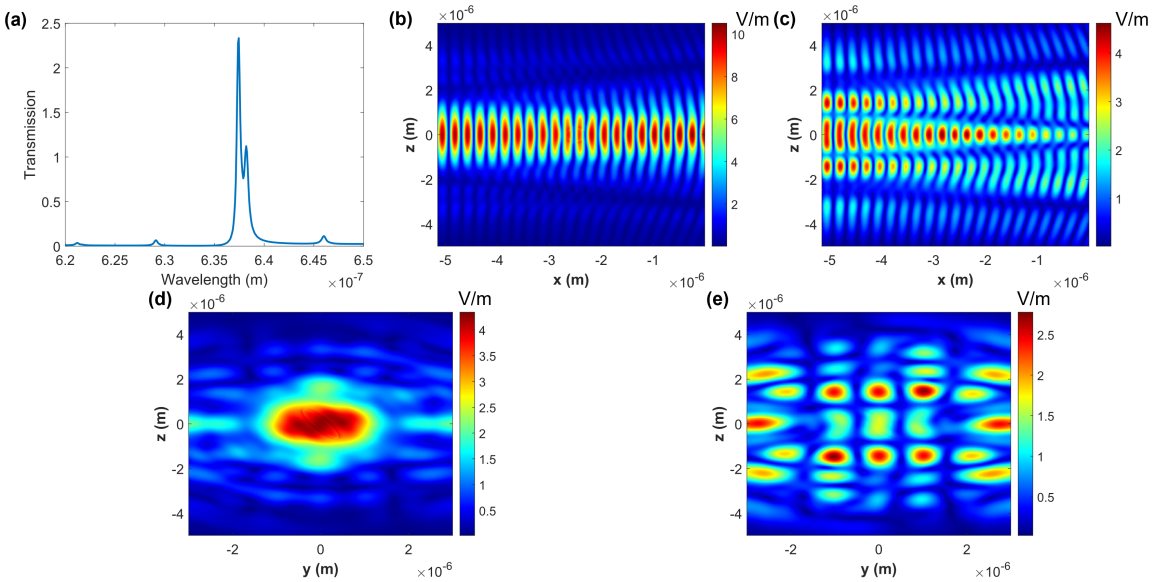


Figure 7.18: Results of the particle rotating 30° in the yz plane. (a) Transmission spectrum. (b), (c) Electric field between two mirrors of the xz plane at the wavelength of 637.44 nm and 638.2 nm. (d), (e) Electric field between two mirrors of the yz plane at the wavelength of 637.44 nm and 638.2 nm. These two wavelengths are the corresponding wavelengths of the split peak.

The wavelengths of the splits in the main peak were similar to before. Since the particle rotated in the yz plane, it was out of the plane when monitoring the electric field of the xz plane. The antinodes at 637.44 nm after the particle were smaller than previous scenarios and the hybridisations with higher-order modes were less at both wavelengths of the split peak, 647.44 nm and 638.2 nm. The electric field changes in the yz plane, the cross-section of an antinode, were also plotted at these two wavelengths. At 637.44 nm, the particle caused perturbation from the centre of the antinode and the shape of the antinode deviated from the Gaussian profile. At 638.2 nm, the edge of the particle could be seen around the position of $y = 0$, $z = 0$, and its impact changed the symmetry of the distribution.

In addition, the simulation where the particle had two different angles in different planes was performed. Figure 7.19 shows the transmission spectrum where the particle rotates 30° in the xy plane and 10° in the xz plane.

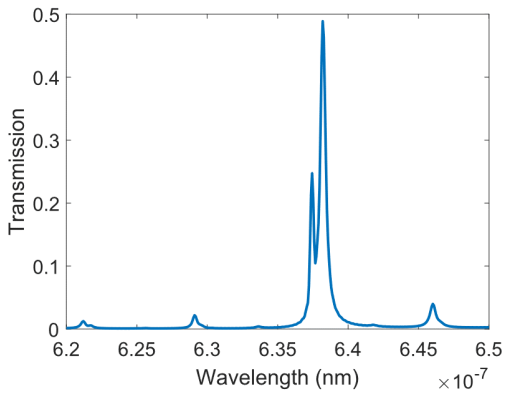


Figure 7.19: Transmitted spectrum with the particle at 30° in the xy plane and 10° in the xz plane.

Compared with the scenario of only 30° in xy plane illustrated in Figure 7.17(a), the transmission spectrum varies minimally. The two wavelengths of the split peak changed from 637.52 nm to 637.44 nm and from 638.27 nm to 638.2 nm. The absolute and the relative intensities of the two split peaks increased slightly.

7.3.3 Position of Rod-shaped Bacteria Particle

In the last section 7.3.2, the centre of the rod-shaped bacteria particle was at the centre of the mode, so it displayed the maximum spectrum splitting in response to the anisotropy of the particle. However, when the particle diffused through the microcavity, it was highly possible that it would not pass through the centre. Therefore, these situations were also explored. Figure 7.20 shows the simulation results where the particle is placed at z=1 µm away from the centre of the antinode with 50° from the x axis in the xy plane. The 2D x-normal frequency- domain field and power monitor placed after the concave mirror was the same as before while the 2D z-normal one between the two mirrors was placed at z = 1 µm away from the centre of the antinode. It was placed in the same xy plane as the particle stayed.

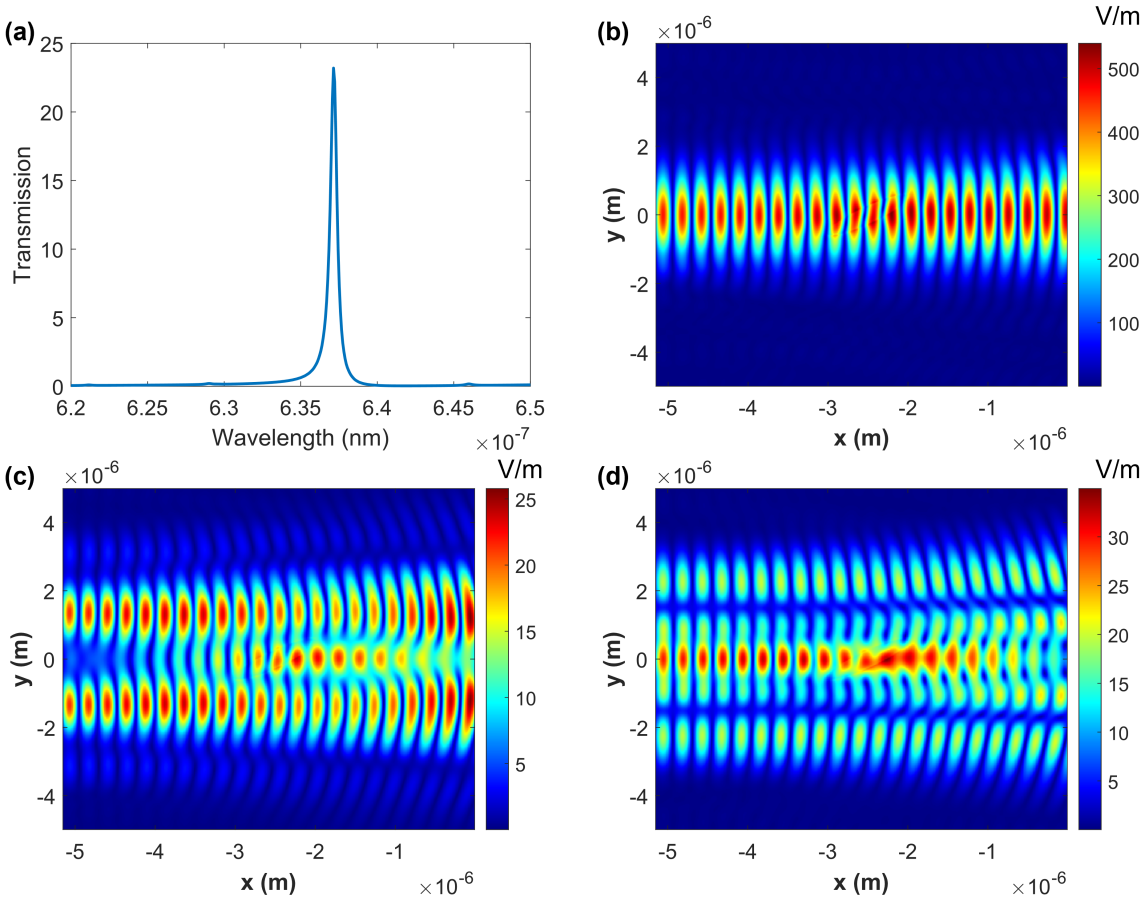


Figure 7.20: Simulation results of a particle placed at z=1 µm away from the centre of the antinode with a rotation angle of 50° from the x axis in the xy plane. (a) Transmission spectrum with the peak wavelength at 637.14 nm. (b)-(d) Electric field profiles between the two mirrors at wavelengths of 637.14 nm, 629.02 nm and 646.02 nm.

Different from the situation illustrated in Figure 7.17, the transmission spectrum (Figure 7.20(a)) only displayed one main peak at 637.14 nm. The two pretty small peaks on either side of the main peak shift to 629.02 nm and 646.02 nm with the electric field profiles presented in Figure 7.20(c) and (d). (c) elucidates higher-order modes of $q = 22$ with the perturbation of the particle. Higher-order modes of $q = 21$ are observed with the perturbation of the particle in (d).

As the splitting disappeared with the deviation of 1 µm in the z-direction, situations with smaller deviations were explored. Figure 7.21 manifests the scenario where

the particle was placed at y = 0.1 µm and z = 0.1 µm away from the centre of the antinode. The transmission monitor stays unchanged while the 2D z-normal one between the two mirrors was placed at z=0.1 µm away from the centre of the antinode with the rotation of 50° from the x axis in the xy plane.

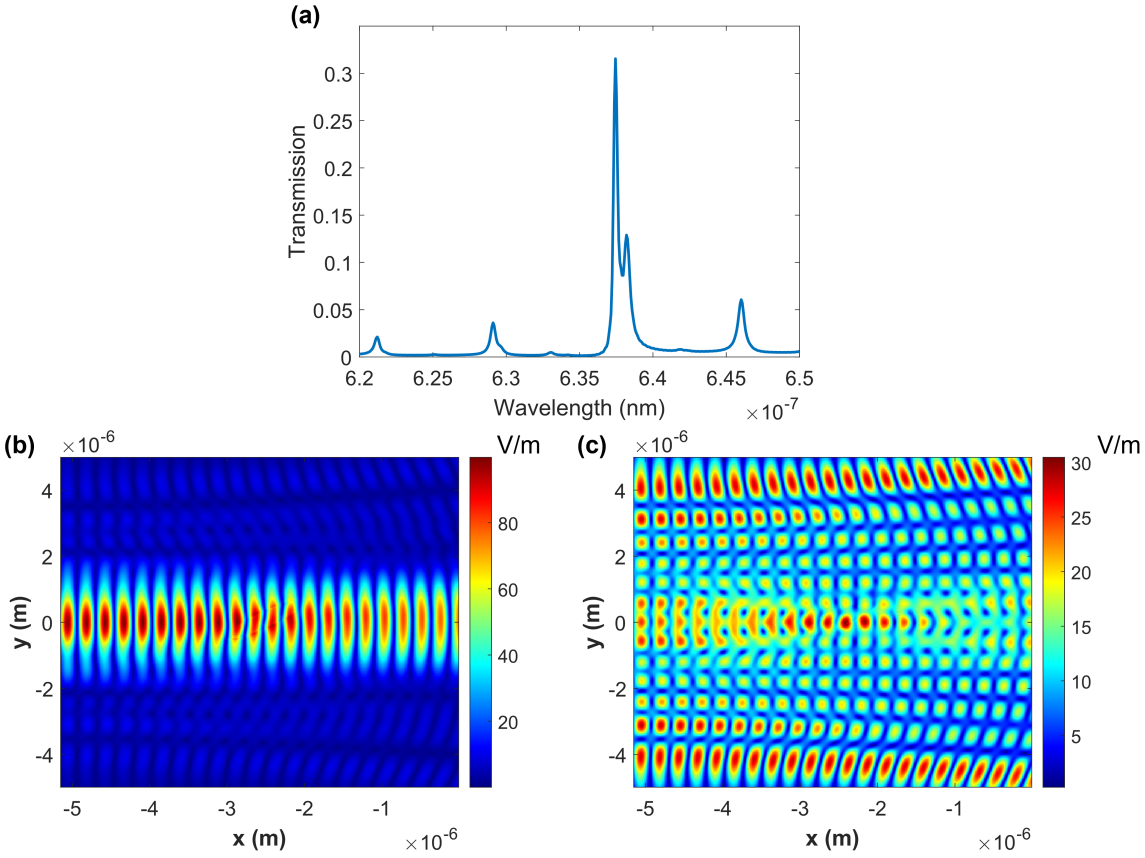


Figure 7.21: Simulation results of a particle placed at y=0.1 µm and z=0.1 µm away from the centre of the antinode with a rotation angle of 50° from the x axis in the xy plane. (a) Transmission spectrum with the split peak wavelength at 637.44 nm and 638.2 nm. (b)-(c) Electric field profiles between the two mirrors at wavelengths of 637.44 nm and 638.2 nm.

Compared with the 50° scenario where the particle was in the centre of the antinode in Figure 7.17(d), the wavelengths of the splits in the main peak remained the same. The electric fields at these two wavelengths exhibited little variation. The dip point changed from 637.74 nm to 637.9 nm. While the transmission at 637.44 nm altered insignificantly, the transmission at 638.2 nm attenuated dramatically. The tiny peaks

between 620 nm and 630 nm, 630 nm and 635 nm, 640nm and 645 nm either increased in transmission or even generated new peaks.

The same position with the particle at 30° from the x axis in the xy plane was also simulated. Figure 7.22 demonstrates the results.

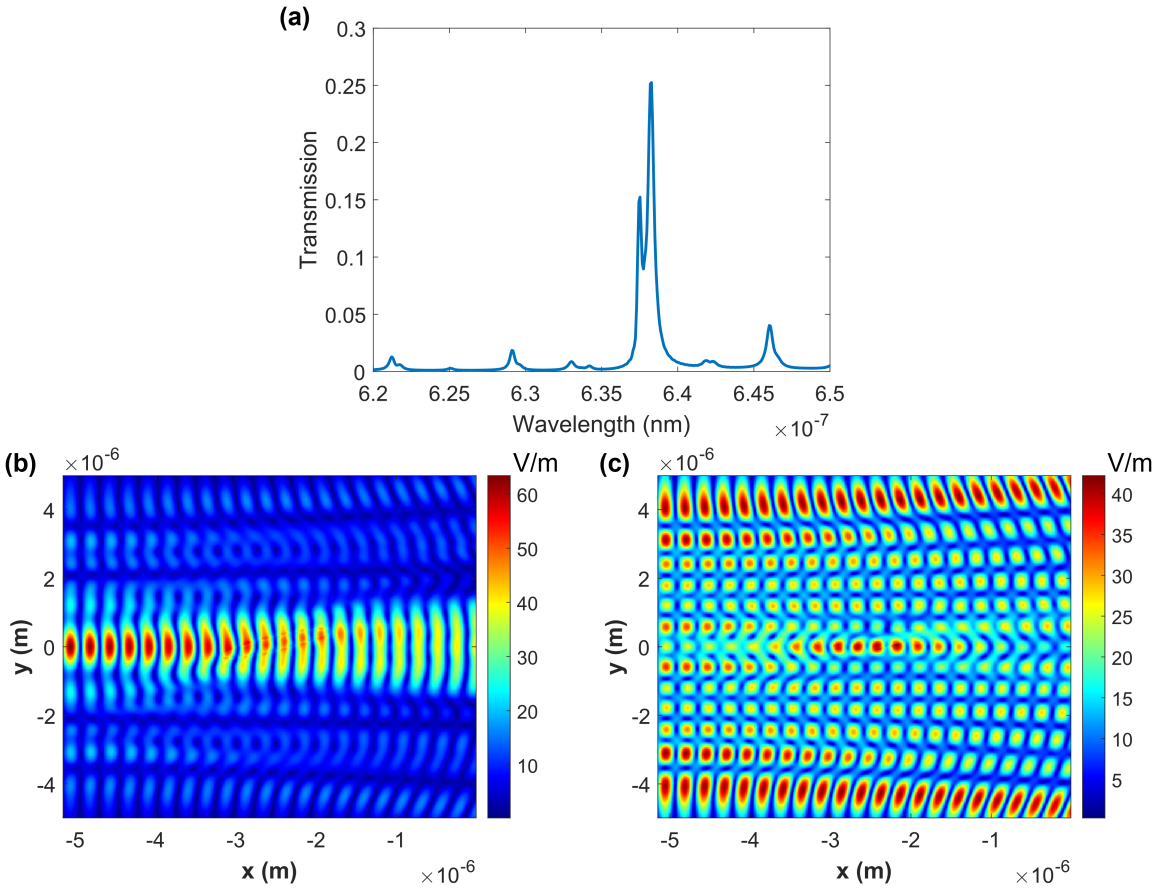


Figure 7.22: Simulation results of a particle placed at y=0.1 µm and z=0.1 µm away from the centre of the antinode with a rotation angle of 30° from the x axis in xy plane. (a) Transmission spectrum with the split peak wavelength at 637.52 nm and 638.27 nm. (b)-(c) Electric field profiles between the two mirrors at wavelengths of 637.52 nm and 638.27 nm.

Compared with the 30° situation where the particle was in the centre of the antinode in Figure 7.17(a), the wavelength of the split main peak shifted from 637.44 nm to 637.52 nm while the other stayed unchanged at 638.27 nm. The absolute and relative intensity of the two split peaks decreased slightly. The two small peaks adjacent to

the main peak on either side showed more splittings. The rest of the small peaks displayed negligible changes. Comparing the electric fields at these two wavelengths of the split peak, (b) demonstrated a marked difference while (c) did not display any prominent difference. The particle seemed to block the transmitted light and the intensities of the electric fields of antinodes after the particle attenuated significantly. However, in both situations, no new modes seemed to be generated. The different changes of 30° and 50° scenarios of the same position of the particle away from the centre confirmed the importance of the angular and translational displacements on the interaction between the particle and light.

7.4 Summary

<table>
<tr><th colspan="2">Monte Carlo</th><th>FDTD</th></tr>
<tr><td>Gold Nanorod</td><td>Rod-shaped Bacteria</td><td>Rod-shaped Bacteria</td></tr>
<tr><td>17.2 mW: free diffusion,
polar angle confirms $\sin\theta$ distribution</td><td>10 mW: trapped in one antinode,
polar angle confirms $\sin\theta$ distribution</td><td>Different orientations of the particle:
Different split peak, different perturbations</td></tr>
<tr><td>500 mW: trapped in different antinodes,
polar angle confirms $\sin\theta$ distribution</td><td>1 mW: free diffusion,
polar angle confirms $\sin\theta$ distribution</td><td rowspan="2">Different positions of the particle:
When away from the antinode for 1 μm,
splits of the peak disappear</td></tr>
<tr><td>5 W: trapped in one antinode,
polar angle deviates from $\sin\theta$ distribution</td><td></td></tr>
<tr><td colspan="2">Optical force plays a less important role in the rotation of a rod-shaped bacteria particle than a gold nanorod</td><td>The orientations and the positions of the particle in the microcavity perturbs the field of the microcavity differently.
No new mode is generated.</td></tr>
</table>

Table 7.1: Summary of the findings of Monte Carlo simulations and FDTD simulations.

The table above shows a summary of the findings of the simulations briefly. In this chapter, the results of theoretical simulations are discussed to understand the interactions between light and particles better and compare with the experimental insights. Two coordinate systems are constructed in Monte Carlo simulations to study the translational and rotational diffusions of gold nanorods and rod-shaped bacteria particles. Different intra-cavity light intensities, including ones used in the experiment,

are utilised to study the trajectories and angular distributions. The free diffusion of gold nanorods and the trapping behaviour of rod-shaped bacteria particles observed in the experiment are confirmed in the simulations. The simulations also explore the trapping behaviour of gold nanorods with a higher intra-cavity optical power and the free diffusion of rod-shaped bacteria particles with a lower intra-cavity optical power. Due to the different responses of metal and dielectric materials, which are not electric conductors, to light, gold nanorods display different behaviours from rod-shaped bacteria particles. When the intra-cavity light intensities increase, the optical torque plays a less important role in the rotational diffusion of a rod-shaped bacteria particle than a gold nanorod.

While Monte Carlo simulations can provide insights into the dynamic diffusions of the particle in the microcavity, they cannot offer information on the transmitted light. Therefore, FDTD simulations are also performed to monitor the changes a rod-shaped bacteria particle brings to the transmission spectrum and the electric field between the two mirrors. Combining the results of these two simulations offers a full picture of the experimental system. However, in FDTD simulations, the positions and orientations of particles have to be fixed, so dynamic processes cannot be achieved. Firstly, the empty cavity is simulated as the blank control sample, displaying a single main peak. When the rod-shaped bacteria particle is placed at the centre of one antinode, different rotating angles present different splittings of the main peak. Rotating in various planes and a combination of two rotating angles are examined. Moving the particle away from the centre of the antinode is simulated and compared with the scenarios when the particle is placed in the centre. The splitting of the main peak in the transmitted spectrum disappears at some point while the disturbances are still clearly visible in the electric field profile between the two mirrors. A smaller deviation from the centre displays differences while maintaining the splitting feature. This

simulation uncovers the disturbance of the particle to the mode profile and confirms that no new mode is generated in this interaction. It also sheds light on other smaller peaks apart from the main peak in the transmitted spectrum, which was not shown in the experiment. In this case, a single gold nanorod is not simulated since it is too small to generate a new Mie resonance mode.

Chapter 8

Conclusions and Outlook

This chapter summarises the key results of this dissertation and discusses potential research directions to explore in the future.

8.1 Conclusions

In this work, a novel method is proposed to perform the shape measurement of single rod-shaped particles in water, namely measuring the aspect ratio of each particle. This technique has been applied in metal and dielectric materials, specifically gold nanorods and rod-shaped bacteria particles. Shape measurement is worth exploring because it has applications in quality control of nanoparticle synthesis and water quality monitoring. Current particle characterisation techniques face limitations such as expensive equipment, highly technical skills, direct processing for liquid samples, single-particle analysis and materials applicability. The optical microcavity sensing method in this work can achieve single-particle analysis for both metal and dielectric materials with real-time monitoring. In addition, the whole apparatus can be miniaturised, displaying great potential in real-world applications.

The optical microcavity enhances the interaction between light and particles and

the open-access feature provides the direct introduction of solution samples to the system. The cavity length is scanned to always sweep through a resonance mode. The shape anisotropy of the particle perturbs the resonant mode generated by the circularly polarised incident light. By capturing the three Stokes parameters to analyse the polarisation state of the transmitted light through the microcavity, polarisability anisotropy parameters can be determined and thus the aspect ratio can be derived. A theoretical model is established to fit curves of Stokes parameters during the resonance. A single-particle event is detected and analysed for gold nanorods and rod-shaped bacteria particles. Statistical results of 30 particles for two types of gold nanorods are discussed and compared with SEM results and around 1% resolution is achieved. For the rod-shaped bacteria particles, the same theoretical model with changes in parameters related to material properties can be applied. However, in this scenario, the accuracy of determining the volume of a single particle impacts the accuracy of the aspect ratio, confirmed by both the theoretical and experimental findings.

Apart from the experimental results, theoretical simulations and calculations are performed to better understand the system and the interaction between particles and light. The theoretical simulations also confirm the diffusion state of gold nanorods and rod-shaped bacteria particles observed in the experiment. Monte Carlo simulations take finite steps in time and simulate the dynamic diffusion processes, including the translational and rotational diffusions of the particle. Different optical powers are employed to see the evolution of particle behaviour in these situations, including a free diffusion and a trapping scenario. Gold nanorods and rod-shaped bacteria particles exhibit differences in the trapping case with different extents of optical force dominance due to material intrinsic differences responding to light. FDTD simulations offer insights into the transmitted light spectrum and changes in the electric

field between the two mirrors to explore the essence of mode change. Rod-shaped bacteria particles are simulated and no new Mie resonance modes are generated, but hybridisations of higher-order modes from adjacent longitudinal modes are observed. Gold nanorods are too small to generate any Mie resonance mode, so they are not simulated. Although FDTD simulations cannot simulate dynamic processes while the particle diffuses, they act as a supplement to Monte Carlo simulations and these two simulations provide a systematic theoretical study of the system. Other theoretical calculations, such as diffusion over a single sweep, optical force and torque, generated heat and cross-section comparisons, are performed to evaluate the system.

8.2 Future Work

With all the accomplished work presented, there are aspects that can be improved on the current experiment and other research directions to look into. Firstly, the current experimental results are enough to demonstrate the method and show its advantages over existing particle analysis methods. However, it is worth increasing the number of particles measured and also expanding the aspect ratio measuring range with potential integrations of multiple laser wavelengths and different dielectric coatings of the optical microcavity if necessary. In this way, the robustness and the application of the system can be further confirmed and expanded. In addition, the difference between SEM results and the optical microcavity sensing technique needs to be looked into more carefully, and TEM could be used for further comparison.

Secondly, in this work, the volume plays a role in determining the accuracy of the aspect ratio, especially for rod-shaped bacteria particles and bigger gold nanorods where absorption does not dominate in the extinction cross-section. To simplify the processing, the averaged volume from SEM images was employed in the data analysis

of gold nanorods and the volume factor was treated as a fitting parameter for rod-shaped bacteria particles. However, it should be noted that not all the information provided by this apparatus has been utilised. The volume factor can in principle be established on a particle-by-particle basis within the same microcavity analysis apparatus, using either the magnitude of the mode shift [152] or the temporal autocorrelation function. Indeed these two parameters can be combined to establish the refractive index of the particle at the probe wavelength, removing the need for independent knowledge of the particle composition.

Thirdly, the data recording of current experiments can be improved. Taking the gold nanorod experiment as an example, the cavity length sweep was at 5 kHz giving a period of 200 ms while the FWHM of the resonance peak was only 1 µs. Collecting only part of the sweep to cover the resonance peak can enhance the efficiency of data collection. For real-world applications, all the data processing should be integrated together so that after collecting all the resonance peaks during a single-particle event, the aspect ratio can be displayed directly.

In addition, for the rod-shaped bacteria particles, a cavity with bigger RoC and lower reflectivity is worth attempting with the current experimental apparatus. It is also worth measuring other types of rod-shaped bacteria particles, such as E.coli, to compare whether there are any differences between different bacteria. Another research direction is the fixed cavity, which utilises a bigger cavity RoC and a bigger cavity length so that the cavity is always at resonance without locking. It uses the superluminescent diode as the light source. This has been employed to perform absorption experiments in our group, and the combination of this idea with my work should generate dynamic time-evolved Stokes parameter signals, from which the aspect ratio can be extracted with a new theoretical model adapted from the current

one.

The samples measured in the experiments were monodisperse with a distribution width of the aspect ratio. It should be possible to measure a polydisperse sample with different aspect ratios and even different materials after integrating the aspect ratio analysis with the combination of the magnitude of the mode shift and the temporal autocorrelation function mentioned above. If all the measured particles do not deviate much in the volume, the same type of diffusion behaviours will be ensured, namely either they all undergo free diffusion or get trapped in the microcavity. Then every particle, no matter what material they are and what aspect ratio they have, should have a similar possibility of diffusing through the microcavity and the measured results can be treated as a randomly selected sample group from the original population. Therefore with the distribution of aspect ratio measurement, the composition of the mixed sample can also be determined and with a bigger sample size, it should be closer to the real composition. In addition, it is also interesting to observe a dynamic change in aspect ratio. For example, the aspect ratio of gold nanorods changes with heat.

Based on the success of the current experiment in the quantitative measurement of rod-shaped particles, more complex shapes are worth exploring, like disk shape, star shape, etc. Certainly, it will be rather difficult to deduce explicit equations for measured Stokes parameters and perform fitting to extract polarisability anisotropy parameters as what was done for rod-shaped particles. However, since the signals are sensitive to the shape of the particle, it is possible that machine learning algorithms can select certain features in signals and achieve species-specific identifications. If this can be achieved, then the classification of different shapes in a mixture sample can also be investigated.

References

1. Li, T. *et al.* Denary oxide nanoparticles as highly stable catalysts for methane combustion. *Nature Catalysis* **4,** 62–70 (2021).
2. Xie, C., Niu, Z., Kim, D., Li, M. & Yang, P. Surface and interface control in nanoparticle catalysis. *Chemical Reviews* **120,** 1184–1249 (2019).
3. Astruc, D. Introduction: nanoparticles in catalysis. *Chemical Reviews* **120,** 461–463 (2020).
4. Sattler, K. D. *Handbook of nanophysics: nanoparticles and quantum dots* (CRC press, 2016).
5. Kelly, K. L., Coronado, E., Zhao, L. L. & Schatz, G. C. The optical properties of metal nanoparticles: the influence of size, shape, and dielectric environment. *The Journal of Physical Chemistry B* **107,** 668–677 (2003).
6. El-Sayed, M. A. Some interesting properties of metals confined in time and nanometer space of different shapes. *Accounts of chemical research* **34,** 257–264 (2001).
7. Taylor, S. *Postharvest handling: a systems approach* (Academic Press, 2012).
8. Li, D. & Liu, S. *Water quality monitoring and management: Basis, technology and case studies* (Academic Press, 2018).
9. Albrecht, T. & Baron, S. *Medical microbiology* (University of Texas Medical Branch at Galveston, Dept. of Microbiology and Immunology, 1996).

10. De Jong, W. H. & Borm, P. J. Drug delivery and nanoparticles: applications and hazards. *International Journal of Nanomedicine* **3,** 133–149 (2008).

11. Blanco, E., Shen, H. & Ferrari, M. Principles of nanoparticle design for overcoming biological barriers to drug delivery. *Nature Biotechnology* **33,** 941–951 (2015).

12. Mitchell, M. J. *et al.* Engineering precision nanoparticles for drug delivery. *Nature Reviews Drug Discovery* **20,** 101–124 (2021).

13. Tan, H. W., An, J., Chua, C. K. & Tran, T. Metallic nanoparticle inks for 3D printing of electronics. *Advanced Electronic Materials* **5,** 1800831 (2019).

14. Su, M. *et al.* Nanoparticle based curve arrays for multirecognition flexible electronics. *Advanced Materials* **28,** 1369–1374 (2016).

15. Guisbiers, G., Van Overschelde, O. & Wautelet, M. Theoretical investigation of size and shape effects on the melting temperature and energy bandgap of TiO2 nanostructures. *Applied Physics Letters* **92** (2008).

16. You, Y., He, L., Ma, B. & Chen, T. High-drug-loading mesoporous silica nanorods with reduced toxicity for precise cancer therapy against nasopharyngeal carcinoma. *Advanced Functional Materials* **27,** 1703313 (2017).

17. Chen, Y., Chen, H. & Shi, J. In vivo bio-safety evaluations and diagnostic/therapeutic applications of chemically designed mesoporous silica nanoparticles. *Advanced Materials* **25,** 3144–3176 (2013).

18. Chen, Y. *et al.* Hollow mesoporous organosilica nanoparticles: a generic intelligent framework-hybridization approach for biomedicine. *Journal of the American Chemical Society* **136,** 16326–16334 (2014).

19. Agency, U. S. E. P. *Legionella : Drinking water fact sheet* Accessed: 5-3-2019.

20. Tuttle, A. R., Trahan, N. D. & Son, M. S. Growth and maintenance of Escherichia coli laboratory strains. *Current protocols* **1,** e20 (2021).

21. Hübschen, G., Altpeter, I., Tschuncky, R. & Herrmann, H.-G. *Materials characterization using nondestructive evaluation (NDE) methods* (Woodhead Publishing, 2016).

22. Zhou, W. & Wang, Z. L. *Scanning microscopy for nanotechnology: techniques and applications* (Springer Science & Business Media, 2007).

23. Garche, J. *et al. Encyclopedia of electrochemical power sources* (Newnes, 2013).

24. Goldstein, J. I. *et al. Scanning electron microscopy and X-ray microanalysis* (springer, 2017).

25. Mondini, S., Ferretti, A., Puglisi, A. & Ponti, A. PEBBLES and PEBBLEJUGGLER: software for accurate, unbiased, and fast measurement and analysis of nanoparticle morphology from transmission electron microscopy (TEM) micrographs. *Nanoscale* **4,** 5356–5372 (2012).

26. Ram, S. Image processing with ImageJ. *Biophoton Int* **11** (2004).

27. Lee, B. *et al.* Statistical Characterization of the Morphologies of Nanoparticles through Machine Learning Based Electron Microscopy Image Analysis. *ACS Nano* **14,** 17125–17133 (2020).

28. Sprünken, D. P. *et al.* Influence of the local environment on determining aspect-ratio distributions of gold nanorods in solution using Gans theory. *The Journal of Physical Chemistry C* **111,** 14299–14306 (2007).

29. Liv, N., Lazić, I., Kruit, P. & Hoogenboom, J. P. Scanning electron microscopy of individual nanoparticle bio-markers in liquid. *Ultramicroscopy* **143,** 93–99 (2014).

30. Sawyer, L., Grubb, D. T. & Meyers, G. F. *Polymer microscopy* (Springer Science & Business Media, 2008).

31. Brydson, R. *Aberration-corrected analytical transmission electron microscopy* (Wiley Online Library, 2011).

32. Erni, R. *Aberration-corrected imaging in transmission electron microscopy: An introduction* (World Scientific Publishing Company, 2015).

33. Ayache, J., Beaunier, L., Boumendil, J., Ehret, G. & Laub, D. *Sample preparation handbook for transmission electron microscopy: techniques* (Springer Science & Business Media, 2010).

34. Nielsen, M. H., Aloni, S. & De Yoreo, J. J. In situ TEM imaging of CaCO3 nucleation reveals coexistence of direct and indirect pathways. *Science* **345,** 1158–1162 (2014).

35. Smeets, P. J., Cho, K. R., Kempen, R. G., Sommerdijk, N. A. & De Yoreo, J. J. Calcium carbonate nucleation driven by ion binding in a biomimetic matrix revealed by in situ electron microscopy. *Nature Materials* **14,** 394–399 (2015).

36. Williamson, M., Tromp, R., Vereecken, P., Hull, R. & Ross, F. Dynamic microscopy of nanoscale cluster growth at the solid–liquid interface. *Nature Materials* **2,** 532–536 (2003).

37. De Yoreo, J. J. & NAJM, S. Investigating materials formation with liquid-phase and cryogenic TEM. *Nature Reviews Materials* **1,** 1–18 (2016).

38. Kim, B. H. *et al.* Liquid-phase transmission electron microscopy for studying colloidal inorganic nanoparticles. *Advanced Materials* **30,** 1703316 (2018).

39. Ohi, M., Li, Y., Cheng, Y. & Walz, T. Negative staining and image classification—powerful tools in modern electron microscopy. *Biological Procedures Online* **6,** 23–34 (2004).

40. Harris, R., Bhella, D. & Adrian, M. Recent developments in negative staining for transmission electron microscopy. *Microscopy and Analysis* **113,** 17 (2006).

41. Chaffey, N. *Principles and techniques of electron microscopy: biological applications. 4th edn* 2001.

42. Brenner, S. & Horne, R. A negative staining method for high resolution electron microscopy of viruses. *Biochimica et Biophysica Acta* **34,** 103–110 (1959).

43. De Carlo, S. & Harris, J. R. Negative staining and cryo-negative staining of macromolecules and viruses for TEM. *Micron* **42,** 117–131 (2011).

44. Harris, J. R., Gebauer, W. & Markl, J. Keyhole limpet haemocyanin: negative staining in the presence of trehalose. *Micron* **26,** 25–33 (1995).

45. Harris, J. R. *Negative staining and cryoelectron microscopy: the thin film techniques* (Garland Science, 2023).

46. Hirai, T., Murata, K., Mitsuoka, K., Kimura, Y. & Fujiyoshi, Y. Trehalose embedding technique for high-resolution electron crystallography: application to structural study on bacteriorhoposin. *Microscopy* **48,** 653–658 (1999).

47. Harris, J. R. & Scheffler, D. Routine preparation of air-dried negatively stained and unstained specimens on holey carbon support films: a review of applications. *Micron* **33,** 461–480 (2002).

48. Harris, J. R., Adrian, M. & Petry, F. Structure of the Cryptosporidium parvum microneme: a metabolically and osmotically labile apicomplexan organelle. *Micron* **34,** 65–78 (2003).

49. Adrian, M., Dubochet, J., Lepault, J. & McDowall, A. W. Cryo-electron microscopy of viruses. *Nature* **308,** 32–36 (1984).

50. Adrian, M., Dubochet, J., Fuller, S. D. & Harris, J. R. Cryo-negative staining. *Micron* **29,** 145–160 (1998).

51. Robin Harris, J. & Adrian, M. Preparation of thin-film frozen-hydrated/vitrified biological specimens for cryoelectron microscopy. *Electron Microscopy Methods and Protocols,* 31–48 (1999).

52. De Carlo, S., El-Bez, C., Alvarez-Rua, C., Borge, J. & Dubochet, J. Cryo-negative staining reduces electron-beam sensitivity of vitrified biological particles. *Journal of Structural Biology* **138,** 216–226 (2002).

53. Nogal, B., Bowman, C. A. & Ward, A. B. Time-course, negative-stain electron microscopy–based analysis for investigating protein–protein interactions at the single-molecule level. *Journal of Biological Chemistry* **292,** 19400–19410 (2017).

54. Harris, J. R. Immunonegative staining: epitope localization on macromolecules. *Methods* **10,** 234–246 (1996).

55. Fernandez-Leiro, R. & Scheres, S. H. Unravelling biological macromolecules with cryo-electron microscopy. *Nature* **537,** 339–346 (2016).

56. Taylor, K. A. & Glaeser, R. M. Electron diffraction of frozen, hydrated protein crystals. *Science* **186,** 1036–1037 (1974).

57. Scheres, S. H. *et al.* Disentangling conformational states of macromolecules in 3D-EM through likelihood optimization. *Nature methods* **4,** 27–29 (2007).

58. Lyumkis, D., Brilot, A. F., Theobald, D. L. & Grigorieff, N. Likelihood-based classification of cryo-EM images using FREALIGN. *Journal of structural biology* **183,** 377–388 (2013).

59. De Oliveira Jr, O., Marystela, F. L., de Lima Leite, F. & Da Róz, A. L. *Nanocharacterization techniques* (William Andrew, 2017).

60. Berne, B. J. & Pecora, R. *Dynamic light scattering: with applications to chemistry, biology, and physics* (Courier Corporation, 2000).

61. Schmitz, K. S. *Introduction to dynamic light scattering by macromolecules* (Elsevier, 2012).

62. Sedlák, M. What can be seen by static and dynamic light scattering in polyelectrolyte solutions and mixtures? *Langmuir* **15,** 4045–4051 (1999).

63. Malm, A. V. & Corbett, J. C. Improved dynamic light scattering using an adaptive and statistically driven time resolved treatment of correlation data. *Scientific Reports* **9,** 13519 (2019).

64. Jana, N. R., Earhart, C. & Ying, J. Y. Synthesis of water-soluble and functionalized nanoparticles by silica coating. *Chemistry of Materials* **19,** 5074–5082 (2007).

65. Glidden, M. & Muschol, M. Characterizing gold nanorods in solution using depolarized dynamic light scattering. *The Journal of Physical Chemistry C* **116,** 8128–8137 (2012).

66. Geers, C. *et al.* A new angle on dynamic depolarized light scattering: number-averaged size distribution of nanoparticles in focus. *Nanoscale* **8,** 15813–15821 (2016).

67. Tirado, M. M., Martínez, C. L. & de la Torre, J. G. Comparison of theories for the translational and rotational diffusion coefficients of rod-like macromolecules. Application to short DNA fragments. *The Journal of Chemical Physics* **81,** 2047–2052 (1984).

68. De la Torre, J. G. & Bloomfield, V. A. Hydrodynamic properties of complex, rigid, biological macromolecules: theory and applications. *Quarterly Reviews of Biophysics* **14,** 81–139 (1981).

69. Perrin, F. Mouvement Brownien d'un ellipsoide (II). Rotation libre et dépolarisation des fluorescences. Translation et diffusion de molécules ellipsoidales. *Journal de Physique et le Radium* **7,** 1–11 (1936).

70. Kim, A., Ng, W. B., Bernt, W. & Cho, N.-J. Validation of size estimation of nanoparticle tracking analysis on polydisperse macromolecule assembly. *Scientific Reports* **9,** 2639 (2019).

71. Crank, J. *The mathematics of diffusion* (Oxford University Press, 1979).

72. Hodoroaba, V.-D., Unger, W. & Shard, A. *Characterization of nanoparticles: measurement processes for nanoparticles* (Elsevier, 2019).

73. Filipe, V., Hawe, A. & Jiskoot, W. Critical evaluation of Nanoparticle Tracking Analysis (NTA) by NanoSight for the measurement of nanoparticles and protein aggregates. *Pharmaceutical Research* **27,** 796–810 (2010).

74. Kashkanova, A. D., Blessing, M., Gemeinhardt, A., Soulat, D. & Sandoghdar, V. Precision size and refractive index analysis of weakly scattering nanoparticles in polydispersions. *Nature Methods* **19,** 586–593 (2022).

75. Koch, A. L. & Ehrenfeld, E. The size and shape of bacteria by light scattering measurements. *Biochimica et Biophysica Acta (BBA)-General Subjects* **165,** 262–273 (1968).

76. Koch, A. L. Theory of the angular dependence of light scattered by bacteria and similar-sized biological objects. *Journal of Theoretical Biology* **18,** 133–156 (1968).

77. Wyatt, P. J. Differential light scattering: a physical method for identifying living bacterial cells. *Applied Optics* **7,** 1879–1896 (1968).

78. Wyatt, P. J. Identification of bacteria by differential light scattering. *Nature* **221,** 1257–1258 (1969).

79. Van De Merwe, W. P., Czégé, J., Milham, M. E. & Bronk, B. V. Rapid optically based measurements of diameter and length for spherical or rod-shaped bacteria in vivo. *Applied Optics* **43,** 5295–5302 (2004).

80. Bronk, B. V., Druger, S. D., Czege, J. & Van De Merwe, W. P. Measuring diameters of rod-shaped bacteria in vivo with polarized light scattering. *Biophysical Journal* **69,** 1170–1177 (1995).

81. Jo, Y. *et al.* Angle-resolved light scattering of individual rod-shaped bacteria based on Fourier transform light scattering. *Scientific Reports* **4,** 5090 (2014).

82. Lindfors, K., Kalkbrenner, T., Stoller, P. & Sandoghdar, V. Detection and spectroscopy of gold nanoparticles using supercontinuum white light confocal microscopy. *Physical Review Letters* **93,** 037401 (2004).

83. Taylor, R. W. & Sandoghdar, V. Interferometric scattering microscopy: seeing single nanoparticles and molecules via Rayleigh scattering. *Nano Letters* **19,** 4827–4835 (2019).

84. Kukura, P., Celebrano, M., Renn, A. & Sandoghdar, V. Imaging a single quantum dot when it is dark. *Nano Letters* **9,** 926–929 (2009).

85. Kukura, P., Celebrano, M., Renn, A. & Sandoghdar, V. Single-molecule sensitivity in optical absorption at room temperature. *The Journal of Physical Chemistry Letters* **1,** 3323–3327 (2010).

86. Taylor, R. W. & Sandoghdar, V. in *Label-free super-resolution microscopy* 25–65 (Springer, 2019).

87. Zernike, F. Diffraction theory of the knife-edge test and its improved form, the phase-contrast method. *Monthly Notices of the Royal Astronomical Society* **94,** 377–384 (1934).

88. Zernike, F. The concept of degree of coherence and its application to optical problems. *Physica* **5,** 785–795 (1938).

89. Zernike, F. How I discovered phase contrast. *Science* **121,** 345–349 (1955).

90. Zernike, F. Phase contrast, a new method for the microscopic observation of transparent objects. *Physica* **9,** 686–698 (1942).

91. Zernike, F. Phase contrast, a new method for the microscopic observation of transparent objects part II. *Physica* **9,** 974–986 (1942).

92. Nomarski, G. *Dispositif Oculaire a Contraste De phase pour microscope* in *Journal De Physique Et Le Radium* **11** (1950), S9–S10.

93. Ignatovich, F. V. & Novotny, L. Real-time and background-free detection of nanoscale particles. *Physical Review Letters* **96,** 013901 (2006).

94. Jacobsen, V., Stoller, P., Brunner, C., Vogel, V. & Sandoghdar, V. Interferometric optical detection and tracking of very small gold nanoparticles at a water-glass interface. *Optics Express* **14,** 405–414 (2006).

95. Liebel, M., Hugall, J. T. & Van Hulst, N. F. Ultrasensitive label-free nanosensing and high-speed tracking of single proteins. *Nano Letters* **17,** 1277–1281 (2017).

96. Cole, D., Young, G., Weigel, A., Sebesta, A. & Kukura, P. Label-free single-molecule imaging with numerical-aperture-shaped interferometric scattering microscopy. *ACS Photonics* **4,** 211–216 (2017).

97. Holanová, K., Vala, M. & Piliarik, M. Optical imaging and localization of prospective scattering labels smaller than a single protein. *Optics & Laser Technology* **109,** 323–327 (2019).

98. Ewers, H. *et al.* Label-free optical detection and tracking of single virions bound to their receptors in supported membrane bilayers. *Nano Letters* **7,** 2263–2266 (2007).

99. Daaboul, G. *et al.* High-throughput detection and sizing of individual low-index nanoparticles and viruses for pathogen identification. *Nano Letters* **10,** 4727–4731 (2010).

100. Ortega Arroyo, J. *et al.* Label-free, all-optical detection, imaging, and tracking of a single protein. *Nano Letters* **14,** 2065–2070 (2014).

101. Piliarik, M. & Sandoghdar, V. Direct optical sensing of single unlabelled proteins and super-resolution imaging of their binding sites. *Nature Communications* **5,** 4495 (2014).

102. Lee, I.-B. *et al.* Interferometric scattering microscopy with polarization-selective dual detection scheme: capturing the orientational information of anisotropic nanometric objects. *ACS Photonics* **5,** 797–804 (2017).

103. Dastjerdi, H. M. *et al.* Optimized analysis for sensitive detection and analysis of single proteins via interferometric scattering microscopy. *Journal of Physics D: Applied Physics* **55,** 054002 (2021).

104. Dahmardeh, M., Mirzaalian Dastjerdi, H., Mazal, H., Köstler, H. & Sandoghdar, V. Self-supervised machine learning pushes the sensitivity limit in label-free detection of single proteins below 10 kDa. *Nature Methods* **20,** 442–447 (2023).

105. Gu, Y., Sun, W., Wang, G. & Fang, N. Single particle orientation and rotation tracking discloses distinctive rotational dynamics of drug delivery vectors on live cell membranes. *Journal of the American Chemical Society* **133,** 5720–5723 (2011).

106. Pluta, M. *Advanced Light Microscopy: Measuring Techniques* (PWN, 1988).

107. Wang, G., Sun, W., Luo, Y. & Fang, N. Resolving rotational motions of nano-objects in engineered environments and live cells with gold nanorods and differential interference contrast microscopy. *Journal of the American Chemical Society* **132,** 16417–16422 (2010).

108. Saxton, M. J. Single-particle tracking: connecting the dots. *Nature Methods* **5,** 671–672 (2008).

109. Zhang, P. *et al.* Analyzing complex single-molecule emission patterns with deep learning. *Nature Methods* **15,** 913–916 (2018).

110. Zhong, Y., Li, C., Zhou, H. & Wang, G. Developing noise-resistant three-dimensional single particle tracking using deep neural networks. *Analytical Chemistry* **90,** 10748–10757 (2018).

111. Song, D. *et al.* Deep Learning-Assisted Automated Multidimensional Single Particle Tracking in Living Cells. *Nano Letters* **24,** 3082–3088 (2024).

112. Link, S., Mohamed, M. B. & El-Sayed, M. Simulation of the optical absorption spectra of gold nanorods as a function of their aspect ratio and the effect of the medium dielectric constant. *The Journal of Physical Chemistry B* **103,** 3073–3077 (1999).

113. Yan, B., Yang & Wang, Y. Comment on "simulation of the optical absorption spectra of gold nanorods as a function of their aspect ratio and the effect of the medium dielectric constant". *The Journal of Physical Chemistry B* **107,** 9159–9159 (2003).

114. Link, S. & El-Sayed, M. Simulation of the optical absorption spectra of gold nanorods as a function of their aspect ratio and the effect of the medium dielectric constant. *The Journal of Physical Chemistry B* **109,** 10531–10532 (2005).

115. Houck, M. M. & Siegel, J. A. *Fundamentals of Forensic Science* (Academic Press, 2015).

116. Gans, R. Über die form ultramikroskopischer silberteilchen. *Annalen der Physik* **352,** 270–284 (1915).

117. Papavassiliou, G. C. Optical properties of small inorganic and organic metal particles. *Progress in Solid State Chemistry* **12,** 185–271 (1979).

118. Mie, G. Beiträge zur Optik trüber Medien, speziell kolloidaler Metallösungen. *Annalen der Physik* **330,** 377–445 (1908).

119. Eustis, S. & El-Sayed, M. A. Determination of the aspect ratio statistical distribution of gold nanorods in solution from a theoretical fit of the observed inhomogeneously broadened longitudinal plasmon resonance absorption spectrum. *Journal of Applied Physics* **100,** 044324 (2006).

120. Kumar, R. *et al.* Determination of the Aspect-ratio Distribution of Gold Nanorods in a Colloidal Solution using UV-visible absorption spectroscopy. *Scientific Reports* **9,** 17469 (2019).

121. Das, S. Binary solutions for overdetermined systems of linear equations. *arXiv preprint arXiv:1101.3056* (2011).

122. Purcell, E. M. & Pennypacker, C. R. Scattering and absorption of light by nonspherical dielectric grains. *Astrophysical Journal* **186,** 705–714 (1973).

123. Draine, B. T. & Flatau, P. J. Discrete-dipole approximation for scattering calculations. *Josa a* **11,** 1491–1499 (1994).

124. Ekici, O. *et al.* Thermal analysis of gold nanorods heated with femtosecond laser pulses. *Journal of Physics D: Applied Physics* **41,** 185501 (2008).

125. Yurkin, M. A. & Hoekstra, A. G. The discrete-dipole-approximation code ADDA: Capabilities and known limitations. *Journal of Quantitative Spectroscopy and Radiative Transfer* **112,** 2234–2247 (2011).

126. Brioude, A., Jiang, X. & Pileni, M. Optical properties of gold nanorods: DDA simulations supported by experiments. *The Journal of Physical Chemistry B* **109,** 13138–13142 (2005).

127. Slaughter, L. S. *et al.* Single-particle spectroscopy of gold nanorods beyond the quasi-static limit: varying the width at constant aspect ratio. *The Journal of Physical Chemistry C* **114,** 4934–4938 (2010).

128. Gage, S. H. Modern dark-field microscopy and the history of its development. *Transactions of the American Microscopical Society* **39,** 95–141 (1920).

129. Calvo, R. *et al.* Size characterization of plasmonic nanoparticles with dark-field single particle spectrophotometry. *Scientific Reports* **12,** 17231 (2022).

130. Wagner, T., Lipinski, H.-G. & Wiemann, M. Dark field nanoparticle tracking analysis for size characterization of plasmonic and non-plasmonic particles. *Journal of nanoparticle research* **16,** 1–10 (2014).

131. Fabry, C. Theorie et applications d'une nouvelle methods de spectroscopie intereferentielle. *Ann. Chim. Ser. 7* **16,** 115–144 (1899).

132. Pérot, A. & Fabry, C. On the application of interference phenomena to the solution of various problems of spectroscopy and metrology. *Astrophysical Journal* **9,** 87 (1899).

133. Atherton, P., Reay, N. K., Ring, J. & Hicks, T. Tunable fabry-perot filters. *Optical Engineering* **20,** 806–814 (1981).

134. Fowles, G. R. *Introduction to modern optics* (Courier Corporation, 1989).

135. Vahala, K. J. Optical microcavities. *Nature* **424,** 839–846 (2003).

136. Kavokin, A. V., Baumberg, J. J., Malpuech, G. & Laussy, F. P. *Microcavities* (Oxford university press, 2017).

137. Trupke, M. *et al.* Microfabricated high-finesse optical cavity with open access and small volume. *Applied Physics Letters* **87,** 211106 (2005).

138. Trupke, M. *et al.* Atom detection and photon production in a scalable, open, optical microcavity. *Physical Review Letters* **99,** 063601 (2007).

139. Steinmetz, T. *et al.* Stable fiber-based Fabry-Pérot cavity. *Applied Physics Letters* **89,** 111110 (2006).

140. Muller, A., Flagg, E. B., Metcalfe, M., Lawall, J. & Solomon, G. S. Coupling an epitaxial quantum dot to a fiber-based external-mirror microcavity. *Applied Physics Letters* **95,** 173101 (2009).

141. Cui, G. *et al.* A hemispherical, high-solid-angle optical micro-cavity for cavity-QED studies. *Optics Express* **14,** 2289–2299 (2006).

142. Dolan, P. R., Hughes, G. M., Grazioso, F., Patton, B. R. & Smith, J. M. Femtoliter tunable optical cavity arrays. *Optics Letters* **35,** 3556–3558 (2010).

143. Trichet, A. A., Dolan, P. R., Coles, D. M., Hughes, G. M. & Smith, J. M. Topographic control of open-access microcavities at the nanometer scale. *Optics Express* **23,** 17205–17216 (2015).

144. Muller, A., Flagg, E. B., Lawall, J. R. & Solomon, G. S. Ultrahigh-finesse, low-mode-volume Fabry–Perot microcavity. *Optics Letters* **35,** 2293–2295 (2010).

145. Bitarafan, M. H. & DeCorby, R. G. On-chip high-finesse Fabry-Perot microcavities for optical sensing and quantum information. *Sensors* **17,** 1748 (2017).

146. Benedikter, J. *et al.* Transverse-mode coupling and diffraction loss in tunable Fabry–Pérot microcavities. *New Journal of Physics* **17,** 053051 (2015).

147. Uphoff, M., Brekenfeld, M., Rempe, G. & Ritter, S. Frequency splitting of polarization eigenmodes in microscopic Fabry–Perot cavities. *New Journal of Physics* **17,** 013053 (2015).

148. Ortiz-Huerta, F. *et al.* Fabrication of hybrid Fabry-Pérot microcavity using two-photon lithography for single-photon sources. *Optics Express* **26,** 33245–33252 (2018).

149. Hunger, D. *et al.* A fiber Fabry–Perot cavity with high finesse. *New Journal of Physics* **12,** 065038 (2010).

150. Trichet, A. *et al.* Open-access optical microcavities for lab-on-a-chip refractive index sensing. *Lab on a Chip* **14,** 4244–4249 (2014).

151. Vallance, C., Trichet, A. A., James, D., Dolan, P. R. & Smith, J. M. Open-access microcavities for chemical sensing. *Nanotechnology* **27,** 274003 (2016).

152. Trichet, A. *et al.* Nanoparticle trapping and characterization using open microcavities. *Nano Letters* **16,** 6172–6177 (2016).

153. Malmir, K., Okell, W., Trichet, A. A. & Smith, J. M. Characterization of nanoparticle size distributions using a microfluidic device with integrated optical microcavities. *Lab on a Chip* **22,** 3499–3507 (2022).

154. Johnson, S. *et al.* Tunable cavity coupling of the zero phonon line of a nitrogen-vacancy defect in diamond. *New Journal of Physics* **17,** 122003 (2015).

155. Dolan, P. *et al.* Robust, tunable, and high purity triggered single photon source at room temperature using a nitrogen-vacancy defect in diamond in an open microcavity. *Optics Express* **26,** 7056–7065 (2018).

156. Colombe, Y. *et al.* Strong atom–field coupling for Bose–Einstein condensates in an optical cavity on a chip. *Nature* **450,** 272–276 (2007).

157. Gallego, J. *et al.* Strong Purcell effect on a neutral atom trapped in an open fiber cavity. *Physical Review Letters* **121,** 173603 (2018).

158. Pscherer, A. *et al.* Single-molecule vacuum Rabi splitting: Four-wave mixing and optical switching at the single-photon level. *Physical Review Letters* **127,** 133603 (2021).

159. Khudaverdyan, M. *et al.* Quantum jumps and spin dynamics of interacting atoms in a strongly coupled atom-cavity system. *arXiv preprint arXiv:0901.3738* (2009).

160. Kalb, N., Reiserer, A., Ritter, S. & Rempe, G. Heralded storage of a photonic quantum bit in a single atom. *Physical Review Letters* **114,** 220501 (2015).

161. Kuhn, A., Hennrich, M. & Rempe, G. Deterministic single-photon source for distributed quantum networking. *Physical Review Letters* **89,** 067901 (2002).

162. Pfeifer, H. *et al.* Achievements and perspectives of optical fiber Fabry–Perot cavities. *Applied Physics B* **128,** 29 (2022).

163. Reiserer, A. & Rempe, G. Cavity-based quantum networks with single atoms and optical photons. *Reviews of Modern Physics* **87,** 1379 (2015).

164. Aspelmeyer, M., Kippenberg, T. J. & Marquardt, F. Cavity optomechanics. *Reviews of Modern Physics* **86,** 1391 (2014).

165. Schliesser, A. & Kippenberg, T. J. in *Advances In Atomic, Molecular, and Optical Physics* 207–323 (Elsevier, 2010).

166. Eichenfield, M., Chan, J., Camacho, R. M., Vahala, K. J. & Painter, O. Optomechanical crystals. *Nature* **462,** 78–82 (2009).

167. Benedikter, J., Moosmayer, T., Mader, M., Hümmer, T. & Hunger, D. Transverse-mode coupling effects in scanning cavity microscopy. *New Journal of Physics* **21,** 103029 (2019).

168. Mader, M., Reichel, J., Hänsch, T. W. & Hunger, D. A scanning cavity microscope. *Nature Communications* **6,** 7249 (2015).

169. Needham, L.-M. *et al.* Label-free detection and profiling of individual solution-phase molecules. *Nature,* 1–7 (2024).

170. Rayleigh, L. CXII. The problem of the whispering gallery. *The London, Edinburgh, and Dublin Philosophical Magazine and Journal of Science* **20,** 1001–1004 (1910).

171. Rayleigh, L. IX. Further applications of Bessel's functions of high order to the Whispering Gallery and allied problems. *The London, Edinburgh, and Dublin Philosophical Magazine and Journal of Science* **27,** 100–109 (1914).

172. Zhi, Y., Yu, X.-C., Gong, Q., Yang, L. & Xiao, Y.-F. Single nanoparticle detection using optical microcavities. *Advanced Materials* **29,** 1604920 (2017).

173. Chiasera, A. *et al.* Spherical whispering-gallery-mode microresonators. *Laser & Photonics Reviews* **4,** 457–482 (2010).

174. Vollmer, F. *et al.* Protein detection by optical shift of a resonant microcavity. *Applied Physics Letters* **80,** 4057–4059 (2002).

175. Hanumegowda, N. M., Stica, C. J., Patel, B. C., White, I. & Fan, X. Refractometric sensors based on microsphere resonators. *Applied Physics Letters* **87,** 201107 (2005).

176. Kippenberg, T., Spillane, S., Armani, D. & Vahala, K. Fabrication and coupling to planar high-Q silica disk microcavities. *Applied Physics Letters* **83,** 797–799 (2003).

177. Park, J. *et al.* Titanium dioxide whispering gallery microcavities. *Advanced Optical Materials* **2,** 711–717 (2014).

178. Armani, D., Kippenberg, T., Spillane, S. & Vahala, K. Ultra-high-Q toroid microcavity on a chip. *Nature* **421,** 925–928 (2003).

179. Vollmer, F., Arnold, S. & Keng, D. Single virus detection from the reactive shift of a whispering-gallery mode. *Proceedings of the National Academy of Sciences* **105,** 20701–20704 (2008).

180. Zhu, J. *et al.* On-chip single nanoparticle detection and sizing by mode splitting in an ultrahigh-Q microresonator. *Nature Photonics* **4,** 46–49 (2010).

181. He, L., Monifi, F., Huang, S. H., Long, G. L. & Yang, L. Highly sensitive detection of nanoparticles with a self-referenced and self-heterodyned whispering-gallery Raman microlaser. *PNAS* **111,** 13255–13256 (2014).

182. Shao, L. *et al.* Detection of single nanoparticles and lentiviruses using microcavity resonance broadening. *Advanced Materials* **25,** 5616–5620 (2013).

183. Hu, Y. *et al.* Mode broadening induced by nanoparticles in an optical whispering-gallery microcavity. *Physical Review A* **90,** 043847 (2014).

184. Jiang, X.-F. *et al.* Highly unidirectional emission and ultralow-threshold lasing from on-chip ultrahigh-Q microcavities. *Advanced Materials* **24,** OP260–OP264 (2012).

185. Gmachl, C. *et al.* High-power directional emission from microlasers with chaotic resonators. *Science* **280,** 1556–1564 (1998).

186. Liu, W., Chen, Y.-L., Tang, S.-J., Vollmer, F. & Xiao, Y.-F. Nonlinear sensing with whispering-gallery mode microcavities: from label-free detection to spectral fingerprinting. *Nano Letters* **21,** 1566–1575 (2021).

187. Huang, S. H. *et al.* Surface-enhanced Raman scattering on dielectric microspheres with whispering gallery mode resonance. *Photonics Research* **6,** 346–356 (2018).

188. Anderson, M. S. Nonplasmonic surface enhanced Raman spectroscopy using silica microspheres. *Applied Physics Letters* **97** (2010).

189. Evans, C. C., Liu, C. & Suntivich, J. TiO2 nanophotonic sensors for efficient integrated evanescent Raman spectroscopy. *ACS Photonics* **3,** 1662–1669 (2016).

190. Mahmoudi, M. *et al.* Variation of protein corona composition of gold nanoparticles following plasmonic heating. *Nano Letters* **14,** 6–12 (2014).

191. Murgida, D. H. & Hildebrandt, P. Disentangling interfacial redox processes of proteins by SERR spectroscopy. *Chemical Society Reviews* **37,** 937–945 (2008).

192. Zhang, X. *et al.* Symmetry-breaking-induced nonlinear optics at a microcavity surface. *Nature Photonics* **13,** 21–24 (2019).

193. Dominguez-Juarez, J. L., Kozyreff, G. & Martorell, J. Whispering gallery microresonators for second harmonic light generation from a low number of small molecules. *Nature Communications* **2,** 254 (2011).

194. Chen, J.-h. *et al.* Microcavity nonlinear optics with an organically functionalized surface. *Physical Review Letters* **123,** 173902 (2019).

195. Picqué, N. & Hänsch, T. W. Frequency comb spectroscopy. *Nature Photonics* **13,** 146–157 (2019).

196. Suh, M.-G., Yang, Q.-F., Yang, K. Y., Yi, X. & Vahala, K. J. Microresonator soliton dual-comb spectroscopy. *Science* **354,** 600–603 (2016).

197. Joannopoulos, J. D., Villeneuve, P. R. & Fan, S. Photonic crystals. *Solid State Communications* **102,** 165–173 (1997).

198. Wang, C., Quan, Q., Kita, S., Li, Y. & Lončar, M. Single-nanoparticle detection with slot-mode photonic crystal cavities. *Applied Physics Letters* **106,** 261105 (2015).

199. Ryckman, J. D. & Weiss, S. Low mode volume slotted photonic crystal single nanobeam cavity. *Applied Physics Letters* **101,** 071104 (2012).

200. Liang, F. & Quan, Q. Detecting single gold nanoparticles (1.8 nm) with ultrahigh-Q air-mode photonic crystal nanobeam cavities. *ACS Photonics* **2,** 1692–1697 (2015).

201. Sancho, J. *et al.* Integrable microwave filter based on a photonic crystal delay line. *Nature Communications* **3,** 1075 (2012).

202. Maigyte, L. & Staliunas, K. Spatial filtering with photonic crystals. *Applied Physics Reviews* **2,** 011102 (2015).

203. Gao, Y. *et al.* High-speed electro-optic modulator integrated with graphene-boron nitride heterostructure and photonic crystal nanocavity. *Nano Letters* **15,** 2001–2005 (2015).

204. Li, M. *et al.* Lithium niobate photonic-crystal electro-optic modulator. *Nature Communications* **11,** 4123 (2020).

205. Baba, T. Slow light in photonic crystals. *Nature Photonics* **2,** 465–473 (2008).

206. Biswas, U., Nayak, C. & Rakshit, J. K. Fabrication techniques and applications of two-dimensional photonic crystal: history and the present status. *Optical Engineering* **62,** 010901 (2023).

207. Tétreault, N. *et al.* Dielectric planar defects in colloidal photonic crystal films. *Advanced Materials* **16,** 346–349 (2004).

208. Cheng, C.-C. & Scherer, A. Fabrication of photonic band-gap crystals. *Journal of Vacuum Science & Technology B: Microelectronics and Nanometer Structures Processing, Measurement, and Phenomena* **13,** 2696–2700 (1995).

209. Feiertag, G. *et al.* Fabrication of photonic crystals by deep x-ray lithography. *Applied Physics Letters* **71,** 1441–1443 (1997).

210. Campbell, M., Sharp, D., Harrison, M., Denning, R. & Turberfield, A. Fabrication of photonic crystals for the visible spectrum by holographic lithography. *Nature* **404,** 53–56 (2000).

211. Bogaerts, W. *et al.* Fabrication of photonic crystals in silicon-on-insulator using 248-nm deep UV lithography. *IEEE Journal of Selected Topics in Quantum Electronics* **8,** 928–934 (2002).

212. Guo, L. J. Nanoimprint lithography: methods and material requirements. *Advanced Materials* **19,** 495–513 (2007).

213. Chow, E., Grot, A., Mirkarimi, L., Sigalas, M. & Girolami, G. Ultracompact biochemical sensor built with two-dimensional photonic crystal microcavity. *Optics Letters* **29,** 1093–1095 (2004).

214. Akahane, Y., Asano, T., Song, B.-S. & Noda, S. High-Q photonic nanocavity in a two-dimensional photonic crystal. *nature* **425,** 944–947 (2003).

215. Noda, S., Chutinan, A. & Imada, M. Trapping and emission of photons by a single defect in a photonic bandgap structure. *nature* **407,** 608–610 (2000).

216. Dorfner, D. *et al.* Silicon photonic crystal nanostructures for refractive index sensing. *Applied Physics Letters* **93,** 181103 (2008).

217. Di Falco, A., O'Faolain, L. & Krauss, T. F. Chemical sensing in slotted photonic crystal heterostructure cavities. *Applied Physics Letters* **94,** 063503 (2009).

218. Lee, M. & Fauchet, P. M. Two-dimensional silicon photonic crystal based biosensing platform for protein detection. *Optics Express* **15,** 4530–4535 (2007).

219. Hsiao, F.-l. & Lee, C. Computational study of photonic crystals nano-ring resonator for biochemical sensing. *IEEE Sensors Journal* **10,** 1185–1191 (2010).

220. Hsiao, F.-L. & Lee, C. Nanophotonic biosensors using hexagonal nanoring resonators: computational study. *Journal of Micro/Nanolithography, MEMS, and MOEMS* **10,** 013001 (2011).

221. Ho, C. P., Li, B., Danner, A. J. & Lee, C. Design and modeling of 2-D photonic crystals based hexagonal triple-nano-ring resonators as biosensors. *Microsystem Technologies* **19,** 53–60 (2013).

222. Wang, J., Wang, C., Han, Z. & Tian, H. On-chip trapping and sorting of nanoparticles using a single slotted photonic crystal nanobeam cavity. *Optics Express* **30,** 11192–11202 (2022).

223. Sünner, T. *et al.* Photonic crystal cavity based gas sensor. *Applied Physics Letters* **92,** 261112 (2008).

224. Jágerská, J., Zhang, H., Diao, Z., Le Thomas, N. & Houdré, R. Refractive index sensing with an air-slot photonic crystal nanocavity. *Optics Letters* **35,** 2523–2525 (2010).

225. Keng, D., McAnanama, S., Teraoka, I. & Arnold, S. Resonance fluctuations of a whispering gallery mode biosensor by particles undergoing Brownian motion. *Applied Physics Letters* **91** (2007).

226. Milonni, P. W. & Eberly, J. H. *Laser physics* (John Wiley & Sons, 2010).

227. Bachor, H.-A. & Ralph, T. C. *A guide to experiments in quantum optics* (John Wiley & Sons, 2019).

228. Siegman, A. E. *Lasers* (University science books, 1986).

229. Dolan, P. R. *Ultra-small open access microcavities for enhancement of the light-matter interaction* PhD thesis (University of Oxford, 2012).

230. Bethe, H. A. & Schwinger, J. *Perturbation theory for cavities* (Massachusetts Institute of Technology, Radiation Laboratory, 1943).

231. Waldron, R. Perturbation theory of resonant cavities. *Proceedings of the IEE-Part C: Monographs* **107,** 272–274 (1960).

232. Dressel, M. & Grüner, G. *Electrodynamics of solids: optical properties of electrons in matter* (Cambridge university press, 2002).

233. Stokes, G. G. On the composition and resolution of streams of polarized light from different sources. *Transactions of the Cambridge Philosophical Society* **9,** 399 (1851).

234. Chandrasekar, S. *Radiative Transfer* (Dover Publications, 1960).

235. Gans, R. Über die form ultramikroskopischer goldteilchen. *Annalen der Physik* **342,** 881–900 (1912).

236. Johnson, P. B. & Christy, R.-W. Optical constants of the noble metals. *Physical Review B* **6,** 4370 (1972).

237. Perrin, F. Mouvement brownien d'un ellipsoide-I. Dispersion diélectrique pour des molécules ellipsoidales. *Journal de Physique et Le Radium* **5,** 497–511 (1934).

238. Koenig, S. H. Brownian motion of an ellipsoid. A correction to Perrin's results. *Biopolymers: Original Research on Biomolecules* **14,** 2421–2423 (1975).

239. Kumar, A. H., Thomson, S. J., Powers, T. R. & Harris, D. M. Taylor dispersion of elongated rods. *Physical Review Fluids* **6,** 094501 (2021).

240. Han, Y., Alsayed, A., Nobili, M. & Yodh, A. G. Quasi-two-dimensional diffusion of single ellipsoids: Aspect ratio and confinement effects. *Physical Review E* **80,** 011403 (2009).

241. Tirado, M. M. & De La Torre, J. G. Rotational dynamics of rigid, symmetric top macromolecules. Application to circular cylinders. *The Journal of Chemical Physics* **73,** 1986–1993 (1980).

242. Nixon-Luke, R. & Bryant, G. A depolarized dynamic light scattering method to calculate translational and rotational diffusion coefficients of nanorods. *Particle & Particle Systems Characterization* **36,** 1800388 (2019).

243. Broersma, S. Viscous force constant for a closed cylinder. *The Journal of Chemical Physics* **32,** 1632–1635 (1960).

244. Shelton, W. A., Bonin, K. D. & Walker, T. G. Nonlinear motion of optically torqued nanorods. *Physical Review E—Statistical, Nonlinear, and Soft Matter Physics* **71,** 036204 (2005).

245. Simpson, S. H., Benito, D. C. & Hanna, S. Polarization-induced torque in optical traps. *Physical Review A—Atomic, Molecular, and Optical Physics* **76,** 043408 (2007).

246. Smith, P., Ashkin, A. & Tomlinson, W. Four-wave mixing in an artificial Kerr medium. *Optics letters* **6,** 284–286 (1981).

247. Ashkin, A., Dziedzic, J. & Smith, P. Continuous-wave self-focusing and self-trapping of light in artificial Kerr media. *Optics letters* **7,** 276–278 (1982).

248. Volpe, G. & Volpe, G. Simulation of a Brownian particle in an optical trap. *American Journal of Physics* **81,** 224–230 (2013).

249. Chang, S.-S., Shih, C.-W., Chen, C.-D., Lai, W.-C. & Wang, C. C. The shape transition of gold nanorods. *Langmuir* **15,** 701–709 (1999).

250. Baffou, G., Quidant, R. & García de Abajo, F. J. Nanoscale control of optical heating in complex plasmonic systems. *ACS Nano* **4,** 709–716 (2010).

251. Kalmykov, Y. P. & Coffey, W. T. *Langevin Equation, The: With Applications To Stochastic Problems in Physics, Chemistry and Electrical Engineering* (World Scientific, 2012).

252. Babič, D., Schmitt, C. & Bechinger, C. Colloids as model systems for problems in statistical physics. *Chaos: An Interdisciplinary Journal of Nonlinear Science* **15,** 026114 (2005).

253. Malmir, K. *Characterization of nanoparticles with optical fluidic cavity* PhD thesis (University of Oxford, 2022).

254. Hajizadeh, F. *et al.* Brownian fluctuations of an optically rotated nanorod. *Optica* **4,** 746–751 (2017).

255. Lehmuskero, A., Ogier, R., Gschneidtner, T., Johansson, P. & Kall, M. Ultrafast spinning of gold nanoparticles in water using circularly polarized light. *Nano Letters* **13,** 3129–3134 (2013).

256. Shao, L., Yang, Z.-J., Andrén, D., Johansson, P. & Kall, M. Gold nanorod rotary motors driven by resonant light scattering. *ACS Nano* **9,** 12542–12551 (2015).

257. Yang, K., Lu, C., Zhao, X. & Kawamura, R. From bead to rod: Comparison of theories by measuring translational drag coefficients of micron-sized magnetic bead-chains in Stokes flow. *PLOS One* **12,** e0188015 (2017).

258. Oberbeck, A. Ueber stationäre Flüssigkeitsbewegungen mit Berücksichtigung der inneren Reibung. *Journal für die reine und angewandte Mathematik* **81,** 62–80 (1876).

259. Yee, K. Numerical solution of initial boundary value problems involving Maxwell's equations in isotropic media. *IEEE Transactions on Antennas and Propagation* **14,** 302–307 (1966).

260. Lam, D. H. *Finite Difference Methods for Electromagnetic Scattering Problems* PhD thesis (Mississippi State University, 1969).

261. Taflove, A. & Brodwin, M. E. Numerical solution of steady-state electromagnetic scattering problems using the time-dependent Maxwell's equations. *IEEE Transactions on Microwave Theory and Techniques* **23,** 623–630 (1975).

262. Stratton, J. A. *Electromagnetic theory* (John Wiley & Sons, 2007).

263. Sheppard, C. Approximate calculation of the reflection coefficient from a stratified medium. *Pure and Applied Optics: Journal of the European Optical Society Part A* **4,** 665 (1995).

264. Sellmeier, W. Ueber die durch die Aetherschwingungen erregten Mitschwingungen der Körpertheilchen und deren Rückwirkung auf die ersteren, besonders zur Erklärung der Dispersion und ihrer Anomalien. *Annalen der Physik* **223,** 525–554 (1872).

265. DeMichelis, C. Laser induced gas breakdown: a bibliographical review. *IEEE Journal of Quantum Electronics* **5,** 188–202 (1969).

266. Shibata, S., Hagen, N., Kawabata, S. & Otani, Y. Compact and high-speed Stokes polarimeter using three-way polarization-preserving beam splitters. *Applied Optics* **58,** 5644–5649 (2019).

267. Schaefer, B., Collett, E., Smyth, R., Barrett, D. & Fraher, B. Measuring the Stokes polarization parameters. *American Journal of Physics* **75,** 163–168 (2007).

268. Analytical, M. *Zetasizer Nano Series User Manual* (2017).

269. Nikoobakht, B. & El-Sayed, M. A. Evidence for bilayer assembly of cationic surfactants on the surface of gold nanorods. *Langmuir* **17,** 6368–6374 (2001).

270. Zhou, X. *et al.* Supragingival microbes. *Atlas of Oral Microbiology: From Healthy Microflora to Disease,* 81–143 (2020).